UNIONE EUROPEA
Fondo Sociale Europeo

REPUBBLICA
ITALIANA

REGIONE CALABRIA
Assessorato Cultura,
Istruzione e Ricerca
Dipartimento 11

La presente Tesi di dottorato è cofinanziata con il sostegno della Commissione Europea, Fondo Sociale Europeo e della Regione Calabria. L'autore è il solo responsabile di questa Tesi e la Commissione Europea e la Regione Calabria declinano ogni responsabilità sull'uso che potrà essere fatto delle informazioni in essa contenute.

To my father

and to the loving memory of Micol

Abstract

The Farneto del Principe dam is located in the Calabria region, a seismically active area in southern Italy.

Analysis of the dynamic behavior of this type of structures requires evaluation of the seismic demands to which it can reasonably be expected to be subjected in future earthquake events.

Demand evaluation usually occurs in two phases: (1) Probabilistic seismic hazard analysis (PSHA) and (2) selection of an appropriate suite of acceleration time series for use in response history analysis. A site-speific PSHA for the Farneto del Principe dam site was developed. The main features of this analysis are the inclusion of two newly implemented seismogenic sources (Lakes fault and subduction interface of the Calabrian arc) and a modern ground motion prediction equation logic tree that includes recent global models. Sensitivity studies are also presented. The results of the PSHA were used to define two target spectra, a Uniform Hazard Spectrum (UHS) and a scenario spectrum (Conditional Spectrum, CS). The target spectra were used for selecting and scaling appropriate acceleration time series suites. The computation of the CS and the time series suites selection were based on the natural periods and mode shapes of the dam numerically evaluated by the Finite Element Method.

On these basis, the reliability of the response history analysis is ensured by the rigorous procedure used to evaluate the acceleration time-histories.

The seismic response of the Farneto del Principe dam to these hazard-consistent ground motion suites was evaluated by means of several two-dimensional numerical analyses. For evaluating the performance of the dam, typical results are presented and discussed.

Acknowledgements

I would like to thank Prof. Giovanni Dente, my supervisor that gave me the opportunity to perform this research and gave me fundamental advices, not only on technical issues, but also on fundamentals of life.

A special thanks goes to Prof. Jonathan P. Stewart, that carefully reviewed a large part of this thesis, gave me precious advices that are for me daily source of inspiration and for gave me the opportunity to live an unforgettable life and research experiencein his group at UCLA.

I want to say thank you to Prof. Ernesto Ausilio, for supporting me during the last years, for the inspiring discussions and suggestions, for the geotechnical (and life!) lessons and for gave me the chance to work close to him, learning from his actions more than from his words.

Thanks to Prof. Enrico Conte, for the technical discussions and for the support that he gave me since I was a young student.

I'm thankful to Prof. Antonello Troncone and Prof. Roberto Cairo, for the several technical discussions and for the long time spent together.

I would like to thank Dr. Vincenzo Spina for the fruitful discussions on the Lakes fault implementation and on the Calabrian tectonic settings, to Dr. Francesco Muto for the suggestions about the Crati Valley fault and on the regional fault setting and to Prof. Ignazio Guerra for the discussions on the Calabrian arc subduction zone implementation in this thesis.

Thanks to Prof. Massimo Mancuso for precious discussions and advices about the modal analysis and about the numerical modeling techniques.

Thanks to the Openquake developers and users, in particular to Dr. D. Monelli, Dr. M. Pagani, and Dr. L. Danciu, for the suggestions about the Openquake PSHA implementation.

Thanks to the UCLA and UNICAL graduate students and Ph.D.

Thanks to my lovely family, my mom and my sister for sustaining me and for making me a better person every day more.

Finally thanks to a special person: Maria Giovanna, thank you for your support in the last three years for being with me even from the opposite side of the world.

TABLE OF CONTENTS

LIST OF FIGURES

LIST OF TABLES

1 Introduction

1.1 Background, Motivation and Scope of the Work

Earth dams and embankments are fundamental structures for human economy and activities. For this reason, the analysis of their behavior under static and dynamic condition is among the most studied argument in the modern geotechnical engineering.

As shown by Penman (1986) (Figure 1.1), in the last two centuries the increasing of world population, the number of large embankment dams and the heights of these structures had a great increment.

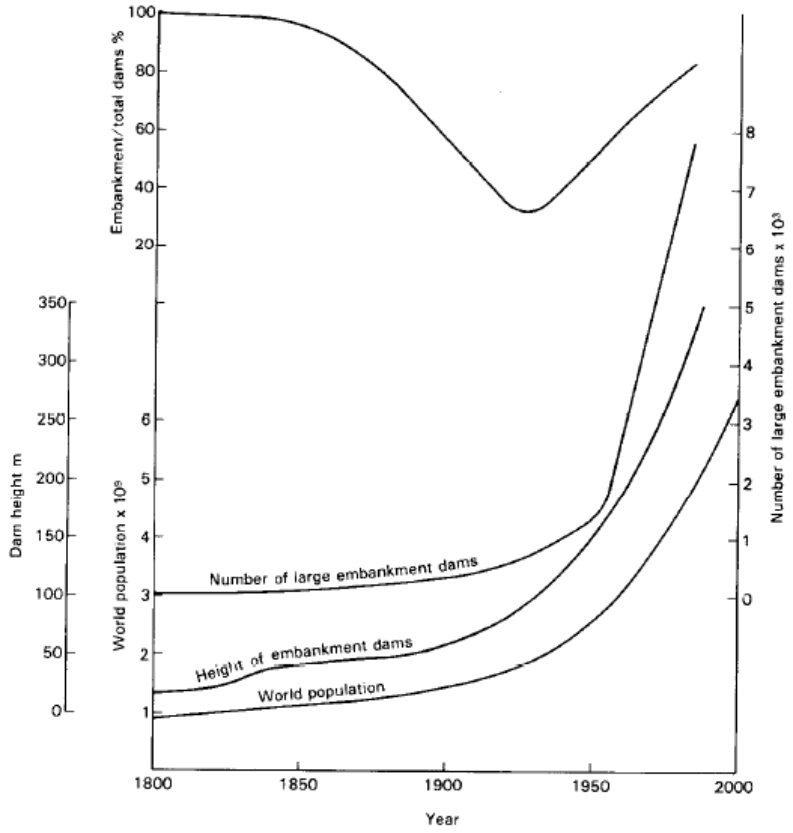

Figure 1.1 Embankment dams statistics 1800-1985 (from Penaman, 1986).

Fundamental improvements to the state-of-the-art of geotechnical engineering was done studying the behavior of earth dams. Casagrande (1961) and Newmark (1965) have made important contributions, not only in earth dam context, but useful for general applications. Seed (1979) improved the knowledge on the geotechnical earthquake engineering taking advantage from the study of the seismic behavior of earth and rockfill dams. Many other researchers and practitioners studied and are studying these structures, because if damages (or even worse, failure) occur to a dam, the consequences could be dramatic.

Under static condition there are essentially three types of causes that are responsible for damaging earth dams: (1) hydraulic (overtopping); (2) seepage problems (e.g. piping); (3) structural (e.g. sliding). Foster et al. (2000) analyzed a world database composed by 1462 earth dams showing that damages and failures, under static conditions, occur in the first five years after the construction (due to errors in the constructions) or after a long period of aging.

Under dynamic conditions, several case studies over the years shown that earthquake can cause damages and failure in earth dams (e.g. the lower San Fernando dam during the 1971 eartquake and the Fujinuma dam during the Tohoku, 2011 earthquake) for different reasons and phenomena (e.g. liquefaction, mass sliding). Several studies are investigated the seismic-induced damages to different types of earth dams, relating the damages to a specific intensity measure: the peak ground acceleration (e.g. Swaisgood, 2003, Ishiara 2010).

In this study, the seismic response of the Farneto del Principe dam in the Calabria region (southern Italy) is presented. The case study was investigated in order to understand the current behavior under static conditions, taking into account the ground-water flow within the dam body by means of several measurements and data available from the monitoring system of the dam. Since the dam is located in a seismically active region, it is obvious that a critical issue is the evaluation of the seismic response of the dam. A fundamental step in forecasting the seismic behavior of an earth dam is the evaluation of the seismic demands to which it can reasonably be expected to be subjected in future earthquake events. This process is not trivial and involves at least two fundamental steps: (1) Probabilistic seismic hazard analysis (PSHA) (Cornell, 1968, McGuire, 2004) to evaluate exceedance probabilities for ground motion intensity measures, and (2) selection of an appropriate suite of acceleration time histories for use in response history analysis. The state-of-practice in Italy as implemented in the most recent Italian Building Code,

(Norme Tecniche per le Costruzioni, NTC, 2008), is based on very old local ground motion prediction equations (Sabetta and Pugliese, 1996; Ambraseys et al., 1996) and on a seismogenic zonation (zonazione sismogenetica, ZS ver. 9) ZS9 (Meletti and Valensise, 2004, Meletti et al., 2008), based only on areal sources with equal rate of seismicity. The most recent Euro-Mediterranean model (SHARE, Giardini et al., 2013), contains more sophisticated elements, but it was derived for the whole European area, so it cannot contains site-specific elements. In this work we present a site-speific PSHA for the Farneto del Principe dam site. The main features of this analysis are the inclusion of two seismogenic sources that are not present in the current Italian stat-of-the-art (Lakes fault and subduction interface of the Calabrian arc) and a modern ground motion prediction equation logic tree that includes recent global models. Sensitivity studies are also presented. The results of the PSHA were used to define two target spectra, a Uniform Hazard Spectrum (UHS) and a scenario spectrum (Conditional Spectrum, CS, Baker and Cornell, 2006). The site-specific UHS and CS were then used as target for selecting and scaling acceleration time series suites to use in numerical analyses. The computation of the CS and the time series suites selection was based on the fundamental period of the dam system (including the foundation) numerically evaluated by solving the eigenvalue problem using the Finite Element Method approach as implemented in the code SAP 2000 (CSI, 2013). The seismic response of the Farneto del Principe dam to both hazard-consistent ground motion suites was evaluated by means of several two-dimensional numerical analyses conducted using an explicit finite difference software specifically developed for geotechnical engineering applications: FLAC 2D (Itasca, 2005).

The results of the analyses were carefully studied according to currently used literature findings. Franklin and Chang (1977) proposed the limit value of a meter for the admissibility of the displacements evaluated by using Newmark-like methods. Seed (1979) defined the same limit value for pseudo-static analysis results. Hynes-Griffin and Franklin (1984), pointed out that the acceptable deformation is not unique, but depends on several variables such as the geometry, the dam type, its zonation the freeboard and the volume of the potential sliding mass. We adopt this last approach, evaluating the seismic response of the Farneto del Principe dam, taking into account its own characteristics.

1.2 Thesis Outline

The thesis is made up by a total of five chapters plus an appendix. Chapter 1 presents the motivation for the current research and the organization of the work.

In Chapter 2 the attention is focused on the dam's materials characterization, and on the static monitoring of the Farneto del Principe dam. This aspect represents a fundamental step for the understanding of the health of the structure and it is the starting point for the evaluation of the seismic response. In the first part of the chapter a summary of the main characteristics of the dam body and foundation materials is given. Furthermore a comprehensive analysis of the available monitoring data is presented. Particular care was devoted to the piezometers analysis that gives useful information about the current dam's health.

Chapter 3 contains a careful review of the current state-of-practice in Italy and Europe about probabilistic seismic hazard analysis. Then a site specific PSHA for the Farneto del Principe dam is presented. The study was conducted by using a new open source software (Openquake engine). This analysis contains several original elements, such as the implementation of the Lakes fault a recently discovered seismogenic source and the Calabrian arc subduction zone interface (neglected in the currently used Italian and European PSHA). Moreover a modern ground motion prediction equation (GMPE) logic tree of recent global models (e.g. BSSA, 2014) was specifically developed. Particular attention was dedicated to the uncertainties related to the parameters that we used in the PSHA implementation, by presenting sensitivity studies. Comparisons with other Italian, European and American models are presented in term of hazard curves and uniform hazard spectra (UHS). Finally particular emphasis on the sources that more likely affect the Farneto del Principe dam site was given, by running and interpreting a disaggregation analysis.

In Chapter 4 a ground motion selection and scaling procedure is presented by using as target the UHS developed in Chapter 3. Furthermore a second suite of motions was developed by calculating a scenario spectrum (the conditional spectrum, CS). The computation of the CS and the time series suites selection was based on the natural periods and mode shapes of the dam numerically evaluated with a numerical eigenvalue problem solution by means of the Finite Element Method implemented in the software SAP 2000.

In Chapter 5 several numerical analyses were carried out by using an explicit finite difference method software (FLAC 2D). In this chapter the main issues related to the numerical modeling of earth dams are discussed and a reliable solution is presented by using appropriate boundary conditions and constitutive models. Typical results for both the ground motions suites (UHS and CS) are presented and discussed.

2 The Farneto del Principe dam

2.1 Introduction to the Case Study

In Italy earth dams have a very long tradition, but starting from the second half of the past century, there was an increasing of construction, while, in the last 20 years there was a rapid stall. It is evident that the majority of the Italian earth dams are now in their "old age stage". It is extensively demonstrated that in this kind of construction damages occur, under static condition: or immediately after the end of construction or several years later, due to their ageing (Foster et al. 2000). These observations, joined to the necessity of the managing institution to ensure the complete functionality of these dams, suggest to pay specific attention to the monitoring of their behavior.

In this study, the attention is focused on the analysis of the behavior under static and dynamic conditions of a dam located in the Calabria region (southern Italy), not far from the city of Cosenza (Figure 2.1). The case study is the Farneto del Principe dam (Figures 2.2 and 2.3).

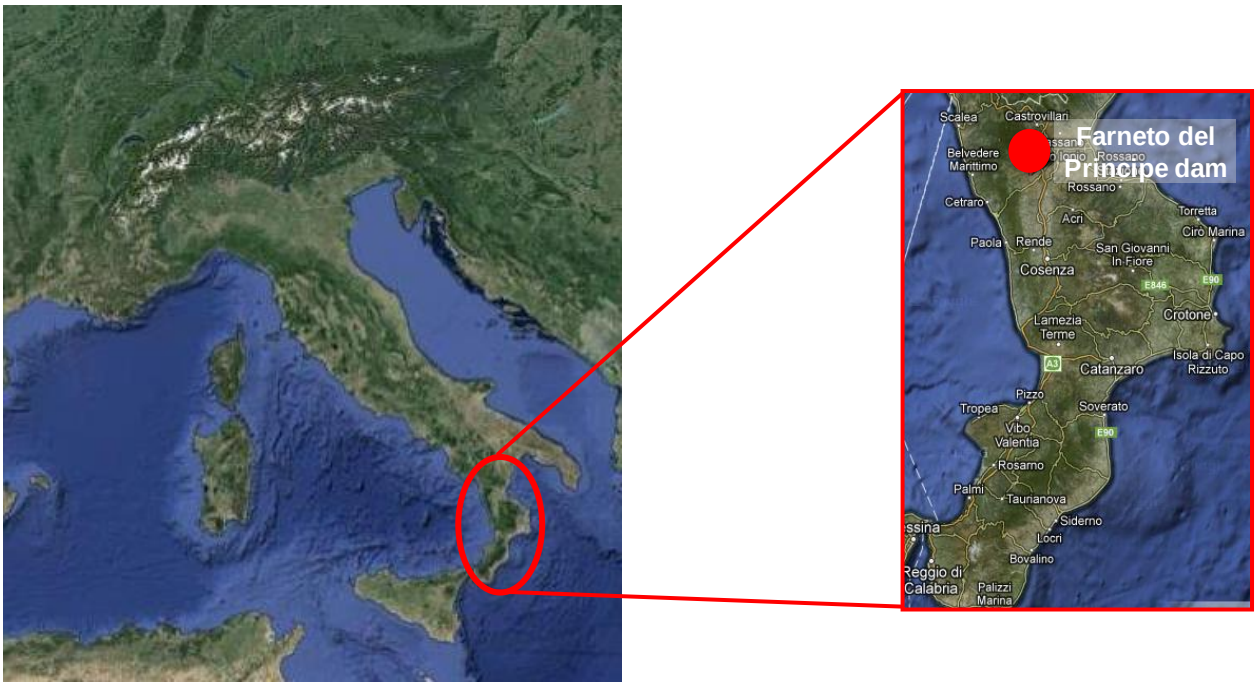

Figure 2.1 **The Farneto del Principe dam location, in the Calabria region (southern Italy).**

Figure 2.2 **Aerial view of the Farneto del Principe dam area in the Calabria region (southern Italy).**

Figure 2.3 **Overview of the Farneto del Principe dam.**

In this section, the attention is focused on the characteristics of the materials, and on the static monitoring of the Farneto del Principe dam. This represents a fundamental step for the understanding of the health of the structure and an important starting point for the evaluation of the seismic response.

The dam objective of the study is a zoned dam, characterized by a central impervious core (composed by clay and silt), used for irrigation and flow balancing. The Farneto del Principe

dam was built between the end of the 70's and the beginning of the 80's, it is in operation from 1989. The maximum authorized water level is 136,30 m on the average sea level (a.s.l.), the crest elevation is 144,40 m a.s.l. and the maximum level of the reservoir is 141,70 m a.s.l.. The height of this dam is about 30 m, the length is more than 1200 m. A summary of the main geometrical characteristics is given in Table 2.1.

Table 2.1 Main geometrical characteristics of the Farneto del Principe dam

Geometrical data	Value
Water storage volume	46 Mm^3
Average height (above the foundation)	27.7 m
Crest length	1240 m
Crest width	7 m
Freeboard (maximum level of the reservoir)*	2.7 m
Freeboard (above the maximum authorized level of the reservoir)*	8.1 m
Upstream face slopes	1:2.5, 1:3, 1:3.5
Downstream face slopes	1:1.85, 1:2.25

* Currently the maximum authorized level of the reservoir is lower than the maximum level of the reservoir.

The dam core is constitued by clay with low permeability, alluvial materials (gravel with sand and sandy gravel) with a high permeability were used for both upstream and downstream shells. The dam core is protected on both sides by two filters (with a thickness of 2 m in total) formed by silt on the core side and by sand and gravel on the shells sides. The dam is founded on an alluvial layer with high permeability, and deformability similar to the shells, that overlay a very stiff clay bed. Because of the high permeability of the alluvial materials on which the dam is founded, in order to avoid ground water flow under the dam body, a cut-off wall was realized, using in part two slurry walls formed by panels excavated in the presence of bentonite mud and in part using a double line of close pile with half meter diameter, without injection of waterproof material. The cut off wall is embedded at least for 3 m into the clay bed for all the dam length. Downstream the core is located an inspection tunnel also used for the collection of the drained water coming from the dam.

The static design of the dam was very accurate and it was made with the geotechnical expert advice of prof. Arrigo Croce, but, at the time of construction the knowledge about the seismic

behavior of this type of structure was very poor. The Farneto del Principe dam is located in a seismically active region characterized by a complex tectonic setting (further information about the seismic sources of southern Italy are given in chapter 3). In this connection, it is very important to evaluate the dam response under seismic excitation.

Several data concerning the geometry, the dam's materials and the static monitoring are available. The first step for performing a reliable seismic analysis of the dam is to determine the stress conditions, taking into account the groundwater flow within the dam body, before the earthquake (Seed 1979).

It becomes obvious the importance of the preliminary analysis voted to the knowledge of the state of the dam in the static field before starting the dynamic response analysis.

As said before, the design phase of the Farneto del Principe dam started at the beginning of the 60's, the construction at the middle of 70's, while the dam started its operation phase in 1989. Due to this timetable it is clear that after half century nowadays, the quantity of documents is huge but the direct knowledge about the structure is small and limited to few people (Figure 2.4, from Bonazzi, 1991). According to Jappelli, 2003, when the age of this kind of structures starts to become significant, the archive information become rare and confused, and the results of monitoring less accurate and incomplete. As expected also for the Farneto del Principe dam, the data currently available are restricted not only in quantity but also in quality.

The objective of this chapter is to obtain an historical-technical synthesis necessary for the evaluation of the current dam's health.

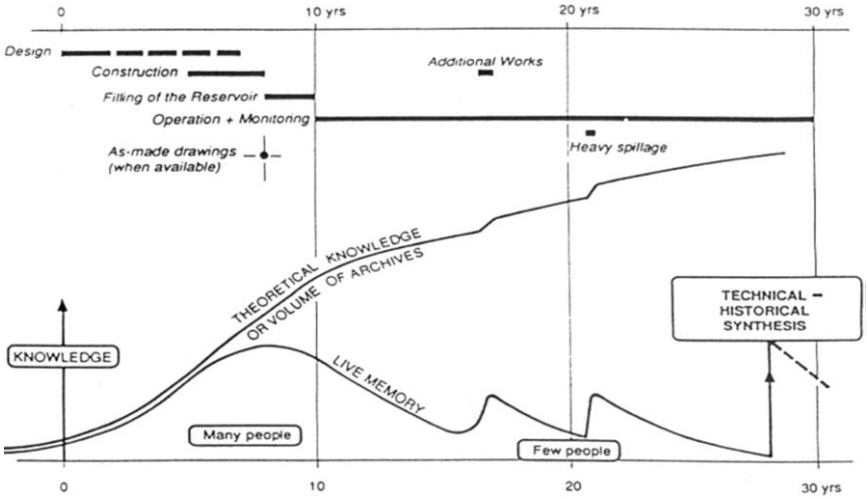

Figure 2.4 Knowledge in the vital cycle of a dam (from Bonazzi, 1991).

2.2 Available Data From Design Phase and Construction Logs

During the design phase of the Farneto del Principe dam several laboratory tests, such as direct shear, triaxial, oedometric tests were performed on undisturbed specimen (and/or reconstituted samples) of the foundation materials (both clay bed and alluvium) and on materials which were candidates for the construction of the dam. During the construction phase, similar tests were performed on the materials that constitute the dam body.

In Table 2.2 a comprehensive summary of the static parameters of the foundation materials (clay bed and alluvium) and of the dam body materials (core and shells) is presented. Table 2.2 shows the mean values and the range of variability where available.

Table 2.2 Summary of the static parameters of the Farneto del Principe dam materials

Symbol	Description	Mean value (Range)			
		Foundation		Dam body	
		Alluvium	Clay bed	Core	Shells
c (kPa)	Cohesion	0	180	80	0
φ (°)	Friction angle	37.5	24	18	40 (39 – 45)
S_U (kPa)	Undrained strength	/	450 (220 – 540)	202 (172 – 232)	/
γ (kN/m)	Unit weight	24.1	21.12 (20.4 – 21.66)	21.31	25.1
γ_d (kN/m)	Dry unit weight	/	17.98 (17.08 – 18.79)	18.07 (17.7 – 18.8)	24.04 (23.5 – 25.07)
γ_s (kN/m)	Particles unit weight	/	27.3	27.3	27
n	Porosity	/	0.36 (0.324 – 0.397)	0.338	0.11
S (%)	Degree of saturation	/	97.2 (89.9 – 100)	95.6	96.7

(continued on next page)

Table 2.2 (cont.) **Summary of the static parameters of the Farneto del Principe dam materials**

Symbol	Description	Mean value (Range)			
		Foundation		Dam body	
		Alluvium	Clay bed	Core	Shells
e	Void ratio	/	0.54 (0.48 – 0.61)	0.51	0.123
PI	Plasticity index	/	18.26 (14.1 – 23.3)	26.16 (22.47 – 29.7)	/
w (%)	Water content	7.5 (7 – 8)	19.54 (16.5 – 23.3)	17.88 (16.39 – 19.55)	4.42 (3.5 – 5.09)
w_L (%)	Liquid limit	/	41.51 (34.5 – 48.8)	45.4 (38.8 – 51.2)	/
w_P (%)	Plastic limit	/	18.26 (20.2 – 25.9)	19.18 (16.23 – 21.4)	/
K (m/sec)	Hydraulic conductivity	$1x10^{-5}$	$1x10^{-10}$ $1x10^{-9}$ - $1x10^{-11}$	$1.29x10^{-9}$	$1x10^{-5}$

For the clay bed materials, information from geophysical in-situ tests, performed during the construction phase, are available. These tests allow to obtain a rough estimation of the average shear wave velocity (V_S) of the clay bed materials that is equal to 1000 m/s. This information is very useful for the numerical model of the dam construction as shown in §5.2.1.

Several grain size distribution curves are available for the foundation materials and for the shells. A confirmation of what was discussed in §2.1 about the archive information is given by the fact that for the core these curves are not available. In Figure 2.5 grain size distribution curves for the clay bed are shown. These materials are characterized by a strong presence of fines content.

In Figure 2.6 grain size distribution curves for the alluvial materials are shown. The range of the curves for these materials is quite large. These soils are mainly characterized by the presence of medium to coarse materials.

Figure 2.7 shows grain size distribution curves for the dam shells. These curves show a range that is similar to the foundation alluvial materials. Likely the materials used to build the dam shells come from the alluvium layers that are present near the dam.

The dam filters on the core sides are composed, on average, by 90% of sand and 10% of gravel. The average composition of the dam filters on the shells sides is characterized by the presence of 50% of sand and 50% of gravel.

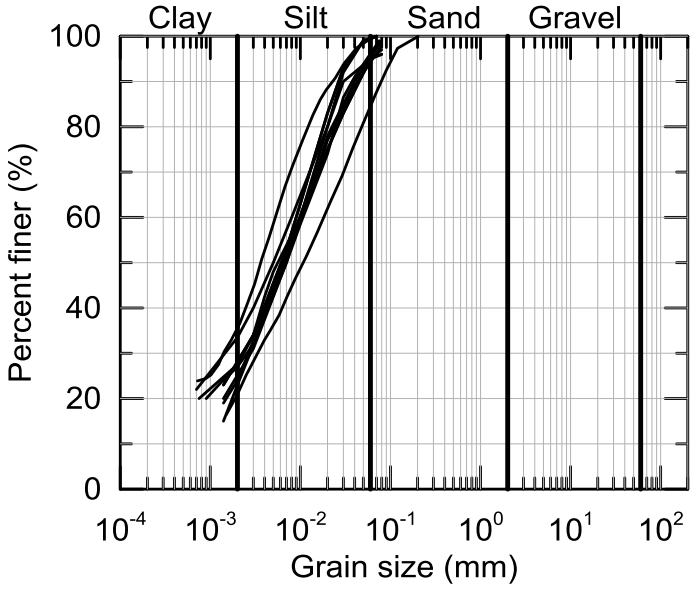

Figure 2.5 Grain size distribution curves for the clay bed materials.

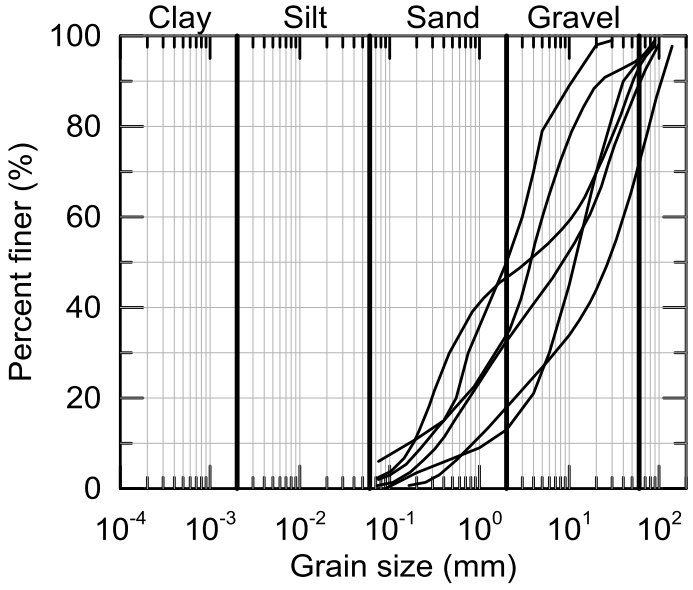

Figure 2.6 Grain size distribution curves for the alluvial materials.

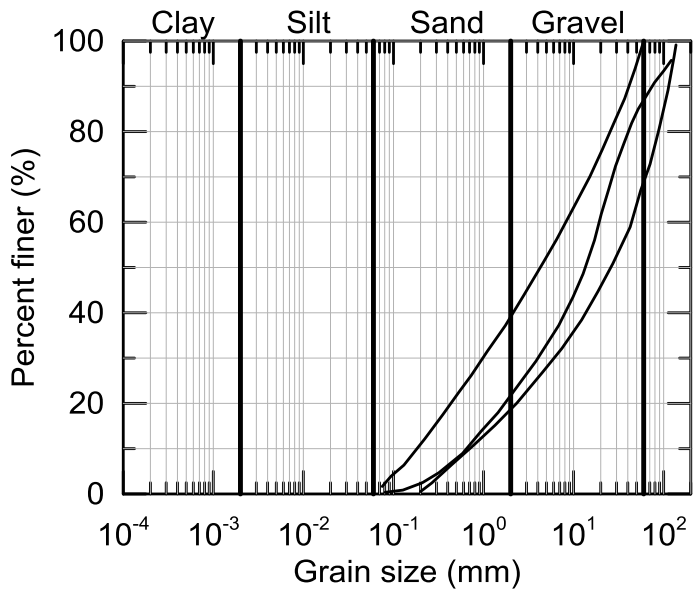

Figure 2.7 Grain size distribution curves for the dam shells materials.

2.3 The Monitoring System of the Farneto del Principe Dam

The Farneto del Principe dam has a complete static monitoring system, but due to the period of its construction, there is an evident lack of dynamic instrumentation.

Four cross sections of the Farneto del Principe dam are instrumented with: rod strain gauges, 32 electro-pneumatic piezometers (eight per each section, four within the dam core and four in the downstream filter on the core side). Other piezometers are located within the dam body, outside the dam (downstream side) and in the right abutment area. In particular, 24 electro-pneumatic piezometers (intended to be used for the ground-water flow control) are located in the inspection tunnel, four Casagrande piezometers (sections 4, 6, 8, 9-10) and four standpipe piezometers (sections 5, 6, 8, 9-10) are located outside the dam body, on the downstream side (not far from rock toe) and three open-tube piezometers are present in the right abutment area. The planimetric view of the monitoring system is reported in Figure 2.8.

The four instrumented cross section are named 2B, 4, 9-10 and 11A (Figure 2.9). The instrumented cross section 4 is shown in Figure 2.10, this cross section is intended to be representative of the others. All the analyses shown in the remainder of this study are referred to this cross section.

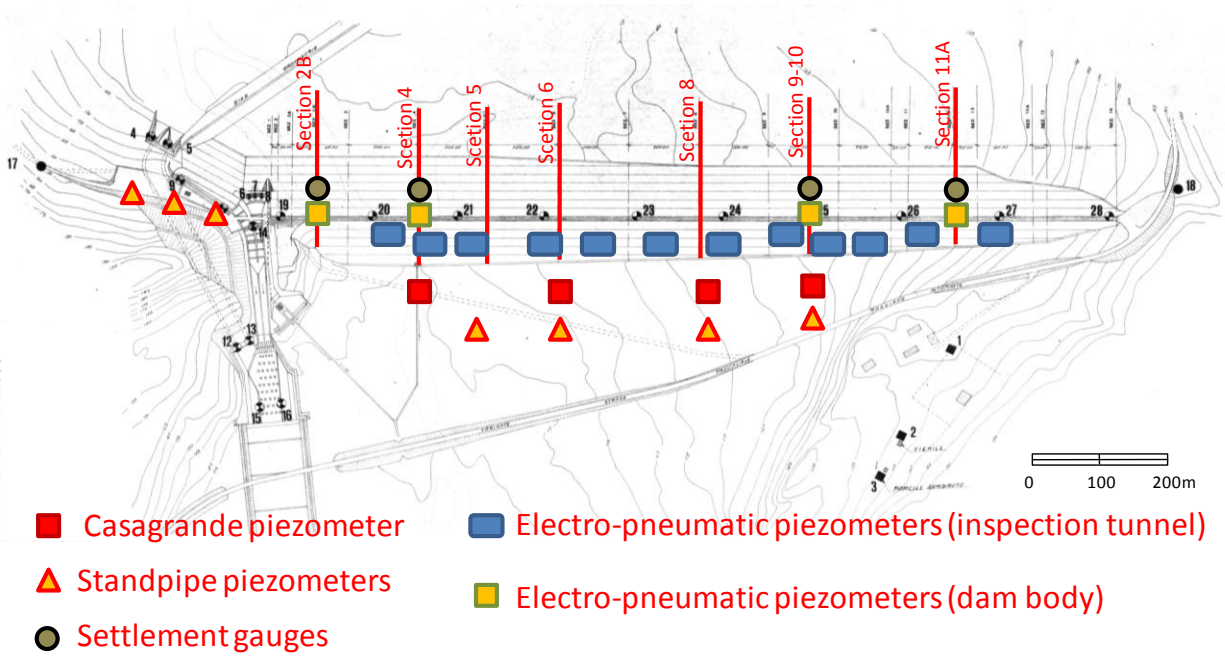

Figure 2.8 **Grain Planimetric view of the Farneto del Principe dam monitoring system.**

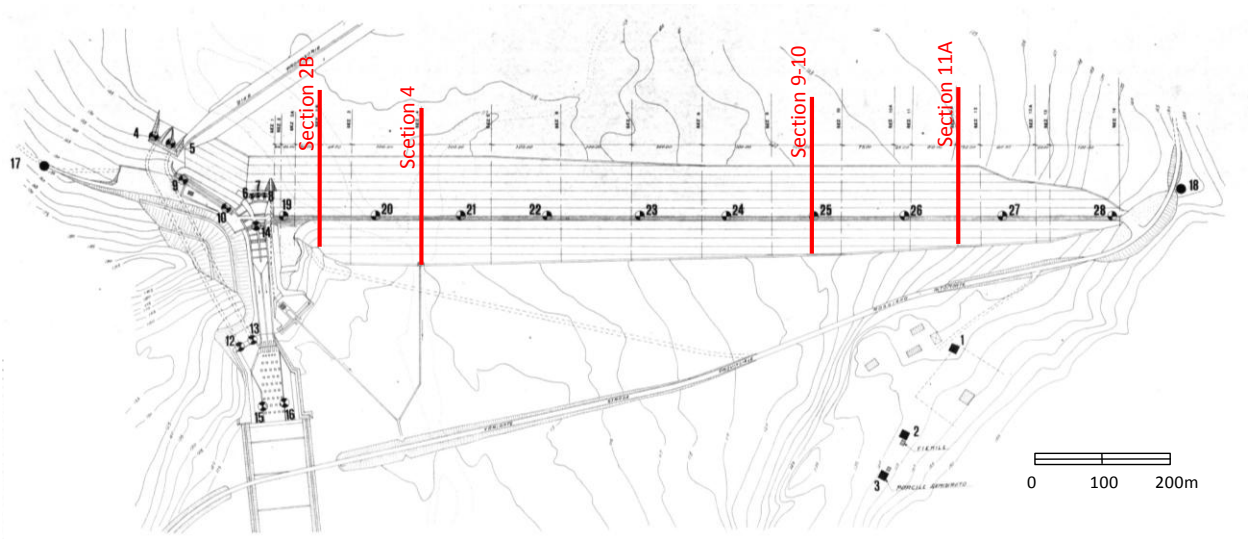

Figure 2.9 **Planimetric view of the four instrumented cross section of the Farneto del Principe dam (2B, 4, 9-10 and 11A).**

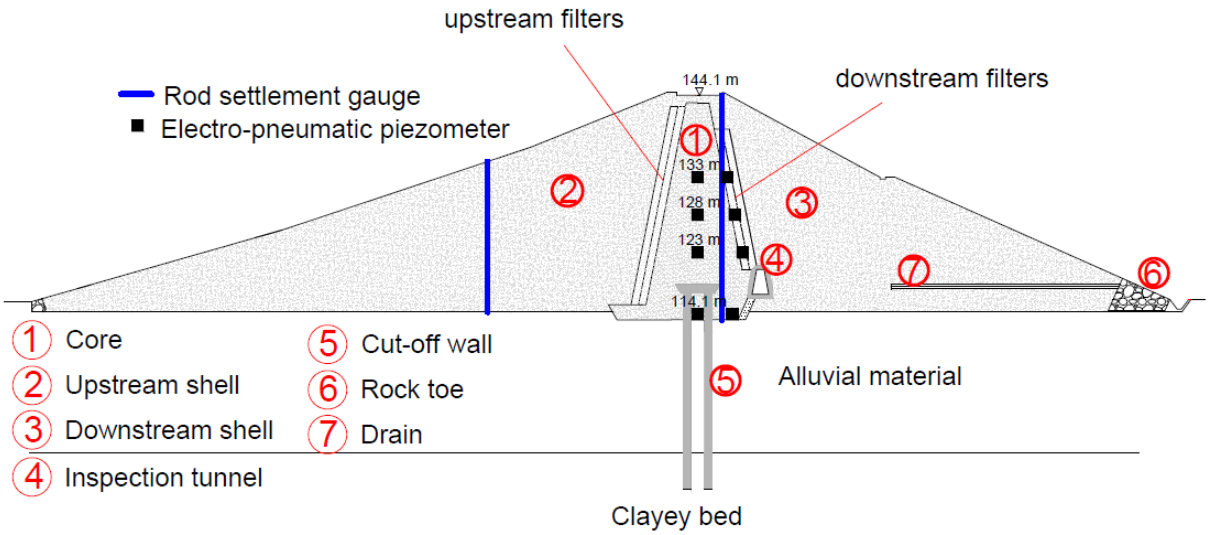

Figure 2.10 Instrumented cross section 4 of the Farneto del Principe dam.

2.3.1 Electro-Pneumatic Piezometers Within the Dam Body and in the Inspection Tunnel

Currently a critical analysis of the available data allows to conclude than only seven electro-pneumatic piezometers within the dam body are working instead of 32 originally installed during the construction phase. These piezometers were intended to be used in order to obtain information about the water level within the core and the ground-water flow within the dam body. About the electro-pneumatic piezometers located in the inspection tunnel, 14 of the 24 originally installed are working fine. These piezometers were placed to have information about the ground-water flow under the dam body and/or through the cut-off wall. These informations are very useful for evaluating the cut-off wall structural integrity. Starting beginning of the operation of the dam from the electro-pneumatic piezometers, did not worked as expected, even though they should be characterized by good reliability and fast response also in materials with low permeability (like the dam core soils). This issue did not allow to evaluate in a reliable manner the ground-water flow within the dam body.

2.3.2 Standpipe and Casagrande Piezometers

The standpipe and the Casagrande piezometers located on the right abutment and outside the dam body are in operation and are working correctly with the exception of the one located in correspondence to section 6. These piezometers are very important for the correct evaluation of several aspects related to the dam's health. In particular, are useful for the correlation between

the ground-water flow under the dam body and for monitoring the variation of the reservoir level. For this reason, they allow to evaluate the presence of infiltrations under the dam body and so the derive the condition of the cut-off wall. Due to the integrity of these piezometers, the information obtained from them overcomes the issues related to the malfunctioning of the electro-pneumatic piezometers in the inspection tunnel. This helps to understand, at least in a simplified manner, the ground-water flow phenomena under the dam body.

2.4 Piezometers Data Interpretation

Taking into account the current knowledge about the monitoring system of the Farneto del Principe dam, it is not easy to interpreter the few data from the electro-pneumatic piezometers. At this stage, the only possibility is to figure out the possible causes of the malfunction of some devices and the dismissing of others. Problem could arise essentially from tubing breaks, leakages, occlusion of the tubes, or problems with the saturation of the porous material and with the membrane of the measuring chamber. All these causes could be related to wrong construction, lack of maintenance and aging.

Different conclusions can be derived for the Casagrande and the standpipe piezometers located in different position outside the dam body. The data from these piezometers gives very important information about the ground-water flow under the dam body.

Figure 2.11(b) shows the data from the Casagrande piezometers located in the sections 8 and 9 and the data from the standpipe piezometers data located in the sections 5, 8 and 9, for the period January 2002 – June 2008. These data are compared with the water level in the reservoir, as shown in Figure 2.11(a) for the same period.

Figure 2.11(c) shows the average monthly rainfall recorded at the Tarsia and Roggiano station. These stations are located close to the dam site. Looking at Figure 2.11 it is possible to notice that the piezometers outside the dam body are not affected by the variation of the water level in the reservoir. This consideration allows to exclude significant ground-water flows under the dam because of the dam core low permeability and because the cut-off wall is likely not broken. We speculate that the constant variations with time observed in the Casagrande and standpipe piezometers can be attributed to the rainfall events seasonality that probably produces the variation of the water level outside the dam body. This remarks is deductible by comparing

the precipitations with the piezometers data. This comparison shows that the peaks (either positive and negative) of the monthly rainfall events are observable with some delay (accounting in a few months) in the piezometers data.

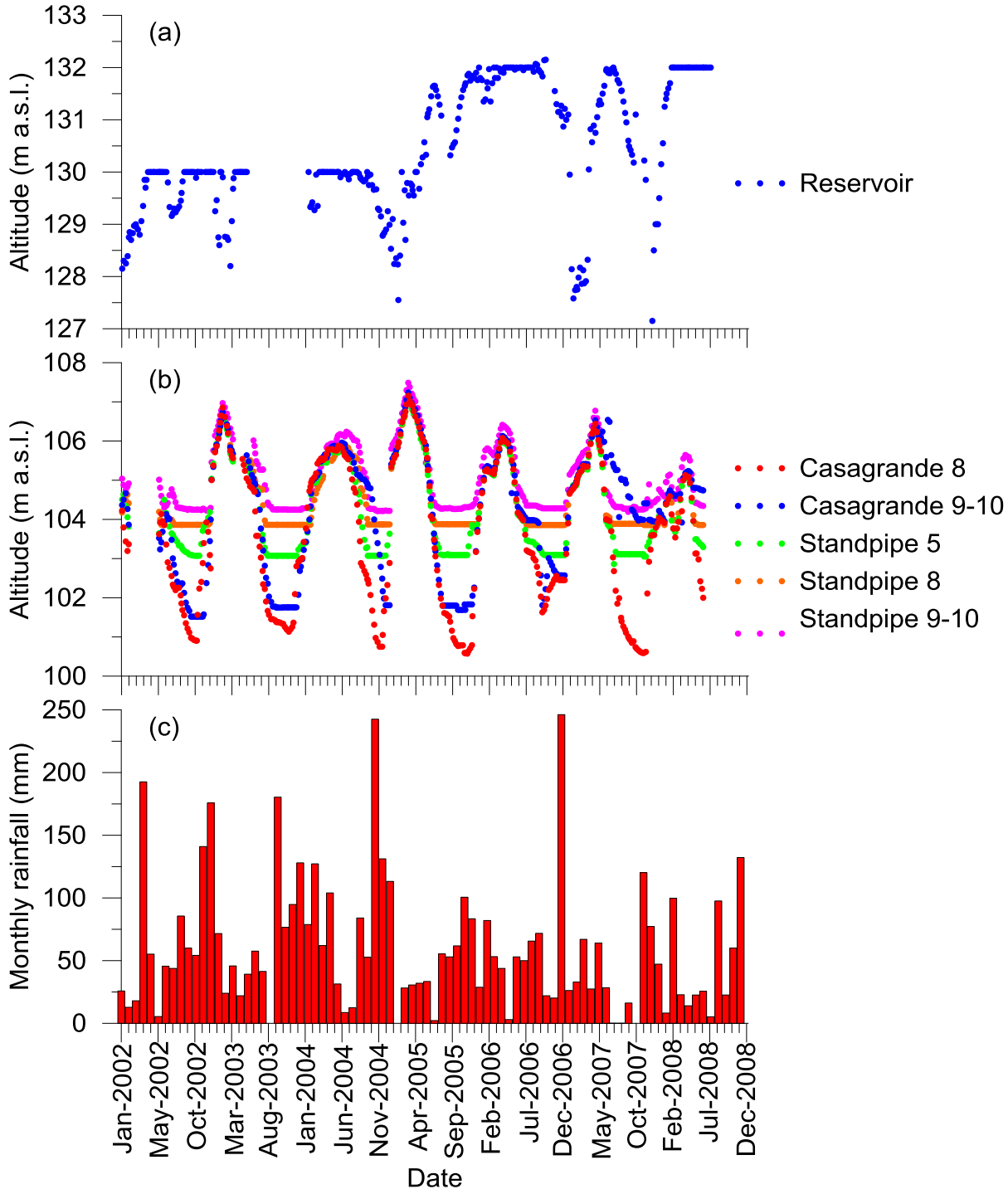

Figure 2.11 **(a) Water level in the reservoir; (b) Casagrande and stand pipe piezometers data; (c) Monthly rainfall. All data are plotted for the period January 2002 to December 2008.**

Another important consideration about the dam's health can be deduced starting from the measurement of the leakages in the inspection tunnel. More specifically, based on the data collected during the period 1991-2011, it is possible to say that water leakage varying in the range 0.015 - 0.53 l/s. These values, taking into account that are relative to all the dam length, can be considered low enough to ensure stability to the dam.

3 Probabilistic Seismic Hazard Analysis for the Farneto del Principe Dam Site

3.1 Probabilistic Seismic Hazard Analysis: State-of-the-Art in Italy and Europe

Analysis of the dynamic behavior of a structure requires evaluation of the seismic demands to which it can reasonably be expected to be subjected in future earthquake events. Demand evaluation usually occurs in two phases: (1) Probabilistic seismic hazard analysis (PSHA) (Cornell, 1968, McGuire, 2004) to evaluate exceedance probabilities for ground motion intensity measures, including pseudo-spectral acceleration (PSA), and (2) selection of an appropriate suite of acceleration time series for use in response history analysis. The results of PSHA are used to define a target spectrum, expressed as a Uniform Hazard Spectra (UHS) or scenario spectrum such as conditional mean spectrum (CMS; Baker and Cornell, 2006), for scaling of the acceleration time series. The state-of-practice for PSHA in Italy, as implemented in the most recent Italian Building Code, (Norme Tecniche per le Costruzioni, NTC, 2008), was developed between 2003 and 2009, in the framework of a national research projects (2004–2006) funded by the Italian Department for Civil Protection (DPC) and carried out by Istituto Nazionale di Geofisica e Vulcanologia (INGV), (MPS working group, 2004; Stucchi et al., 2011) and it is based on the following features:

- Parametric Catalogue of Italian Earthquakes, CPTI04 developed by a working group of experts since 1999 (Working group CPTI, 1999, 2004);
- Seismogenic zonation (zonazione sismogenetica, ZS ver. 9) ZS9 (Meletti and Valensise, 2004, Meletti et al., 2008), based only on areal sources with equal rate of seismicity (Figure 3.1);
- Ground Motion Prediction Equations (GMPEs) used: Sabetta and Pugliese (1996), based only on Italian earthquakes; Ambraseys et al. (1996), based on European earthquakes; two combinations of regionalized GMPEs derived from Malagnini et al. (2000, 2002), Morasca et al. (2002), De Natale et al. (1988), and Patanè et al. (1994; 1997). Montaldo et al. (2005) provides further details on these regional GMPEs.

The logic tree used for the Italian PSHA is shown in Figure 3.2.

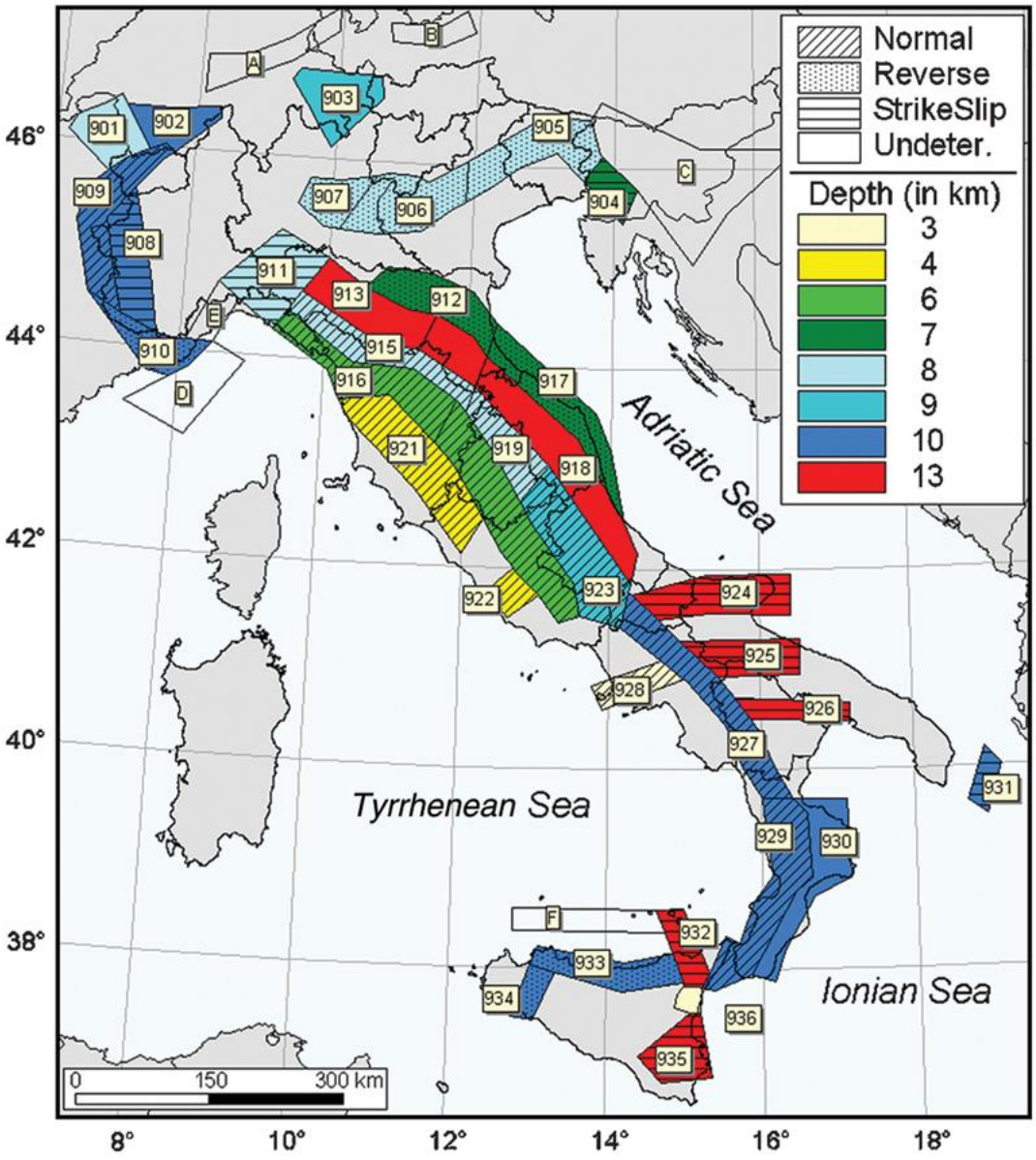

Figure 3.1 **Seismogenic zonation ZS9. The numbers in the boxes identify the earthquake source zones; the colors refer to the mean seismogenic depth (in km); the superimposed shadings refer to the predominant focal mechanism. The source zones with letters were not used in the assessment (from Stucchi et al., 2011).**

The most recent regional PSHA for the Euro-Mediterranean region is represented by the products released by the Seismic Hazard Harmonization in Europe project (SHARE), in particular the model that is described here is the so called "2013 European Seismic Hazard

Model" (ESHM13) (Giardini et al., 2013). This model was developed with a community-based approach (see Danciu et al., 2013) and involved working groups from several countries.

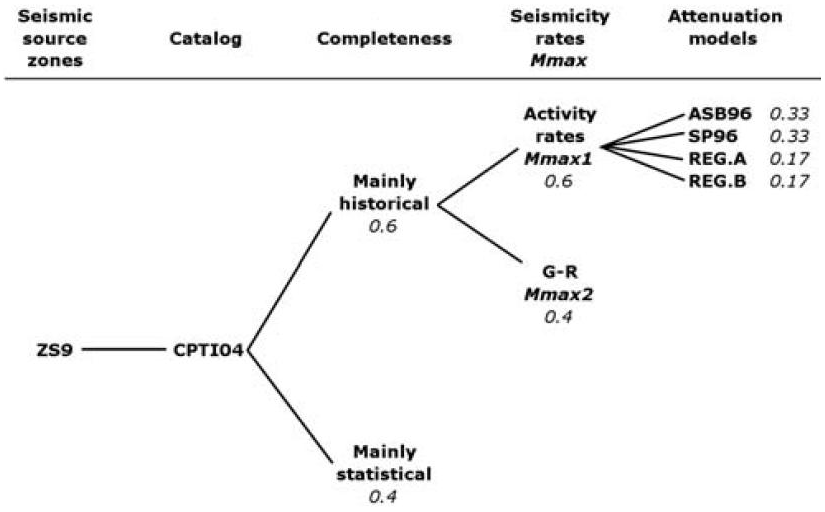

Figure 3.2 Logic tree used in the Italian PSHA (from Stucchi et al., 2011).

The main features of the SHARE model are:

1. Earthquake catalogue SHEEC (1000 – 2006) ver. 3.3 (Stucchi et al., 2012, Grünthal et al., 2013), which is used to define seismic zones (next item);
2. Seismogenic source definition, which is comprised of three branches representing alternate interpretations of the characteristics of future earthquake events so as to capture epistemic uncertainty. The models are listed below:
    a. Area source model (Figure 3.3) for seismic zone 9 - ZS9 (Meletti and Valensise, 2004, Meletti et al., 2008).
    b. Faults Sources + Background model (Figure 3.4): Different distributions of earthquakes are used for different **M** ranges, as shown in Figure 3.5. For $\mathbf{M} \geq 6.4$, earthquakes are assumed to only occur on fault sources (which are defined as identified planar faults, which in some cases represent complex and distributed fault systems; Basili et al., 2008, 2009). The geometric and kinematic parameters that characterize these sources are given in Figure 3.6. For $\mathbf{M} < 6.4$, earthquakes are assumed to occur within the background zones shown in Figure 3.4. This fault sources / background model can only be used where fault sources are mapped; where this information is missing this model is not considered .

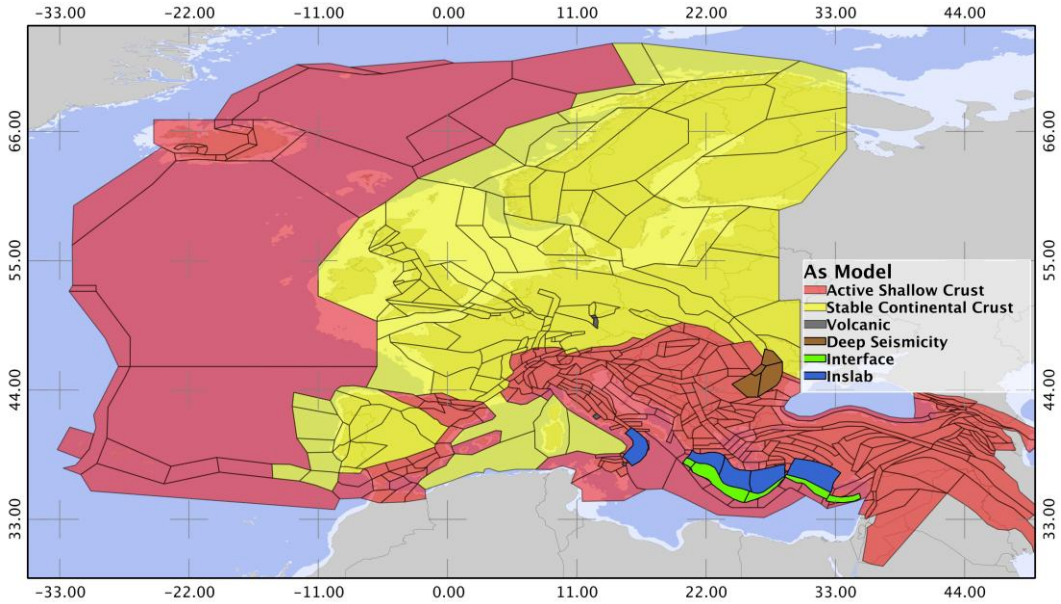

Figure 3.3 **Area sources for the SHARE-Euro-Mediterranean model (from Danciu et al., 2013).**

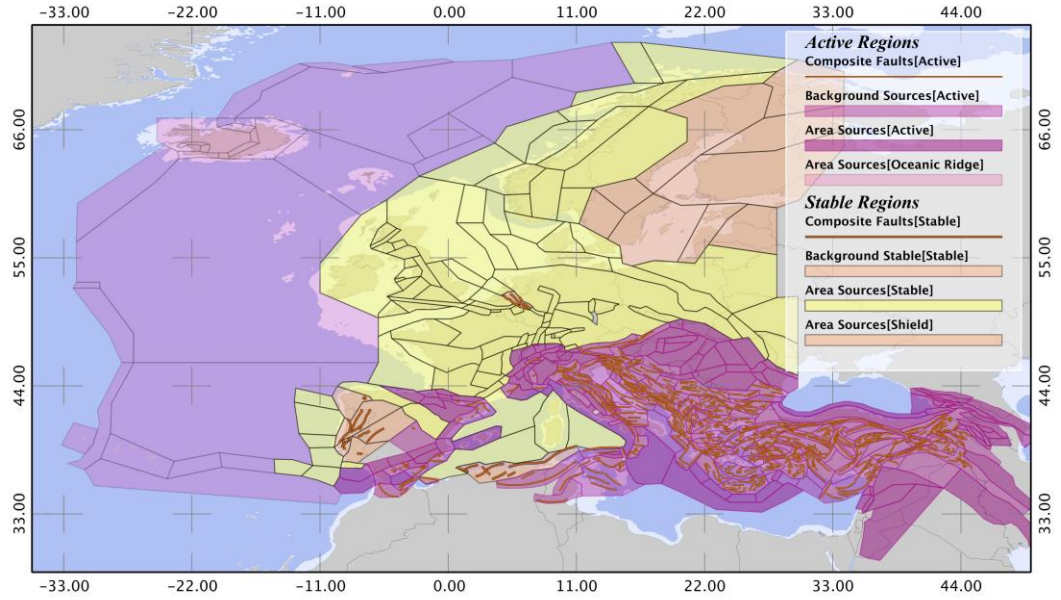

Figure 3.4 **Fault sources + Background zones for the SHARE- Euro-Mediterranean model (from Danciu et al., 2013).**

c. Stochastic earthquake source model (referred to as SEIFA – smoothed SEIsmicity and FAults model): This model is based on the approach of Hiemer et al. (2013, 2014), in which kernel-smoothing methods are applied to smooth earthquake observations in space such that the 'smoothed' catalogue and observed seismicity

have common cumulative distribution functions during the observation period. The approach is applied to estimate future earthquake potential through spatially continuous probability distributions. The SEIFA model applies a kernel-smoothing approach to observed earthquake locations and slip rates on mapped seismic sources (both crustal faults and subduction interfaces). The SEIFA model is based on two probability density maps:

i. One map is obtained by smoothing past seismicity. In this model, there is an estimation of the focal mechanism density obtained by calculating at each point a weighted set of moment tensors, where the weights are proportional to the distances between the observed moment tensors and the point of interest.

ii. A second map is obtained by smoothing fault moment rate contributions. For mapped faults, this map contains the same type of information as the seismicity map. The same smoothing methods are applied by converting the fault sections to point sources having a moment rate and average focal mechanism inferred from the fault section geometry (see also Ward, 2007). The fault sections used in this analysis may be individual segments or combinations of segments. Required information for each section includes its location (latitude and longitude of reference point, length, width, strike, dip), rake, and long-term slip rate. To define the average focal mechanism (moment tensor) for a given source, the strike and dip angle are estimated from the corresponding fault section geometry and the rake angle is taken from the fault database. In this way all faults are simplified to a "catalog" of moment rate point sources that is based purely on fault geometry and slip rates. This catalogue can then be utilized to generate synthetic earthquake catalogues.

The Area source (2a) and Faults Sources + Background (2b) models are referred to as zone-based branches (related to actually mapped sources). The stochastic earthquake source model (2c) is referred to as a Kernel-smoothed branch.

The earthquake source logic tree used in the SHARE model is shown in Figure 3.7.

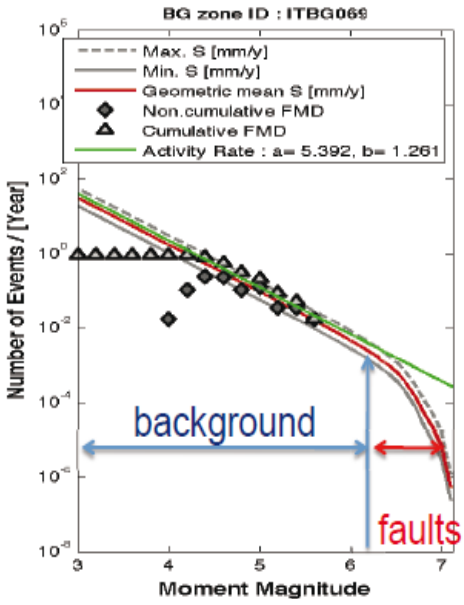

Figure 3.5 Scheme of the different magnitude distributions for the Fault sources + Background model.

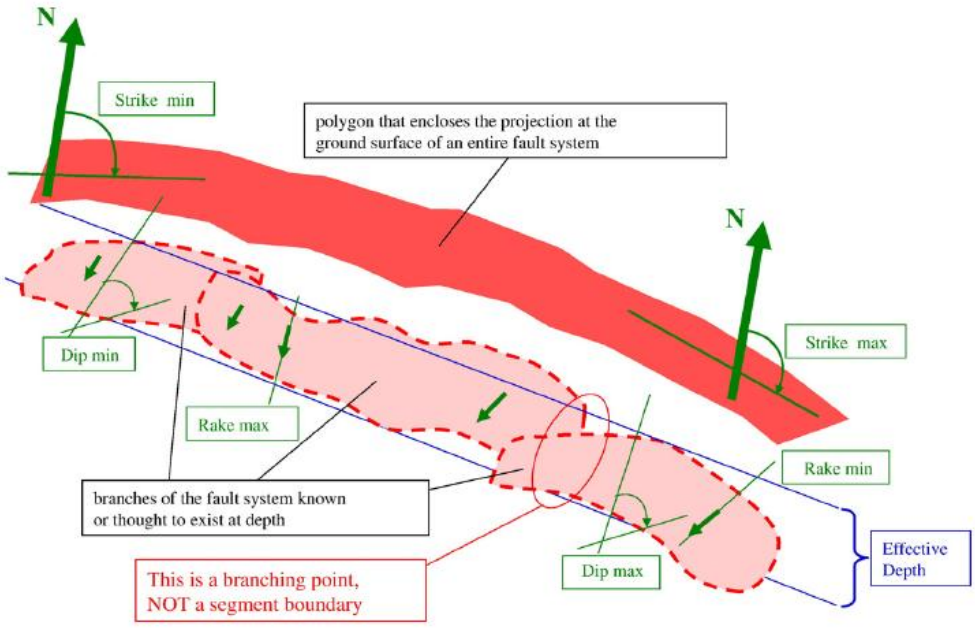

Figure 3.6 Schematic representation of a fault source and its geometric and kinematic characteristics (from Basili et al., 2008).

3. Ground Motion Prediction Equations (GMPEs): Several GMPEs were chosen representing various tectonic regimes in Europe. Figure 3.8 shows the GMPE logic tree with the weight assigned to the different branches (Delavaud et al., 2012). The tectonic

regions present in the European model are: Stable Continental Regions (SCR), Active Shallow Crustal Regions (ASCR), Subduction Zones (SZ), Volcanic zones and Vrancea.

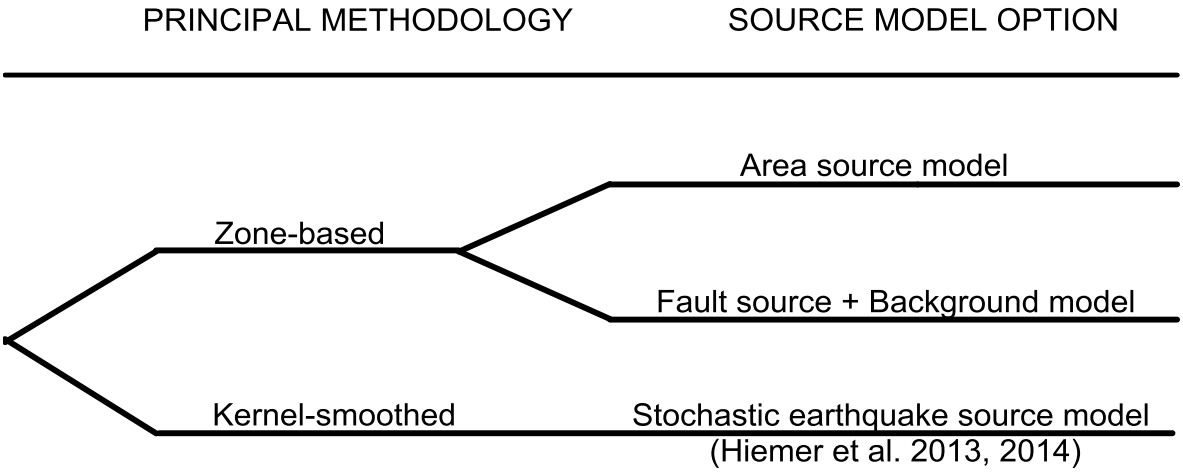

Figure 3.7 Earthquake sources logic tree of the SHARE Euro-Mediterranean model.

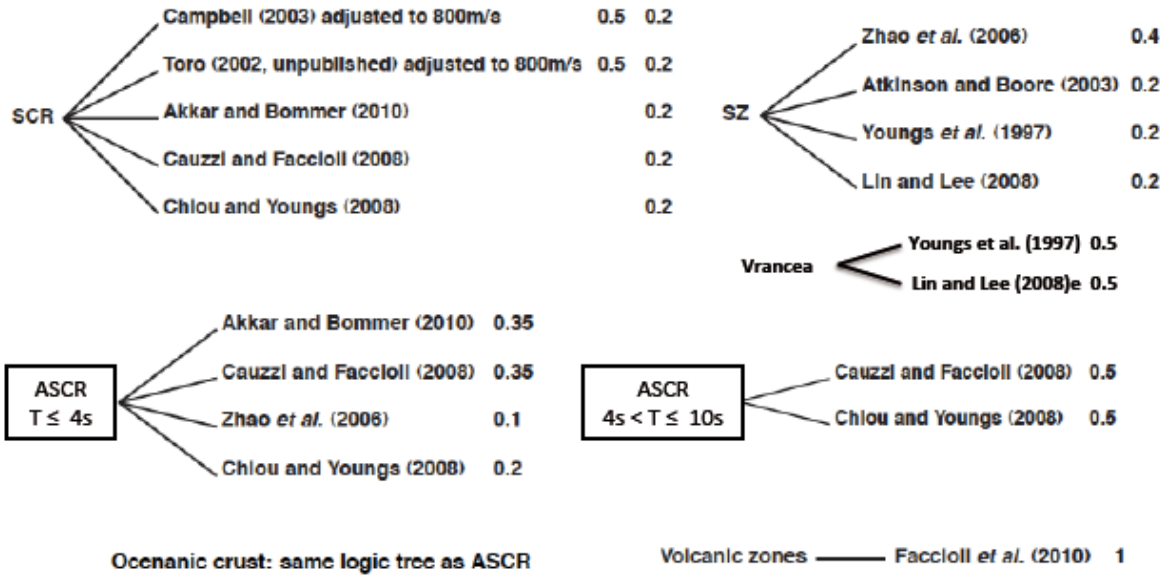

Figure 3.8 GMPE logic tree for the SHARE – Euro-Mediterranean Model (adapted from Woessner, Giardini and the SHARE consortium, 2012).

3.2 OpenQuake Engine for Seismic Hazard Analysis

The OpenQuake (OQ) platform (Silva et al., 2014) was selected for performing site-specific PSHA for the Farneto del Principe Dam. This software was selected because it includes features introduced in the SHARE Euro-Mediterranean project. OQ is an open-source platform that was

developed during the Global Earthquake Model (GEM) project. The OQ framework is illustrated in Figure 3.9.

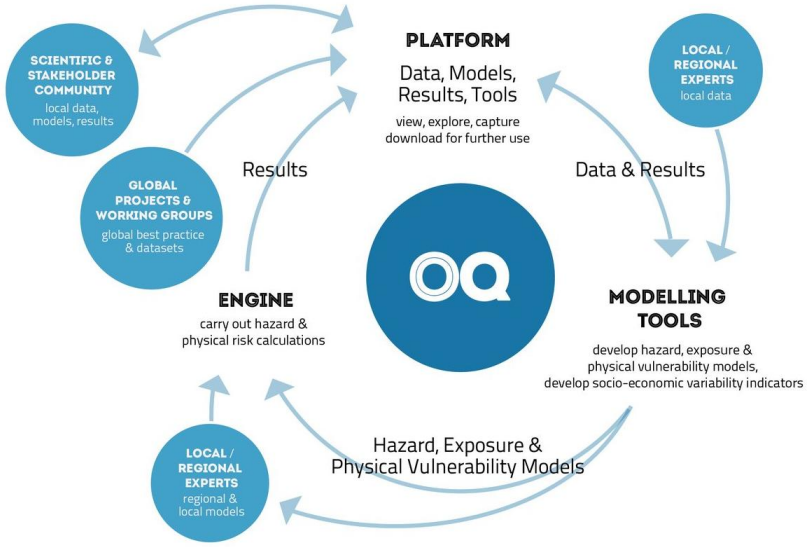

Figure 3.9 The OpenQuake engine project features (from http://www.globalquakemodel.org/openquake, accessed on October 23rd 2014).

During its development, the OQ platform was verified for several test cases against computed hazard from other codes included in a Pacific Earthquake Engineering Research (PEER) validation project (Thomas et al., 2010). The satisfactory comparison between the PEER and OQ results for several test cases are presented by Pagani et al. (2014a).

OQ analyses can be executed in the command line of a computer running the software within a Linux operating system, referred to as the 'ubuntu 12.04 LTS distribution'. OQ is comprised of two calculators: the hazard module and the risk module. The two modules are capable of performing several types of analyses. The OQ hazard calculator was used in this study and is described further below. The risk calculator was not used, but is described by Silva et al. (2014).

The hazard module utilizes a python-based library of models for earthquake ruptures, magnitude-frequency distributions, magnitude-area scaling relationships, and GMPEs. This library is accessible through an open web repository.

The library includes the following options for characterizing earthquake sources:

1. Point source: This is the basic source type used to model distributed seismicity. The area sources described below contain point sources. Point sources are not actually points of null dimension. Rather, they represent the centroid of planar ruptures projected onto the ground surface. Hence they can be described solely by a latitude and longitude. Assumptions used to generate rupture planes from a point source are:
    - The shape of the ruptures are rectangular;
    - The hypocenter is located at the centroid of the rupture;
    - The rupture plane is constrained in depth such that it does not extend above the ground surface (which comprises the shallowest possible 'upper seismogenic depth') or below a maximum seismogenic depth (Figure 3.10).

    For a given point source location on the Earth's surface, ruptures can be generated for a range of magnitudes according to the selected magnitude-frequency distribution. The size and shape of the rupture planes are determined using magnitude-area scaling relationships, given a specified aspect ratio (ratio of fault length to width). Ruptures modeled as point sources can have various strike and dip angles for their rupture plane and a range of hypocentral depths between the upper and lower seismogenic depths.

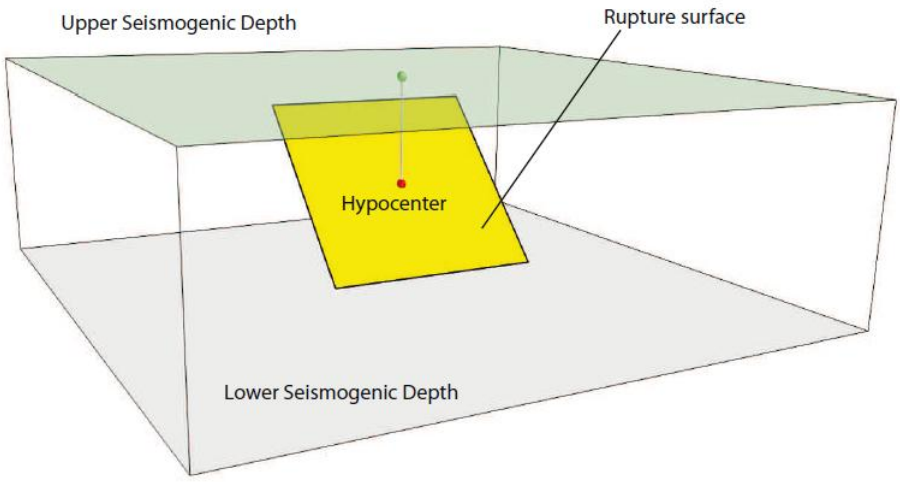

Figure 3.10 Single rupture in a point source (from Butler et al., 2014).

2. Area source: An area source consists of an arbitrary geometric shape at the ground surface having a particular magnitude-recurrence relationship. They are defined based on seismicity patterns and are commonly employed when fault locations are unknown.

Earthquakes within area sources are taken as point sources (Item 1 above) distributed randomly within the area. A depth component is added to area sources by assuming a distribution of hypocentral depths that is derived from the earthquake catalogue (in SHARE model, this is simplified to a single value of hypocentral depth taken as the average from the earthquake catalogue). Area sources are the most frequently adopted source type for European national and regional PSHA. In the SHARE Euro-Mediterranean model, both crustal seismogenic zones and subduction intra-slab zones are modeled using area sources.

3. Simple fault source: This source type is used for shallow seismogenic faults (referred to in §3.1 as Type 2b – 'Fault sources + Background zones' in the SHARE Euro-Mediterranean model). Simple fault sources are defined geometrically by means of the fault trace, which is the vertical projection of the shallowest portion of the fault to the ground surface. This fault trace can have multiple linear segments, the locations of which are given by a series of geodetic coordinates (latitudes and longitudes). The 3D fault surface is defined from the fault trace combined with fault dip, upper and lower seismogenic depth, and rake angle (using the convention of Aki and Richards, 2002). Accordingly, the fault surface consists of series of connected rectangles. Earthquake locations are simulated using a floating rupture source approach whereby hypocenters can occur anywhere on any segment. The earthquake magnitude follows a specified magnitude-frequency distribution. The rupture area follows magnitude-area scaling relations and any user-specified aspect ratio can be used.

4. Complex fault source: This source type is used for subduction interfaces and shallow crustal sources having complex geometry. The geometry of complex faults is defined by two fault edges (at the top and bottom the fault surface). Each edge is defined by a series of points with specified geodetic coordinates (latitude, longitude) and depth; dip is not specified but is constrained by the edges. The fault surface itself can be taken as planar or curved between the edges. The floating rupture process is the same as for simple fault sources.

5. Characteristic fault source: In this source, the rupture always occupies the entire fault area. It is used for faults or fault segments that are believed to produce characteristic

earthquakes of comparable size (Schwartz and Coppersmith, 1984). The characteristic earthquake is typically implemented for a fault in a hybrid manner whereby smaller **M** earthquakes are characterized using a truncated exponential model. No faults are modelled using the characteristic model in SHARE nor in the present study.

The occurrence of earthquakes on these source types is assumed to be uniformly distributed in space (within area sources or along faults) and to occur in time according to a Poisson process.

The OQ hazard module performs classical PSHA, Monte-Carlo event-based PSHA (Musson, 2000), disaggregation (Bazzurro and Cornell, 1999), and scenario-based deterministic seismic analysis. The classical PSHA produces hazard curves, Uniform Hazard Spectra (UHS) and hazard maps using the procedure of Field et al. (2003). Calculations of this type were used in this study and for the SHARE Euro-Mediterranean PSHA modeling.

OQ has functionality to allow implementation, debugging, and testing of new GMPEs. This was used in the present work to implement an NGA-West 2 model for application in Italy. OQ also has functionality to allow for user-specified logic trees to address epistemic uncertainties. The main disadvantage of the current release of the software is its non user-friendly interface (command-line driven) and the inconvenience of only being supported by Linux platforms.

3.3 Source Models for Farneto del Principe Dam Site

The Farneto del Principe dam site is in the Calabria region of southern Italy. Further information on the site coordinates and geotechnical conditions are given in Chapter 2.

As shown in Figure 3.11, the site-specific PSHA for the subject site was performed in OQ using the area sources model (AS model; Type 2a in §3.1) and the ‘fault sources and background zones’ model (FSBG model, 2b). These source types comprise two branches in the logic tree having equal weight. The kernel-based SEIFA model (2c) was not used; the rationale for this choice is that the kernel-based smoothing approach is conceptually alike to 2a and 2b when source locations are reasonably well established, as is the case in the region of the subject site. Hence, adding a third branch for model type 2c does not capture additional epistemic uncertainty (sensitivity studies presented in §3.5.4 show that including a SEIFA branch in the logic tree does not affect hazard ordinates). Accordingly, the additional computational cost for adding kernel-based model in this study was judged to not be worthwhile.

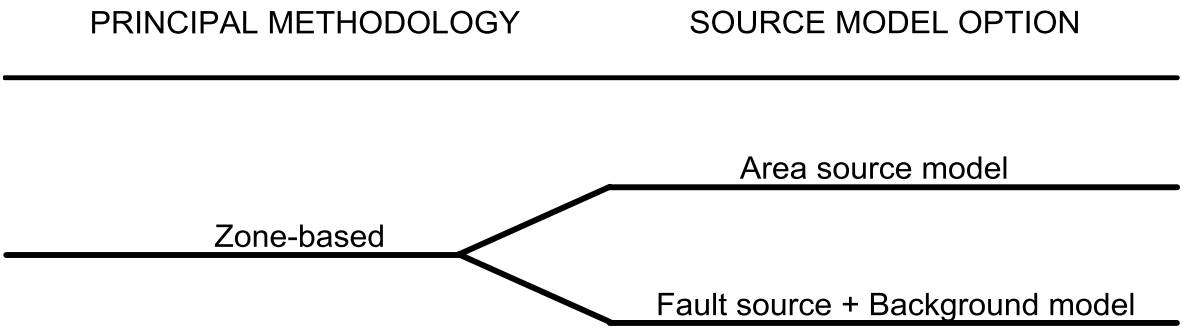

Figure 3.11 Sources logic tree and weights used in this study.

The following sections present details of the two source models types. In this study, only sources with distances ≤ 250 km to the subject site are considered.

3.3.1 The Area Sources Model (AS Model)

The area source model for the present study is taken from seismogenic zone 9 (ZS9) from Meletti and Valensise (2004) and Meletti et al. (2008); with the parameters adopted in the SHARE Model (Giardini et al., 2013). Earthquakes are assumed to follow a truncated exponential distribution between a minimum magnitude of $\mathbf{M}_{min}$=4.7 and a maximum magnitude ($\mathbf{M}_{max}$) that is varied as described further below. The *b* value sets the likelihood of earthquakes of different **M** whereas the cumulative *a* value (where 10^a = annual number of earthquake with **M** > 0) sets the earthquake rate in time.

Maximum magnitude ($\mathbf{M}_{max}$) defines the largest earthquake in a given zone and is unknown. One estimate of $\mathbf{M}_{max}$ is from the largest observed earthquake ($\mathbf{M}_{obs}$). If the historic earthquake catalogues extend back substantially longer in time than the return period of $\mathbf{M}_{max}$, then $\mathbf{M}_{obs}$ is a good estimate of $\mathbf{M}_{max}$. Even though the Italian catalogue goes back in time to A.D. 1000 (CPTI04 catalogue by Working Group CPTI, 2004), and is considered sufficiently well sampled so as to be 'complete' since 1450 (Woessner et al., 2012), this observation period is too short to be confident that $\mathbf{M}_{obs}$ is a safe estimate of $\mathbf{M}_{max}$.[1] Accordingly, our logic tree considers four estimates of $\mathbf{M}_{max}$ as follows:

[1] In the study region of southern Italy, the observation period goes back to A.D. 1000, as with the overall Italian region. Hence, its duration is approximately 1000 years. However, the seismicity rates in the region are such that the estimated return period range on $\mathbf{M}_{obs}$ is 1100 to 5000 years. Hence, one cannot safely assume that the observation period is long enough to have observed the $\mathbf{M}_{max}$, which would presumably have an even longer return period.

- $\mathbf{M}_{obs}$ (weight = 0.5);
- $\mathbf{M}_{obs}$ + 0.2 (weight = 0.2);
- $\mathbf{M}_{obs}$ + 0.4 (weight = 0.2);
- $\mathbf{M}_{obs}$ + 0.6 (weight = 0.1).

Values of parameters *a* and *b* for each area source are estimated from the historical and recorded seismicity using the SHEEC catalogue (ver. 3.3). In that catalogue, attempts are made to decluster aftershocks from mainshocks and the parameters are based on mainshock data. The same *b* value is used for all source types, whereas *a* values are selected in consideration of the relative number of normal, reverse and strike-slip earthquakes located within the source zone.

As shown in Figure 3.12, eleven area sources are located within 250 km of the site and are included in this analysis. Each area source has three identification numbers (IDs) corresponding to normal, reverse, and strike-slip mechanisms. Hence, 33 areas source IDs are tracked in the analysis. Source parameters $\mathbf{M}_{obs}$, *a*, and *b* are given for each source zone in Table 3.1. The subject site is located in area source 319, which has $\mathbf{M}_{obs}$ = 7.7 (Giardini et al., 2013).

3.3.2 The Fault Sources and Background Zones Model (FSBG Model)

As shown in Figure 3.13, the fault sources and background zones model (FSBG model) for the subject region is a hybrid of fault sources as well as background zones and area sources. The fault sources are either individual or composite seismogenic sources from Basili et al. (2008, 2009). Fault sources are represented by known ‘simple’ or ‘complex’ faults (defined in §3.2, list items 3 and 4). Figure 3.14 shows the shallow crustal fault sources considered in the present analysis, including the Crati Valley fault (source 015) that is the closest fault source to the site (details in §3.3.3) and the Lakes fault that is newly implemented here as a simple fault in OQ (§3.3.4). Not shown in Figure 3.14 is the fault at the subduction interface, which is introduced in the present work and discussed in §3.3.5.

Area sources are included in the FSBG model for regions without mapped faults. For these regions, the source characterization in the FSBG branch is identical to that in the AS model as defined in §3.3.1. They are included here so that the FSBG branch is complete with respect to the geographic distribution of sources (i.e., if area sources were not included, large portions of Italy, especially off-shore areas, would appear as aseismic in this branch).

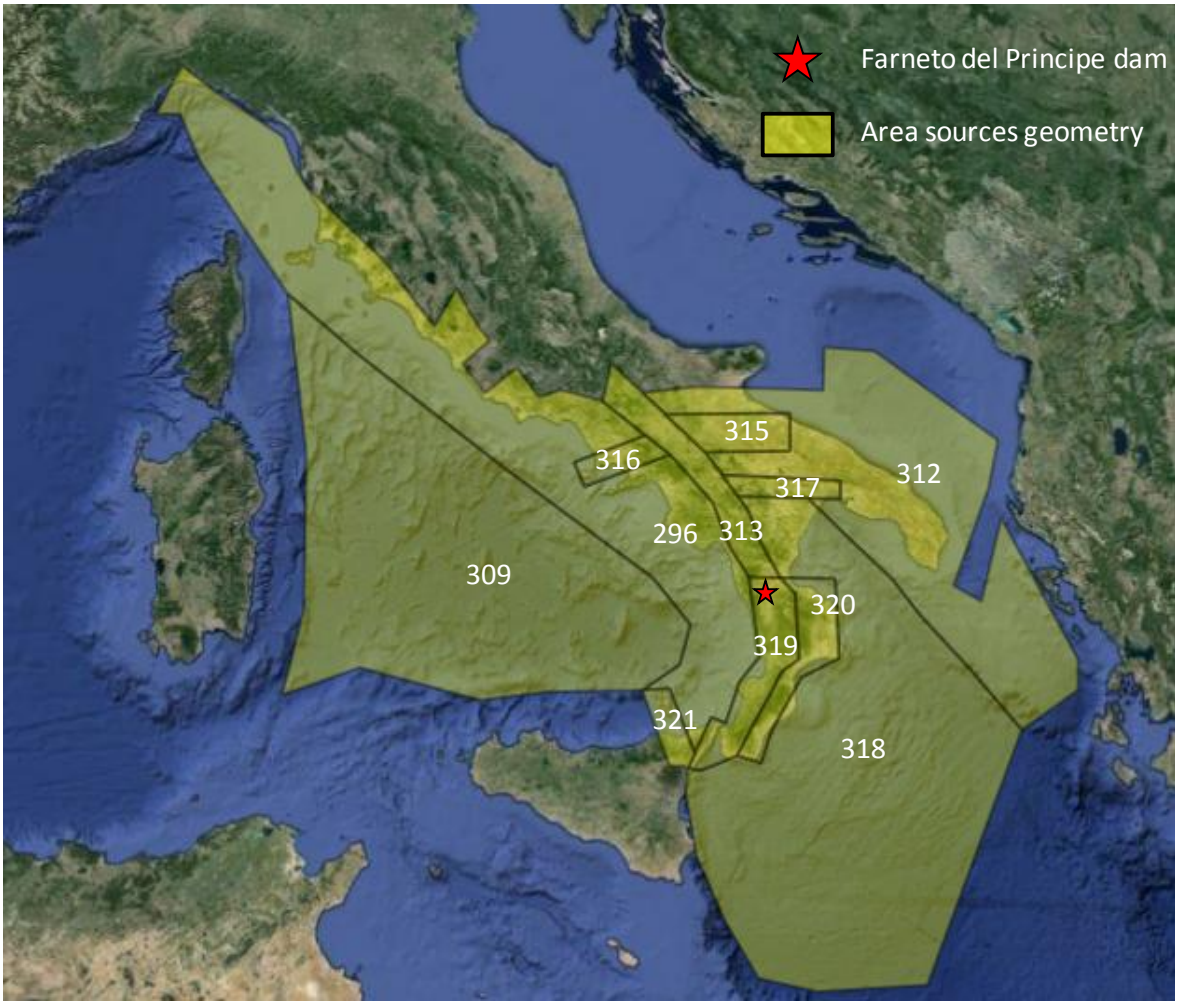

Figure 3.12 **The Area sources used in the PSHA with the correspondent source identification numbers.**

Table 3.1 **Summary of the parameters used for the implementation of the AS model. The first ID # for each source applies to normal fault mechanisms, the second to reverse, and the third to strike-slip.**

Source	ID	a_{inc}^{*}	*b value*	M_{obs}
296	291	3.0688	-1	6.5
	292	3.2449		
	293	3.4667		
309	264	2.8443	-1	6.5
	265	2.6682		
	266	3.0661		

(continued on next page)

Table 3.1 (cont.) **Summary of the parameters used for the implementation of the AS model. The first ID # for each source applies to normal fault mechanisms, the second to reverse, and the third to strike-slip.**

Source	ID	a_{inc}*	*b value*	M_{obs}
312	330	3.2118	-1	6.5
	331	2.8438		
	332	3.3667		
313	333	3.0877	-0.9	7.7
	334	3.4235		
	335	2.3096		
315	339	3.0442	-1	7.7
	340	3.38		
	341	2.2661		
316	342	2.4677	-1	6.5
	343	3.3128		
	344	2.7688		
317	345	2.8442	-1	7.7
	346	3.18		
	347	2.0661		
318	348	3.2112	-1	7.9
	349	2.8432		
	350	3.3661		
319	351	3.0877	-0.9	7.7
	352	3.4235		
	353	2.3096		
320	354	3.2442	-1	7.7
	355	3.58		
	356	2.4661		
321	357	3.5964	-1.1	7.7
	358	3.9322		
	359	2.8182		

*Incremental *a* values, defined such that the annual rate of earthquakes within the magnitude range of $\mathbf{M}\pm\Delta\mathbf{M}/2$ is $10^{(a_{inc}-b\mathbf{M})}$. $\Delta\mathbf{M} = 0.2$ is the magnitude bin width.

Figure 3.15 shows area sources and background zones. Background zones are a special type of area source containing faults. Area sources do not align perfectly with background zones at the edges; thus, the edges of area sources were adjusted to fit the background zones as needed in

accordance with SHARE documentation (http://www.efehr.org:8080/jetspeed/portal/hazard.psml; last accessed October 27, 2014).

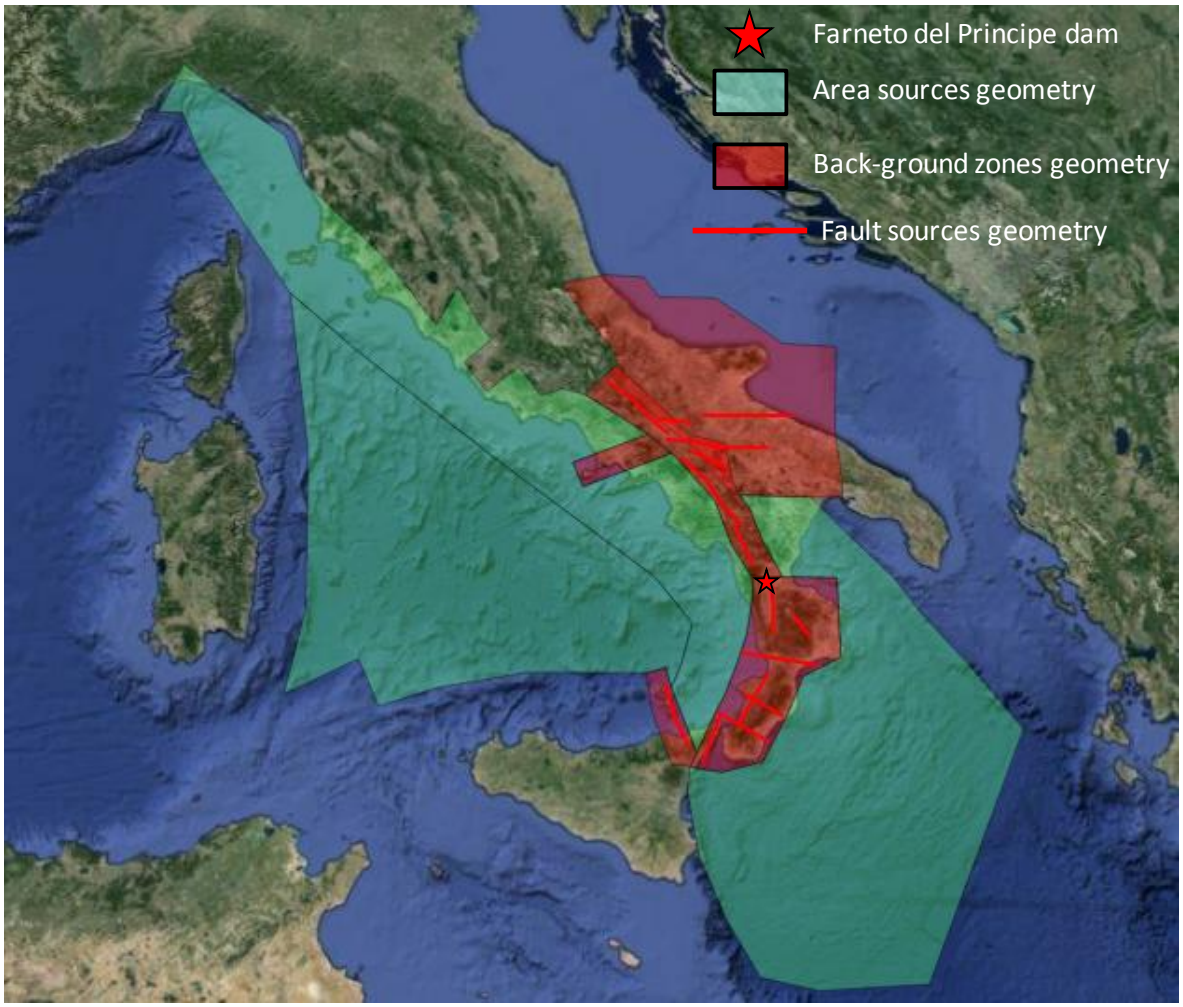

Figure 3.13 Overview of the complete FSBG model.

As described in §3.1, **M** ≥ 6.4 earthquakes are assumed to occur on finite faults and smaller events in background zones. SHARE recommendations were followed (Woessner et al., 2012) in which the maximum magnitude ($\mathbf{M}_{max}$) is assigned to finite faults as follows:

1. Aspect Ratio (AR) is calculated from fault length and width (L and W, respectively):

$$AR = {}^{L}/_{W} \tag{3.1}$$

2. The applied Aspect Ratio (AR^*) is constrained below a limit of 3:

$$AR^* = \left\{ \begin{array}{cc} AR & if\ AR < 3 \\ 3 & if\ AR \geq 3 \end{array} \right\} \tag{3.2}$$

3. An effective length (L_{eff}) is derived from AR^*:

$$L_{eff} = W \cdot AR^{*} \tag{3.3}$$

4. The effective area (A_{eff}) is calculated as:

$$A_{eff} = W \cdot L_{eff} \tag{3.4}$$

It should be noted here that the use of A_{eff} as derived from Eq. (3.4) will be smaller than the actual fault area whenever the actual fault aspect ratio $AR > 3$. This represents a flaw in the SHARE recommendations for extended faults.

5. Using L_{eff}, W and A_{eff}, $\mathbf{M}_{max}$ was evaluated as the mean of four magnitude-area scaling equations recommended by the SHARE Euro-Mediterranean model (Wells and Coppersmith, 1994, Kagan, 2002, Leonard, 2010, Hanks and Bakun, 2002, 2008). These estimates of $\mathbf{M}_{max}$ will be under-predicted for sources with $AR > 3$ due to the use of an artificially low fault area A_{eff} in Step (4). The impact of this problem with the SHARE recommendations will be investigated in future research.

Figure 3.14 Fault sources (finite faults) used in this study.

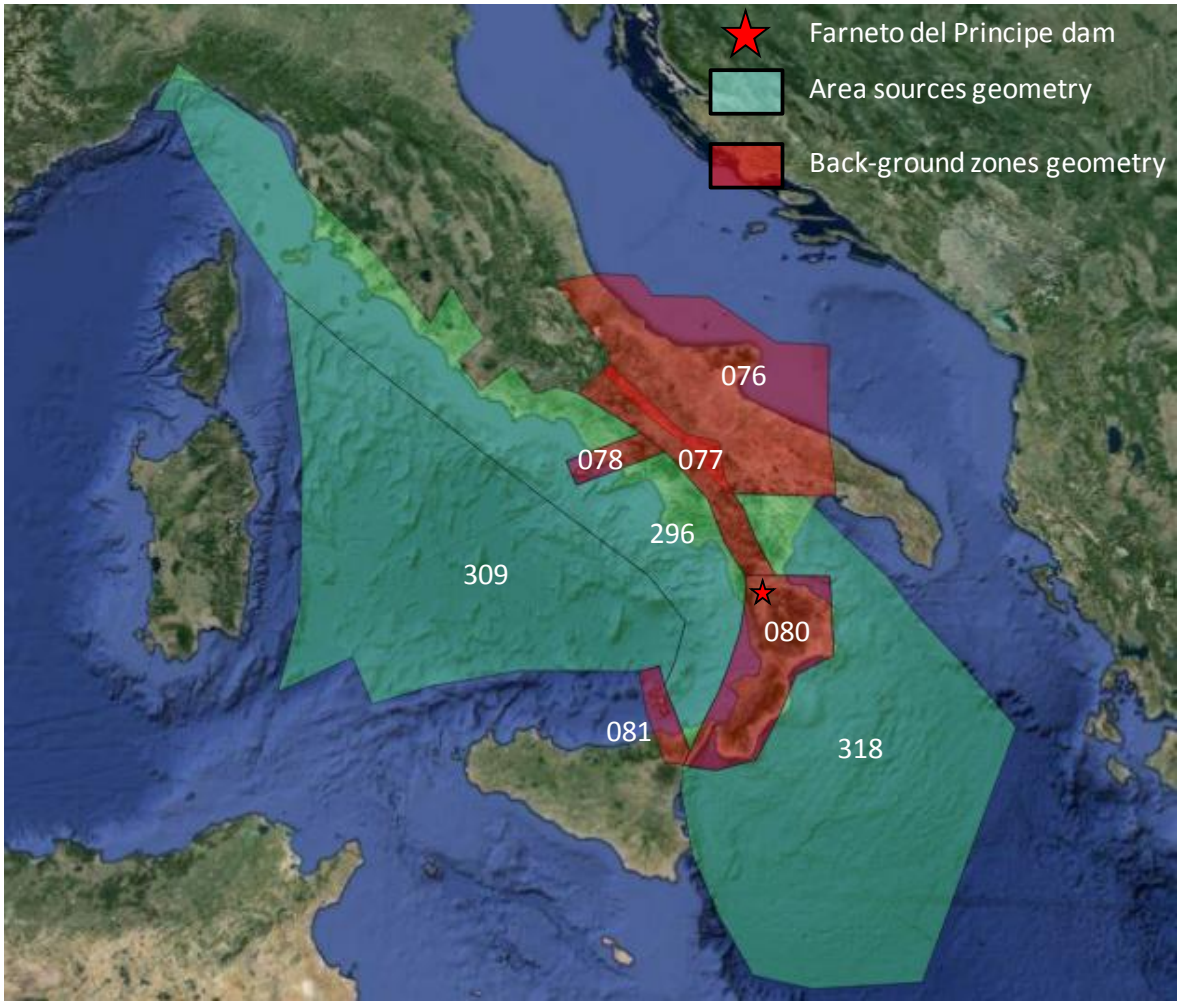

Figure 3.15 **Background zones and area sources used in the FSBG model for this study.**

Uncertainty in $\mathbf{M}_{max}$ for fault sources is not considered in the main logic tree for this study.. Instead, $\mathbf{M}_{max}$ uncertainty is considered separately in sensitivity analyses presented in §3.5.4.

Earthquake rates for faults and background zones in the FSBG model are set in consideration of balancing moment build-up and release. Moment build-up ($\dot{M}_0$) for a fault is computed as:

$$\dot{M}_0 = \mu \cdot s \cdot A_{eff} \tag{3.5}$$

where μ is fault friction, A_{eff} is effective fault area, and s is slip rate. Moment release is the product of earthquake rate and the weighted average moment for earthquakes on the fault, which is sensitive to the probability density function on **M** (and hence to b and $\mathbf{M}_{max}$). By balancing moment building up and release, the rate of earthquakes can be computed, which is directly related to the a value (Anderson and Luco, 1983). This approach was implemented by Bungum

(2007) and used in the SHARE model (as documented at: http://www.efehr.org:8080/jetspeed/portal/hazard.psml, last accessed October 27, 2014). Moment build-up computed using Eq. (3.5) is subject to under-prediction error for extended faults as discussed previously due to the use of A_{eff}.

The parameters used for the implementation of the fault sources and background zones are summarized in Tables 3.2 and 3.3, respectively. The area sources used in this model have the same characteristic and parameters as the sources used in the AS-model.

Table 3.2 Summary of the parameters used for the implementation of the FSBG model

Source ID	*a value*	*b value*	M_{max}
042	4.26205	1.218	7.6
016	2.20777	0.793	7.2
055	0.97664	0.793	6.8
082	1.60513	0.793	6.8
080	1.04329	0.793	6.8
053	1.62688	0.793	7
068	1.14016	0.793	7
015	1.3673	0.793	6.8
038	1.21588	0.739	7
034	1.18182	0.739	7.2
063	2.02179	0.844	7.2
089	1.47429	0.844	7
084	2.00385	0.844	7.2
004	1.40067	0.844	7
024	1.23063	0.739	7.2
Lakes*	1.815	0.793	6.7

*For more information about the parameters used for the implementation of the Lakes fault, see §3.3.1.4

Table 3.3 Summary of the parameters used for the implementation of the background zones in the FSBG model

Source	ID	a_{inc} *	*b value*	M_{max}
076	961	2.4849	0.844	6.3
	962	1.7067	0.844	
	963	2.8207	0.844	

(continued on next page)

Table 3.3 (cont.) **Summary of the parameters used for the implementation of the background zones in the FSBG model**

Source	ID	a_{inc} *	*b value*	M_{max}
077	964	1.7909	0.739	6.3
	965	1.0128	0.739	
	966	2.1267	0.739	
078	967	1.9532	0.977	6.3
	968	2.7983	0.977	
	969	2.2543	0.977	
080	970	1.5865	0.793	6.3
	971	1.7226	0.793	
	972	1.9844	0.793	
081	973	3.4582	1.218	6.3
	974	3.6343	1.218	
	975	3.8561	1.218	

* Incremental *a* values, defined such that the annual rate of earthquakes within the magnitude range of $\mathbf{M}\pm\Delta\mathbf{M}/2$ is $10\text{^}(a_{inc}\text{-}b\mathbf{M})$. $\Delta\mathbf{M} = 0.2$ is the magnitude bin width.

3.3.3 Characterization of the Crati Valley Fault

Fault source 015 in Table 3.2 and Figure 3.14, which is the Crati Valley fault, is the most proximate finite fault source for the dam site. Accordingly, a special attention was directed to the characterization of this source to verify the accuracy of its parameterization for hazard analysis.

As shown in Figure 3.16 the Crati Basin is located on the Tyrrhenian side of northern Calabria. It is a tectonic depression (graben) developed between the coastal range and the Sila Massif. The Crati Basin is oriented north-south (N-S) and is bounded by two approximately N-S striking normal fault systems. The western normal fault dips to the east and the eastern normal fault dips to the west. This graben-fault system has been the subject of recent research and the tectonic evolution and activity of the system is still debated (Van Dijk et al., 2000; Monaco and Tortorici, 2000; Tansi et al., 2005, 2007; Spina et al., 2009, 2011; Brozzetti et al., 2012).

Spina et al. (2009) show that the west side of the Crati fault system is comprised of three east-dipping en-echelon faults (Montalto Uffugo–Rende Fault, MRF; S. Marco Argentano–S. Fili Fault ,MMF; Fagnano Fault, FF). They also show that the eastern border is considerably more complex, with a series of west-dipping normal faults as shown in Figure 3.16(b). The Crati Basin

extension is related to fault slip rates and dip angles, which have been evaluated in prior work as described further below. As shown in Figure 3.17(a), the northern and southern limits of the Crati fault system is well constrained by the roughly east-west striking Pollino fault (PFZ) on the north side and the Falconara-Cosenza fault zone (FCFZ) to the south. Spina et al. (2011), reconstruct the tectonic evolution of the Crati Basin, showing that the geometry and the extension of the system are consistent with the fault model implemented in the SHARE Euro-Mediterranean PSHA in which the more active side of the graben is to the east.

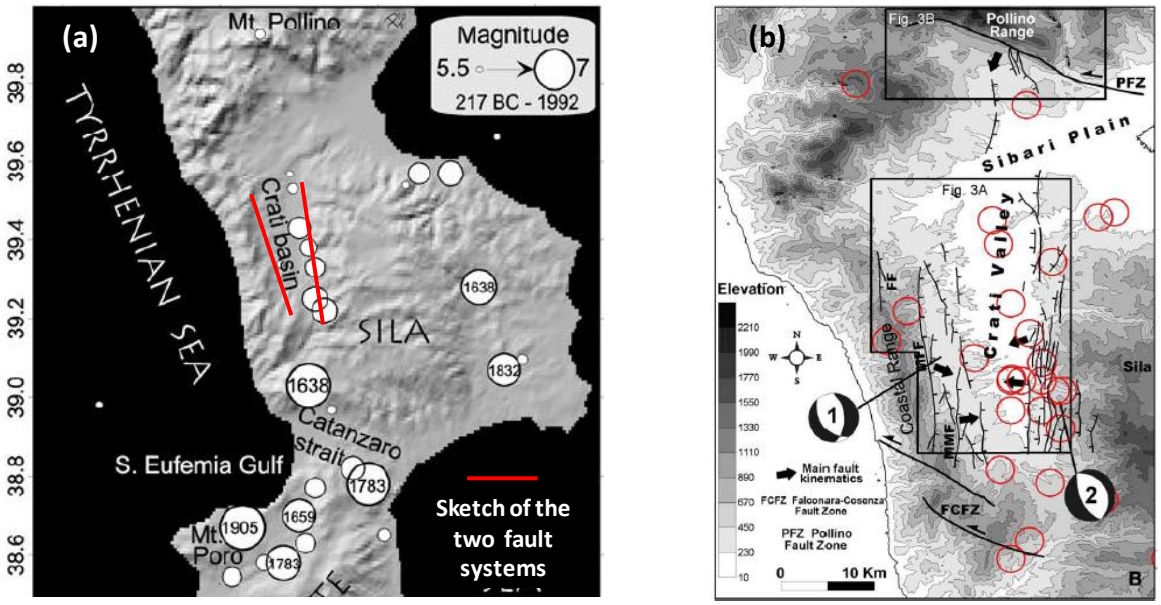

Figure 3.16 **(a) Shaded relief view of the area of interest with the sketches of the two fault systems (Crati Basin) and the historical events with magnitude 5.5 from 217 B.C. to 1992. The first known event occurred in 91 B.C., the last reported is 1978 (Working Group CPTI [1999] source, adapted from Galli and Bosi, 2002); (b) Seismicity distribution in the Crati Basin. Black arrows show mean kinematic vectors along faults (from Spina et al., 2009).**

The relatively high activity on the eastern margin of Crati Valley is further supported by geological and geomorphological observations of drainage pattern, deformation of the top of the metamorphic substratum (along with the overlying Pleistocene units) and radon anomalies (e.g: Carobene and Damiani, 1985; Molin et al., 2004; Tansi et al., 2005) as synthesized in DISS 3.1.1 web commentary (http://diss.rm.ingv.it/dissHTML/ITCS015TXT.html, last accessed October 29, 2014). While the fault on the western edge of the graben is well expressed geologically and morphologically, there is no evidence of Holocene activity. As shown in Figure 3.16 and 3.17(b),

historic and instrumental seismic activity is present along both lineaments, but is more pervasive on the east side (Tansi et al., 2005; Spina et al., 2009, 2011).

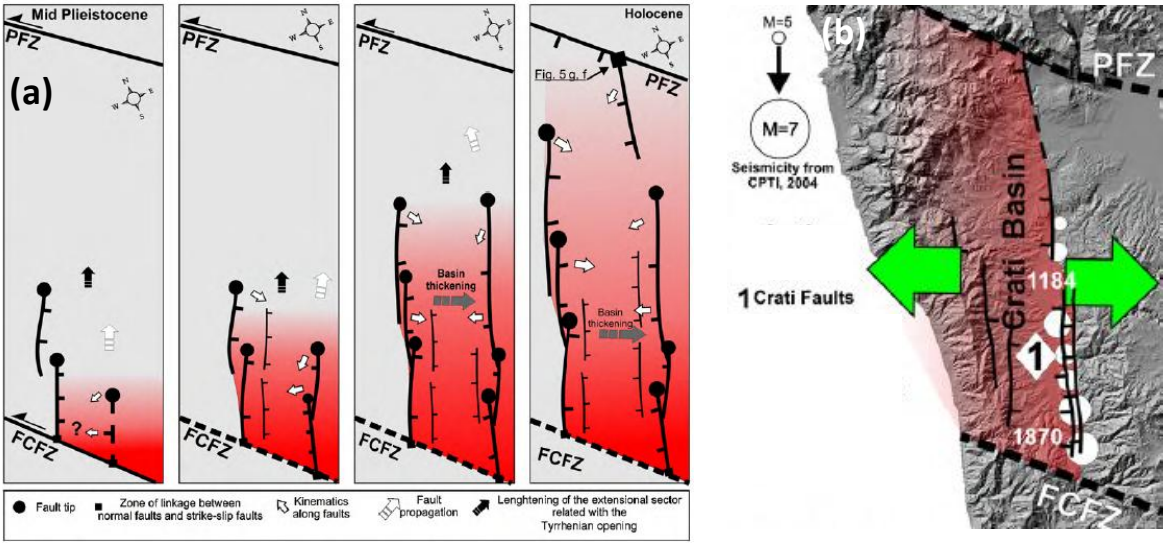

Figure 3.17 **(a) Time-space propagation of extension within the Crati Basin from Middle Pleistocene to Holocene times (from Spina et al., 2010). (b) View of northern Calabria showing rough distribution of macroseismic areas for M> 5earthquakes (from DISS Working Group, 2009), Spina et al. (2011)**

Based on this evidence, we model only the eastern side of The Crati Valley as having a seismogenic source that is defined between upper and lower seismogenic depths of 1 and 10 km, respectively. The faults on the western border are considered inactive in the FSBG model. The eastern side of the Crati valley is modeled as a simple fault in this study. Its geometry and the parameters characterizing magnitude distribution and earthquake rate match those used in the SHARE model (given in Table 3.2).

3.3.4 Implementation of the Lakes Fault

The Lakes fault is shown in Figure 3.14 and its fault parameters are listed in Table 3.2. This fault is not included among the seismogenic sources included in the the SHARE model (Giardini et al., 2013). We identified this fault through review of recent literature presenting the results of paleoseismic analysis (Galli and Bosi, 2003; Galli et al., 2004, 2007; Spina et al., 2004; 2006, 2007). As shown in Figure 3.15, the Lakes fault is located on the north-eastern side of the Calabria region approximately 60 km from the dam site. Due to its close proximity, we implemented the Lakes fault as a finite fault source.

Galli and Bosi (2003) analyzed primary historical sources of the catastrophic March–June 1638 Calabrian earthquakes and conducted paleoseismic analyses along the Lakes fault alignment (the fault was unknown prior to their work). They opened four trenches and found five late-Holocene surface faulting events, the last one being compatible with the June 9 1638 earthquake. These analyses motivated a shift of the June 1638 epicenter as shown in Figure 3.18. They interpret the mechanism as an oblique normal fault. Galli et al. (2007) opened a fifth trench to correlate fine alluvial units across the fault, in particular organic and/or charred material suitable for absolute dating. The surface faulting events identified by Galli and Bosi (2003) and Galli et al. (2007) are dated: 21st century BC, 12th century BC, 3rd century BC, between the 6th and 7th century AD (after 645–691 A.D. and before 798–893 A.D.), and June 1638 (average time between events of 900 years). Spina et al. (2007) performed structural analyses using a geo-statistical approach to characterize the geometric, dimensional and kinematic characteristics of the Lakes Fault. They found that the Lakes fault is comprised of two main right stepping segments arranged *en-echelon* that behave as a unique structure, because are linked through relay zones made up of minor faults (hard linkage). They also showed that the rake is mainly strike-slip for most of the fault length.

We model the Lakes Fault as a 33 km long, left lateral (strike-slip), SW dipping feature. The maximum magnitude assigned to the fault is $\mathbf{M}_{max}$=6.7 based on the average obtained from three magnitude-area scaling relationships: Leonard (2010), Hanks and Bakun (2002, 2008) and Wells and Coppersmith (1994). The width and the area used are W=15 km and A_{eff}=495 km respectively (note that the fault aspect ratio of ~2 is less than three, so the fault area bias noted in §3.3.2 it not present in this case). The $\mathbf{M}_{max}$ assigned to the Lakes fault, calculated using these magnitude area scaling relationships, is consistent with the maximum magnitude historically observed on the fault. We take the dip and rake as 60° and 150°, respectively. The Gutenberg-Richter *b* value is taken as 0.793 based on historical seismicity data for the background zone in which the Lakes fault is located. The *a* value was computed as 1.815 via moment balance using a slip rate, estimated by Galli and Bosi (2003), of s = 1.2 mm/yr, the aforementioned fault dimensions, and a truncated exponential PDF for magnitude.

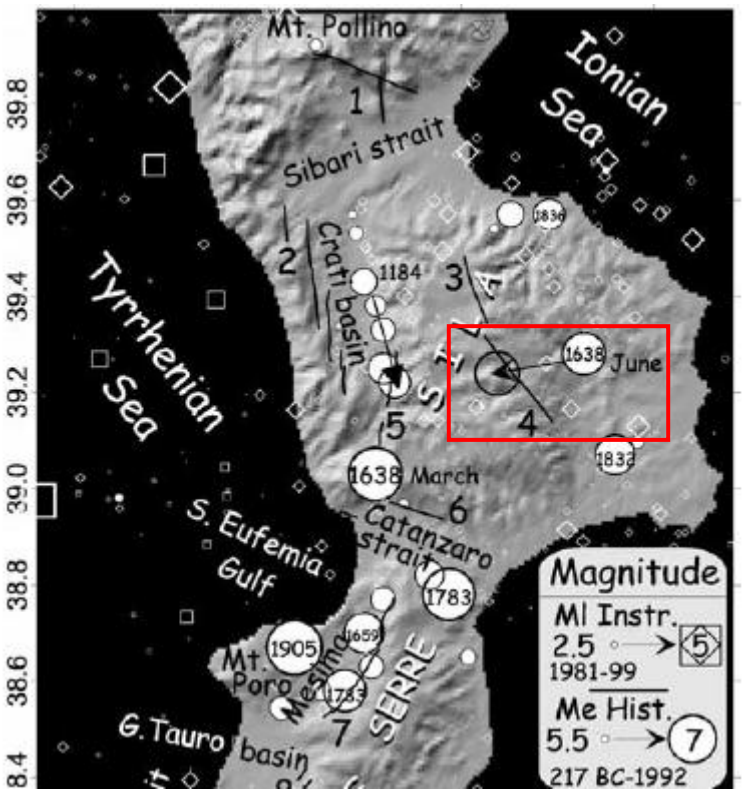

Figure 3.18 **The Lakes fault (in the red rectangle), #4 in figure and the shift of the June 1638 earthquake epicenter after paleoseismic analyses (adapted from Galli and Bosi, 2003).**

3.3.5 The Calabrian Arc Subduction Zone

The Calabrian arc subduction zone accommodates subduction of the Ionian oceanic segment of the African plate beneath the Tyrrhenian continental segment of the Eurasian plate. Figure 3.19 shows the extent of the seismogenic portion of the subduction interface and in-slab region. The dam site falls within the surface projection of these source regions, indicating that subduction sources may be a significant cause of activity affecting the hazard.

Three types of earthquakes occur in this region:

1. In-slab earthquakes, which occur in the region marked in Figure 3.19. These are considered in the SHARE Euro-Mediterranean model using one area source polygon (shown in Figure 3.19) with five associated depths and three focal mechanisms (33% for normal, 33% for strike-slip, and 34% for thrust/reverse). The incremental *a* values used across the 15 sources are 2.33 for 10 normal and strike-slip sources and 2.34 for five

thrust/reverse sources, based on seismicity from deep earthquakes. A constant b = 0.9 was used for all sources.

2. Interface earthquakes, which occur between the lines marking the upper and lower seismogenic depths in Figure 3.19. This source of earthquakes is not considered in the SHARE model.
3. Shallow crustal earthquakes, which are modelled using a combination of area and fault/background sources as described earlier.

We adopt the SHARE model for in-slab and shallow crustal activity (with addition of Lakes fault as described in §3.3.4). We add an interface model using a complex fault source (this source type is defined in §3.2). We consider geodetic observations to constrain interface activity and derive a maximum magnitude of 8.1 from a recent magnitude-area scaling relation proposed for subduction zones (Strasser et al., 2010). Uncertainty in $\mathbf{M}_{max}$ is taken into account such that the largest considered value is about 8.6 (about 1.7 standard deviations above the mean; details in §3.5.4.3). The complex fault interface source, as modelled in OQ, is shown in Figure 3.19. Depths to the interface top and bottom are 10 km and 60 km, respectively.

In the remainder of this section, we describe further the geology of the subduction zone, geodetic and seismic constraints used in support of the fault model, and the process used to parameterize the fault model.

Figure 3.20 shows plan and profile views of the geologic structure of the Calabrian arc subduction zone (Van Dijk et al., 2000), which is the last remaining oceanic crust subduction in the region (de Voogd et al., 1992; Faccenna et al., 2001, 2004; D'Agostino et al., 2008). The tectonic structure constitutes the forearc belt of the active subduction of the Ionian basin. Figure 3.21 indicates that the subducting slab consists of a narrow Wadati-Benioff zone (Anderson and Jackson, 1987; Giardini and Velonà, 1991; Selvaggi and Chiarabba, 1995; Chiarabba et al., 2005) dipping toward the northwest at about 70° (Pepe et al., 2010). An active volcanic arc is present at the location of the Aeolian Islands as shown in Figure 3.21. The Calabrian arc accretionary wedge developed due to the SE-NW Africa/Eurasia convergence, presently occurring at a very slow rate, as reported by recent GPS studies (Calais et al., 2003; Reilinger et al., 2006; Serpelloni et al., 2007; D'Agostino et al., 2008; Devoti et al., 2008). Laterally, the seismically active portion of the slab is not longer than 250 km, less than its down-dip width,

resulting in one of the smallest seismically active in-slab sources in the world (Chiarabba et al., 2005).

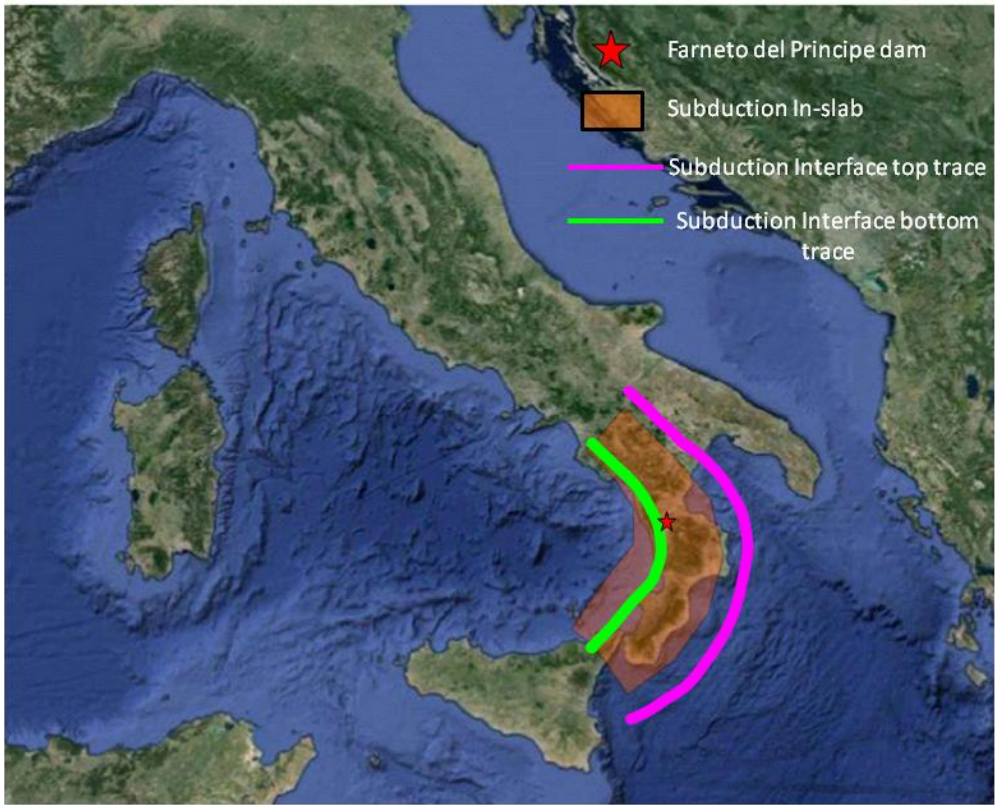

Figure 3.19 Geometry of the subduction in-slab and interface as implemented in this study.

Geodetic observations using GPS data have been interpreted to gain insight into the subduction mechanism including the rate of convergence between the Ionian oceanic crust and the Calabrian continental curst. The GPS data are widely spaced and as such are most suitable for macro-scale analyses. As a result, there is a large uncertainty associated with the subduction zone convergence rate and the spatial distribution of relative displacements. In this regard, Slejko et al. (2010) state:

> *"(1) the knowledge of the seismogenic faults in Italy is incomplete in terms of the number of faults and their geometric and seismic characteristics and (2) constraints from geodetic data are problematic because the number of permanent global positioning satellite (GPS) stations in Italy is small, the fact that they have only been in operation a short time interval*

(about 5 years), and the campaign measurements provide velocities with a large associated uncertainty.".

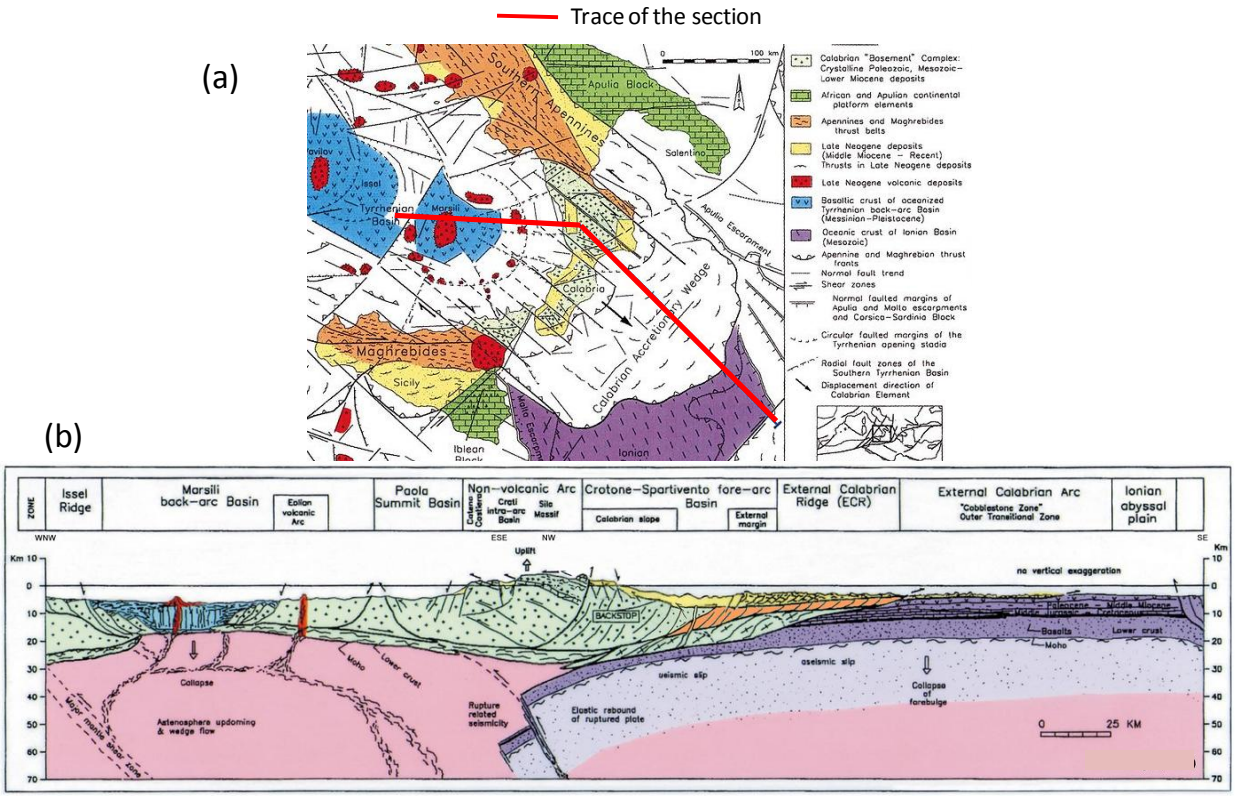

Figure 3.20 **(a) Geological framework of the Central Mediterranean region; (b) Crustal section of the Central Mediterranean region (from Van Dijk et al., 2000).**

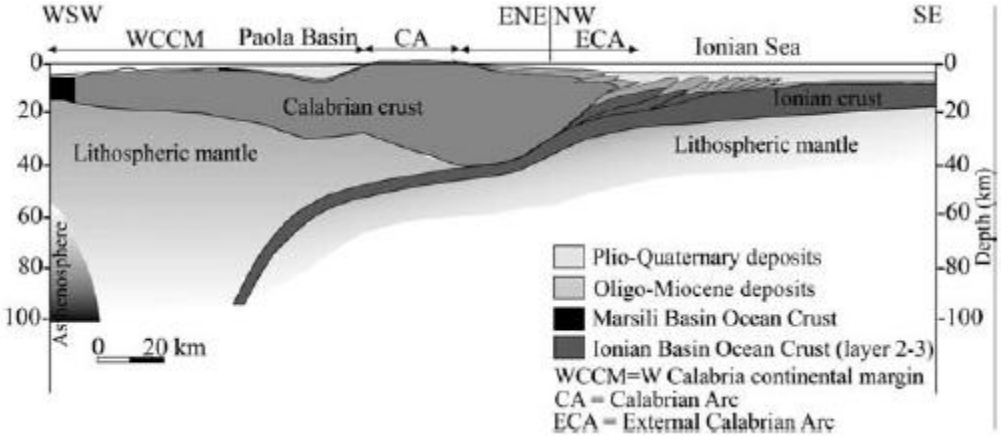

Figure 3.21 **Cross section from the Marsili ocean crust (southern Tyrrhenian) to the Ionian foreland displaying the lithospheric setting of the "Ionian Subduction zone" (from Pepe et al., 2010).**

Slejko et al. (2010) interpreted geodetic strain rate across the Italian territory from GPS-based horizontal velocities discretized into four large circular domains defined by radii of 100 to 300 km (Figure 3.22). This approach was adapted from similar work in California (Ward, 2007). The geodetic strain rate was then converted to seismic moment rate ($\dot{M}_0$). This conversion is sensitive to crustal thickness, which was taken as 10 km by Slejko et al. (2010) due to a relative paucity of hypocenters below that depth. Due to the shallow depth, this approach does not allow for the possibility of subduction-related seismicity (in-slab and interface).

Slejko et al. (2010) also present a finite element model of the Italian crust to estimate the rate of moment release (considering only characteristic earthquakes) on sources very similar to those in the SHARE model. The two sets of moment rates (build-up from GPS observations and release from FEM analysis) have a large misfit, with the release being an order of magnitude smaller. Slejko et al. (2010) explain this result as follows:

> *"This discrepancy is motivated by the fact that the (moment rate) in each domain from GPS observations is given by the sum of the (moment rates) released as characteristic earthquakes plus that released as distributed seismicity and as aseismic creep, while the (moment rate) from geophysical modelling refers only to the contribution of the characteristic earthquakes."*

We speculate that another reason for the discrepancy could be the omission of a large source, which in the Calabria region could be the subduction zone.

Mattei et al. (2007) used GPS data to investigate the evolution of the Calabrian arc. They find that the GPS data do not facilitate the analysis of a reliable strain field. They also suggest that the convergence rates required to explain crustal movements in the early Pleistocene are not present today, indicating that a slow-down may be occurring. Figure 3.23 shows that Calabria together with the southern Apennines and Apulia, has an independent motion with respect to both Nubia (5 mm/yr to ESE) and Eurasia (3 mm/yr to NNE), as well as a distinct motion relative to Sicily, with a tectonic boundary between Sicily and Calabria presently located in the Messina Straits area. The possible role of subduction in the accommodation of these differential motions is not discussed.

Angelica et al. (2013) describe the presence of deep seismicity due to the Calabrian arc subduction zone as follows:

> *"Italian seismicity (http://csi.rm.ingv.it/) can be considered as superficial, since the hypocenters are concentrated at depths of less than 50 km except in the area beneath the Calabrian arc, and is affected also by a deeper seismicity that reveals the presence of a subduction zone along a NW-dipping Benioff plane (Chiarabba et al., 2005)."*

As shown in Figure 3.24(a), Angelica et al. (2013) compile GPS velocities for the Italian territory, which are combined with seismicity to estimate strain rates as shown in Figure 3.24(b). However, they do not describe how the subduction zone accommodates observed strain rates.

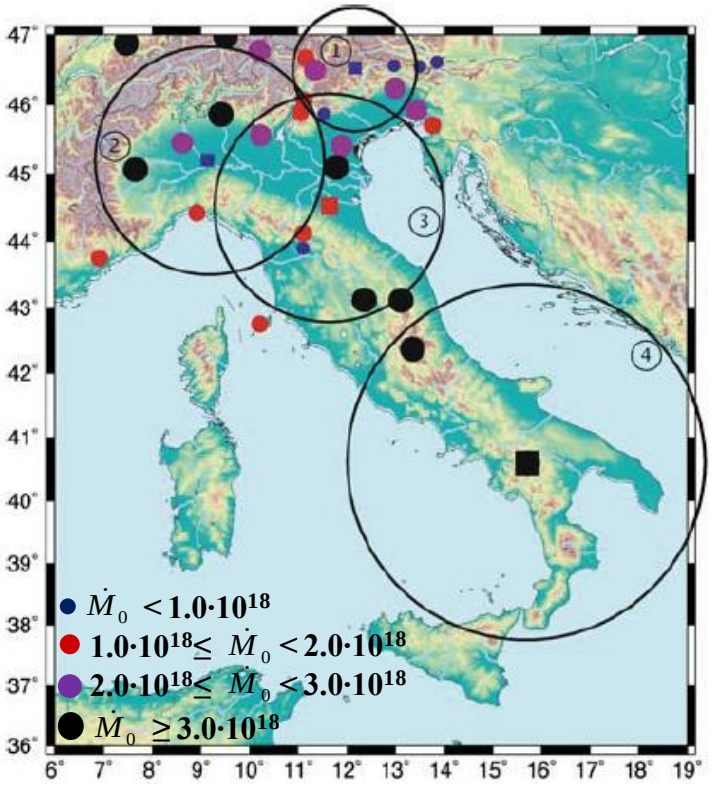

Figure 3.22 **$\dot{M}_0$ (in N·m/year) computed from GPS observations. The central GPS station of each domain is marked by a square with size and color according to its $\dot{M}_0$. The numbered large circles identify the four domains: 1 eastern Alps, 2 western Alps, 3 central Apennines, 4 southern Apennines (from Slejko et al., 2010).**

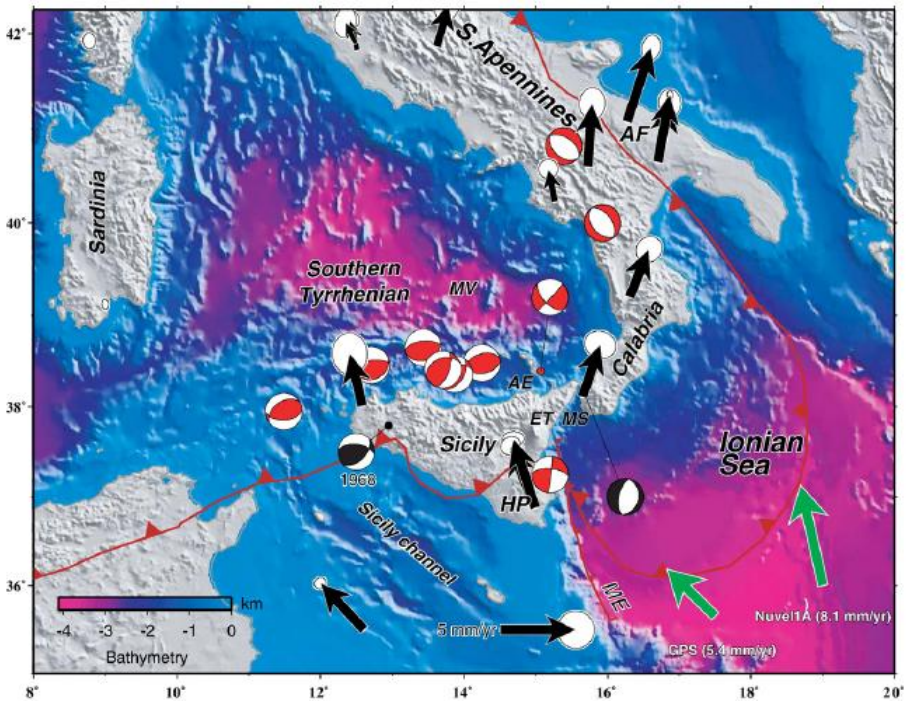

Figure 3.23 **Regional map of southern Italy including present-day Eurasia-fixed velocity field and seismicity of the Calabrian Arc (modified from D'Agostino and Selvaggi, 2004). Crustal focal mechanisms are selected from the CMT Catalog (MwN5, in red) and from Anderson and Jackson (1987) in black. Green arrows show the predicted convergence between Nubia and Eurasia according to the Nuvel-1A model and the GPS-derived pole of rotation (from Mattei et al., 2007).**

While the aforementioned geodetic studies provide tantalizing evidence for the significance of the subduction boundary, none interpret the GPS data so as to estimate the convergence rate at the plate boundary. Such an inference is provided by D'Agostino et al. (2011), who state:

> "*we propose that the reference frame appropriate to evaluate the motion of the CA relative to the lower plate should be attached to those parts of the foreland most probably attached to the Ionian lithosphere, i.e. the Apulian block. The Apulia-fix GPS velocity field (Figure 3.25) shows a southeastward migration of the CA in agreement with the shortening directions observed in the most recently deformed part of the Ionian wedge [Gutscher et al., 2006; Minelli and Faccenna, 2010]. These findings strongly suggest that the CA is migrating relative to Ionian lithosphere and approximately 2 mm/yr of convergence is absorbed in the Ionian wedge.*"

The manner by which this convergence is accommodated within the crust is uncertain:

> *"More obscure is the style of deformation and seismogenic potential in the Ionian wedge. The limited extent of the GPS network limits the resolution capability to detect locking of the subduction interface, especially if the coupled zone extends principally offshore."*

Mastrolembo Ventura (2012) also evaluated the convergence rate from GPS data and sought to understand how it is accommodated by deforming tectonic structures in the region using an elastic block model. She provides two hypotheses for convergence rates – 2-3 mm/yr and 5-6 mm/yr, which are somewhat higher than those of D'Agostino et al. (2011). Those alternate rates are coupled with alternate crustal deformation hypotheses. Figure 3.26 shows the scheme of the tectonic blocks in the area that were considered. Figures 3.27 and 3.28 illustrate two mechanisms associated with the two convergence rates. In summarizing these results, Mastrolembo Ventura (2012) states:

> *"Importantly, the convergence rates across the Ionian-Calabrian subduction interface differ by a factor of two depending on which plate the Ionian oceanic lithosphere belongs to. The SE-ward displacements of the Calabrian stations with respect to the Ionian block occur at rates of 5 mm/yr and 2.5 mm/yr with respect to Nubia or to the Ionian-Apulian plate, respectively (see figs. 3.27 and 3.28). Therefore, it is of fundamental importance for the evaluation of the seismic potential of the Calabrian region to understand how this convergence is eventually accommodated along the subduction interface, and if its deformation signal may be overprinted on the measured velocity gradient across the Messina Straits. An Ionian-fixed velocity field is the appropriate reference frame realization for our objective, allowing us to implement a relatively simple block geometry while accounting for the two end-member kinematic boundary conditions along the Ionian-Calabria plate contact. This is realized by implementing two different experiments (figs. 3.27 and 3.28), the first one considering the Ionian block as part of Nubia (i.e., using*

Nubia-fixed velocities), and the second one considering the Ionian block as part of the Apulian microplate (i.e., using Apulia-fixed velocities).”

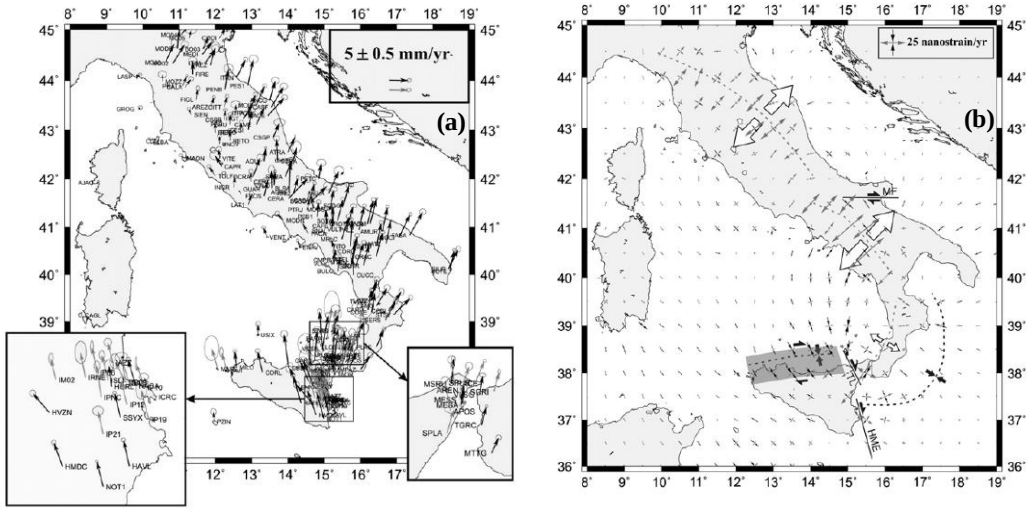

Figure 3.24 **(a) GPS velocities and associated error ellipses for the entire Italy. Black arrows for permanent stations; gray arrows for surveys; (b) Combined final strain rates resulting from joint inversion of GPS and seismic data. White arrows across dashed gray lines indicate the main extension areas; solid lines stand for strike-slip faults in the significant shear strain zones; dashed black line with converging black arrows indicates the compression front of the chain in the Ionian sea; the gray shadowed area indicates a transpressive regime affecting the northern off-shore of Sicily. (adapted from Angelica et al., 2013).**

In summary, we have three estimates of convergence rate across the Calabrian subduction zones: 2.5 mm/yr (D’Agostino et al., 2011), 2-3 mm/yr and 5-6 mm/yr (Mastrolembo Ventura, 2012). We consider the defensible range of convergence rates to be 2 to 6 mm/yr. This convergence should be accommodated within the subduction zone by in-slab and interface earthquakes. As mentioned previously, we adopt the SHARE model characterization of in-slab earthquakes. We characterize interface moment release using alternate slip rates of 2-6 mm/year. The moment release rate ($\dot{M}_0$) associated with the 2-6 mm/yr slip rate range is 0.76 to 2.2 $\times$ 10^{25} dyne-cm/yr, using an assumed *b* value of 0.9 (inferred from regional deep seismicity). Corresponding *a* values are 3.8 to 4.3. These rates are considerably higher than the moment release rate for the in-slab earthquakes of 0.39 dyne-cm/yr, which corresponds to an *a* value of 3.7. The sensitivity of the hazard results to the range of interface slip rates (and associated rates of moment release) is presented in § 3.5.4.3.

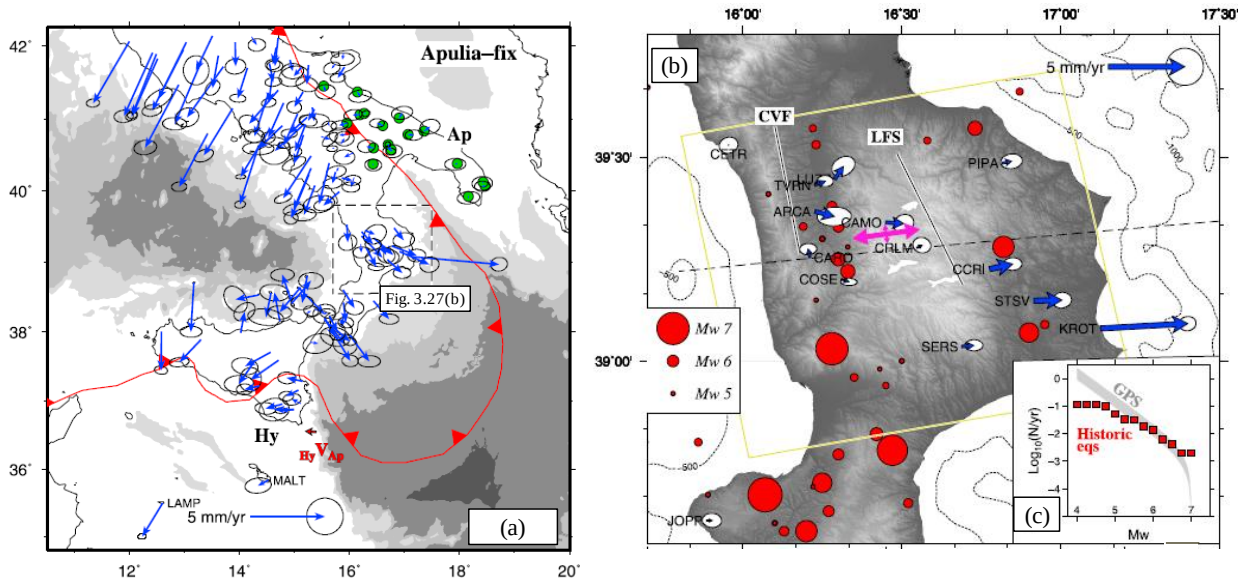

Figure 3.25 **(a) GPS velocity fields in the Apulian reference frame. The sites used to determine the relative Eulerian vector are marked with green circles. The red arrow shows the motion of the Hyblean region relative to Apulia; (b) Zoom of the GPS velocities in Northern Calabria, red circles are M > 5 earthquakes from the CPTI04 catalogue in the interval 1500 A.D. to the present. CVF, Crati Valley Fault System; LFS, Lakes Fault System. (c) Cumulative magnitude-frequencies of CPTI04 seismicity from 1500 A.D. to the present (adapted from D'Agostino et al., 2011).**

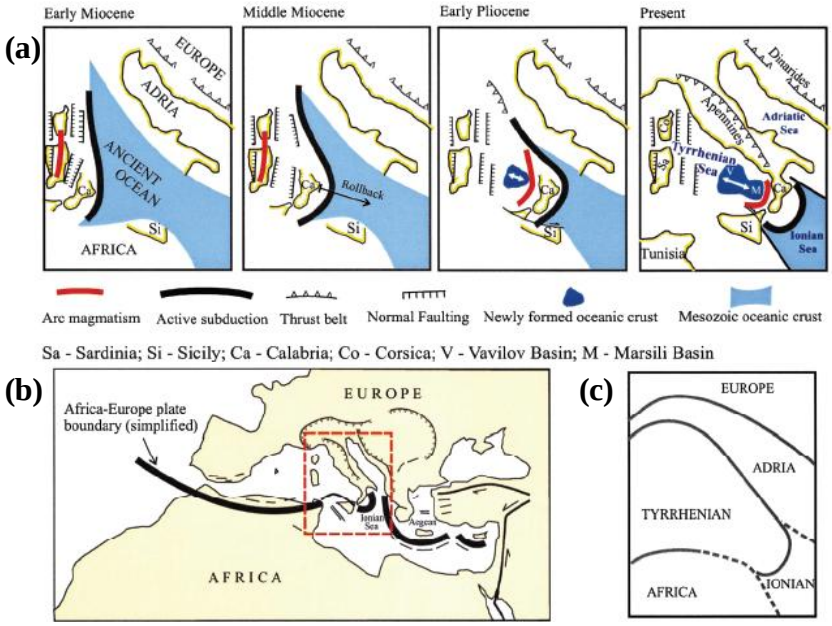

Figure 3.26 **(a) Schematic reconstruction of the central Mediterranean since the Miocene. The eastward retreat of the Tyrrhenian-Apennines subduction system was associated with the closure of a Mesozoic basin and opening of the Tyrrhenian Sea. (b) Regional map showing the studied area (in red frame) within the Europe-Africa convergence zone. (c) Five plates and microplates in the studied area (adapted from Gvirtzman and Nur, 2001).**

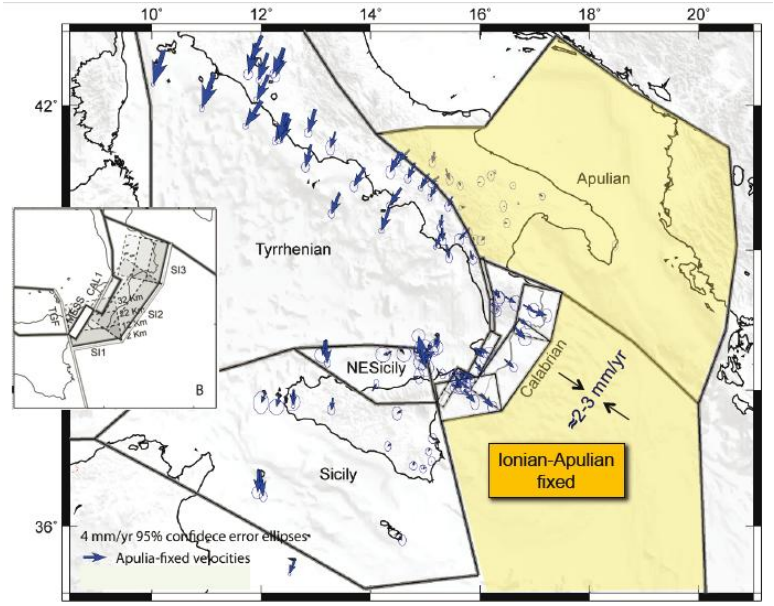

Figure 3.27 **Block model geometry and horizontal GPS velocities (with 95% confidence ellipses) rotated into the Apulia fixed reference frame. Convergence rate across the Ionian-Calabrian subduction interface assuming the Ionian litosphere belonging to the Apulian plate is also shown. (B) Zoom of the Calabrian fault system. For the western Calabrian normal Fault system (CAL1) and the Tindari-Giardini Fault system (TGF) the locking depth varies from 0 to 20 km, whereas for the Calabrian subduction interface (SI1, SI2, and SI3) the locking depth varies from 0 to 40 km (from Mastrolembo Ventura, 2012).**

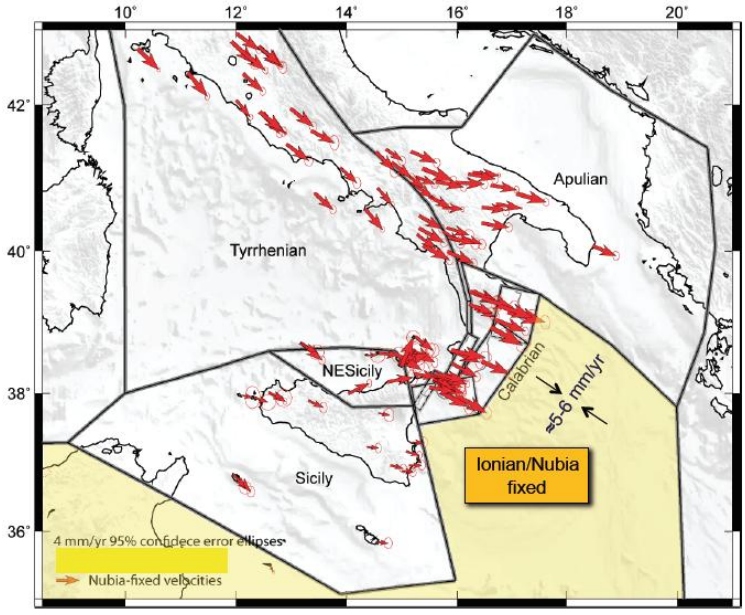

Figure 3.28 **Block model geometry and horizontal GPS velocities (with 95% confidence ellipses) rotated into the Nubia-fixed reference frame. The Ionian plate is assumed moving with Nubia. Ionian-Calabrian convergence rate is shown (from Mastrolembo Ventura, 2012).**

3.4 GMPE Logic Tree

A ground motion prediction equation (GMPE) relates the log mean and standard deviation of a ground motion intensity measure (such as pseudo-spectral acceleration (PSA) at a given oscillator period) to explanatory variables related to earthquake source, path and site effects. These variables typically include moment magnitude, various metrics of source-to-site distance, style of faulting (faulting mechanism), and site condition.

GMPEs are used with source models in PSHA (e.g. Cornell, 1968, McGuire, 2004). In the sections that follow, we describe the pre-selection of a series of GMPEs considered for application in the hazard analyses for the subject site; we compare the median predictions from pre-selected GMPEs over a parameter space, which is used for final GMPE selection; and we describe the implementation of a recent GMPE that was selected for use in the present application but which had not been previously coded in OQ.

3.4.1 Pre-Selection of GMPEs

GMPEs are usually derived at least in part from regression of empirical data. Those data and the resulting GMPEs are typically compiled separately for three distinct different tectonic encountered globally: active crustal regions (ACRs) that produce shallow crustal earthquakes, subduction zones (SZs) that produce deep earthquakes on the subducting slab (in-slab activity) and interface events, and stable continental regions (SCRs), among others.

Douglas (2014) summarized 365 GMPEs for the prediction of PGA and 232 for the prediction of PSA ordinates. Hence, the selection of a tractable number of GMPEs for a given application is a significant consideration in PSHA. One fundamental decision faced by the analyst is whether to use GMPEs specific to a country or geographic region versus models derived using global data for the tectonic regime. Local GMPEs have the potential advantage of reflecting local geologic and tectonic conditions, which may differ from those produced by global models. However, the size of databases used for local models are often very limited and may be inadequate to constrain the model over the parameter space required in PSHA. This is especially problematic for large magnitudes, which are unlikely to have been observed in significant numbers for local regions. Global GMPEs draw from much larger databases and

hence are better constrained over the useful parameter range, but may have some bias with respect to local conditions (e.g., rates of distance attenuation and/or site effects).

The PSHA for the Italian building code (MPS working group, 2004; Stucchi et al., 2011) emphasizes local GMPEs at various geographic scales. An Italy-specific GMPE from Sabetta and Pugliese (1996) was used, which is based on an Italian earthquake database (Sabetta and Pugliese, 1987). Also considered was a European model by Ambraseys et al. (1996). Finally, a series of GMPEs specific to sub-regions in Italy by Malagnini et al. (2000, 2002), Morasca et al. (2002), De Natale et al. (1988), and Patanè et al. (1994; 1997) were used.

GMPEs used in the SHARE Euro-Mediterranean model were selected by an expert panel (Delavaud et al., 2012) and are as follows for ACRs:

- Akkar and Bommer (2010) – regional model for Mediterranean and middle east;
- Cauzzi and Faccioli (2008) – global model, but principally comprised of Japanese data;
- Zhao et al. (2006) – model for both ACRs and SZs using data mainly from Japan (almost 90% of the total) plus events from California and Iran;
- Chiou and Youngs (2008a) – part of NGA-West1 project, uses global database by Chiou et al., 2008b).

Recently in the framework of the Global Earthquake Model (GEM) Global GMPEs project, coordinated by the Pacific Earthquake Engineering Research Center (PEER), an international expert panel recommended GMPEs for application in PSHA for ACRs, SZs, and SCRs (Stewart et al., 2015). For ACRs, the selected GMPEs were: Akkar and Bommer (2010), Zhao et al. (2006) and Chiou and Youngs (2008a). These GMPEs were selected in consideration of various desirable scaling characteristics described further in the next section and to have the source databases be somewhat distinct in the selected models (Europe, Japan, global, respectively).

In the pre-selection of GMPEs for this study, we considered precedent from prior work in Italy and Europe, various levels of regionalization (from Italy-based to global), and relative levels of model sophistication. The pre-selected models are:

- Italian models: Sabetta and Pugliese (1996) and Bindi et al. (2011).
- European models: Ambraseys et al. (1996) and Akkar and Bommer (2010).

- Global models: Cauzzi and Faccioli (2008), as modified by Faccioli et al. (2010); Zhao et al. (2006); and Boore et al. (2014) (hereafter BSSA14). BSSA14 was developed in the NGA-West2 project (Bozorgnia et al., 2014). The NGA-West2 models supersede those from the original NGA project, including Chiou and Youngs (2008a), which had been selected by SHARE and GEM. BSSA14 contains a regional adjustment specific to Italy to account for a faster rate of anelastic attenuation (Scasserra et al., 2009).

Table 3.4 summarizes key attributes of the pre-selected GMPEs, including the database, magnitude scale and range, source-to-site distance type and range, and the predicted intensity measures (PSA, PGA and/or PGV).

Table 3.4 Characteristics of pre-selected GMPEs for PSHA of Farneto del Principe site

GMPE	Database	Magnitude range and type*	Distance range and type**	Response variables***
Sabetta and Pugliese (1996)	Italian (1976 – 1984)	4.6 – 6.8 M_S (>5.5) M_L (≤5.5)	1.5 – 100 km R_{epi}, R_{jb}	PGV, PGA PSA (0.04 – 4.0 sec)
Ambraseys et al. (1996)	European (1969 – 1994)	4.0 – 7.9 M_S	0 – 260 km R_{jb} (M_S>6) R_{epi} (M_S≤6)	PGA PSA (0.1 – 2.0 sec)
Akkar and Bommer (2010)	Mediterranean and Middle Eastern (1973 – 2003)	5.0 – 7.6 **M**	0 – 99 km R_{jb}	PGV, PGA PSA (0.01 – 3.0 sec)
Faccioli et al. (2010)	Worldwide Mainly Japanese (1995 – 2005)	4.5 – 7.6 **M**	0.2 – 200 km R_{rup}	PGA PSA (0.05 – 20.0 sec)
Zhao et al. (2006)	Mainly Japanese plus Western USA and Iran (1968 – 2003)	5.0 – 8.3 **M**	0 – 300 km R_{rup}	PGA PSA (0.05 – 5.0 sec)

(continued on next page)

Table 3.4 (cont.) Summary of the characteristics of the pre-selected GMPEs

GMPE	Database	Magnitude range and type*	Distance range and type**	Response variables***
Bindi et al. (2011)	Italian (1972 – 2009)	4.1 – 6.9 **M**	0 – 200 km R_{jb}	PGV, PGA PSA (0.04 – 2.0 sec)
BSSA (2014)	Worldwide (NGA2 – West) (1935 – 2011)	3.0 – 7.9 **M**	0 – 400 km R_{jb}	PGV, PGA PSA (0.01 – 10.0 sec)

*Ms = surface wave magnitude; M_L = local magnitude; **M** = moment magnitude.

**R_{jb} = closest distance to surface projection of rupture surface, referred to as Joyner and Boore (1981) distance; R_{epi} = Epicentral distance; R_{rup} = rupture distance.

***PGA = Peak ground acceleration; PGV = peak ground velocity SA = Spectral acceleration (periods in seconds).

3.4.2 GMPE Comparisons and Selection

We seek to select GMPEs from the pre-selected models listed in Table 3.4 for application in PSHA. Factors considered in the selection include those used for the GEM project (Stewart et al., 2015) in combination with the need to capture features specific to the application region in southern Italy. One of the key considerations in the GEM selections was comparative interpretation of GMPE scaling with respect to magnitude, distance, and period. Site scaling is not of interest in the present work because the hazard analysis is being performed for firm site conditions.

Comparisons of the pre-selected GMPEs are complicated by non-uniform magnitude scales, distance metrics, and the lack of focal mechanism terms in the older GMPEs by Sabetta and Pugliese (1996) and Ambraseys et al. (1996). We seek to compare GMPE median scaling with respect to moment magnitude (**M**), distance to surface projection of fault (R_{jb}), and oscillator period. We emphasize comparisons for normal faulting conditions, since this is the dominant focal mechanism near the Farneto del Principe site.

With regard to focal mechanism, for the older GMPEs of by Sabetta and Pugliese (1996) and Ambraseys et al. (1996), we apply multiplicative correction factors to the GMPE median (in arithmetic units) for different styles of faulting, following the approach of Bommer et al. (2003). The specific factors that were applied were derived by Stucchi et al. (2011) and are given in

Table 3.5. These correction factors were previously used in the PSHA for the Italian building code.

Table 3.5 Style of faulting correction factors

Model	Normal	Reverse	Strike-slip
Sabetta and Pugliese (1996)	0.89	1.15	0.94
Ambraseys et al. (1996)	0.88	1.13	0.93

Magnitude scale conversions are required for Sabetta and Pugliese (1996) and Ambraseys et al. (1996) to convert from surface wave and local magnitude (M_S and M_L) to moment magnitude (**M**). All other pre-selected GMPEs use moment magnitude. The Sabetta and Pugliese (1996) GMPE has different magnitude definitions for two ranges of earthquake size: M_L for $M_L \leq 5.5$ and M_S for $M_S > 5.5$. We first convert local to surface wave magnitude following the recommendations of Gasperini et al. (2004):

$$M_S = \begin{cases} \dfrac{(M_L + 0.584)}{1.079}, & M_L \leq 5.5 \\ M_S, & M_S > 5.5 \end{cases} \tag{3.6}$$

Surface wave magnitude is then converted to moment magnitude using the approach of Lolli et al. (2014), which is considered valid for Italian earthquakes:

$$\mathbf{M} = \exp(1.421 + 0.108 \cdot M_S) - 1.863 \tag{3.7}$$

The Ambraseys et al. (1996) GMPE is defined for M_S and the conversion in Eq. (3.7) was applied.

We adopt R_{jb} as the reference distance metric (Joyner and Boore, 1981), because it captures finite source effects, approximately captures hanging wall effects, and has practical utility given the common usage of area and background sources in the source modeling. The adoption of R_{jb} requires distance metrics used in other GMPEs (epicentral distance, $R_{epi,}$ and rupture distance R_{rup}) to be converted to R_{jb} for the comparative GMPE scaling plots. The conversion is based on the Kaklamanos et al. (2011) approach in which dip angle is estimated from focal mechanism and hypocentral depth and fault dimensions are estimated from **M**. This information, combined with an assumption regarding hypocenter location along the fault width, allows the fault

geometry to be fully defined, which in turn enables the relative values of R_{jb} and R_{rup} to be evaluated.

Figure 3.29 shows the various parameters describing fault geometry, assuming a planar source (the only missing parameter in the figure is the along-strike fault length, L). The parameters shown in the figure that have not been introduced previously are top of rupture depth (Z_{tor}), horizontal distance from site to a line drawn along the fault strike above the shallowest portion of the fault (R_x) and fault width (W). The average dip angles (δ) for a given style of faulting (normal, reverse or strike-slip) are as shown in Table 3.6. The dip angles in the table are modified from the guidelines of Chiou and Youngs (2008b).

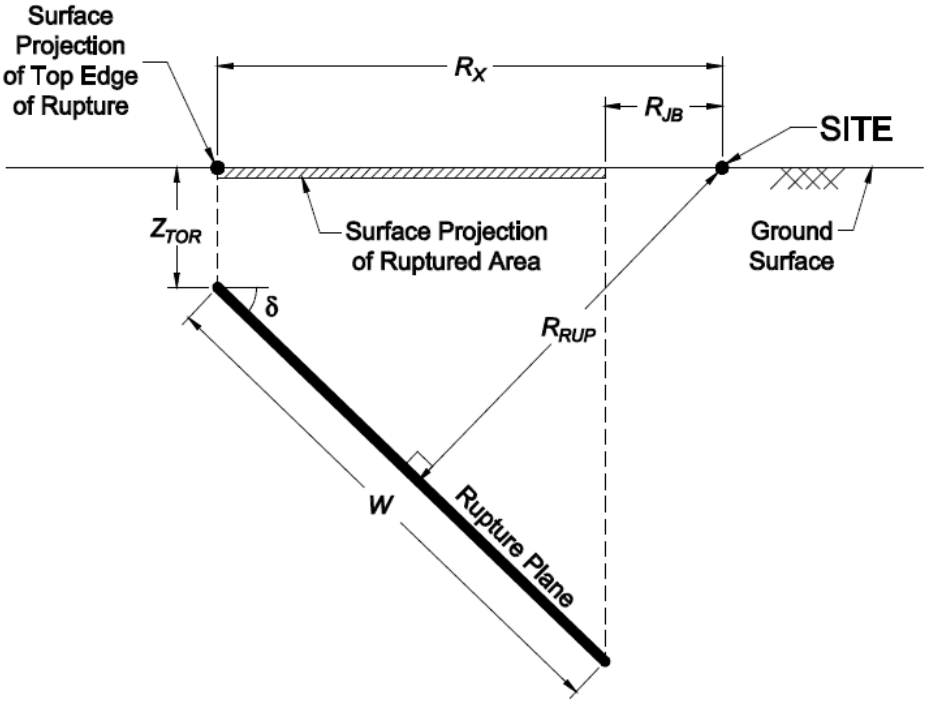

Figure 3.29 **Scheme of an earthquake source and distance measures using a vertical cross-section through a fault rupture plane (from Kaklamanos et al., 2011).**

Table 3.6 **Dip angle estimation for a given style of faulting (Kaklamanos et al, 2011).**

Style of faulting	Dip angle, δ (deg)
Normal	50
Reverse	40
Strike-slip	90

Hypocentral depth (Z_{HYP}) is estimated from **M** using the linear relationships from Scherbaum et al. (2004):

$$Z_{HYP} = \begin{cases} 5.63 + 0.68 \cdot \boldsymbol{M}, & strike - slip\ faults \\ 11.24 - 0.2 \cdot \boldsymbol{M}, & non - strike - slip\ faults \end{cases} \tag{3.8}$$

Down-dip rupture width (W) and along-strike length (L) are estimated from **M** and style of faulting by using the logarithmic relationships by Wells and Coppersmith (1994):

$$W = \begin{cases} 10^{-0.76+0.27 \cdot \boldsymbol{M}} & strike - slip\ faults \\ 10^{-1.61+0.41 \cdot \boldsymbol{M}} & reverse\ faults \\ 10^{-1.14+0.35 \cdot \boldsymbol{M}} & normal\ faults \end{cases} \tag{3.9a}$$

$$L = \begin{cases} 10^{-2.57+0.62 \cdot \boldsymbol{M}} & strike - slip\ faults \\ 10^{-2.42+0.58 \cdot \boldsymbol{M}} & reverse\ faults \\ 10^{-1.88+0.50 \cdot \boldsymbol{M}} & normal\ faults \end{cases} \tag{3.9b}$$

Assuming that the hypocenter is located 60 percent down the fault width, as suggested by Mai et al. (2005), it is possible to define the depth to top of rupture (Z_{TOR}) as:

$$Z_{TOR} = Z_{HYP} - (0.6 \cdot W \cdot \sin \delta) \tag{3.10}$$

We take the hypocenter location along the fault length as uniformly distributed and assume the hypocenter to be centered within the rupture length. With these parameters defined, the fault location is full specified, allowing R_{rup} to be computed from R_{jb} and vice-versa.

For the Sabetta and Pugliese (1996) and Ambraseys et al. (1996) models, a conversion between R_{epi} and R_{jb} was used (Montaldo et al., 2005). This conversion was developed for earthquakes with $M_S \geq 6$ using European data as follows:

$$R_{jb} = 3.5525 - 0.8845 \cdot R_{epi} \tag{3.11}$$

We recognize that with the definition of the finite source that the use of Eq. 3.11 is not required and may be inconsistent with other fault parameters. This issue will be addressed in subsequent refinements of the ground motion computations.

Based on the above conversions, all the pre-selected GMPEs can be compared on common sets of axes in terms of their spectral shapes, magnitude-scaling, and distance-scaling. The comparisons are shown in trellis charts similar in format to those used in the GEM project

(Stewart et al., 2015). All trellis plots are prepared for a normal style of faulting mechanism and rock site conditions (V_{S30} = 800 m/s).

Figure 3.30 shows PSA trellis chart for **M** = 5, 6, and 7 and R_{jb} = 10, 30, 100 km using the pre-selected GMPEs. The spread between models is much greater at 100 km than for shorter distances in each **M** bin. This is unexpected because the available data at large distance is generally much greater than at close distance, hence model variability should be minimized.

However, the variability in this case is driven in part by functional form – the BSSA14, Zhao et al. (2006), Akkar and Bommer (2010), and Bindi et al. (2011) models include an anelastic attenuation term (and have lower PSA at large distance) whereas the Faccioli et al. (2010), Sabetta and Pugliese (1996) and Ambraseys et al. (1996) models do not. The spectra for the Faccioli et al. (2010) model often have unusual shapes, which could be due to a limited number of records having rock-like site conditions (discussed also in Stewart et al. 2015). For the largest magnitude and largest distances the Sabetta and Pugliese (1996) and the Ambraseys et al. (1996) models are high relative to other models. The Bindi et al. (2011) and BSSA14 models, which include local effects and relatively large databases, predict the lowest values.

Figure 3.31 shows distance-scaling for the pre-selected GMPEs for PSA at three oscillator periods: T = 0 (PGA), 0.3s, and 1.0 sec. The effect of the anelastic attenuation term is evident by curvature in the attenuation plots for distances larger than about 70-100 km; these effects are evident for PGA and 0.3 sec PSA but not for 1.0 sec PSA. The BSSA14, Zhao et al. (2006), Akkar and Bommer (2010), and Bindi et al. (2011) models exhibit effective anelastic attenuation. The models of Faccioli et al. (2010), Sabetta and Pugliese (1996) and Ambraseys et al. (1996) do not have anelastic attenution terms. As noted previously, the Sabetta and Pugliese (1996) and Ambraseys et al. (1996) models often predict larger ground motions than the other models.

Figure 3.32 shows the magnitude-scaling of the pre-selected GMPEs for R_{jb} = 10, 30, 100 km and oscillator periods 0, 0.3, and 1.0 sec. The models of Faccioli et al. (2010), Bindi et al. (2011), Sabetta and Pugliese (1996) and Ambraseys et al. (1996) do not exhibit magnitude saturation effects, because the ordinates scale linearly with **M** over the range considered. Magnitude saturation effects are well established from GMPEs that utilize data sets that include large **M** events. Hence, GMPEs lacking this effect are deficient for hazard applications, which typically are very sensitive to predictions for large-**M** conditions.

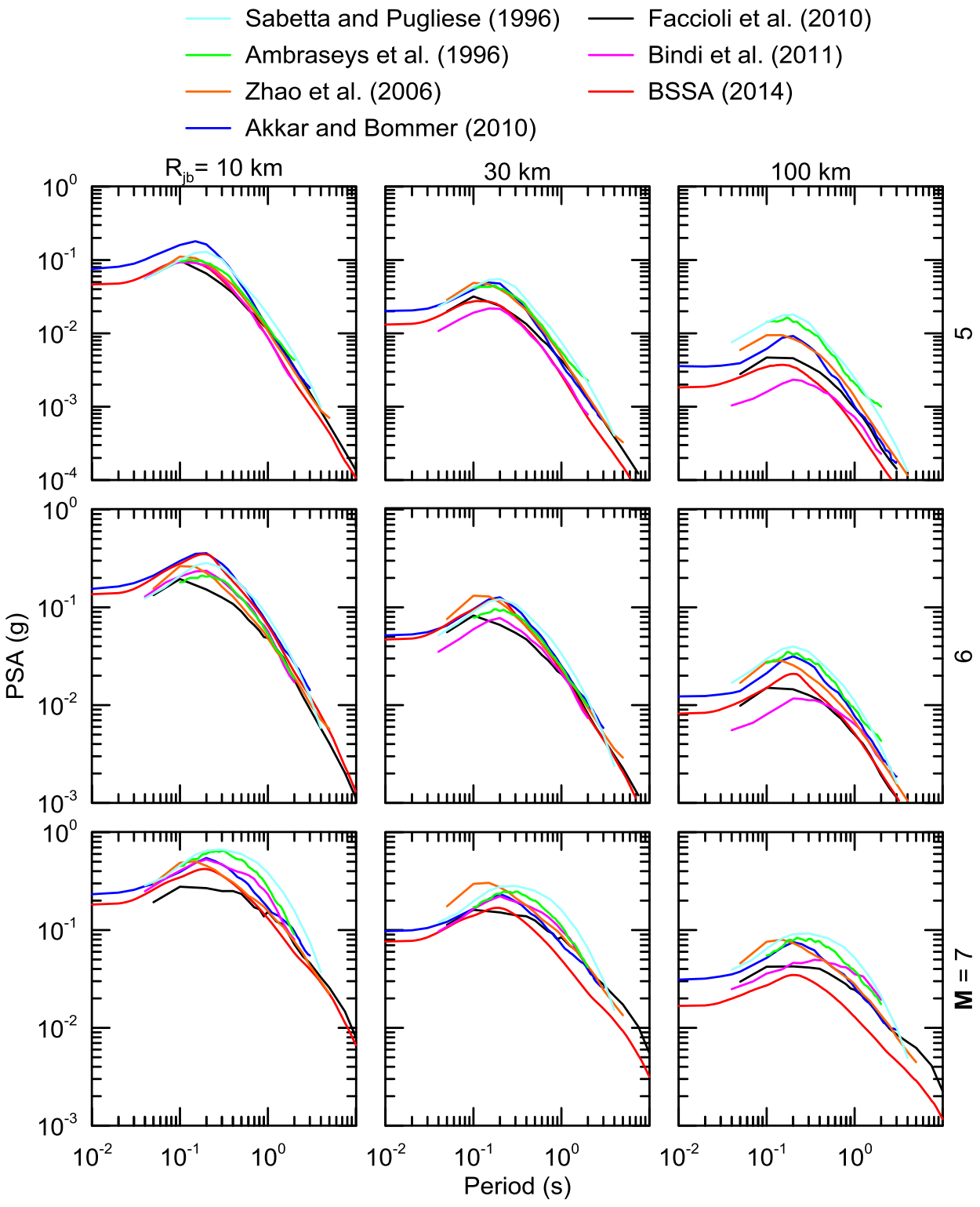

Figure 3.30 **Trellis chart showing predicted PSAs for pre-selected GMPEs for M= 5, 6, 7, R_{jb} = 10, 30, 100 km and rock site conditions (V_{S30} = 800 m/s).**

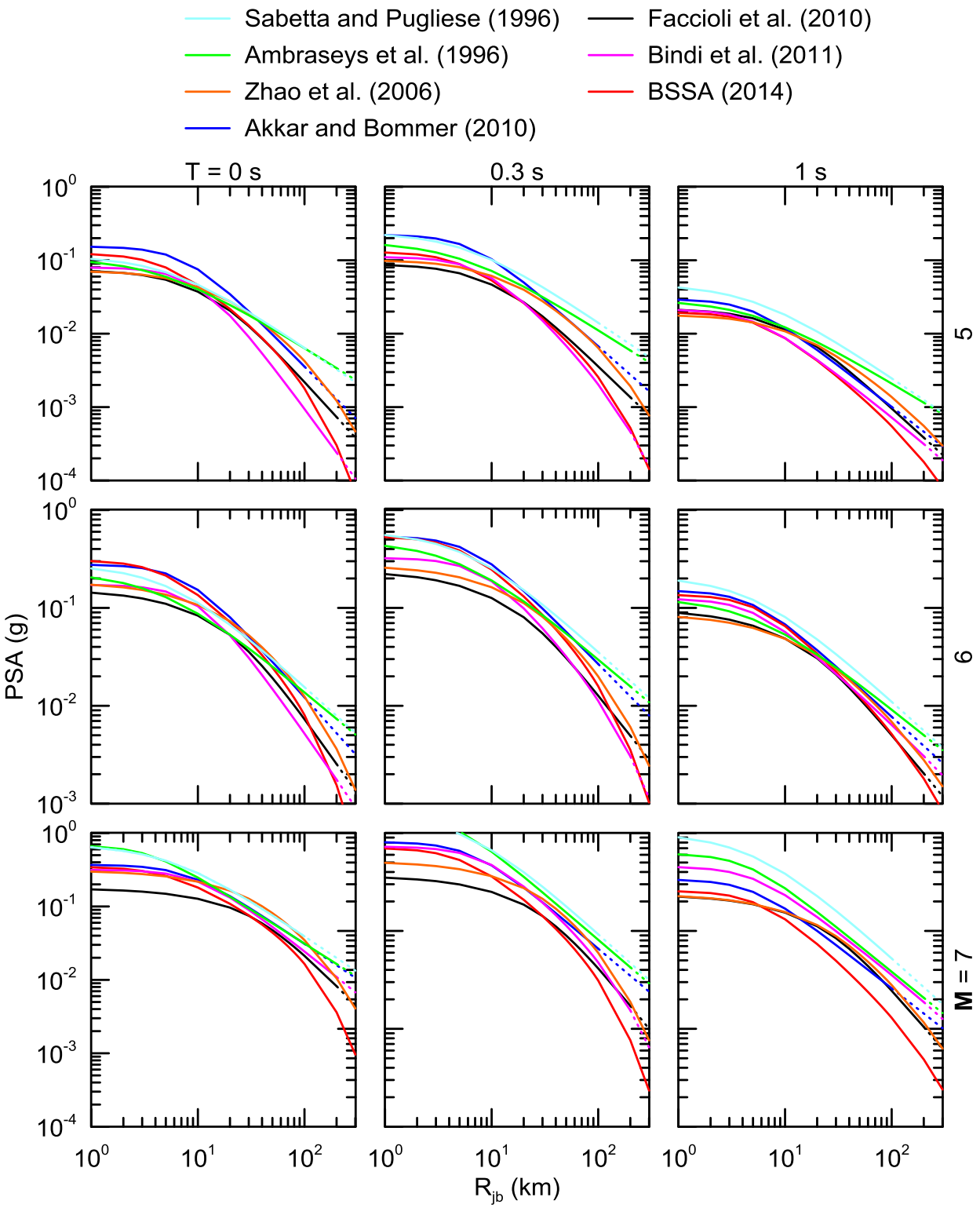

Figure 3.31 **Trellis chart showing distance-scaling for pre-selected GMPEs for M = 5, 6, 7, T = 0s, 0.3s and 1s and rock site conditions (V_{S30} = 800 m/s). Dotted lines indicate where the scenario falls outside the published distance range for the model.**

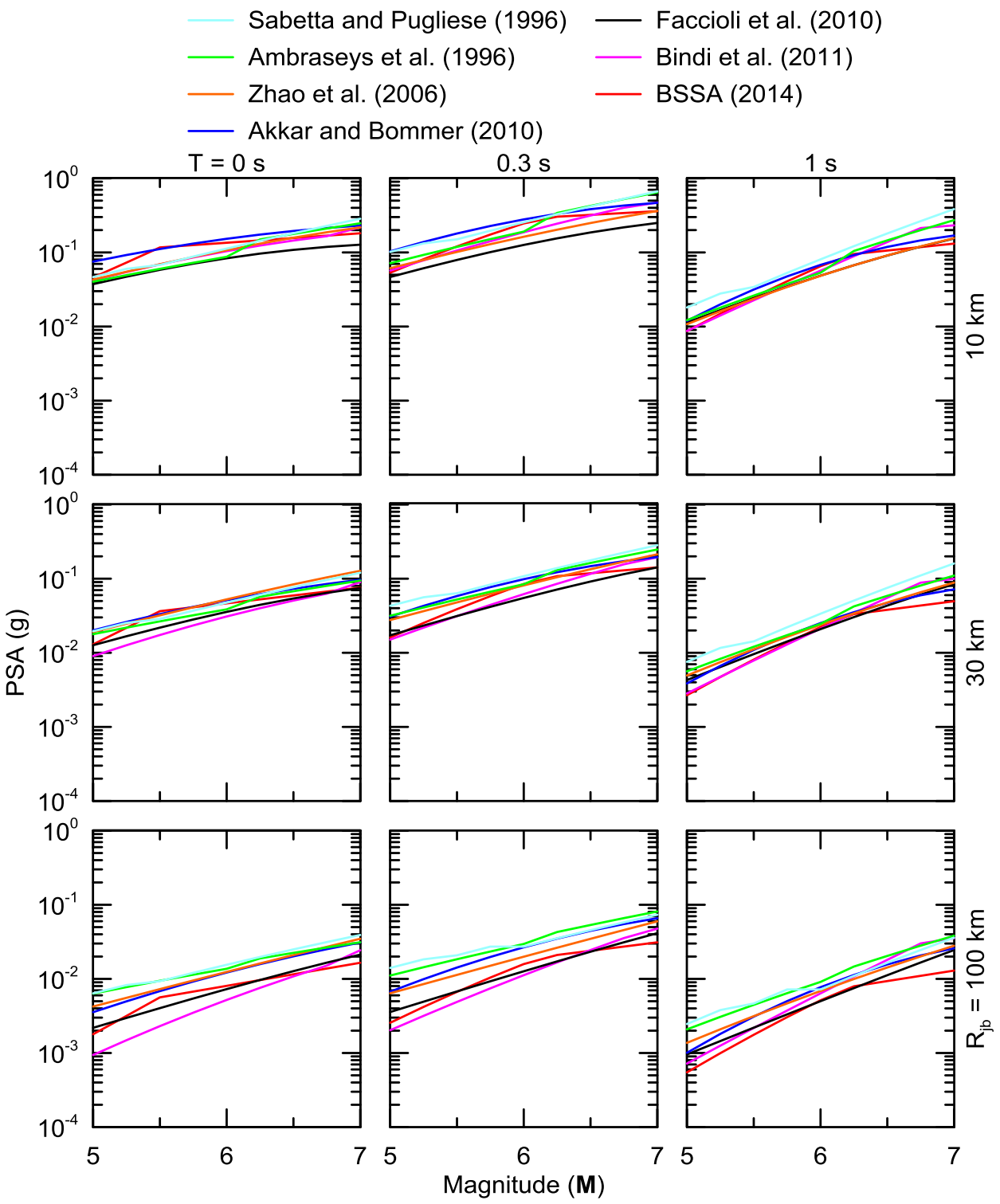

Figure 3.32 **Trellis chart showing magnitude-scaling for pre-selected GMPEs for M = 5, 6, 7, R_{jb} = 10, 30, 100 km and rock site conditions (V_{S30} = 800 m/s).**

In consideration of these observations from trellis plots, we select three models that we consider technically defensible and to capture epistemic uncertainties. The selected models are:

Akkar and Bommer (2010), Zhao et al. (2006), and BSSA14. These are the same models recommended for ACRs for the GEM project (Stewart et al., 2015), except that BSSA14 has replaced Chiou and Youngs (2008a). The models exhibit desirable scaling characteristics, including anelastic attenuation and the magnitude saturation effects. The BSSA14 model has the desirable attribute of having a regional adjustment for anelastic attenuation effects, to capture faster attenuation in Italy as compared to ACRs generally.

GMPEs for subduction zone ground motions have been selected previously by the SHARE project (Delavaud et al., 2012) and GEM project (Stewart et al., 2015). GMPEs selected for use in both projects are Zhao et al. (2006) and Atkinson and Boore (2003), which capture variable rates of distance attenuation that capture epistemic uncertainty. We select these same models. While the GEM project also selected Abrahamson et al. (2015), this model was not selected for the present application because it is not currently implemented in OQ.

Figure 3.33 shows the GMPE logic tree used in this study for ACRs and SZs. We give equal weight to the models in each branch.

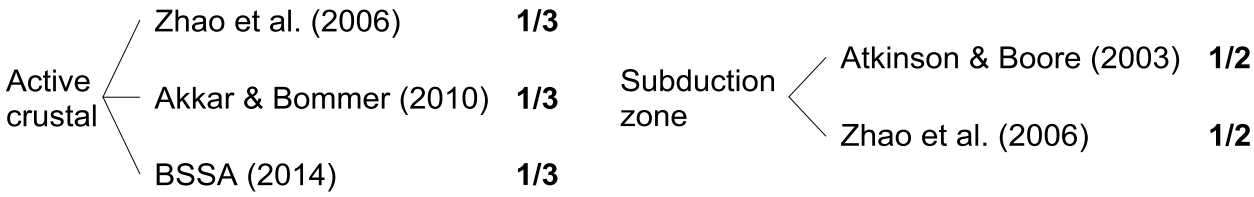

Figure 3.33 GMPE logic tree for active crustal regions and subduction zones (in-slab and interface) used in this study

3.4.3 BSSA (2014) Implementation in OQ Engine

We implemented the BSSA14 model in OQ as part of this project. According to Pagani et al. (2014a), the incorporation of new GMPEs is among the most important challenges for maintaining PSHA software in the long-term. The OQ developers facilitate the implementation of new GMPEs by extending or creating base classes (or templates), which ensure that new GMPEs output the information required by the software. Following GMPE coding and implementation, test tables are defined to check the correct implementation/coding of a new GMPE. A test table provides medians and standard deviations for all possible combinations of the predictor variables in the GMPE functional form Once test tables are defined, typically from

codes provided by GMPE authors, OQ implements a testing protocol (discussed in §3.2) for comparing medians and standard deviations for many combinations of predictor variables.

Ground motions are predicted from the BSSA14 GMPE as follows:

$$lnY = F_E(\mathbf{M}, mech) + F_P\left(R_{jb}, \mathbf{M}, region\right) + F_S\left(V_{S30}, R_{jb}, \mathbf{M}, z_1\right) + \varepsilon_n \sigma(\mathbf{M}, V_{S30}, R_{jb}) \quad (3.12)$$

were *lnY* represents the natural logarithm of a ground motion intensity measure (PGA, PGV or PSA); F_E, F_P and F_S represent functions for source ("E" for "event"), path ("P") and site ("S") effects, respectively, while ε_n is the fractional number of standard deviations of a single predicted value of *lnY* away from the mean, and, σ is the total standard deviation of the model. The predictor variables are magnitude (**M**), source-to-site distance (R_{jb}), average shear wave velocity in the upper 30m (V_{S30}), basin depth parameter (z_1) and the parameter *mech*, used to distinguish among style of faulting (*mech*=1, for strike-slip (SS), 2 for normal (NS), 3 for reverse (RS) and 0 for unspecified).

The source (event) function (F_E) is given as:

$$F_E(M, mech) = \begin{cases} e_0 U + e_1 SS + e_2 NS + e_3 RS + e_4(\mathbf{M} - \mathbf{M}_h) + e_5(\mathbf{M} - \mathbf{M}_h)^2 & \mathbf{M} \leq \mathbf{M}_h \\ e_0 U + e_1 SS + e_2 NS + e_3 RS + e_6(\mathbf{M} - \mathbf{M}_h) & \mathbf{M} > \mathbf{M}_h \end{cases} \quad (3.13)$$

where *U*, *SS*, *NS*, and *RS* are dummy variables, with a value of 1 to specify strike-slip, normal-slip, and reverse-slip fault types, respectively, and 0 if the fault type is unspecified; the hinge magnitude $\mathbf{M}_h$ is period-dependent, and e_0 to e_6 are model coefficients.

The path function (F_p) is given as:

$$F_P\left(R_{jb}, \mathbf{M}, region\right) = \left[c_1 + c_1\left(\mathbf{M} - \mathbf{M}_{ref}\right)\right] ln\left(\frac{R}{R_{ref}}\right) + (c_3 + \Delta c_3)\left(R - R_{ref}\right) \quad (3.14)$$

where

$$R = \sqrt{R_{jb}^2 + h^2} \quad (3.15)$$

c_1, c_2, c_3, M_{ref}, R_{ref} and h are model coefficient. Parameter c_3 is the apparent anelastic attenuation coefficient and Δc_3 is the regional correction to this coefficient that depends on the geographic region. The authors of this model provide tables containing a regional correction derived specifically for Italy and Japan (which show similarly fast distance attenuation trends). This regional correction for Italy was used in the OQ implementation of this model.

The site function is given by:

$$F_S\left(V_{S30}, R_{jb}, \boldsymbol{M}, z_1\right) = \ln(F_{lin}) + \ln\left(F_{nl}\right) + F_{\delta z_1}(\delta z_1) \tag{3.16}$$

where F_{lin} represents the linear component, F_{nl} the nonlinear component of site amplification, and $F_{\delta z1}$ the effects of basin depth. When z_1 is unknown, the recommended default value of δ_{z1} is 0, which turns off the adjustment factor. This is a reasonable condition because the remaining elements of the model are "centered" on a condition of no F_{dz1} adjustment (Boore et al., 2014). In the OQ implementation used in this study, δ_{z1} was set to 0.

The linear component of the site amplification model (F_{lin}) is given by:

$$\ln\left(F_{lin}\right) = \begin{cases} cln\left(\dfrac{V_{S30}}{V_{ref}}\right) & V_{S30} \leq V_c \\ cln\left(\dfrac{V_c}{V_{ref}}\right) & V_{S30} > V_c \end{cases} \tag{3.17}$$

where c describes the V_{S30} scaling, V_c is the limiting velocity beyond which ground motions no longer scale with V_{S30} and V_{ref} is the site condition for which the amplification is equal to one (taken as 760 m/s).

The non-linear component of the site amplification model (F_{nl}) is given by:

$$\ln(F_{nl}) = f_1 + f_2 ln\left(\frac{PGA_r}{f_3}\right) \tag{3.18}$$

where f_1, f_2 and f_3 are model coefficients and PGA_r is the median peak horizontal acceleration for reference rock condition (V_{S30} = 760 m/s). Parameter f_2 represents the degree of nonlinearity and is given as:

$$f_2 = f_4\{exp[f_5(\min(V_{s30}, 760) - 360]\} - exp[f_5(760 - 360)] \tag{3.19}$$

where f_4 and f_5 are model coefficients.

The total standard deviation σ is partitioned into components that represent between-event variability (τ) and within-event variability (ϕ) as.

$$\sigma\left(\boldsymbol{M}, R_{jb}, V_{S30}\right) = \sqrt{\phi^2\left(\boldsymbol{M}, R_{jb}, V_{S30}\right) + \tau^2(\boldsymbol{M})} \tag{3.20}$$

The between-event variability is given as:

$$\tau(\boldsymbol{M}) = \begin{cases} \tau_1 & \boldsymbol{M} \leq 4.5 \\ \tau_1 + (\tau_2 - \tau_1)(\boldsymbol{M} - 4.5) & 4.5 < \boldsymbol{M} < 5.5 \\ \tau_2 & \boldsymbol{M} \geq 5.5 \end{cases} \quad (3.21)$$

The within-event standard deviation is given as:

$$\phi(\boldsymbol{M}, R_{jb}, V_{S30}) = \begin{cases} \phi(\boldsymbol{M}, R_{jb}) & V_{S30} \geq V_2 \\ \phi(\boldsymbol{M}, R_{jb}) - \Delta\phi_V \left(\dfrac{\ln\left(V_2/V_{S30}\right)}{\ln\left(V_2/V_1\right)} \right) & V_1 \leq V_{S30} \leq V_2 \\ \phi(\boldsymbol{M}, R_{jb}) - \Delta\phi_V & V_{S30} \leq V_1 \end{cases} \quad (3.22)$$

where

$$\phi(\boldsymbol{M}, R_{jb}) = \begin{cases} \phi(\boldsymbol{M}) & R_{jb} \leq R_1 \\ \phi(\boldsymbol{M}) + \Delta\phi_R \left(\dfrac{\ln\left(R_{jb}/R_1\right)}{\ln\left(R_2/R_1\right)} \right) & R_1 < R_{jb} \leq R_2 \\ \phi(\boldsymbol{M}) + \Delta\phi_R & R_{jb} > R_2 \end{cases} \quad (3.23)$$

The implementation of the BSSA14 model in OQ was performed creating a new python class, the complete code is provided in Appendix B**.** The OQ verification tools were used to compare BSSA14 medians and standard deviations as implemented in OQ and in test tables built using a Matlab™ script. More than 10000 checks were performed, a summary of which is given in Table 3.7. If a maximum tolerable discrepancy is set as 0.5%, the success rate of the tests is 100%.

Table 3.7 Summary of the tests performed in the newly implemented GMPE (BSSA, 2014)

Value	Average discrepancy (%)	Maximum discrepancy (%)	Standard deviation
Median	0.1186	0.4749	0.0866
Total standard deviation	0.0347	0.0881	0.0209

3.5 Hazard Results for Farneto del Principe Dam Site

3.5.1 Hazard Curves

A fundamental outcome of PSHA is the relationship between probability of exceedance within a specified time interval and the intensity measure amplitude, which is known as a seismic hazard curve.

Seismic hazard curves for the Farneto del Principe dam site were computed for the intensity measures (IMs) of PGA as well as PSAs at the elastic first-mode natural period of the system (dam plus deformable foundation) T_1 = 0.25 sec, second elastic natural period T_2 = 0.125 sec, 0.5 sec (twice T_1), 1.0 sec (four times T_1) and 0.15 sec (period having the maximum PSA). Further information and details about the calculation of the elastic natural periods of the dam system are provided in §4.1. Hazard curves are computed for all combinations of source models and GMPEs to account for epistemic uncertainties. OQ internally assembles a cumulative distribution function (CDF) of computed probabilities for a given IM that takes into account their relative weights. Based on that weighted CDF, percentiles of probability are evaluated by OQ for a given value of IM. In Figure 3.34, the median (50^{th}), 5^{th}, 25^{th}, 75^{th} and 95^{th} percentile hazard curves are shown for the six selected intensity measures.

Figure 3.35 shows a representative plot of computed probabilities of exceedance vs. quantile for the IM of 0.25 sec PSA at a ground motion amplitude of 0.1g. The median probability (0.5 quantile) for this amplitude is 0.086. As shown in Figure 3.35, the distribution of probabilities about the median is better approximated as normal than log normal. The coefficient of variation of the fit distribution is approximately 0.5. This is a large scatter that reflects a strong impact of epistemic uncertainty in the hazard estimates at the site. Inspection of Figure 3.34 indicates that the general features of the distribution in Figure 3.35 do not always hold, but are relatively common, especially at high hazard levels (low probabilities). We recognize that confidence intervals on the mean hazard curve are generally of greatest practical interest – these will be added in subsequent refinements of the ground motion computations.

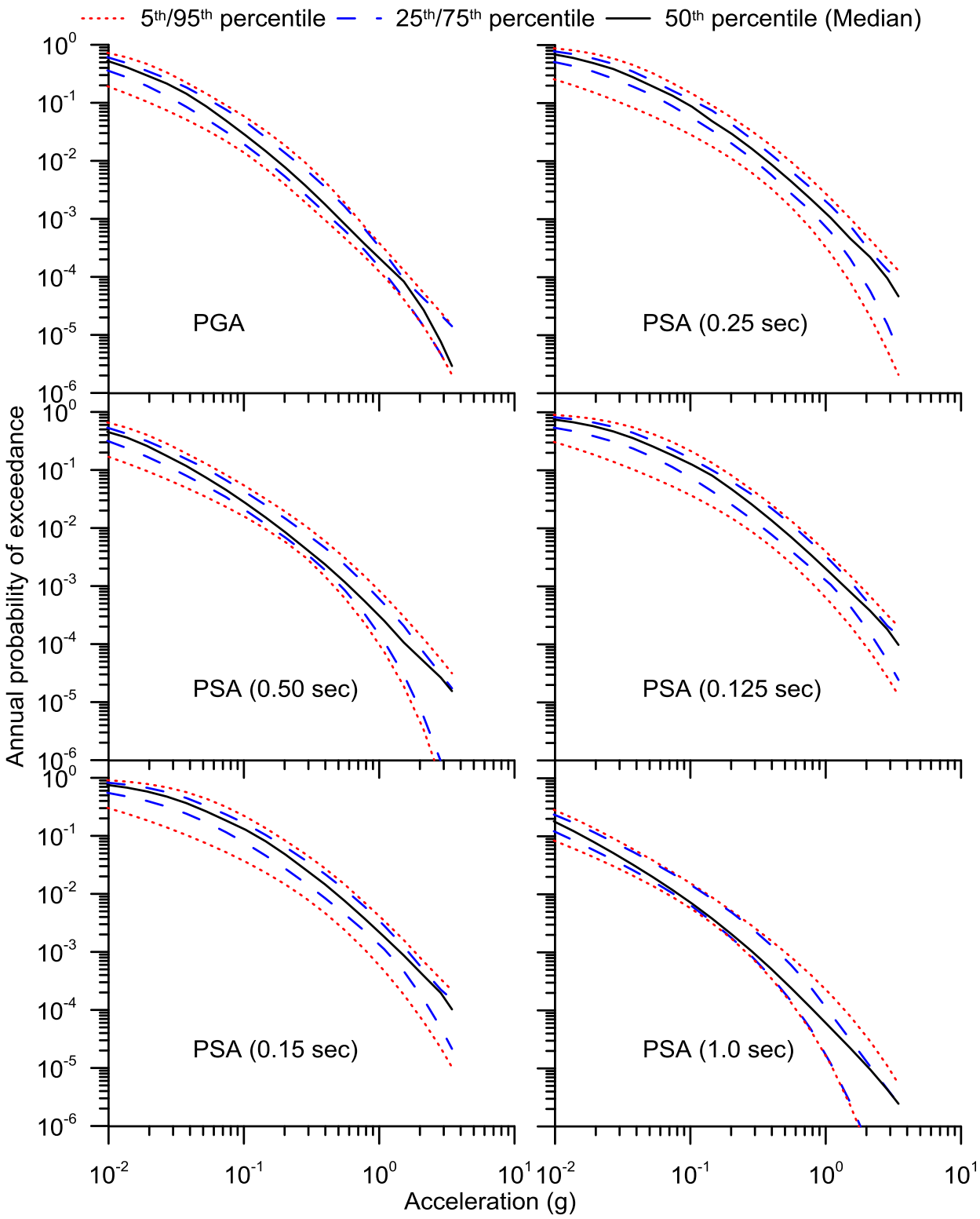

Figure 3.34 **Percentile seismic hazard curves for Farneto del Principe dam site for several intensity measure levels.**

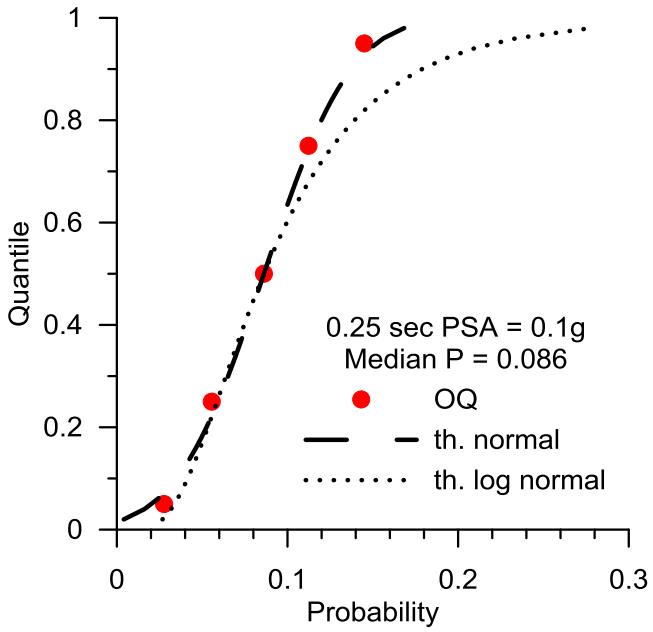

Figure 3.35 Computed probabilities of exceedance vs. quantile for the IM of 0.25 sec PSA at a ground motion amplitude of 0.1g.

To provide context on the level of hazard at the Farneto del Principe dam site, we compare the median hazard for PGA and 1.0 sec PSA to results for two other locations in the western and central United States. The western US (WUS) location is in Los Angeles, CA (Lat. 34.05372 deg, Lon. -118.24273 deg) and is known to be among the most active seismic region in the world. The central US located is Clinton, IL (Lat. 40.1536 deg, Lon. -88.9645 deg), which is a stable continental region. Hazard results for the WUS and central US sites are provided by the Hazard Curve Application of the United States Geological Survey (USGS), which provides mean values of acceleration for selected hazard levels; http://geohazards.usgs.gov/hazardtool/application.php (last accessed February 15 2015).

Figure 3.36 compares mean hazard curves for the subject site in Calabria, and the Los Angeles, CA and Clinton, IL comparison sites. As expected, the CEUS site has much lower hazard. The PGA hazard for the Italian and Los Angeles sites are comparable for PGA, while the 1.0 sec PSA hazard is higher in Los Angeles, due to the presence of faults producing larger **M** events (the discrepancy increases with oscillator period).

Probabilistic analysis of the response of systems to earthquakes involves the convolution of hazard curves with system fragility. The convolution uses the absolute value of the slope of the hazard curve, which we compute as:

$$f_X(x) = \frac{\partial v(IM)}{\partial IM} \tag{3.24}$$

where $f_X(x)$ represents the probability density for ground motion level x and $\delta v(IM)$ is the differential on the exceedance rate of IM (practically equal to the differential of the annual exceedance probability). Numerically differentiating the rock-hazard curve of Figure 3.37, we obtain corresponding slopes $f_X(x)$ in Figure 3.37. The patterns in slope mirror those for hazard.

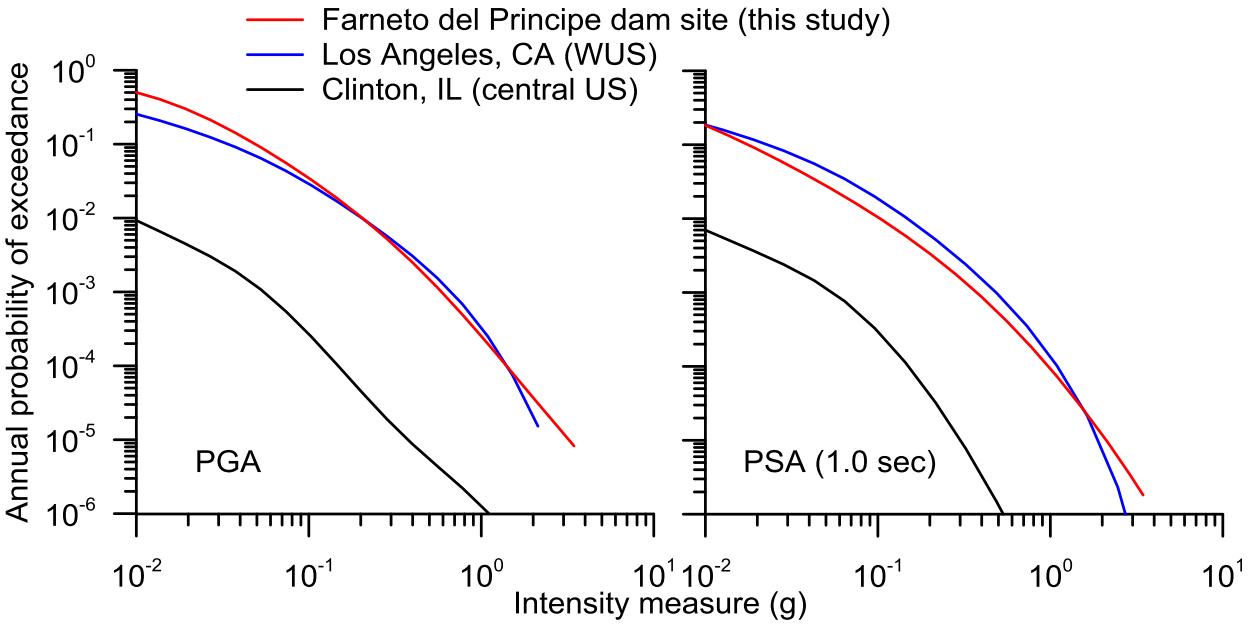

Figure 3.36 **Mean seismic hazard curves for Farneto del Principe dam site (This study), Los Angeles, CA (WUS) and Clinton, IL (central US).**

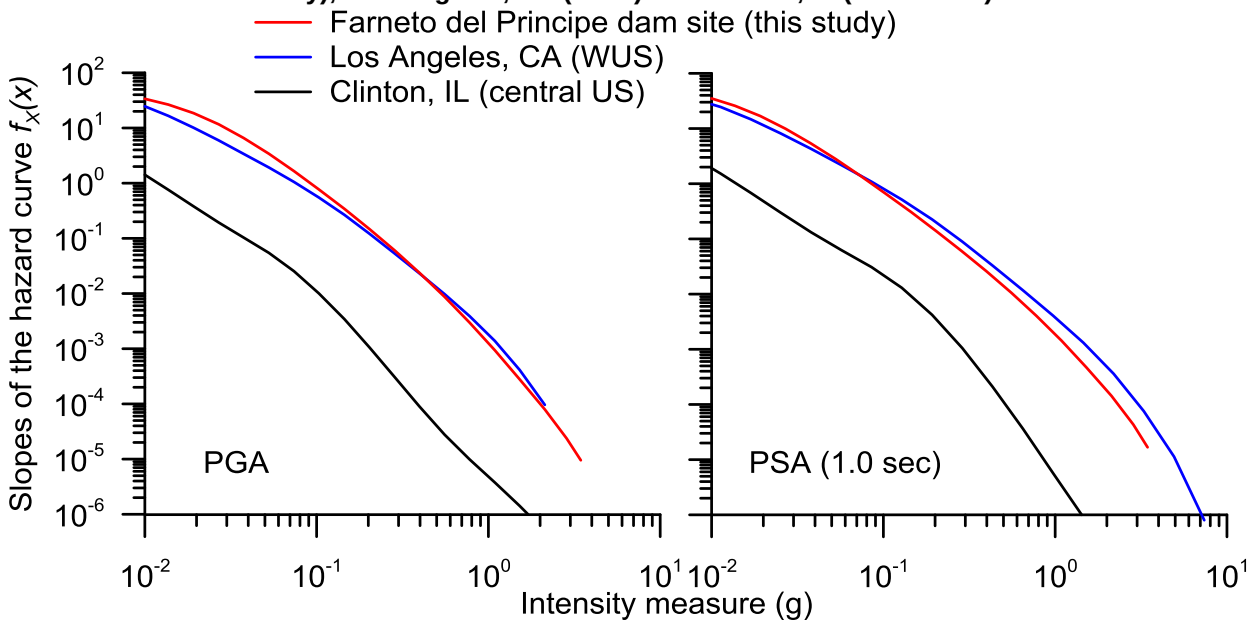

Figure 3.37 **Slopes of the mean hazard curves for Farneto del Principe dam site (This study), Los Angeles, CA (WUS) and Clinton, IL (central US).**

3.5.2 Uniform Hazard Spectra (UHS)

Uniform hazard spectra (UHS) are PSA ordinates sharing a common probability of exceedance for a specified time span. The UHS is a common product of PSHA, often being used for response spectrum methods of analysis for structures or as the target spectrum for acceleration time series scaling/modification.

For application to the Farneto del Principe dam site, we select return periods associated with a 10% and 2% probabilities of exceedance in 50 years (T_R = 475 and 2475 years, respectively). The T_R = 475-year hazard level is considered representative of moderate events that are reasonably likely to affect the structure in its design life. The T_R = 2475-year hazard level represents for large relevant dams, such as the Farneto del Principe dam, "*the collapse limit state performance level*" according to the Italian code for dam design and safety (Decreto Ministeriale, D.M. June 14, 2014).

Figure 3.38 shows median UHS for the two hazard levels at the subject site. We use median ordinates in this case for compatibility with previous Italian sources; in general we prefer mean ordinates per McGuire et al. (2005). Also shown for reference are median UHS for this site derived using the SHARE Euro-Mediterranean model (Giardini et al., 2013) and from two Italian national sources:

1. PSHA performed for the Italian Department for Civil Protection (DPC) by Istituto Nazionale di Geofisica e Vulcanologia (INGV) as part of national research projects from 2004–2006 (MPS working group, 2004; Stucchi et al., 2011). Labelled as 'INGV-DPC' in Figure 3.37, these spectral ordinates were obtained from the web-site http://esse1-gis.mi.ingv.it/ (last accessed 20 December 2014). The hazard results provided from this source are median values.

2. A simplified shape representing approximately the UHS from (1) for application in the Italian Building Code by the Consiglio Superiore dei Lavori Pubblici (Norme Tecniche per le Costruzioni, NTC, 2008). This UHS is labelled 'Italian Building Code (2008)'.

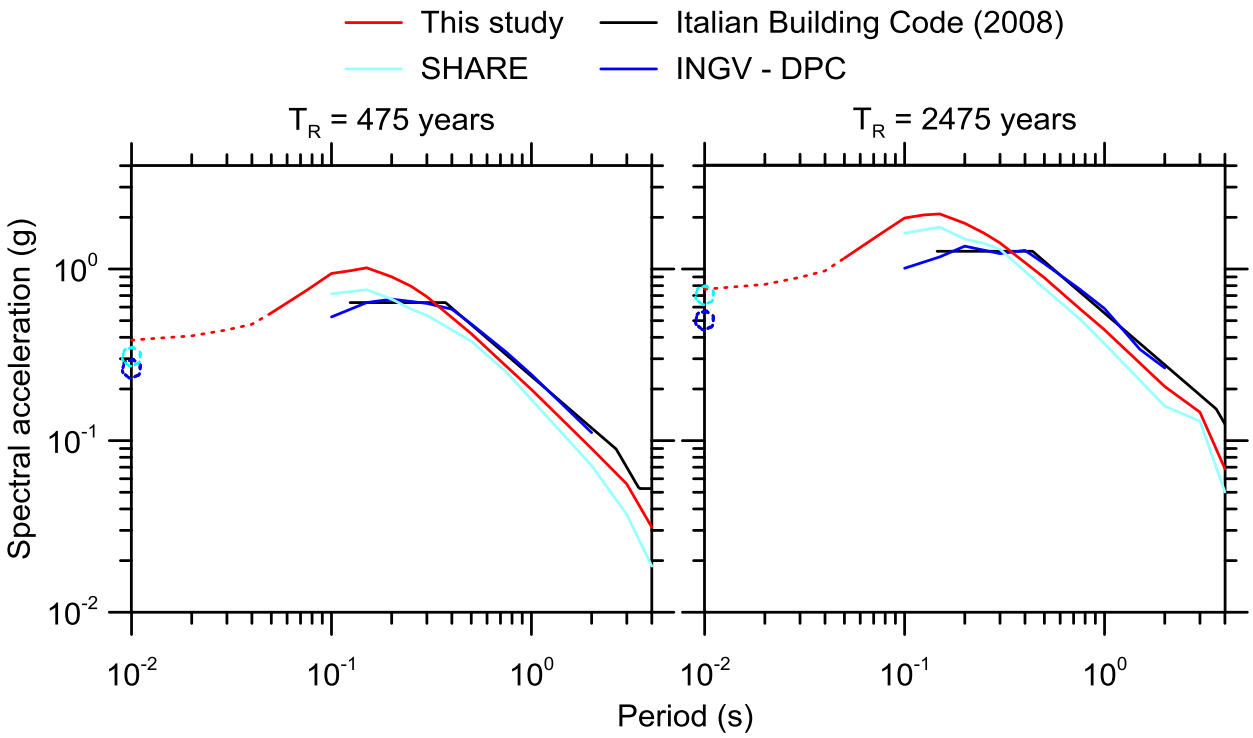

Figure 3. 38 **Comparison of the median UHS from this study, the SHARE Euro-Mediterranean model (Giardini et al., 2013), the Italian INGV-DPC model (MPS working group, 2004; Stucchi et al., 2011) and the Italian Building Code (M.LL.PP., 2008). The dotted lines represent the intervals in which the shape was corrected in a deterministic sense (using the GMPEs defined in those intervals) to fill in the missing parts of the spectra. The open circles represent PGA for those GMPEs that don't have the intermediate spectral ordinates.**

The UHS from the present analysis peaks at about 0.15 sec, which is consistent with the shape from the SHARE model but distinct from that in the Italian code and national PSHA, which peaks at around 0.2-0.4 sec. The different spectral shape is likely caused by the use of older GMPEs (Sabetta and Pugliese, 1996 and Ambraseys et al., 1996) in the analyses for the Italian national PSHA. Those GMPEs have some significant differences from contemporary models including a limited number of events in the catalogues, a lack of rock-like records and certain deficiencies in their functional form (details in §3.4.2). The SHARE Euro-Mediterranean model produces a similar spectral shape to the results of the present analysis, presumably due to the use of relatively modern GMPEs in the logic tree.

An important characteristic in Figure 3.38 is that the present UHS has larger PSA ordinates that those from SHARE or the Italian national PSHA, especially for oscillator periods < 0.4 sec. As shown subsequently through sensitivity analyses, we believe this to be caused by our

inclusion of the Lakes fault and subduction interface of the Calabrian arc, which were neglected in the prior PSHA, as well as differences in the GMPEs. For larger oscillator periods, our UHS ordinates are between those from SHARE (which are lower) and the Italian national PSHA (higher). The uniformly higher results from Italian national PSHA are influenced by the older GMPEs that were used, which as shown in §3.4.2, predict higher median PSAs than newer models.

The UHS developed in this study can strictly only be defined over the most restrictive range of oscillator periods in the selected GMPEs. This range excludes PSA for $T < 0.05$ sec due to PSA being undefined in this range by the Zhao et al. (2006) GMPE. We approximately define the UHS shape for these periods as follows:

1. We compute the UHS using the complete logic tree (using all the selected GMPEs) for PGA and PSA for $T > 0.05$ sec;
2. We evaluate the controlling scenario for the selected hazard levels using disaggregation (§3.5.3);
3. We compute deterministic PSA shapes relative to T using the GMPEs that include short-T PSAs (BSSA14, Akkar and Bommer, 2010). This range is $T < 0.05$ sec;
4. The shape from (3) is used to interpolate the UHS between 0.05 sec and 0.01 sec (used to represent PGA). The results of this interpolation are shown with dotted lines in Figure 3.38.

3.5.3 Disaggregation of the Seismic Hazard

For each seismic source, PSHA accounts for all magnitudes and their relative likelihood of occurring within the defined range of $\mathbf{M}_{min}$ to $\mathbf{M}_{max}$. Moreover, for each source and **M** combination, all possible site-source distances are considered, along with their relative likelihoods, by randomizing the rupture location on the fault. Finally, for each **M** and distance combination, the full distribution of ground motion IMs is considered in accordance with the log mean and standard deviation from the GMPE.

Disaggregation identifies the source, distance, and ground motion percentiles that contribute most strongly to the computed hazard (Bazzurro and Cornell, 1999). Disaggregation results are not unique – they depend on the IM and hazard level considered. For example, UHS ordinates at

different periods will in general produce different disaggregation results. OQ disaggregation classifies relative contributions of different parameter combinations as follows (Pagani et al. 2014b):

1. Magnitude (**M**);
2. Distance to rupture surface-projection (Joyner-Boore distance; R_{jb});
3. Longitude and latitude of rupture surface-projection closest point (longitude, latitude);
4. Tectonic region type (TRT);
5. The percentile of ground motion intensity conditional on **M** and R_{jb}, represented in terms of epsilon (ε) as:

$$\varepsilon = \frac{\ln im - \mu_{\ln}\left(\mathbf{M}, R_{jb}, V_{S30}\right)}{\sigma_{\ln}\left(\mathbf{M}, R_{jb}, V_{S30}\right)} \tag{3.25}$$

where *im* is the ground motion intensity at the hazard level for which the disaggregation is computed, and $\mu_{\ln}$ and $\sigma_{\ln}$ are the statistical moments of a GMPE in natural log units, which in general can depend on magnitude, distance, and site condition.

The parameters listed above create a five-dimensional model space (*ms*) that is discretized into a finite number of bins. Each combination of parameters (but with ε omitted) defines a model space bin *ms* = (**M**, R_{jb}, long/lat, TRT) for which the probability of *IM* exceeding level *im* at least once in a time span Δ*t* is computed as (Pagani et al., 2014b):

$$P(IM > im|\Delta t, ms) = 1 - \prod_{i=1}^{I}\prod_{j=1}^{J}\begin{cases} P_{rup_{ij}}(IM < im|\Delta t) & if rup_{ij} \in ms \\ 1 & otherwise \end{cases} \tag{3.26}$$

where *i* is an index for source (associated with a location and **M**) and *j* is an index for rupture location within the source, which sets the distance. The quantity P_{rupij} is the probability of *IM* < *im* in time Δ*t* given that rupture *j* within source *i* has occurred. In other words, it is the probability that this rupture does not produce ground motions that exceed *im*. If the rupture *j* within source *i* has not occurred (the rupture doesn't belong to the *im* bin), then the probability that this rupture does not produce a 'special event' (ground motion that exceed *im*) is equal to 1. As such, Eq. (3.26) considers all possible ε, hence this equation is not used for the ε part of disaggregation. The disaggregated probability from Eq. (3.26) is based on the assumption that

earthquake ruptures in different bins are independent, therefore the union of exceedance probabilities for all ruptures and sources contained within *ms* (left side of Eq. 3.26) can be computed from one minus the product of non-exceedance probabilities.

Although this expression (Eq. 3.26) is not immediately intuitive, consider two overlapping events *A* and *B*. The probability of the union of these events is $P(A \cup B) = P(A) + P(B) - P(A \cap B)$, where $\cap$ indicates the intersection of these events. If *A* and *B* are independent, the intersection probability $P(A \cap B) = P(A) \times P(B)$. This union probability is akin to the left side of Eq. (3.26) in that we want the union of all ruptures and sources that meet the ground motion exceedance requirement. The right side of Eq. (3.26) asserts that $P(A \cup B) = 1 - P(\bar{A})P(\bar{B})$, where the overbar indicates 'not'. Recognizing that $P(\bar{A}) = 1 - P(A)$ and substituting, the original expression for $P(A \cup B)$ is recovered. Hence, Eq. 3.26 correctly represents the union of exceedance probabilities across ruptures and sources.

The OQ disaggregation calculator allows is configured to create several types of disaggregation histograms. We use the following:

- Magnitude disaggregation;
- Distance disaggregation;
- Magnitude-Distance disaggregation;
- Latitude-Longitude disaggregation;
- Magnitude-Distance-Epsilon disaggregation;
- Latitude-Longitude-Magnitude disaggregation.

The disaggregation performed by OQ (Eq. 3.26) is different from classical disaggregation (e.g., Bazzurro and Cornell, 1999). The OQ disaggregation provides, for a given bin *ms*, the conditional probability of (at least one) ground motion exceedance in time span Δt. Classical disaggregation could in principal provide this quantity as well. However, by convention the results are expressed differently. The rates of 'special events' that produce *IM* > *im* within model space bins (*ms*) = ν_{ms} are computed, from which exceedance probabilities are computed. Those exceedance probabilities are then normalized by the corresponding probabilities for the full

parameter space (all *ms*) (rate = ν), which provides a relative contribution (RC) for each *ms* as follows:

$$RC(ms) = \frac{1 - \exp(-\nu_{ms}\Delta t)}{1 - \exp(-\nu\Delta t)} \tag{3.27}$$

The sum of RCs across all *ms* is unity.

The OQ disagreggation results can be readily converted to normalized disaggregation results. Recognize that the numerator in Eq. 3.27 can be re-written as follows based on the properties of a Poisson process:

$$P(IM \geq im|\,\Delta\, t, ms) = 1 - e^{-\nu_{ms}\,\Delta\, t} \tag{3.28}$$

The left side of Eq 3.28 is known from Eq. 3.26, so the numerator in Eq. 3.27 is known.

The denominator in Eq. (3.27) can be similarly written as:

$$P(IM \geq im|\Delta t) = 1 - e^{-\nu\Delta t} \tag{3.29}$$

The left side of Eq. 3.29, $P(IM > im|\Delta t)$, is obtained as one minus the product of non-exceedence probabilities for the different *ms* as:

$$P(IM > im|\Delta t) = 1 - \prod_{ms}\Big(1 - P(IM > im|\Delta t, ms)\Big) \tag{3.30}$$

By these calculations, the relative contributions in Eq. 3.27 can be obtained.

Using the above approach, classical disaggregation of the complete model for the Farneto del Principe dam site was performed using OQ, for a return period of 2475 years and 0.25 sec PSA. The period T = 0.25 represents the first elastic natural period of the dam plus the deformable foundation (further details on the natural periods and mode shapes are provided in §4.1).

Figure 3.39 shows the distance disaggregation, which indicates that the hazard is controlled by close sources (R_{jb} less than 35 km). These likely include the Crati valley fault (§3.3.3) in combination with area and background sources. Since we are using the R_{jb} distance metric for two of the three GMPEs used for the shallow crustal tectonic regime, faults underlying the site, including the nearest area source (ITAS 319) can contribute at zero distance. The subduction zone GMPEs, use the R_{rup} distance metric, for this reason, the subduction sources will not contribute at distances less than the closest distance to the interface, which is 50 km. The mean

and mode distances are 25.5 and 2.5 km (center of first bin), respectively. We recognize that disaggregations associated with specific sources are standard practice in the US, but this capability is not available in OQ.

Figure 3.40 presents the magnitude disaggregation, which shows that there is an important contribution to the hazard from large magnitude events (>7.5). Although OQ does not allow the relative contributions of specific sources to be identified, there are a limited number of options for these large **M** contributions. One contributor is area sources, specifically 318 and 319, which are north of the site and encompassing the site, respectively. Those area sources have largest observed earthquakes of $\mathbf{M}_{obs}$ = 7.9 and 7.7, respectively. Per §3.3.1, we consider maximum magnitudes as high as $\mathbf{M}_{max}$ = 8.5 and 8.3 for these sources within the logic tree. The second contributor is the subduction interface associated with the Calabrian arc, which has a mean value of $\mathbf{M}_{max}$ = 8.1 (§3.3.5) (the largest considered magnitude is 8.6 in §3.5.4, but only the mean value of $\mathbf{M}_{max}$ is considered in the main logic tree). The third contributor is the subduction in-slab area source that is adapted from area source 318 with $\mathbf{M}_{obs}$ = 7.9 and a largest considered $\mathbf{M}_{max}$ in the logic tree of 8.5 Hence, the roughly 5% relative contribution that is shown for the **M** 8.5-9.0 bin is produced by area source 318 (including its use for the subduction in-slab area source). The mean and mode magnitudes are 7.3 and 7.75, respectively. We recognize that the large in-slab earthquakes being treated as area sources with magnitudes above ~ 7.5 is unrealistic; refinements of this element of the fault modeling will be considered in subsequent work.

Figures 3.41 and 3.42 show respectively the latitude-longitude (Lat-Long) and the latitude-longitude-magnitude disaggregation (Lat-Long-**M**). These confirm the essential findings from the distance and **M** disaggregation plots, namely the controlling influence of close distance and large **M** events at this return period.

Figures 3.43 and 3.44 show the magnitude-distance (**M**-R_{jb}) and the magnitude-distance-epsilon (**M**-R_{jb}-ε) disaggregation, respectively. These plots show that events with R_{jb} less than 5 km and **M** = 6-8 control the T_R = 2475 yr hazard 0.25 sec PSA. We expect these are a combination of area source 319 (the area source encompassing the dam site) and the Crati Valley fault (which is the most proximate finite fault source to the dam site). The mean magnitude and distance of $\bar{\mathbf{M}} = 7.4$ and $\overline{R_{jb}} = 26km$ do not correspond to a scenario with a high relative contribution. Figure 3.44 shows that the epsilon values controlling the hazard are in the range of

2 to 3. These are relatively extreme values of ground motion, higher than is typical in the western US (where controlling epsilons at this return period are typically in the range of 1 to 2).

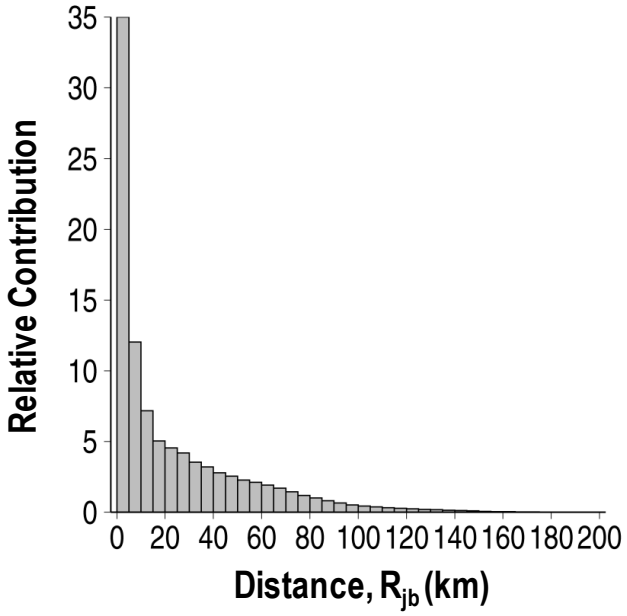

Figure 3.39 Distance disaggregation for PSA (0.25s) at Farneto del Principe dam site.

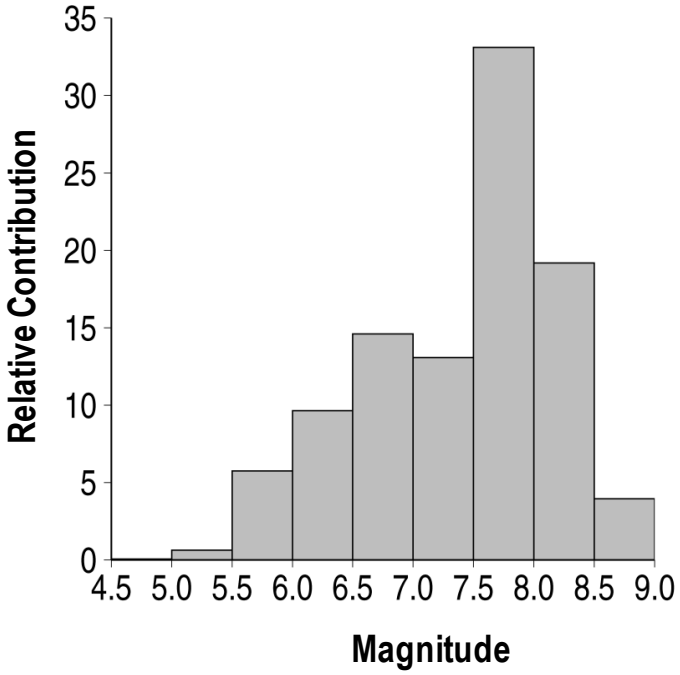

Figure 3.40 Magnitude disaggregation for PSA (0.25s) at Farneto del Principe dam site.

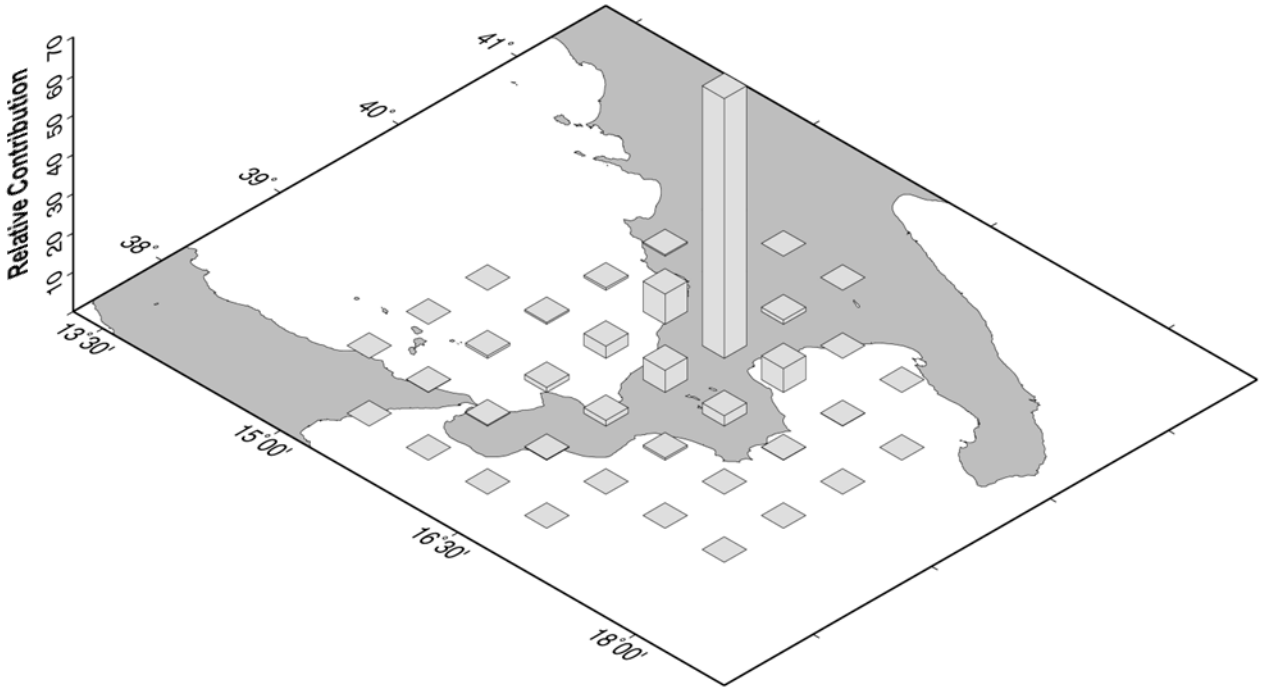

Figure 3.41 **Lat-Long disaggregation for PSA (0.25s) at Farneto del Principe dam site.**

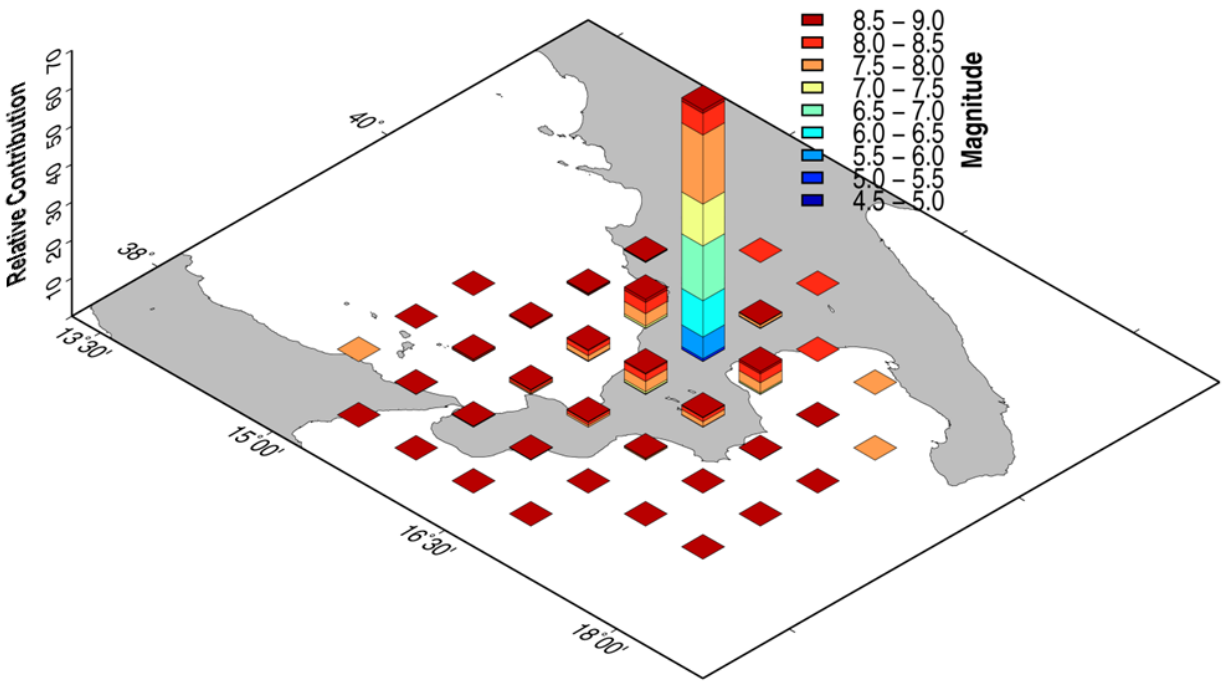

Figure 3.42 **Lat-Long-M disaggregation for PSA (0.25s) at Farneto del Principe dam site.**

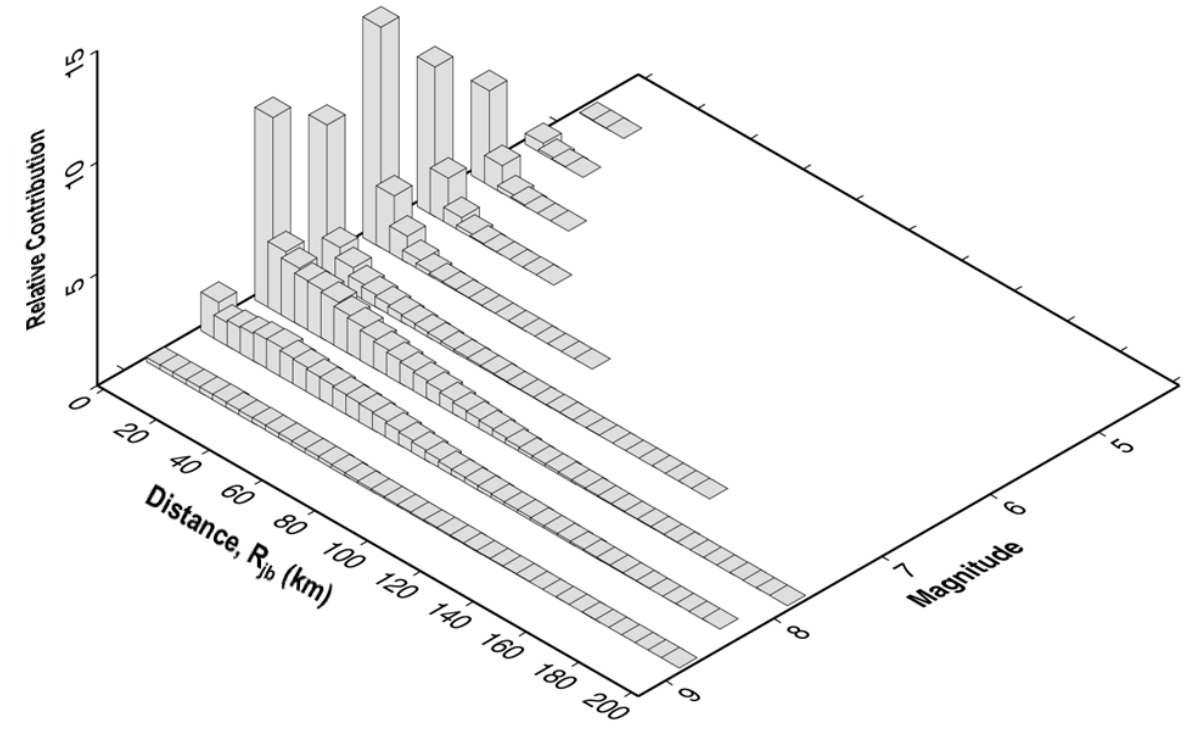

Figure 3.43 M-R_{jb} disaggregation for PSA (0.25s) at Farneto del Principe dam site.

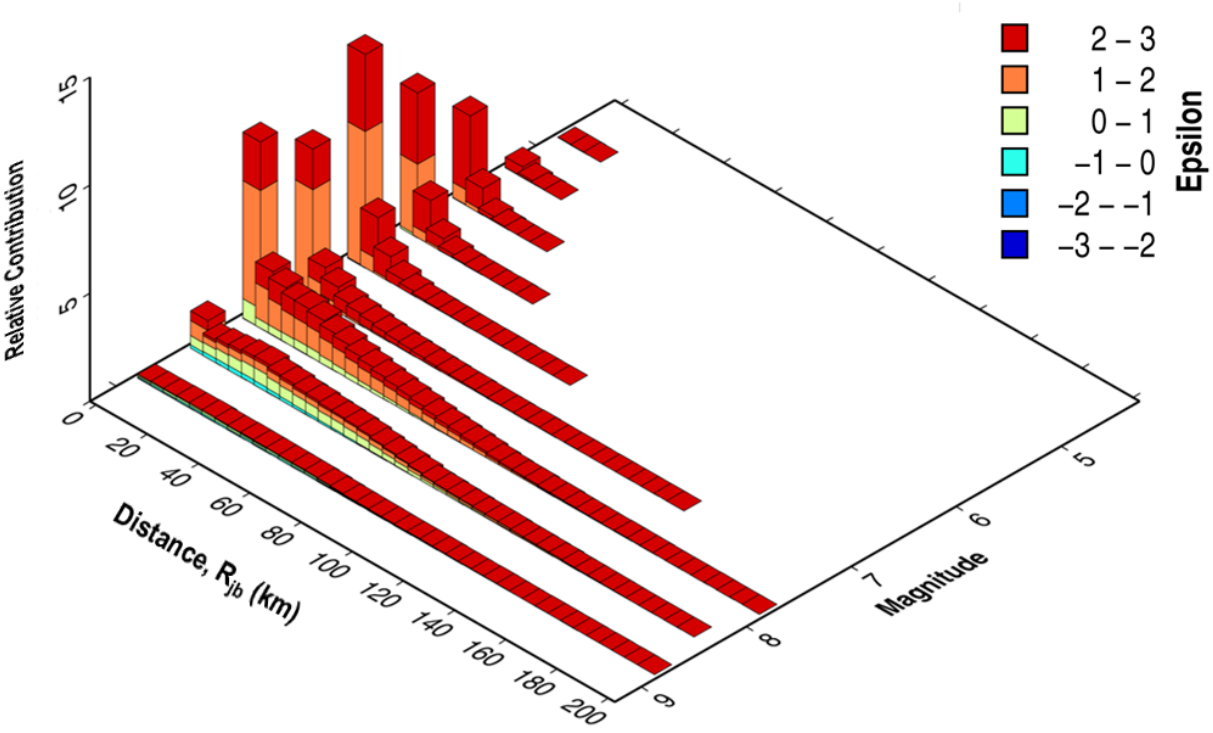

Figure 3.44 M-R_{jb}-ε disaggregation for PSA (0.25s) at Farneto del Principe dam site.

3.5.4 Sensitivity Studies

3.5.4.1 Impact of the Kernel-Smoothed Source Model

In §3.1 the SHARE model was presented. This model contains a Kernel-smoothed source model that is not implemented in this study (the source models used in this study are discussed in §3.3). We found that for the Farneto del Principe dam site the Kernel-smoothed branch does not significantly affect the hazard computed using the SHARE model. Figure 3.45 shows hazard curves for a range of oscillator periods for the Farneto del Principe dam site using the SHARE model with and without the Kernel-smoothed branches. The differences between the two sets of results are judged to be sufficiently small that the Kernel-smoothed branch can be omitted, although percent differences between the two sets of analyses have not been computed.

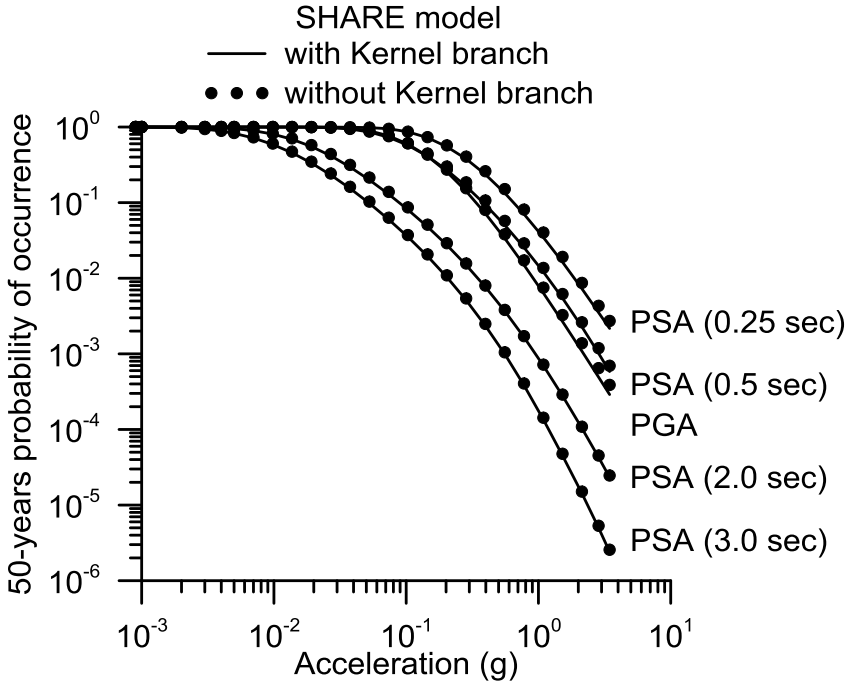

Figure 3.45 **Comparisons of the hazard curves for the Farneto del Principe dam site for Δt = 50 years based on the complete SHARE model and the SHARE model without the kernel-based branch.**

3.5.4.2 Uncertainty in Maximum Magnitude for Fault Sources

As discussed in §3.3.2, uncertainty in the maximum magnitude ($\mathbf{M}_{max}$) of fault sources is not included in the main logic tree and hence does not impact the hazard results presented in §3.5.1-3.5.3, including the disaggregations. We investigate this source of epistemic uncertainty in this section (for shallow crustal fault sources) and the next (for the subduction interface).

Our approach is based on first order second moment principles (Baker and Cornell 2003; Melchers 1999). We consider mean values of $\mathbf{M}_{max}$ in combination with mean ± √3 times the standard deviation of $\mathbf{M}_{max}$. The weights are assigned as:

- $\mathbf{M}_{max}+\sigma_M\sqrt{3}$; weight: 1/6 (this branch is called $\mathbf{M}_{max}(^{+})$);
- $\mathbf{M}_{max}$; weight: 2/3 (this branch is called $\mathbf{M}_{max}$);
- $\mathbf{M}_{max}$ $-\sigma_M\sqrt{3}$; weight: 1/6 (this branch is called $\mathbf{M}_{max}(^{-})$).

Mean values of $\mathbf{M}_{max}$ are taken from three magnitude-area scaling relationships: Wells and Coppersmith (1994); Hanks and Bakun (2002, 2008), where applicable; Leonard (2010). The standard deviation term σ_M is taken from Wells and Coppersmith (1994).

For faults in which the maximum magnitude $\mathbf{M}_{max}$ is close to 6.4, the branch $\mathbf{M}_{max}(^{-})$, can be lower than 6.4, which per our protocols, would cause the source to be only within the area source branch of source modeling. This issue was managed as follows:

- PZ1: Fault sources + Background zones – the assigned minimum magnitude for fault sources only in the branch $\mathbf{M}_{max}$ $(^{-})$ is 5.5;
- PZ2: Fault sources + Background zones – the assigned minimum magnitude for fault sources in all branches is 5.5;
- PZ3: Fault sources without Background zones – the assigned minimum magnitude for fault sources in all branches is 5.5;
- PZ4: Fault sources without Background zones – the assigned minimum magnitude for fault sources only in the branch $\mathbf{M}_{max}(^{-})$ is 5.5.

In the sensitivity analyses reported in this section, $\mathbf{M}_{max}$ uncertainties are addressed only for the FSBG source model branch of the logic tree shown in Figure 3.11 (area sources are ignored). Hence, the analyses reported here are not meant as a replacement to the general hazard results given in Sections 3.5.1-3.5.3. We consider fault sources and background zones for PZ1 and PZ2 and fault sources only for PZ3 and PZ4 (background zones are omitted). Area sources and the subduction interface are omitted in the analyses reported in this section.

Figure 3.46 shows uniform hazard spectra (UHS) computed using a logic tree in which the three branches of $\mathbf{M}_{max}$ given previously are considered. UHS are plotted separately for the four

considered configurations of fault and background sources PZ1-PZ4 along with a case in which $\mathbf{M}_{max}$ is fixed at the mean value. For the case in which $\mathbf{M}_{max}$ is fixed, $\mathbf{M}_{min}$ is taken as 6.4 and background zones are used, which is consist with the implementation in §3.3.2. The main findings of this analysis are as follows: (1) consideration of M_{max} uncertainties has no appreciable effect on UHS ordinates; (2) the elimination of background sources (cases PZ3 and PZ4) reduces UHS ordinates by 19-45% approximately at T_R = 475 and 3-20% at T_R = 2475 yr. These results indicate that the analyses reported previously in Sections 3.5.1-3.5.3 do not consider an inappropriately low level of epistemic uncertainty as a result of not including logic tree branches with variations in $\mathbf{M}_{max}$.

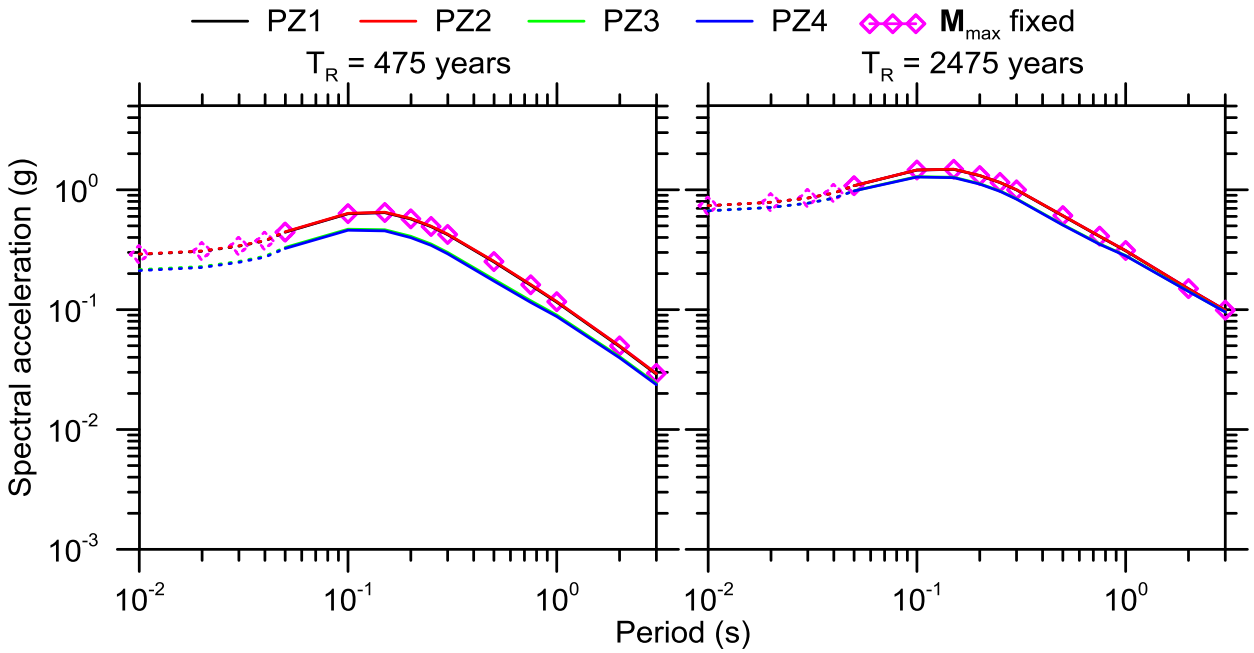

Figure 3.46 **UHS for the PZ1-PZ4 configurations along with a case in which M_{max} is fixed at the mean value. The dotted lines (and symbols) represent the intervals in which the shape was corrected in a deterministic sense (using the GMPEs defined in those intervals) to fill in the missing parts of the spectra.**

Figure 3.47 shows uniform hazard spectra (UHS) for the PZ1 configuration of fault and background sources, for three $\mathbf{M}_{max}$ branches: $\mathbf{M}_{max}(^{+})$, $\mathbf{M}_{max}(^{-})$, mean $\mathbf{M}_{max}$. The PZ1 configuration includes background zones and uses a minimum magnitude for fault sources of 5.5. For both return periods, the UHS for $\mathbf{M}_{max}$, $\mathbf{M}_{max}(^{+})$ and $\mathbf{M}_{max}(^{-})$ branches of the logic tree are practically identical. The maximum differences between spectral ordinates in the figure is 1% to 7% for T_R=475 years and 0.5% to 6% for T_R=2475 years. The larger differences come from the larger periods.

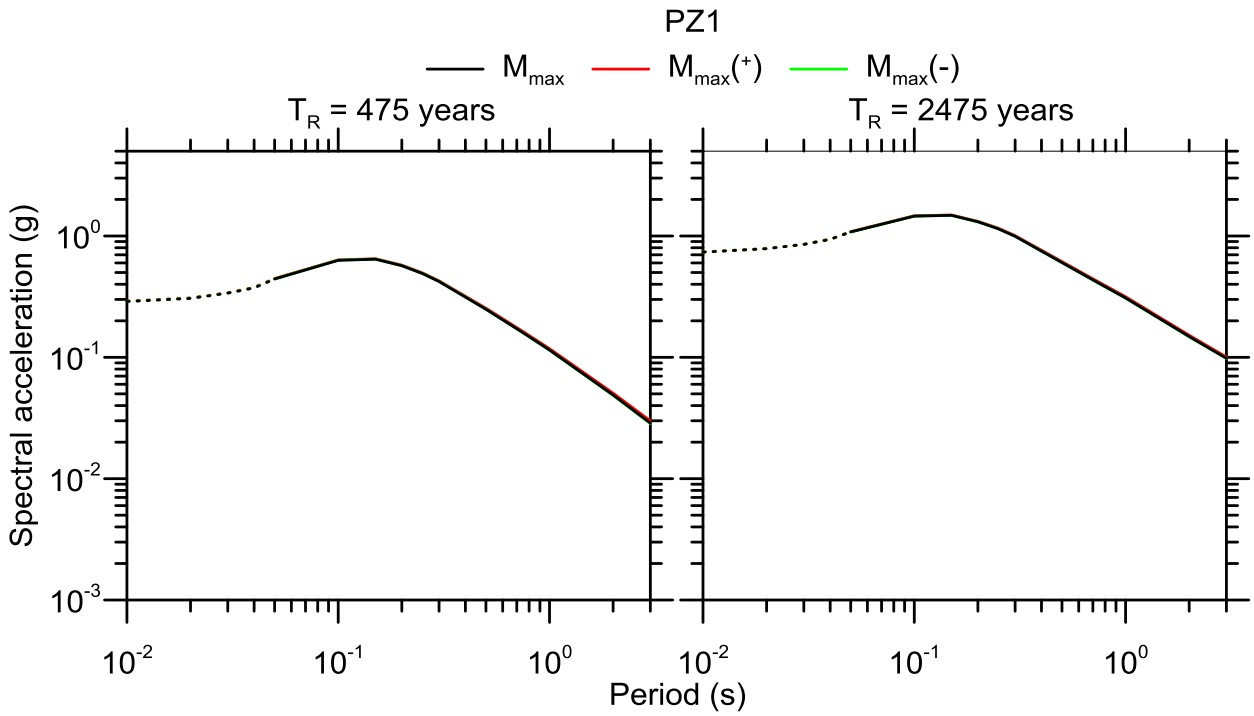

Figure 3.47 **UHS obtained addressing the M_{max} uncertainties for for the PZ1 configuration of fault and background sources, for three M_{max} branches: $M_{max}(^{+})$, $M_{max}(^{-})$, mean M_{max}. The dotted lines (and symbols) represent the intervals in which the shape was corrected in a deterministic sense (using the GMPEs defined in those intervals) to fill in the missing parts of the spectra.**

3.5.4.3 Uncertainties Related to the Implementation of the Subduction Interface

An important feature introduced in this study is the subduction interface of the Calabrian arc. The main features of the implementation of this source are described in §3.3.5. The mean value of the maximum magnitude was calculated using the Strasser et al. (2010) magnitude-area and magnitude-length scaling for subduction interface, Equations 3.32 and 3.33:

$$\mathbf{M} = 4.868 + 1.392\log(L) \pm \sigma \quad (3.32)$$

$$\mathbf{M} = 4.441 + 0.846\log(A) \pm \sigma \quad (3.33)$$

where L = 250 km is the rupture length, A = 12500 km^2 is the rupture area, while the associated standard deviations are σ = 0.277 for Eq. 3.32 and σ = 0.286 for Eq. 3.33. The $\mathbf{M}_{max}$ = 8.1 used for this source is the average of the values obtained by Equations 3.32 and 3.33.

The Gutenberg-Richter recurrence relation parameters used (as described in §3.3.5) are b = 0.9 and a = 3.8 (for the slip rate lower bound, s_{lower}), and b = 0.9 and a = 4.3 (for the slip rate upper bound, s_{upper}).

The $\mathbf{M}_{max}$ uncertainties are treated using the same logic tree approach described in §3.5.4.2, with the difference that in this case the Area sources (AS model) are included in the analysis. In this case the three branches for the $\mathbf{M}_{max}$ uncertainties are combined with the slip rate lower and the upper bound, resulting in a logic tree made up of six branches:

- $\mathbf{M}_{max}+\sigma\sqrt{3}$; weight: 1/12 ($\mathbf{M}_{max}(^{+})$ + slip rate upper bound (s_{upper}));
- $\mathbf{M}_{max}+\sigma\sqrt{3}$; weight: 1/12 ($\mathbf{M}_{max}(^{+})$ + slip rate lower bound (s_{lower}));
- $\mathbf{M}_{max}$; weight: 1/3 ($\mathbf{M}_{max}$ + slip rate upper bound (s_{upper}));
- $\mathbf{M}_{max}$; weight: 1/3 ($\mathbf{M}_{max}$ + slip rate lower bound (s_{lower}));
- $\mathbf{M}_{max}-\sigma\sqrt{3}$; weight: 1/12 ($\mathbf{M}_{max}(^{-})$+ slip rate upper bound($s_{upper}$));
- $\mathbf{M}_{max}-\sigma\sqrt{3}$; weight: 1/12 ($\mathbf{M}_{max}(^{-})$+ slip rate bound ($s_{lower}$)).

Figure 3.48 shows weighted average uniform hazard spectra (UHS) computed using a logic tree in which the six branches of $\mathbf{M}_{max}$ and slip rate given above are considered. Also shown are results for the case in which the subduction interface is not modeled (marked as 'Without interface') and the case in which $\mathbf{M}_{max}$ was fixed at the mean value (marked as '$\mathbf{M}_{max}$ fixed'). The difference in the UHS for the shorter return period (T_R = 475 years, probability of exceedance equal to 10% in 50 years) is higher than for the longer return period (T_R = 2475 years, probability of exceedance equal to 2% in 50 years). The mean UHS developed by considering uncertainties in maximum magnitude and slip rate is nearly identical to that developed using the mean value of $\mathbf{M}_{max}$. For this reason we used mean values of $\mathbf{M}_{max}$ and slip rate in the final PSHA for the subject site.

Figure 3.49 shows individual UHS for each of the six logic tree branches. The differences in the UHS ordinates are larger for T_R = 475 years than for T_R = 2475 years. The maximum differences between spectral ordinates in the figure is 10% to 34% for T_R=475 years and 5% to 17% for T_R=2475 years. The larger differences come from the larger periods.

In Figure 3.50, the hazard curves for five different oscillator periods are shown for the cases with and without the interface. The hazard curves were computed for the following oscillator periods: T = 0 (PGA), 0.25, 0.5, 1 and 2 seconds. In Figure 3.51 the discrepancies between the models with and without the interface, are plotted against spectral ordinate (acceleration). The

effect of the subduction interface increase proportionally with increasing oscillator period, until a certain threshold (T = 1s).

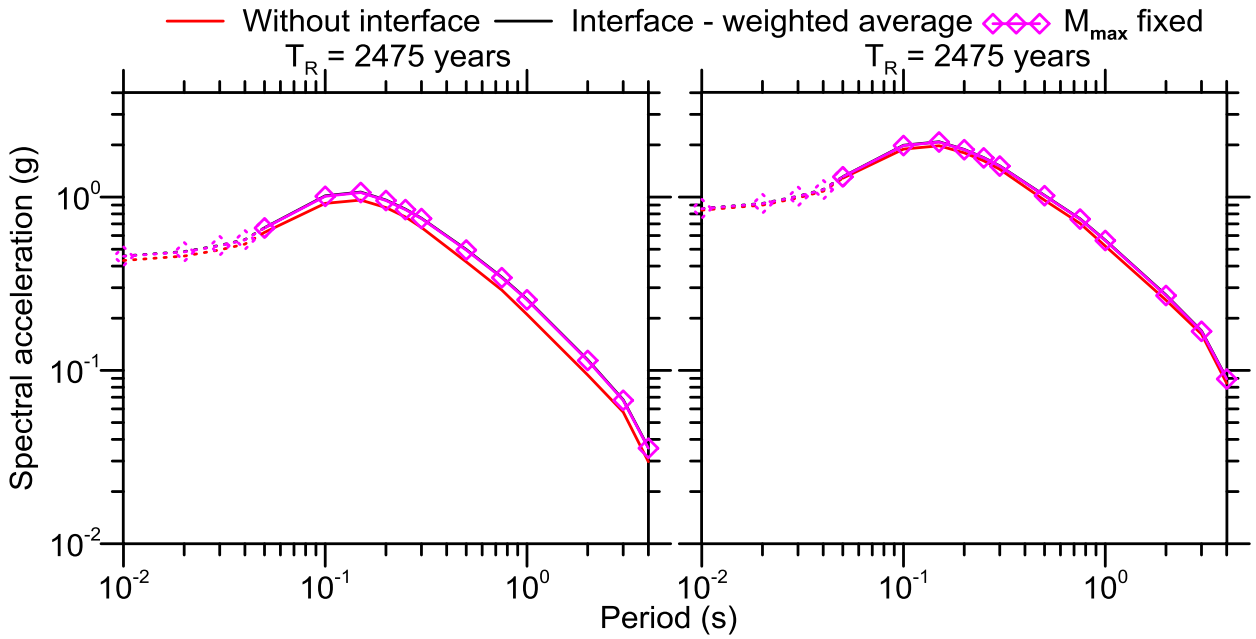

Figure 3.48 **UHS for two cases with the interface: M_{max} fixed, weighted average per bulleted list in this section and for the case without the subduction interface, and. The dotted lines represent the intervals in which the shape was corrected in a deterministic sense (using the GMPEs defined in those intervals) to fill in the missing parts of the spectra.**

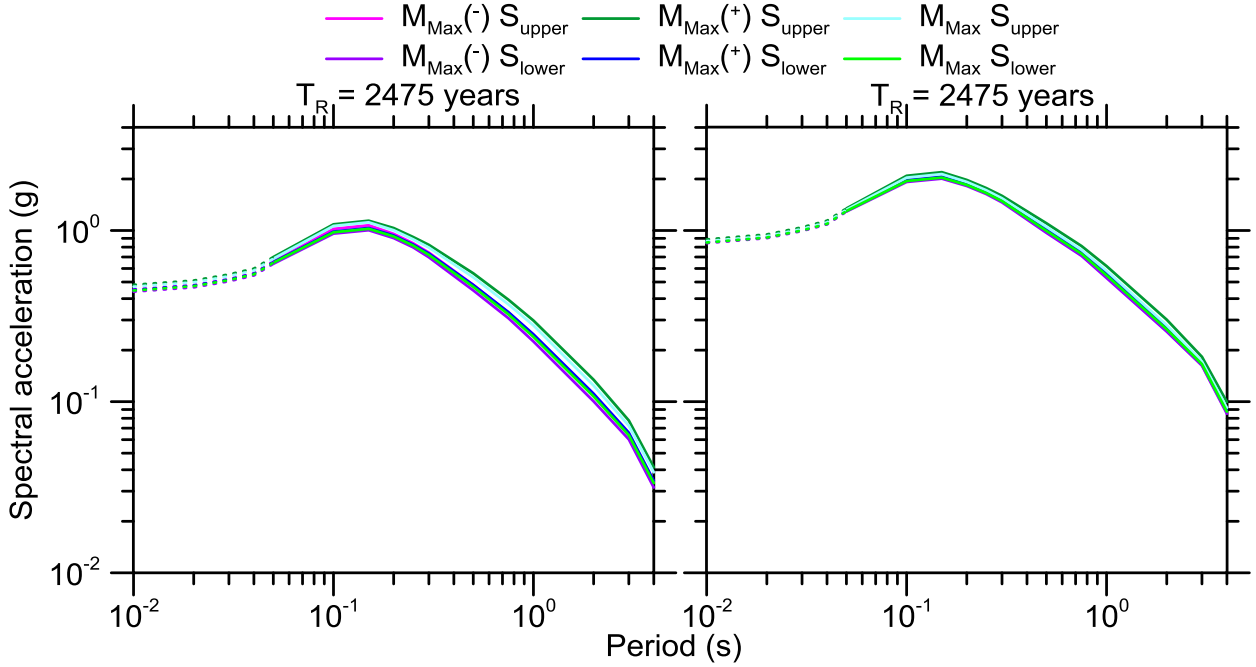

Figure 3.49 **UHS for the six logic tree branches. The dotted lines represent the intervals in which the shape was corrected in a deterministic sense (using the GMPEs defined in those intervals) to fill in the missing parts of the spectra.**

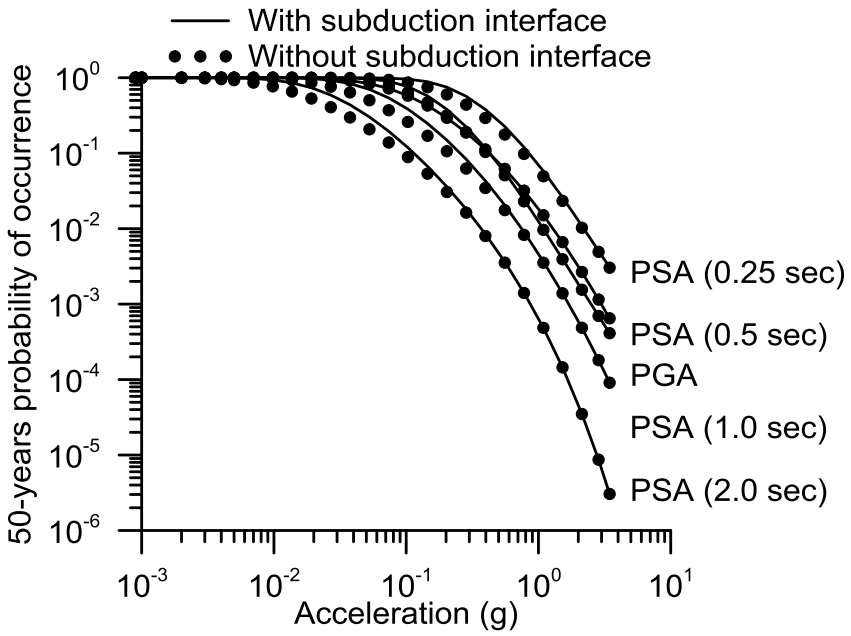

Figure 3.50 **Comparison among the hazard curves of the models with and without the subduction (SZ) interface for five structural periods.**

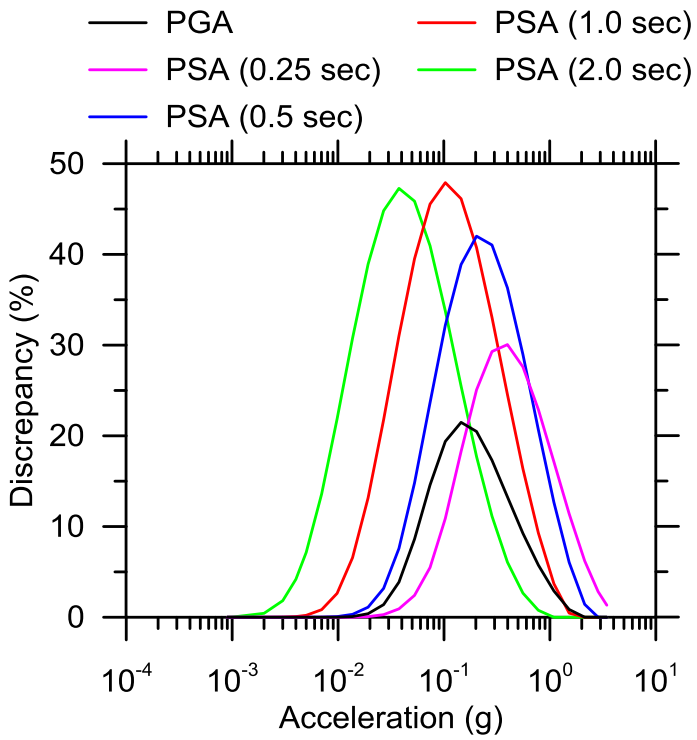

Figure 3.51 Discrepancies between the models with and without the interface, for PGA, PSA (0.25 sec), PSA (0.5 sec), PSA (1.0 sec) and PSA (2.0 sec).

3.5.4.4 Relative Effect of the Different GMPEs

The logic tree for the principle PSHA reported in §3.5.1-3.5.3 includes alternate GMPEs as shown in Figure 3.33. In this section, we investigate the sensitivity of mean hazard results to the consideration of different GMPEs. This is done by performing PSHA using each GMPE in isolation with the original source model (as described in §3.3).

Figure 3.51 compares mean hazard curves for the overall model (originally presented in §3.5.1) with mean hazard curves using the same source model with a single GMPE for SCRs (the logic tree for SZs was not changed). Five ACR GMPEs were considered for this sensitivity analysis:

- BSSA (2014);
- Bindi et al. (2011);
- Akkar and Bommer (2010);
- Faccioli et al. (2010);
- Zhao et al. (2006).

The results in Figure 3.52 show that the Akkar and Bommer (2010), Zhao et al. (2006) and the BSSA14 models exhibit generally compatible trends. As expected, since these GMPEs were selected to be part of the overall model, their shapes are similar to the curve of the complete (overall) model for all the intensity measures. The Bindi et al. (2011) model tends to give lower accelerations than the overall model for low hazard levels and higher accelerations for high hazard levels. Hazard results predicted by the Faccioli et al. (2010) model often fall below those for the other GMPEs.

Figure 3.53 compares UHS for the Farneto del Prinicpe dam site between the overall model (this study) and the individual GMPEs. The shape of the spectra from the selected GMPEs are similar; those not selected have some unusual features, especially Faccioli et al. (2010), which has several kinks in the spectrum.

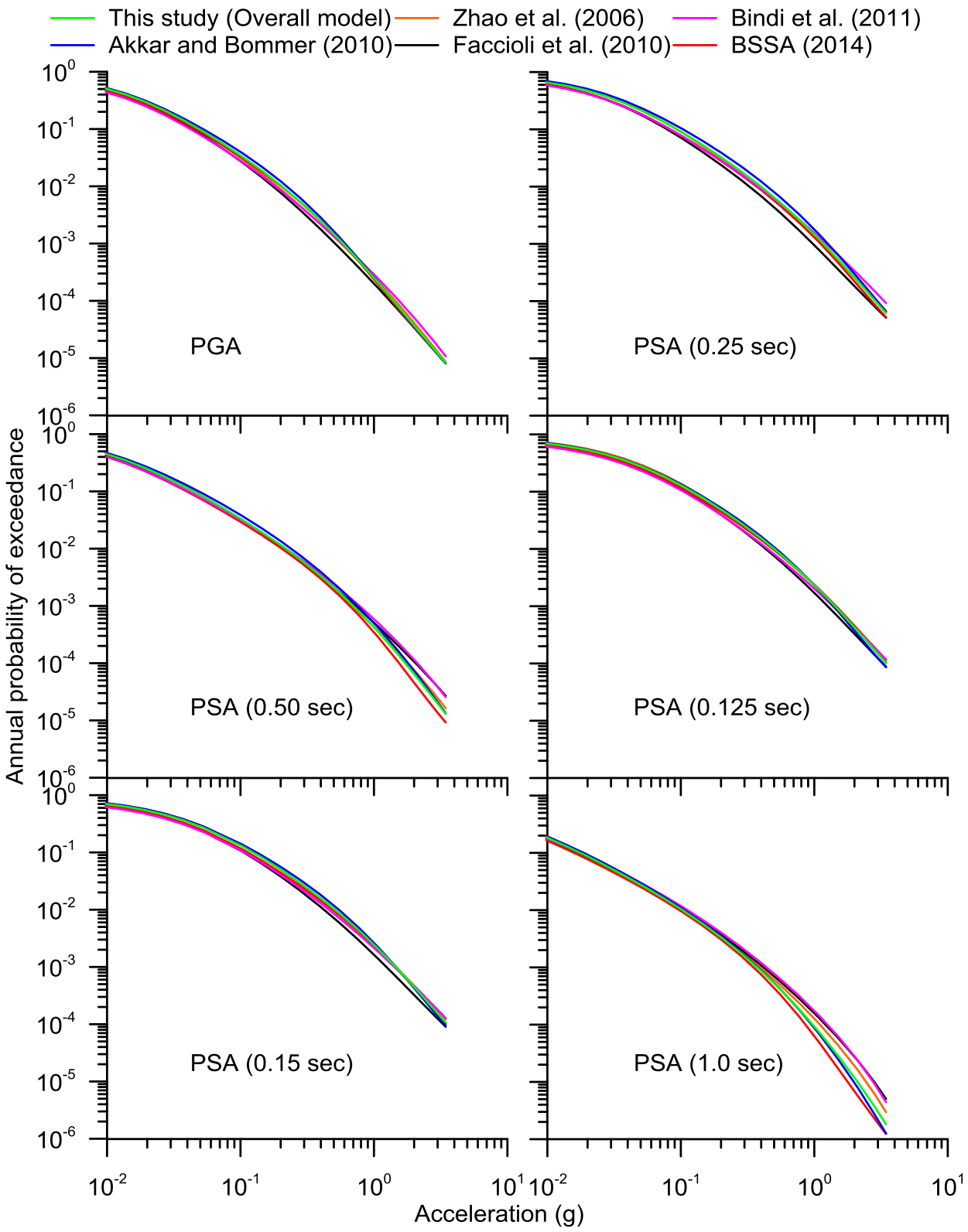

Figure 3.52 **Mean hazard curves for the overall model (this study) and the single GMPEs.**

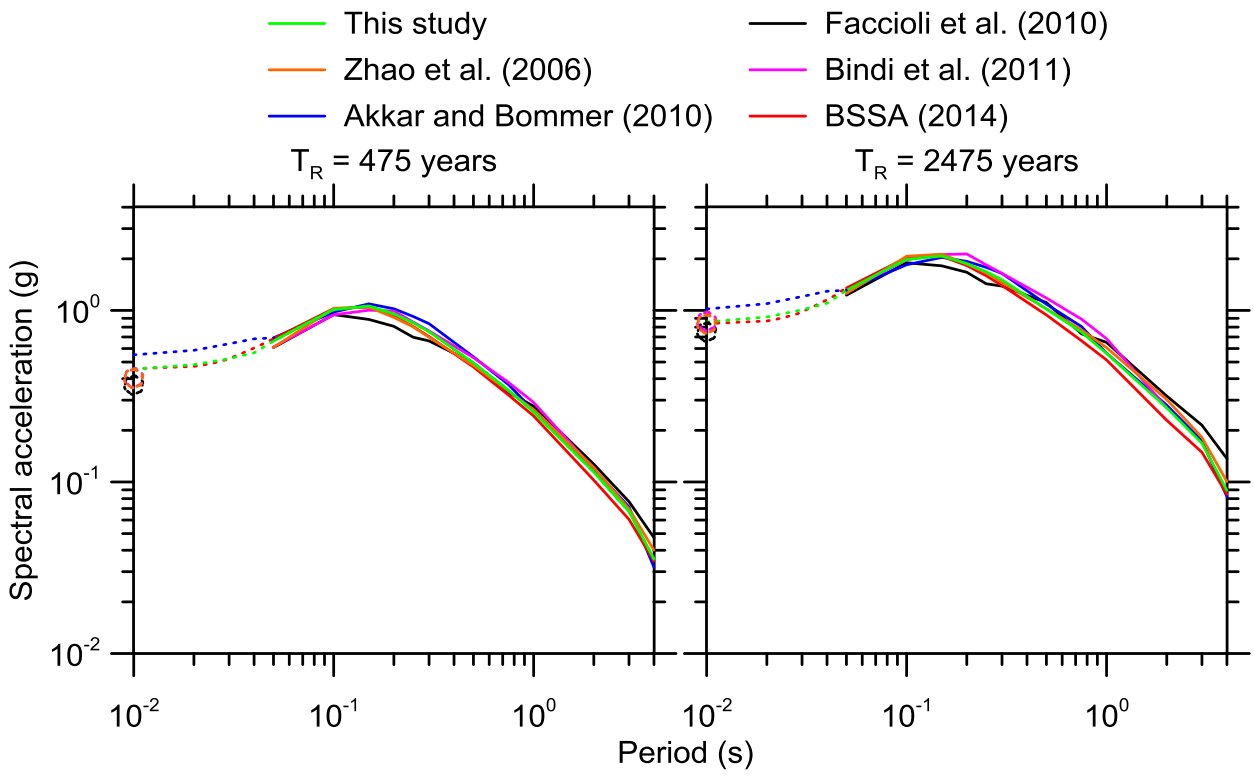

Figure 3.53 **Comparison among the UHS of the complete model (this study) and five different approaches that use one of the pre-selected GMPEs at a time. The dotted lines represent the intervals in which the shape was corrected in a deterministic sense (using the GMPEs defined in those intervals) to fill in the missing parts of the spectra. The open circles represent PGA for those GMPEs that don't have the intermediate spectral ordinates.**

3.5.4.5 Relative Contribution to the Hazard of the FSBG and AS Models

The hazard curves and the disaggregation analyses shown in previous sections were computed putting together the results of both source models: AS model and FSBG model. It seems that the FSBG model has a smaller contribution to the hazard than the AS model, this could be a pitfall of this hybrid model, therefore it is important to focus attention on this issue. Since it is important to evaluate whether the weights of the two source models are balanced or not, it is necessary to calculate the relative contribution to the hazard of both source models.

It is possible to calculate the relative significance of the two type of sources, using the approach described below:

1. Evaluate the Intensity Measure Level (IML) of the total (mean) hazard curve, given the selected probability of exceedance (POES) that is 10% in 50 years in this example (IM_C), as shown in Figure 3.54;

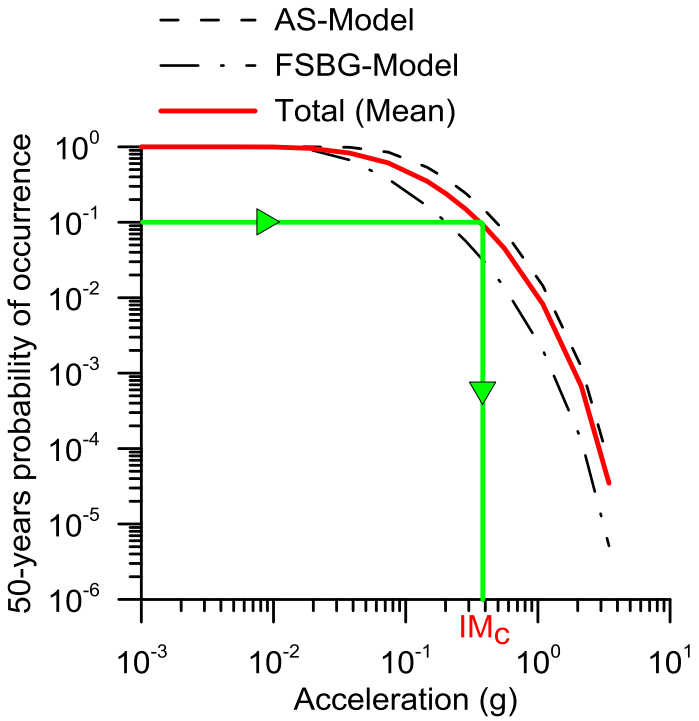

Figure 3.54 **Intensity Measure Level (IML) of the total (mean) hazard curve, given the selected probability of exceedance (POES).**

2. Given IM_c, evaluate the probabilities of exceedance of that IML for hazard curves that are computed using the two different source models in isolation: P^*_1 for the AS model and P^*_2 for the FSBG model. These results are shown in Figure 3.55;

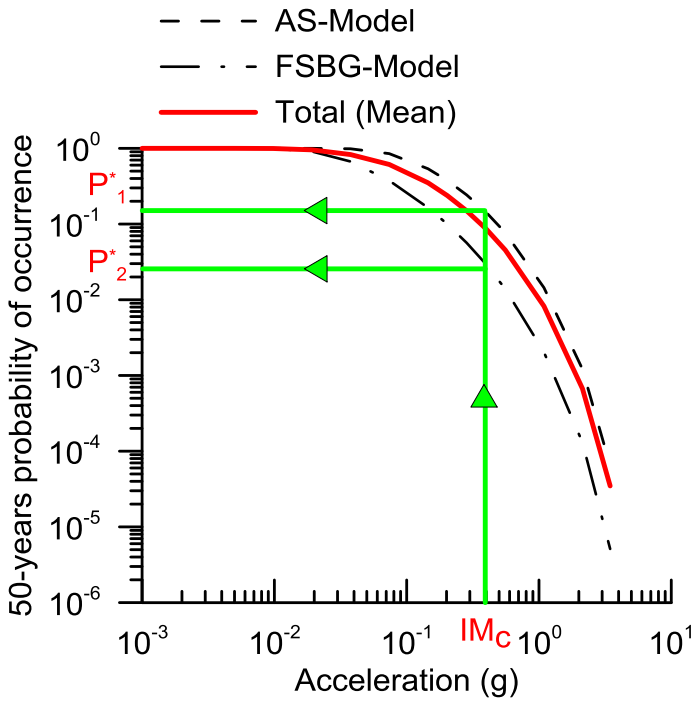

Figure 3.55 **Probabilities of exceedance of the selected IML for the two different hazard curves.**

3. Given P^*_1 and P^*_2, evaluate rates ν^*_{IM1} and ν^*_{IM2} under the assumption of Poissonian process:

$$P = 1 - e^{-\nu^*_{IM} \cdot \Delta t} \tag{3.34}$$

where, in this case, POES = P^*_1; P^*_2 and Δt = 50 years.

4 With ν^*_{IM1} and ν^*_{IM2} known, evaluate rates ν^*_1 and ν^*_2 as follows:

$$\upsilon^*_i \approx \upsilon^*_{IMi} \cdot RC_i \tag{3.35}$$

where RC_i are the relative contributions relative to the hazard of either fault sources (Equation 3.27).

5 Evaluate the total relative contribution(that is the relative contribution to the hazard of both fault sources): *RC(*)* for the chosen POES (10% in 50 years), using Equation 3.36:

$$RC(*) = \frac{\left(\upsilon^*_1 + \upsilon^*_2\right) \big/ 2}{\upsilon_{IMc}} \tag{3.36}$$

where ν_{IMc} is the total rate given by the disaggregation (average of the ν_{IMi}).

6 Evaluate the relative significance (disaggregation weights) of the two type of sources (recall the weight assigned originally to each source type is 50% each) as follows:

$$RS(*)_i = \frac{\upsilon_i \big/ 2}{\upsilon_{IMc}} \tag{3.37}$$

Applying the approach described above it is possible to show that for the PSHA and disaggregation computed in this study, the relative significance for the hazard of the Area sources (AS model) is about 80%, the relative significance of the FSBG model is about 20%. Almost the same results were obtained using the same approach, but using $\mathbf{M}_{\text{obs}}$ as maximum magnitude for the Area sources, instead of $\mathbf{M}_{\text{obs}}$ + 0.6. This clearly shows that the pitfall is not only related to the addressing of the maximum magnitude uncertainties, but could be related to something else. These results are unexpected, therefore it is worth understanding why there is this big difference in the relative significance of the two models, and, eventually how to handle these results.

It is important to figure out whether the Area sources are introducing somehow, something that is not physically consistent with the reality. It is possible that the AS model introduces a

huge rate of moment release, which is bigger than the real one, because of the uncertainties related to the rate of occurrence (*a* values for each IDs of the areas), the evaluation of the $\mathbf{M}_{max}$ and the addressing of the $\mathbf{M}_{max}$ uncertainties. To confirm this hypothesis, we back calculated the rate of moment release on each source of the two types of source.

Recalling the main equation used in the applied procedure, the rate of moment build up ($\dot{M}_0$) on a fault during a period without earthquakes is:

$$\dot{M}_0 = \mu A s \tag{3.38}$$

where *A* is the Area of the fault, μ represents the friction between the two fault blocks that is equal to $\mu = 3 \cdot 10^{11} dyne/cm^2$ and s is the slip rate.

The rate of moment release can be expressed by Equation 3.39:

$$\dot{M}_0 = \nu \cdot \int_{m^0}^{m^u} f(m) \cdot M_0(m) dm \tag{3.39}$$

where ν is the Poisson rate of $m>m_0$ earthquakes, m^0 and m^u are the minimum and maximum magnitude respectively, *f(m)* is the probability density function (PDF) of the magnitude distribution and $\boldsymbol{M_0(m)}$ is the well-known relation of Hanks and Kanamori (1979), given by:

$$M_0 = 10^{1.5m+16.05} \tag{3.40}$$

Several rates of moment release were calculated in this study:

- $\dot{M}_0{}^1$: relative to the area sources (AS model) with m^0=4.7, m^u=$\mathbf{M}_{obs}$, Equation 3.39 becomes:

$$\dot{M}_0{}^1 = \sum_{allAreas} 10^{a-b\cdot 4.7} \cdot \int_{m^0}^{m^u} \frac{b \ln(10) \cdot 10^{-b\cdot(m-4.7)}}{1-10^{-b\cdot(M_{obs}-4.7)}} \cdot 10^{1.5m+16.05} dm \tag{3.41}$$

- $\dot{M}_0{}^2$: relative to the area sources (AS model) with m^0= $\mathbf{M}_{obs}$, m^u=($\mathbf{M}_{obs}$+0.6), Equation 3.39 becomes:

$$\dot{M}_0{}^2 = \sum_{allAreas} 10^{a-b\cdot M_{obs}} \cdot \int_{M_{obs}}^{M_{obs}+0.6} f(m) \cdot 10^{1.5m+16.05} dm \tag{3.42}$$

It is necessary to underline that *f(m)* is not the previously used PDF for a truncated exponential recurrence law, in Equation 3.40, but differs case by case because of the different weights in the $\mathbf{M}_{max}$ logic tree for the AS model.

- $\dot{M}_0^{\,3}$: relative only to the Background zones of the FSBG model with m^0= 4.7, m^u= 6.3, Equation 3.39 becomes:

$$\dot{M}_0^{\,3} = \sum_{allBackgroundzones} 10^{a-b\cdot 4.7} \cdot \int_{4.7_s}^{6.3} \frac{b\ln(10)\cdot 10^{-b\cdot(m-4.7)}}{1-10^{-b\cdot(6.3-4.7)}} \cdot 10^{1.5m+16.05} dm \qquad (3.43)$$

- $\dot{M}_0^{\,4}$: relative only to the Fault sources of the FSBG model with m^0= 6.4, m^u= $\mathbf{M}_{max}$ Equation 3.39 becomes:

$$\dot{M}_0^{\,4} = \sum_{allFiniteFaults} 10^{a-b\cdot 6.4} \cdot \int_{6.4_s}^{M_{Max}} \frac{b\ln(10)\cdot 10^{-b\cdot(m-6.4)}}{1-10^{-b\cdot(M_{Maxs}-6.4)}} \cdot 10^{1.5m+16.05} dm \qquad (3.44)$$

The PDFs used for the Area sources, sum up to 1 for the integral from 4.7 to $\mathbf{M}_{obs}$+0.6, as showed in Figures 3.56 and 3.57 for the area source 319, plotted here as example.

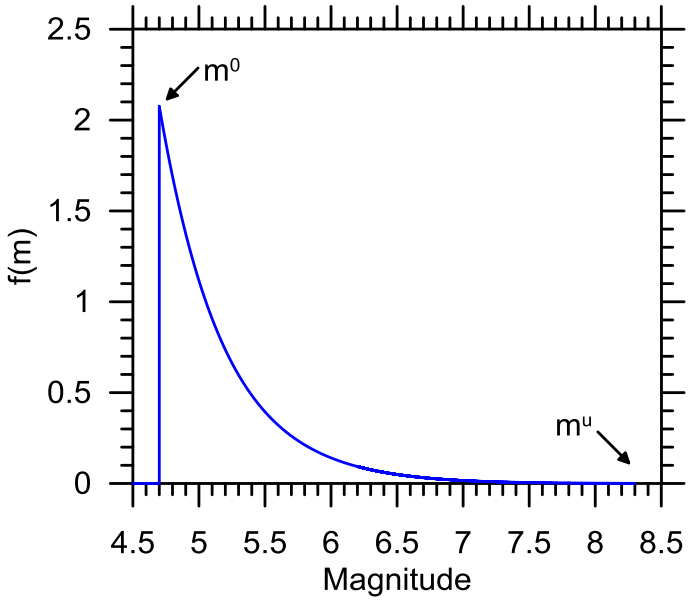

Figure 3.56 PDF for the Area source 319, the integral of this curve from m^0=4.7 to m^u=M_{obs}+0.6=8.3 sum up to 1.

Using the above described equations, the following results were obtained:

$$\dot{M}_0^{\,1} = \sum_{allAreas} 10^{a-b\cdot 4.7} \cdot \int_{m^0}^{m^u} \frac{b\ln(10)\cdot 10^{-b\cdot(m-4.7)}}{1-10^{-b\cdot(M_{obs}-4.7)}} \cdot 10^{1.5m+16.05} dm = 1.92\cdot 10^{25}\, dyne\cdot\frac{cm}{year}$$

$$\dot{M}_0^{\,2} = \sum_{allAreas} 10^{a-b\cdot M_{obs}} \cdot \int_{M_{obs}}^{M_{obs}+0.6} f(m)\cdot 10^{1.5m+16.05} dm = 6\cdot 10^{21}\, dyne\cdot\frac{cm}{year}$$

$$\dot{M}_0^{\,3} = \sum_{allBackgroundzones} 10^{a-b\cdot 4.7} \cdot \int_{4.7_s}^{6.3} \frac{b\ln(10)\cdot 10^{-b\cdot(m-4.7)}}{1-10^{-b\cdot(6.3-4.7)}} \cdot 10^{1.5m+16.05} dm = 4.56\cdot 10^{23}\, dyne\cdot\frac{cm}{year}$$

$$\dot{M}_0^{\,4} = \sum_{allFaultSources} 10^{a-b\cdot 6.4} \cdot \int_{6.4_s}^{M_{Max}} \frac{b\ln(10)\cdot 10^{-b\cdot(m-6.4)}}{1-10^{-b\cdot(M_{Max_S}-6.4)}} \cdot 10^{1.5m+16.05} dm = 8.26\cdot 10^{23}\, dyne\cdot\frac{cm}{year}$$

It was also calculated $\dot{M}_0^{\,5}$ which is the total rate of moment release for the FSBG including the area sources that are actually included among the sources used in the FSBG model:

$$\dot{M}_0^{\,5} = \dot{M}_0^{\,3} + \dot{M}_0^{\,4} + \sum_{Areas\_in\_FSBG} \dot{M}_0 + \sum_{Subdcution\_Interface} \dot{M}_0 = 1.34\cdot 10^{25}\, dyne\cdot\frac{cm}{year}$$

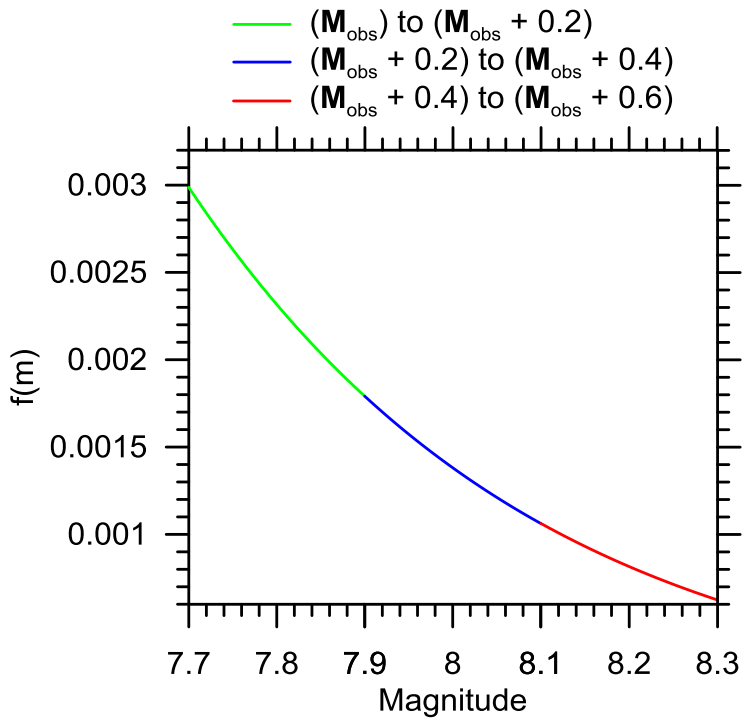

Figure 3.57 Zoom of the previously showed PDF (Figure 3.56) between M_{obs} = 7.7 and M_{obs}+0.6 = 8.3.

The rates of moment release, calculated for all the source types, shown that there is an introduction of a spurious rate of moment release due to the area sources. This effect is probably caused by the overestimation of the earthquake activity rates (estimated only using the earthquake catalogues) and the maximum magnitudes. This last observation shows that, assigning the maximum historically observed magnitude within the whole region to all the area

sources plus three increment (approach implemented in the SHARE Euro-Mediterranean model for the maximum magnitude on the area sources and explained in §3.3.1), drive to a too conservative model that results to be inconsistent in respect of the actual rate of moment release. The analyses performed, show a pitfall in this approach in which the hazard of a site is area sources-dominated. To avoid these errors it will be necessary to better define the occurrence rates, coupling historical and recorded seismicity and geological information such as the slip rates. As already pointed out by Woessner et al. (2012), it is obvious that in the calculation of the activity rates for the fault sources, the geological information such as the actual slip rate on the faults, play an important role, differently than in the AS model, where the catalogue and its completeness are fundamental.

Starting from these considerations, it will be possible in the future, to better calibrate the earthquake occurrence rate (using both historical earthquakes and geological information if possible) and the uncertainties related to the maximum magnitudes on the area sources (AS model), which should encourage to have a better understanding of the finite seismogenic faults present within a certain area, in order to get rid of this hybrid approach, going toward a more modern logic tree using only fault sources and if necessary background zones.

The above described inconsistencies cause an error in the whole model, because, the cumulative slip rates for all sources is clearly not consistent with reality, it would be ideal to perform comparisons between the modeled and the actual slip rates derived from geodetic data. However it is still problematic because the number of permanent Global Positioning Satellite (GPS) stations in Italy is small, they have only been in operation over a short time interval (about 10 years), and the campaign measurements provide velocities with a great associated uncertainty (Slejko et al., 2010). Recently several authors have tried to take advantage of this small period of observation to produce a reliable definition of the geodetic strain rates in Europe and Italy (see also §3.3.5), but as showed by Angelica et al. (2013), the accuracy, the resolution and the uncertainties related to these techniques allow to have a complete understanding of the main regional trends, while the evaluation of strain rates related to single sources is still challenging. In order to make comparisons between geodetic information and PSHA model slip rates, is necessary to transform magnitude-area scaling into corresponding slip-length scaling (Shaw, 2013). This approach allows direct comparisons to be made taking advantage of Surface Slip-

Length Data and/or geodetic data, once these techniques will give really accurate and detailed data also for the area of interest (southern Italy).

4 Acceleration time series selection and scaling

Selection of an appropriate suite of input motions for use in response history analysis plays an important role in the seismic design and analysis process. Acceleration time series are typically selected and scaled to fit target spectra. In this chapter two different suites of recorded input motions are selected and scaled to be consistent over a selected period range with an uniform hazard target spectrum (UHS) and a scenario conditional mean spectrum (CMS). In order to constrain the period range for which the average response spectra of the suites need to fit properly the target spectra, the knowledge of the important periods of the structure is necessary. In this chapter the methodology used for the selection and scaling of the acceleration time series to use in dynamic analyses of the Farneto del Principe dam is shown.

4.1 Numerical Evaluation of Natural Frequencies and Mode Shapes of Farneto del Principe Dam

The knowledge of the natural mode shapes and frequencies (periods) is a fundamental step in understanding the behavior of structures (such as a zoned earth dam) under dynamic excitation. These characteristics are even more important in the probabilistic seismic hazard analysis context. Indeed the evaluation of critical scenario(s) using techniques such as disaggregation analyses (as shown in section 3.3.5, chapter 3) and the definition of a suitable target spectrum for use in response history analysis (e.g. uniform hazard spectrum, conditional mean spectrum), require at least the knowledge of the fundamental frequency (defined as the first natural frequency) of the system. In this paragraph a linear elastic modal analysis is presented, using a numerical solution of the generalized eigenvalue problem obtained by the Finite Element Method (FEM) through the software Sap2000 Research Ultimate V17 (CSI, 2013).

The undamped free-vibration mode shapes and frequencies for the case study were calculated, solving the generalized eigenvalue problem (Equation 4.1):

$$[K - \Omega^2 M]\Phi = 0 \tag{4.1}$$

where K is the stiffness matrix, M is the diagonal mass matrix, Ω^2 is the diagonal matrix of eigenvalues, and Φ is the matrix of corresponding eigenvectors (mode shapes).

Each eigenvalue-eigenvector pair is called natural vibration mode of the dam. The modes are identified by numbers from *1* to *n* in the order in which the modes are found by the program.

The eigenvalue is the square of the circular frequency, ω, for that mode. The cyclic frequency (f) is related to ω by Equation 4.2, while the period period (T) is the inverse of f (Equation 4.3):

$$f = \frac{\omega}{2\pi} \tag{4.2}$$

$$T = \frac{1}{f} \tag{4.3}$$

The numerical model was set-up specifying a maximum number of modes to be find equal to 100 and a convergence tolerance of 10^{-9}.

As discussed in Chapter 2, there are not available direct measures of the shear wave velocity profiles for the materials of the Farneto del Principe dam, for this reason, a brief review of available data was performed. Several measurements performed on similar Italian dam were taken into account.

For the Bilancino and the Camastra dams, several data are available (Pagano et al., 2008, Mancuso, 1995). Measurements obtained by means of SASW technique for the core materials are shown in Figure 4.1. For these dams, it seems that the variation of the shear modulus of the core with depth is not an appreciable.

In Figure 4.2 the cross section of the Camastra dam is reported, while, in Figure 4.3 the partial cross section of the Bilancino dam is shown (this section is representative of the period in which the measurements were taken: during the construction phase).

For the Camastra dam, other two shear modulus profiles obtained by means of SASW technique are available for the downstream shell. In Figure 4.4a the measurements show that there is a variability of the small strain shear modulus with depth. Figure 4.4b shows only a portion of the downstream shell where it is difficult to evaluate an appreciable trend.

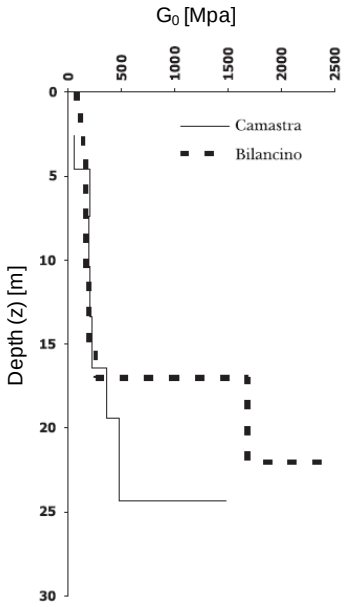

Figure 4.1 **Small strain shear modulus (G_0) measured by the SASW technique with depth (from Mancuso, 1995)**

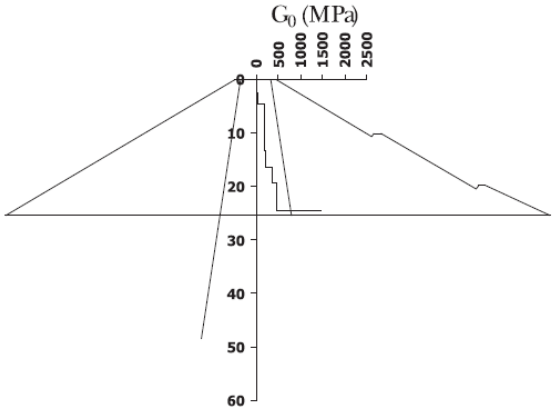

Figure 4.2 **Cross section of the Camastra dam with the small strain shear modulus (G_0) measured in the core axis by the SASW technique as a function of depth (from Pagano et al., 2008)**

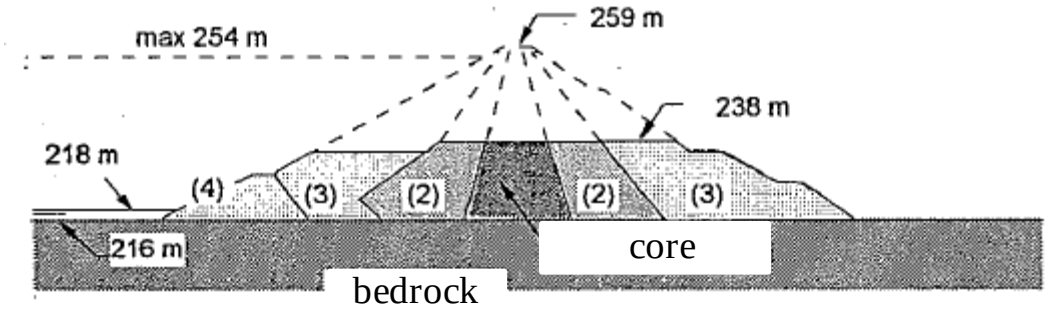

Figure 4.3 **Cross section of the Bilancino dam at the moment of the measurements (adapted from Mancuso, 1995)**

The available data taken from a seismic tomography for the San Valentino dam (courtesy of Prof. F. Federico) are shown in Figure 4.5. The cross section of the dam is shown in Figure 4.6. The interpretation of this seismic tomography shows that there is not an appreciable variation of the shear wave velocity with depth in the core. Moreover it is possible to notice that there is a clear variation with depth of the shear wave velocity in the shells. The gradient of the variation in the case of the downstream shell seems to be slightly different than the gradient in the upstream shell. This difference should be due to the effect of the groundwater flow within the dam body.

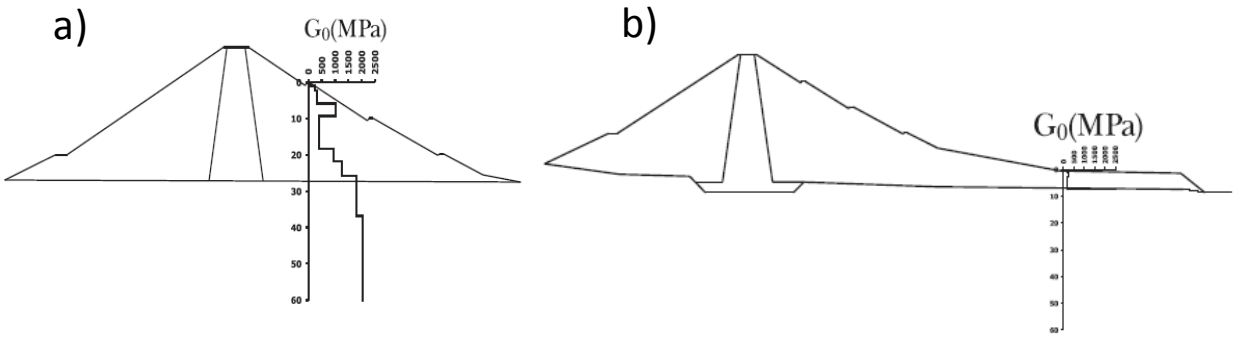

Figure 4.4 **Cross section of the Camastra dam with the small strain shear modulus (G0) measured in the downstream shell axis by the SASW technique as a function of depth (from Pagano et al., 2008)**

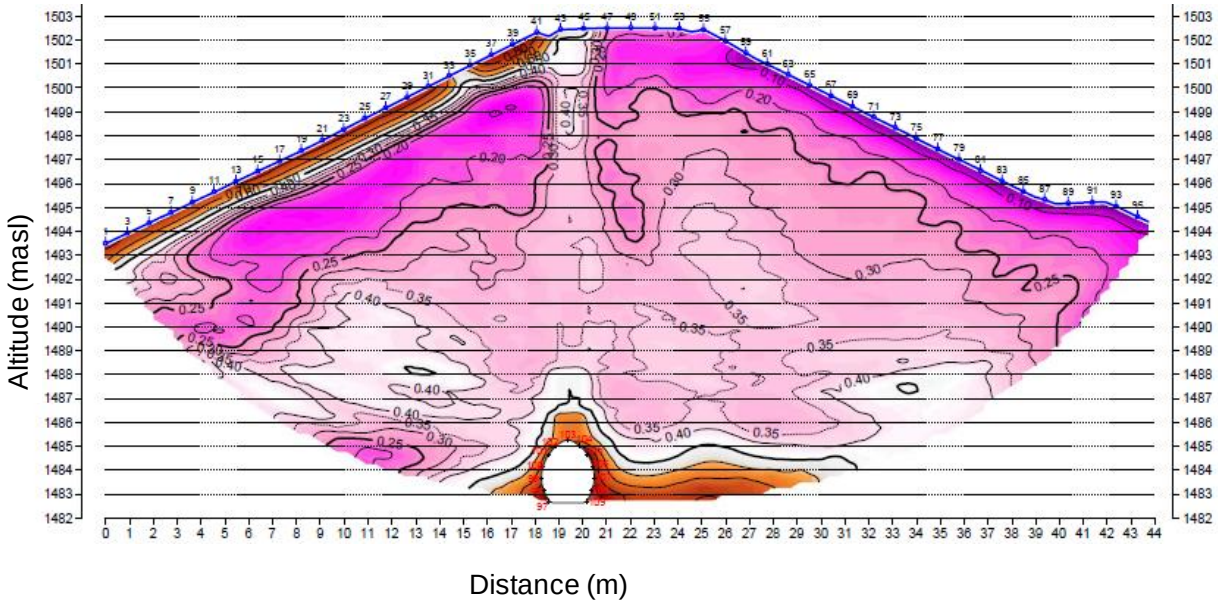

Figure 4.5 **Seismic tomography of a cross section of the San Valentino dam, the colored contours show the isolines of the shear wave velocities in km/s (courtesy of Prof. F. Federico).**

In the last few decades several authors investigated the effect of the shear wave velocity (and so, of the shear modulus) variation with depth for different conditions and soil types, Ambrasyes (1959), Seed and Idriss (1969), Dobry et al. (1971), Schreyer (1977), Gazetas (1982), Dakoulas and Gazetas (1985), Towata (1996) and more recently Rovithis et al. (2011). The scheme used by Dakoulas and Gazetas (1985), in Figure 4.7, accounts for a shear modulus (G) profile in dams and embankments dependent on an inhomogeneity factor m (Equation 4.4) varying from 0 to 1. This range of variation of m is acceptable for dams, because it was found that in newly-constructed fill-type dams the soil type and the age are essentially uniform and so the shear modulus doesn't exhibit a great variation (Towata, 1996).

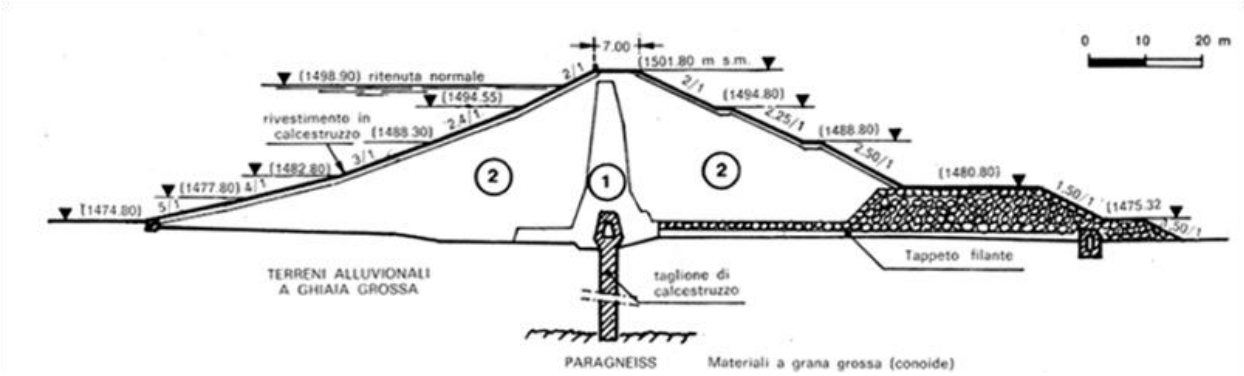

Figure 4.6 Cross section of the San Valentino dam (from Jappelli et al., 1981).

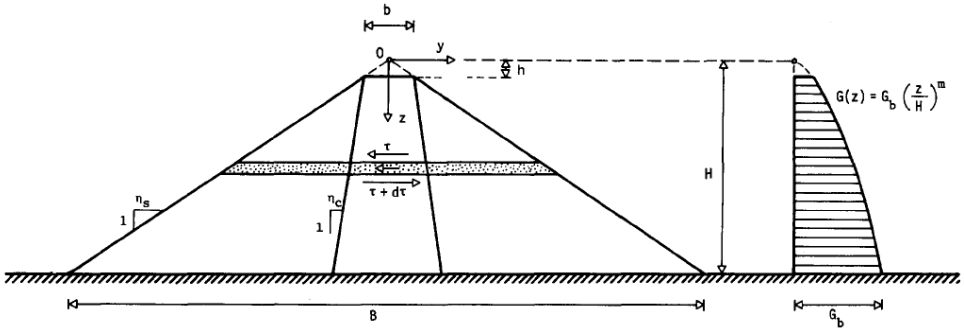

Figure 4.7 Variation of the shear modulus with depth (from Dakoulas and Gazetas, 1985).

$$G(z) = G_b \left(\frac{z}{H}\right)^m \tag{4.4}$$

In this study, it was decided, taking into account the measurements V_S profiles in other similar Italian earth dams, to apply for the Farneto del Principe dam the well-known Equation 4.5:

$$V_S = V_H \left[b + (1 - b) \frac{z}{H} \right]^n \tag{4.5}$$

where V_H is the shear wave velocity at the base of the model, z is the depth starting from the top of the model, H is the height of the model (of the dam in this case), n is the inhomogeneity factor, that accounts for the variation of V_S with depth (notice that m previously used in Equation 4.4 is differently defined as the inhomogeneity factor relative to the shear modulus profile), b is defined by Equation 4.6:

$$b = \left(\frac{V_0}{V_H} \right)^{1/n} \tag{4.6}$$

The geometrical scheme used is shown in Figure 4.8 (adapted from Rovithis et al., 2011).

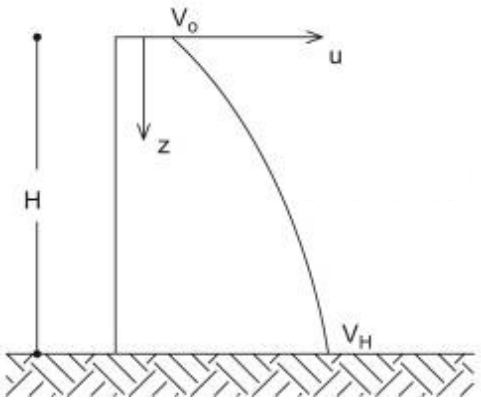

Figure 4.8 Shear wave velocity profile scheme (adapted from Rovithis et al., 2011).

Using Equation 4.5, starting from the observed shear wave velocity profile, it was estimated an inhomogeneity factor n = 0.25, with V_H = 550 m/s and V_0 = 250 m/s for the shells of Farneto del Principe dam. For the core, it was decided to use a constant V_S = 250 m/s (inhomogeneity factor n = 0, according to previous studies for overconsolidated clays, e.g. Richart et al., 1970 Hardin and Drnevic., 1972). This choice can be motivated because the expected depth-effect on the *VS* profile should be smaller and the impact on the modal analysis of this variation can be considered negligible. This value seems to be a good rough estimation coherent with the measurements of San Valentino, Camastra and Bilancino dam cores.

The parameters used as input for the performed modal analyses are shown in Table 4.1.

In order to take into account the effect of the groundwater flow within the dam body, a phreatic surface correspondent to the maximum allowable level of the reservoir was

hypothesized. According to Bishop and Height (1977), it was decided to take into account the effect of saturation using a Poisson's ratio equal to 0.49 for the materials below the water table.

Table 4.1 Parameters used for the modal analyses of the Farneto del Principe dam

Parameter	Above the phreatic surface		Below the phreatic surface		Foundation
	Core	Shells	Core	Shells	
γ (kN/m^3)	18	24	21.3	25.1	24.1
Poisson's ratio	0.35	0.33	0.49	0.49	0.33
V_S (m/s)	250	Variable	250	Variable	650

Two models were investigated in the numerical experimentation. The first model is represented by the dam fixed at the base (Figure 4.9). The color gradients in Figure 4.9 represent the variation of the shear modulus with depth. The cross section used in the analyses is section 4 (§2.3, Figures 2.9, 2.10).

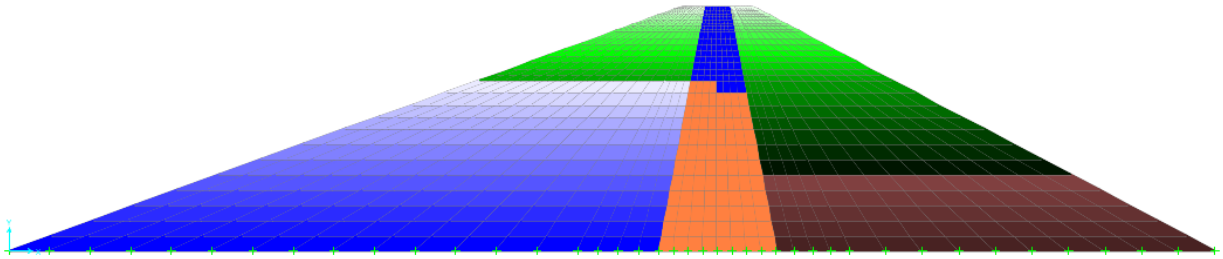

Figure 4.9 Mesh and geometry of the fixed base model of the Farneto del Principe dam.

The objective of the modal analysis here shown is the evaluation of the natural periods and mode shapes of the dam. The modal analysis results will be used to provide a constraint for the target spectra of the horizontal component of seismic motions. For this reason only the most important (in term of modal participating mass ratios, $MPMR_i$) translational horizontal modes are shown. In Figure 4.10a and 4.10b, the first and the second natural mode shapes, respectively, are shown. The first (fundamental) natural period results to be $T_1 \approx 0.197$ sec, with an associated modal participating mass ratios $MPMR_1 \approx 62\%$. The periods (T_i) and modal participating mass ratios ($MPMR_i$) for the higher modes result to be $T_2 \approx 0.097$ sec and $MPMR_2 \approx 12\%$; $T_3 \approx 0.063$ *sec* and $MPMR_3 \approx 2\%$; $T_4 \approx 0.038$ sec and $MPMR_4 \approx 2\%$. The modal participating mass ratios do not sum up to 100%, this simply because there is a "dispersion" of contribution in spurious modes and in vertical modes, that have mainly, but not totally, vertical component.

A comparison among the results obtained with 3 well-know formulations usually used for the evaluation of the natural periods of dams and the FEM results obtained for the fixed base model is shown in table 4.2.

Equation 4.7 shows the classical homogeneous shear beam solution commonly used for earth dam (e.g. Dakoulas and Gazetas, 1985).

$$T_i = \frac{2\pi}{\beta_i}\frac{H}{V_S} \tag{4.7}$$

where β_i is a parameter that depends on the geometry of the dam (provided the authors for several modes). Equation 4.7 for the case of $i=1$, the fundamental period of the dam (T_1), become the well-known Equation 4.8:

$$T_1 = 2.61\frac{H}{V_S} \tag{4.8}$$

In Equations 4.9 to 4.11 the inhomogeneous shear beam solution is shown (Dakoulas and Gazetas, 1985). This solution differs from the approach described by Equation 4.7, because accounts for the inhomogeneity of the dam materials, the shear wave velocity variation with depth within the dam body and the actual geometry of the dam.

$$T_i = \frac{16\pi}{(4+m)(2-m)a_i}\frac{H}{\overline{V_S}} \tag{4.9}$$

where m is the inhomogeneity factor previously discussed (for $m = 0$, homogeneous case, $a_i \equiv \beta_i$, Equation 4.9, can be reduced to Equation 4.7) and provided by the authors for different dam geometries ($m = 0.57$ for the Farneto del Principe dam); a_i, is a parameter (for the i^{th} mode) dependent by the inhomogeneity factor m and the properties (stiffness, geometry, etc.) of the dam, that is provided by the authors by means of tables for characteristic values of m; H is the total height of the dam (Figure 4.7), while $\overline{V_S}$ is the average shear wave velocity of the dam calculated using Equation 4.10:

$$\overline{V_S} = \frac{4}{4+m}\frac{1-\lambda^{2+m/2}}{1-\lambda^2}C_b \tag{4.10}$$

where C_b is the shear wave velocity at the base of the dam and λ is the so-called truncation ratio of the dam, and is equal to 0.05 for the case study, Equation 4.11:

$$\lambda = \frac{h}{H} \tag{4.11}$$

The analytical solution for free undamped vibrations in a single homogeneous layer over rigid base (Jacobsen, 1930) is reported in Equation 4.12.

$$T_i = \frac{4}{2i-1}\frac{H}{V_S} \tag{4.12}$$

As already pointed out by Dakoulas and Gazetas (1985), the inhomogeneous shear beam solution, provides an underestimation of natural periods for the first modes compared to FEM solutions. This difference mainly depends on the ratio of the average shear wave velocity between core and shells.

Table 4.2 Summary of the main results obtained for the two analyzed models of the Farneto del Principe dam

Mode	Homogeneous shear beam (Gazetas and Dakoulas, 1985)	Inhomogeneous shear beam (Gazetas and Dakoulas, 1985)	single homogeneous layer (Jacobsen, 1930)	This study (FEM solution)
1	0.168	0.169	0.257	0.197
2	0.073	0.080	0.086	0.097
3	0.047	0.052	0.051	0.063
4	0.034	0.038	0.037	0.038

In order to take into account the impact of soil structure interaction (SSI) effects on the modal analysis, in a second numerical model, the deformability of the foundation was introduced. The SSI effect of the deformable foundation was taken into account modeling the foundation (for section 4, 17 m deep below the level of the base of the dam), composed essentially by sand and gravel, as a continuous layer with a constant shear wave velocity profile of 650 m/s. The mesh of the model was horizontally extend for 75m in both directions from the edges of the dam. The model shown in Figure 4.11 is essentially equivalent to the previous one (Figure 4.10), but with the flexible foundation. On the lateral boundaries the vertical displacements are restraints, while the base is fixed in both directions. The main issue of this approach is that the modal participating mass ratios are not significant, because, even though the lateral extent of the mesh doesn't influence the natural periods, they have a big influence on the modal participating mass ratios. However, earth dams are first-mode-dominated structure, and the case study, as already

pointed out in the previous analysis, follows this rule. For this reason, the knowledge of the modal participating mass ratios, especially for the higher modes, doesn't really matter.

The modal analysis for the flexible base model shows that the deformability of the foundation has an important impact on the natural periods of the dam. In particular, the first natural period, in this case, is T_1 = 0.240 sec. Comparing this period with the one obtained for the fixed base model, it is possible to notice that elongation of the fundamental period ΔT_1 = 22%. Also for the second natural period ($T2$ = 0.126 sec) there is an elongation due to the SSI effect that in this case is even more important, indeed, ΔT_2 = 29%. In Figure 4.12 the first and the second mode shapes respectively, for the flexible base model are shown.

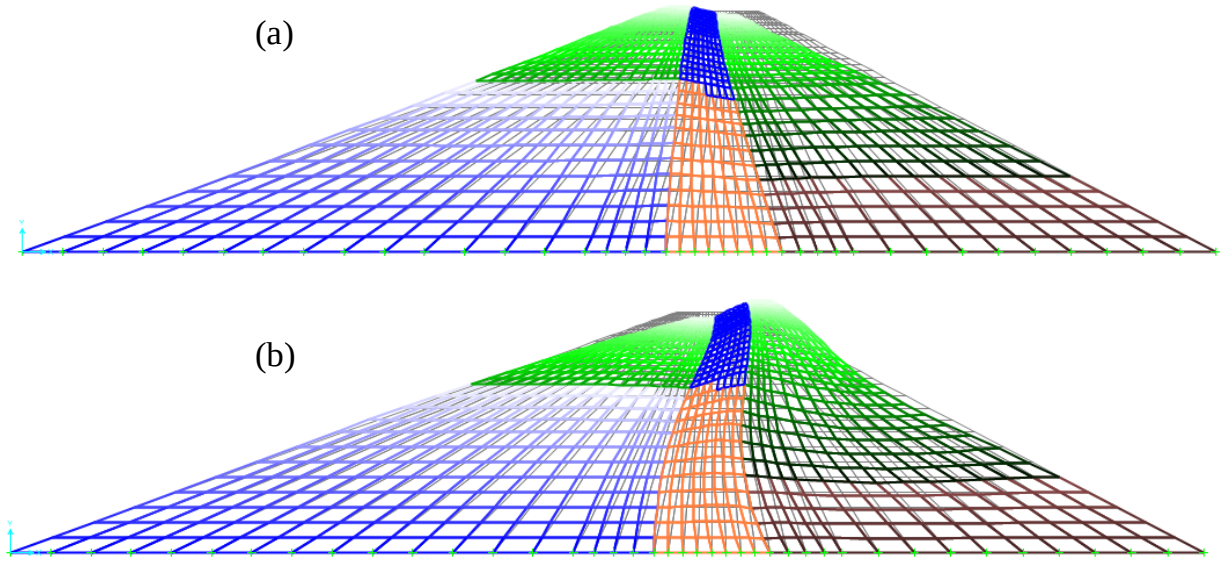

Figure 4.10 (a) first mode shape, (b) second mode shape of the fixed base model.

A summary of the most important findings in terms of natural periods, modal participating mass ratios and elongation of the periods to the SSI effect is presented in table 4.3.

Table 4.3 Summary of the main results obtained for the two analyzed models of the Farneto del Principe dam

Model	Period (sec)		Elongation (%)		*MPMR* (%)	
	T_1	T_2	ΔT_1	ΔT_2	Mode 1	Mode 2
Fixed base	0.197	0.097	-	-	62*	12*
Flexible base	0.240	0.126	22	29		

*The modal participating mass ratios for the flexible base model were considered useless (because of the presence of the foundation), as discussed above

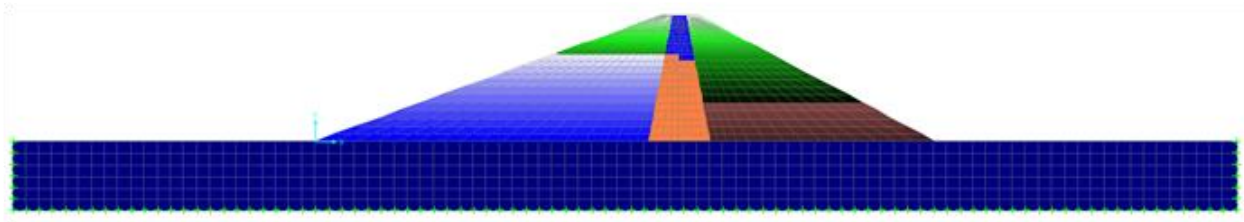

Figure 4.11 **Mesh and geometry of the flexible base model of the Farneto del Principe dam.**

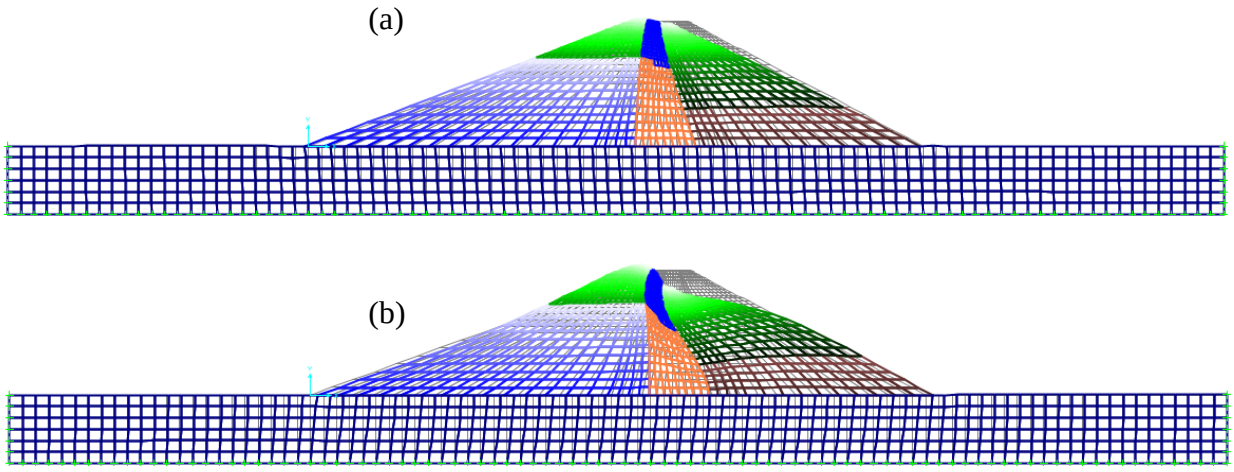

Figure 4.12 **(a) first mode shape, (b) second mode shape of the flexible base model.**

4.2 Pre-Selection of the Ground Motions

The fundamental period and mode shape of the dam, shown in section 4.1, represent useful information that can be used as starting point for pre-selecting candidate ground motions to be scaled to fit the target spectra. These findings are not usable alone, for this reason, in the remainder of this section, a strategy to perform a pre-selection of ground motions is shown.

The definition of a driving scenario (e.g. a bin of magnitude and source-to-site distance) for the hazard of the site, it is a crucial step in the ground motion selection. In section 3.3.5, the disaggregation of the seismic hazard for the Farneto del Principe dam was presented. Disaggregation analysis strongly depends on the hazard level being disaggregated and on the definition of the intensity measure to use. If the spectral acceleration of interest is *Sa(T)*, then, both disaggregation, and selected time histories, depend on that structural period *T* that becomes an important factor. In order to take care about the structural response, in this study, the spectral

acceleration of interest was defined as $SA(T_1=0.25s)$, where T_1 is the first natural period of the whole system (dam plus deformable foundation), evaluated numerically in the previous section.

The results for the probabilistic seismic hazard disaggregation of the seismic hazard for $SA(T_1=0.25s)$, show that the magnitude and source-to-site distance ranges that mostly contribute to the hazard of the site are **M** = 5.5 – 8 and R = 0 – 35 km (M is defined as the moment magnitude **M**; the source-to-site distance R is defined as the Joyner and Boore, 1981 distance R_{jb}). These ranges were used in pre-selecting candidate ground motion time histories to use in the numerical analyses. Besides **M** and R, an further criterion was added in the pre-selection procedure, the candidate ground motions should be selected for rock-like (or very stiff soil) site conditions. The parameter used for this purpose is V_{S30} expressed in m/s, a preferable value equal to 760 m/s was implied.

On the basis of the above presented criteria, 13 earthquake horizontal components were pre-selected, from the PEER NGA West-2 Ground Motion Database (ngawest2.berkeley.edu/ last accessed January 28th 2015) as shown in Table 4.4.

Table 4.4 Pre-selected ground motion components

Earthquake name*	Station	Year	Mechanism	Magnitude (M)	Source-to-site distance (R_{jb})	V_{S30} (m/s)
Irpinia (IT)	Bisaccia	1980	Normal	6.9	17.51	997
Whittier Narrows (CA)	Pasadena - CIT Kresge Lab	1987	Reverse oblique	5.99	6.78	967.07
Loma Prieta (CA)	Gilroy array #1	1989	Reverse oblique	6.93	8.84	1428.14
Landers (CA)	Lucerne	1992	Strike-slip	7.28	2.19	1369
Northridge (CA)	Vasquez Rocks Park	1994	Reverse	6.69	23.1	996.43
Kobe (JP)	Kobe University	1995	Strike-slip	6.9	0.9	1043

(continued on next page)

Table 4.4 (cont.) **Pre-selected ground motion components**

Earthquake name*	Station	Year	Mechanism	Magnitude (M)	Source-to-site distance (R_{jb})	V_{S30} (m/s)
Kocaeli (TU)	Gebze	1999	Strike-slip	7.51	7.57	792
Tottori (JP)	SMNH10	2000	Strike-slip	6.61	15.58	967.27
Parkfield (CA)	PARKFIELD - TURKEY FLAT #1 (0M)	2004	Strike-slip	6	4.66	906.96
Umbria (IT)	Gubbio	1984	Normal	5.6	14.67	922
L'Aquila (IT)	L'Aquila - V. Aterno - Colle Grilli	2009	Normal	6.3	0	685
Iwate (JP)	IWT010	2008	Reverse	6.9	16.26	825.83
Duzce (TU)	IRIGM 496	1999	Strike-slip	7.14	4.21	760

*The abbreviation used are defined as follows: IT: Italy; CA: California (USA); JP: Japan; TU: Turkey.

The 40% of the total and the 64% for **M** ≥ 5.5 of the ground motions for normal mechanism in the PEER NGA West-2 database comes from Italian earthquakes. This is reflected in the pre-selection of the events, where, for normal style of faulting, only Italian earthquakes are present.

In addition to Italy, other three active seismic areas are comprised in the pre-selected events: California (five events), Turkey (two events) and Japan (three events).

The selection of earthquake ground motion records for evaluating the seismic performance of the Farneto del Principe dam requires consideration of several different ground motion characteristics. According to Gazetas et al. (1981), in order to evaluate the seismic behavior of an embankment it is necessary to perform a series of analyses using several input motions to obtain a possible range of responses. Shome et al. (1998) show that seven simply scaled time histories may provide an acceptably low dispersion in the estimated response of the structure. More recently, Stewart et al. (2001), state:

> *"It is preferable to use a large number of time histories without modifying their response spectral shapes, in order to sample the response of the structure to ground motions having different phasing and response spectral shape.".*

The Italian code for dam design and safety (D.M. June 14, 2014) refers to the Italian building code (M.LL.PP., 2008), about the number of inputs to use in response history analysis for seismic design and analysis process of dams. The code prescribes to use a minimum of three time histories and takes the maximum value of the peak response quantities; if seven (or more) time histories are used, the mean value of the peak response quantities could be used.

The latest version of the Federal guideline for dam safety (FEMA-65, 2005), prescribes to use three or more time histories for nonlinear analyses, suggesting that it is desirable to have additional time histories because of the importance of phasing (pulse sequencing) to nonlinear response. In this study each ground motion suite comprises seven time histories.

Thirteen inputs were pre-selected based on the selected magnitude-distance window. A further refinement is necessary to end up with the ground motions choice. According to the recent literature on the argument (e.g. Shome et al., 1998, Stewart et al., 2001; Bommer and Acevedo, 2004; Pagliaroli and Lanzo, 2008; Kramer et al., 2012; Haselton et al., 2014), additional criteria are used (and listed below) to constrain the choice for both suites: a) Period range: according to Haselton and Baker (2006) the spectral shape has significant effects on collapse capacity estimation. Accordingly the average spectrum of each suite of motion should be consistent with the target spectrum over a broad period range. The NIST GCR 11-917-14 report (NIST, 2011) suggests to use a period range or interval for scaling ground motions consistent with a UHS or CMS. The recommended intervals are: $0.2T_{1,min}$ - $3T_{1,max}$ for moment frame buildings and $0.2T_{1,min}$ - $2T_{1,max}$ for shear-wall or braced frame buildings. $T_{1,min}$ ($T_{1,max}$) is the lesser (greater) of the first mode translational periods along the two horizontal axes of the building. No period ranges are given for earth dams or similar structure. In this study, it was decided to use the interval $0.2T_1$ - $4T_1$. $T_1 \approx 0.25$ sec is the fundamental period of the dam system (as shown in section 4.1). The chosen period range in this study is T = 0.05 sec – 1 sec. This broad interval was chosen in order to take into account both short periods (accounting for higher modes effects) and long periods (accounting for inelastic behavior that drives to an elongation of the natural periods); b) Style of faulting: according to Bommer and Acevedo (2004), inclusion of style-of-faulting in the record selection is not vital. Nonetheless, in this study, it was decided to use focal mechanisms in order to constrain the input choice. The normal style of faulting is the one that most likely affect the hazard of the site (see chapter 3). For this reason It was decided to add the largest possible number of signals produced by normal faults; c) Pulse-like motions: as

shown in the seismotectonic study performed in chapter 3, the Farneto del Principe dam site hazard should not be affected by near fault effects. Pulse-like motions unlikely affect the site of interest. Accordingly, we decided to minimize the number of pre-selected motions with this feature; d) No multiple inputs from the same event: a single earthquake-dominated suites is not acceptable. From a single earthquake, only one records is selected; e) Lowest usable frequency: according to Wang et al. (2013), an additional criterion for an input choice should be the lowest useable frequency. In this study it was decided to select ground motions with a lowest useable frequency equal or lower than of 0.4 Hz. This limit is used to ensure representative ground motions until a longest usable period equal to T = 2.5 second; f) No outlier motions: the mean spectrum of a suite that match a target spectrum can include motions whose individual spectra fall far above (or below) the mean at some frequencies (outlier motions). Analyses using these motions may significantly affect nonlinear response (Kramer et al., 2012). Accordingly, in this study, outlier motions are manually eliminated from the suites; g) Time-domain linear scaling: the effect of scaling on the selected ground motion can be profound. In this study, only uniform time-domain linear scaling is performed (no adjustments or matching are allowed). In order to reduce the scaling-induced changes in ground motions, the maximum tolerable scaling factor (*SF*) in this study is set equal to 10, while the mean tolerable scaling factor of the suites is set to 4.

4.3 Ground Motion Selection and Scaling Using the UHS as Target Spectrum

The pre-selected inputs are the starting point for the choice of a suite of seven ground motions to use in the time history analyses. The UHS is a commonly used target spectrum. This spectrum represents an envelope of spectral values associated with multiple ground motions created for a given hazard level. Accordingly, it is generally a conservative target spectrum. In this section the development of a suite of ground motions selected and linearly scaled to be consistent with the UHS for a return period of T_R = 2475 years, for the Farneto del Principe dam is presented. More information on the process used to develop this target spectrum are provided in section 3.3.4.

On the basis of the criteria discussed in section 4.2, the time histories comprised in the suite were selected adding a quantitative measure useful to evaluate how well a time series conforms to the target spectrum. This measure is the mean squared error (*MSE*) of the difference between

the spectral accelerations of the record (SA_{record}) and of the target (SA_{target}). The *MSE* definition is shown in Equation 4.13:

$$MSE = \frac{\sum_i w(T_i)\left\{ln\left[SA_{target}(T_i)\right] - ln[SF \cdot SA_{record}(T_i)]\right\}^2}{\sum_i w(T_i)} \quad (4.13)$$

where T_i is the ith period and $w(T_i)$ is a weight function used to assign relative weights to different parts of the period range of interest. The trivial case of $w(T_i) = 1$ is used to assign the same for the whole range of interest. *MSE* provides a measures of the misfits between the spectral shape of the input and of the target taking into account the entity of the used scaling factor. The time histories selected are listed in table 4.5, with the MSE and the SF used. The used weight function is $w(T_i) = 1$ for the period range 0.05 sec – 1 sec.

Table 4.5 Selected ground motion components for UHS

Earthquake name	Station	Year	Mechanism	M	R_{jb}	V_{S30} (m/s)	*MSE*	*SF*
Irpinia (IT)	Bisaccia	1980	Normal	6.9	17.51	997	0.26	8.6
Loma Prieta (CA)	Gilroy array #1	1989	Reverse oblique	6.93	8.84	1428.14	0.12	1.9
Tottori (JP)	SMNH10	2000	Strike-slip	6.61	15.58	967.27	0.17	5.3
Parkfield (CA)	PARKFIELD - TURKEY FLAT #1 (0M)	2004	Strike-slip	6	4.66	906.96	0.09	4.2
L'Aquila (IT)	L'Aquila - V. Aterno -Colle Grilli	2009	Normal	6.3	0	685	0.12	1.8
Iwate (JP)	IWT010	2008	Reverse	6.9	16.26	825.83	0.06	2.7
Duzce (TU)	IRIGM 496	1999	Strike-slip	7.14	4.21	760	0.18	1.4

The average values for the suite are: $\overline{MSE} \cong 0.14$; $\overline{SF} \cong 3.7$.

The unscaled selected time histories are shown in Figure 4.13. In Figure 4.14(a) the seven selected and scaled inputs are shown together with the target UHS and the target ± a standard deviation (σ). Figure 4.14(b) shown the target spectrum and the mean of the suite. The red area

depicts the period range used for the selection. The goodness of the fit is acceptable also out of the range of periods for which the selection was done.

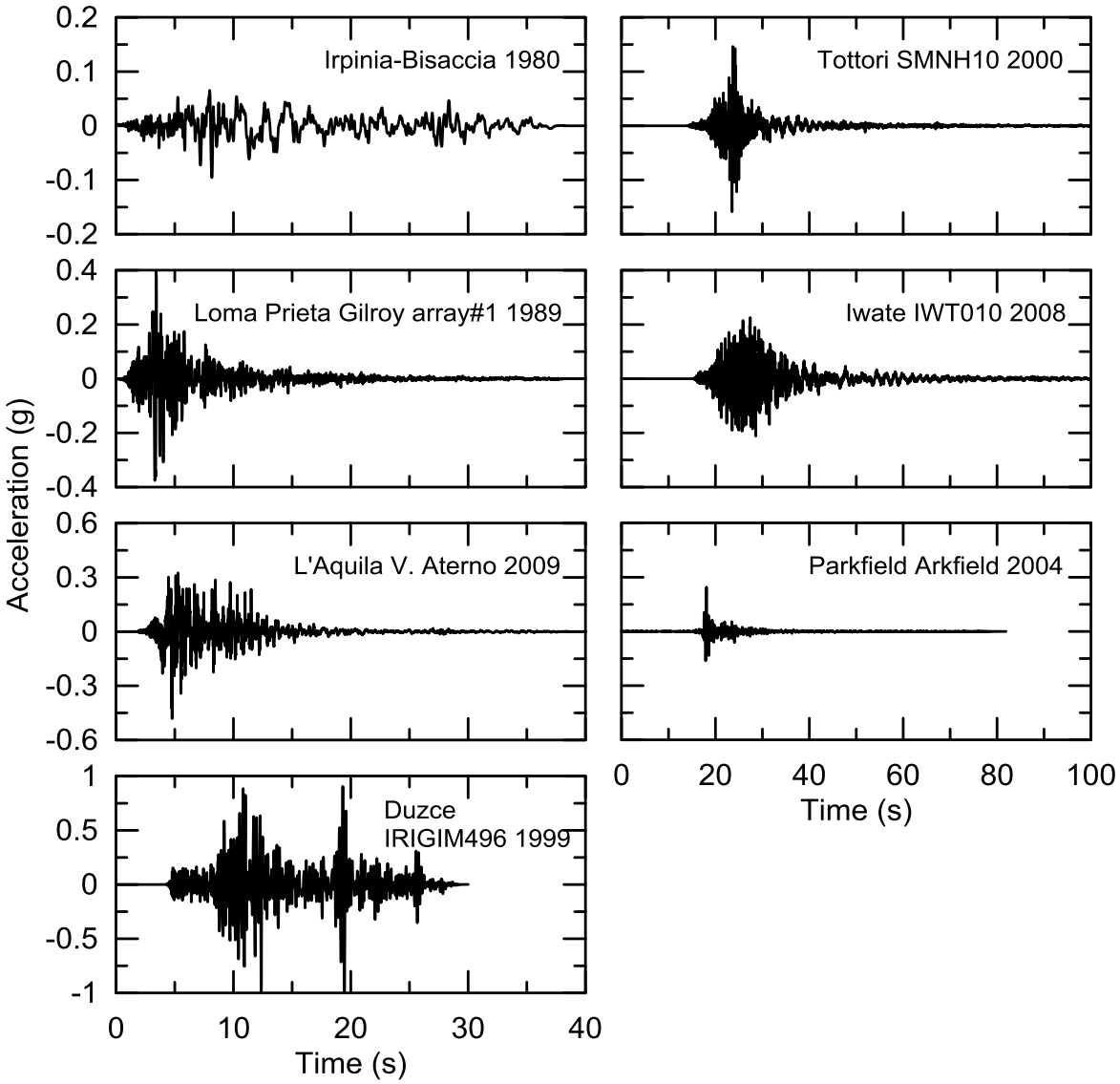

Figure 4.13 The seven unscaled selected time histories using the UHS as target spectrum.

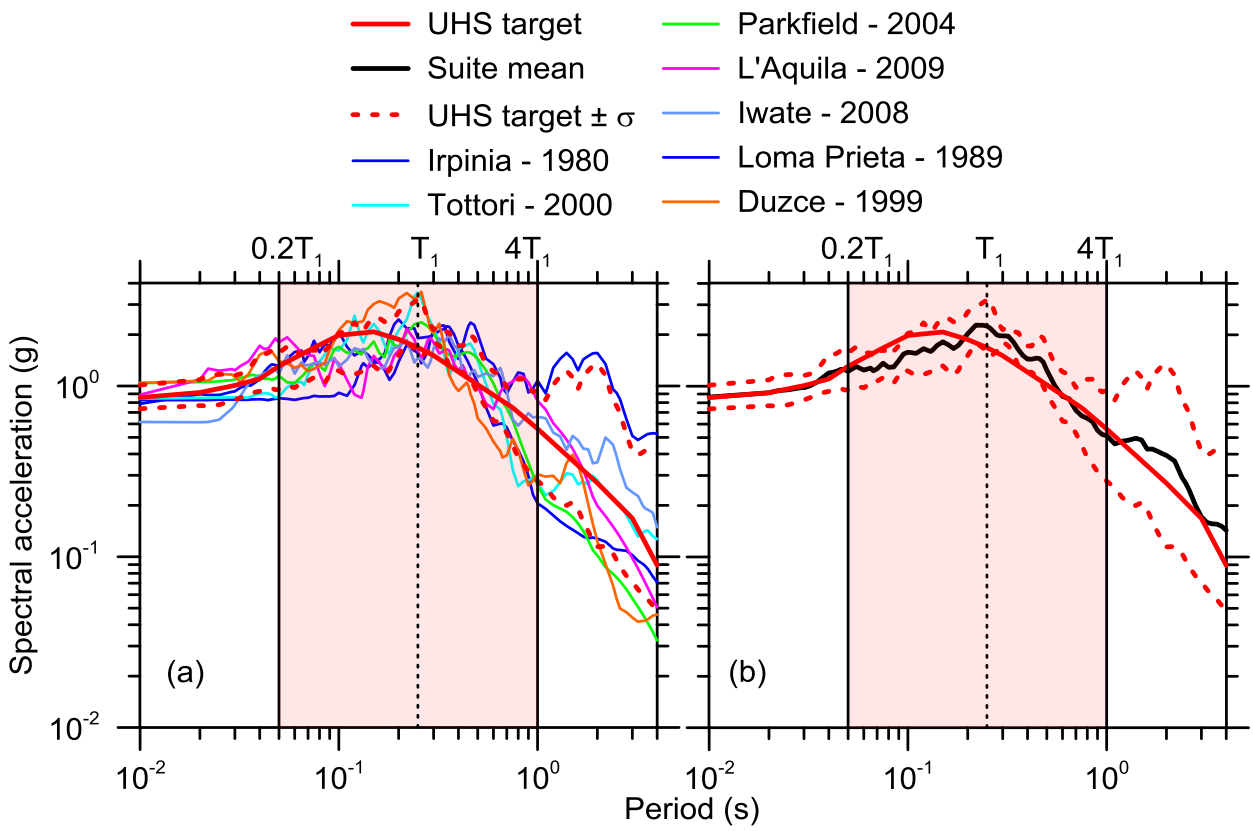

Figure 4.14 **(a) chosen inputs and, (b) mean of the suites for the target UHS.**

4.4 The Conditional Spectrum as Suitable Target Spectrum

4.4.1 Overview of the Conditional Spectrum Computation Procedure

This UHS, obtained from a PSHA is essentially defined as the envelope of the spectral amplitudes at all periods that are exceeded with a given probability in a selected time span. This spectrum conservatively implies that large-amplitude spectral values will occur at all periods within a single ground motion. It can a conservative target spectrum for seismic analysis of structures, especially for very rare levels of ground motion (e.g., Bommer et al., 2000; Naeim and Lew, 1995; Reiter, 1990), where it is most unlikely that high amplitude spectral values are observed at all periods in a single ground motion set. Baker (2011) shown that the UHS can be an unsuitable target for selecting and scaling ground motion to use as input in dynamic analysis.

Baker and Cornell (2006) and Baker (2011) proposed a method to reduce the UHS into a scenario spectrum, they termed this response spectrum as conditional mean spectrum (CMS). It consists of the mean values of the spectrum at all periods, conditional on spectral acceleration

value at a single period (defined as the conditioning period T^*). The CMS by definition is less conservative than the UHS with the exception of the spectral acceleration at the conditioning period (T^*). The CMS was initially proposed with an emphasis on the mean spectrum and less attention on the variability in the spectrum. More recently Abrahamson and Al-Atik (2010) and Lin et al. (2013), termed as conditional spectrum (CS) the probability distribution of log spectral acceleration (SA) values, conditional on a spectral value at a conditioning period. The CMS is the mean value of the CS distribution.

Prior to compute the CS it is necessary to define an important parameter involved in its calculation. This parameter is ε that is defined as the number of standard deviations by which a given mean natural log spectral value of the controlling scenario spectrum (for a given magnitude and distance) differs from the mean natural log predicted by the UHS, given as:

$$\varepsilon(T) = \frac{\ln SA(T) - \mu_{lnSA}(\mathbf{M}, R, T)}{\sigma_{lnSA}(T)} \tag{4.14}$$

where ln*SA(T)* is the natural log of the spectral acceleration of the UHS at period *T*, $\mu_{lnSA}(\mathbf{M}, R, T)$ and $\sigma_{lnSA}(T)$ are the mean natural log spectral value and standard deviation, respectively, at period T, for a given scenario defined by **M** and *R*. The last two parameters are computed using GMPEs.

In the remainder of this section the steps to compute the CS for T_R = 2475 years are described as follows:

1. Determine the conditioning period T^*. In this study $T^*=T_1$=0.25 sec, where T_1 is the first natural period of the system (dam plus foundation), evaluated with a linear elastic modal analysis as discussed in §4.1;
2. Determine the target *SA* at the conditioning period T^*. The target $SA(T^*)$ is a result of the PSHA, this value can be taken from the UHS (§3.5.3).
3. Define the controlling scenario in terms of magnitude and distance (**M**-*R*). This can be done disaggregating the seismic hazard into **M** and *R*. As shown in §3.5.3, for the selected return period, for Farneto del Principe dam site we found that the controlling scenario is represented by $\bar{\mathbf{M}} = 7.39$ and $\bar{R} = 25.5$ km.

4. Compute the controlling scenario spectrum (for the target $\bar{\mathbf{M}}$ and $\bar{R}$) mean $\mu_{lnSA}(\mathbf{M},R,T)$ and standard deviation $\sigma_{lnSA}(T)$ of log spectral acceleration at all periods using a GMPE (further details about the issue of combining multiple GMPEs are discussed in §4.4.2.

5. Using equation 4.14 calculate $\varepsilon(T=T^*)$, the number of standard deviations of difference between the natural log of the UHS value $SA_{UHS}(T^*)$ and mean natural log spectral value of the controlling scenario spectrum $\mu_{lnSA}(\mathbf{M},R,T^*)$. Equation 4.14 can be re-written as:

$$\varepsilon(T^*) = \frac{\ln SA_{UHS}(T^*) - \mu_{lnSA}(\mathbf{M}, R, T^*)}{\sigma_{lnSA}(T^*)} \tag{4.15}$$

6. Compute $\bar{\varepsilon}(T_i)$ defined as the conditional mean ε for the other periods, based on the correlation between $\varepsilon(T^*)$ and ε at different periods $\rho(T_i,T^*)$, as shown in Equation 4.16. Not all GMPEs have published correlation models, however, generic model are available. In this study we used the Baker and Jayaram (2008) correlation model.

$$\bar{\varepsilon}(T_i) = \varepsilon(T^*)\rho(T_i, T^*) \tag{4.16}$$

7. Compute the CMS by combining the information of step 4 (mean and standard deviation of log spectral acceleration) and step 6 (conditional mean ε). The natural log of the CMS is given as:

$$\mu_{lnSA(T_i)|lnSA(T^*)} = \mu_{lnSA}(\mathbf{M}, R, T_i) + \bar{\varepsilon}(T_i)\sigma_{lnSA}(T_i) \tag{4.17}$$

where $\mu_{lnSA(T_i)|lnSA(T^*)}$ is the natural log value of CMS at period T_i conditioned at period T^*.

8. Compute the conditional standard deviation of ε at period T_i ($\sigma_{\varepsilon(T_i)|\varepsilon(T^*)}$) through Equation 4.18:

$$\sigma_{\varepsilon(T_i)|\varepsilon(T^*)} = \sqrt{1 - \rho^2(T_i, T^*)} \tag{4.18}$$

In the approach shown above, we defined the CS as the probability distribution of log spectral acceleration (SA) values, conditional on a spectral value at a conditioning period. The CMS ($\mu_{lnSA(T_i)|lnSA(T^*)}$) is the mean value of the distribution. The CS is fully described by conditional means, standard deviations and correlations.

In the CS computation procedure the evaluation of the controlling scenario for the hazard of the selected site is an important factor. In this connection it worth to specify which scenario we used in this study for Farneto del Principe dam site.

The mean values of **M** and *R* (Magnitude and source-to-site distance respectively), obtained as output of the disaggregation of the seismic hazard (§3.5.3) are $\bar{\mathbf{M}} = 7.39$ and $\bar{R} = 25.5$ km. These values are used as basis for the CS computation. Using mean values of **M** and *R* as final summary statistics is very convenient, especially because they are simple to understand, and to compute. Furthermore, in most cases these values represent a meaningful way to represent the driving scenario for the hazard of a selected site, but, rigorously, they do not represent the values that most likely contribute to the higher hazard level at the site (Bazzurro and Cornell, 1999). On the other hand the modal values ($\mathbf{M}^*$ and R^*) represent actual sources that define the most hazardous scenario, unfortunately the use of modal values have a big disadvantage, because they are sensitive to the bin width. For these reasons, even though the mean values $\bar{\mathbf{M}}$ and $\bar{R}$, could not be representative of single actual sources (or equivalently to a realistic scenario), we decided to use them in the analyses.

4.4.2 How to Combine Multiple GMPEs for CS Computation

In §3.4 the GMPE logic tree used for Farneto del Principe dam site PSHA is shown. When only one GMPE is used, the procedure to compute the CS is straightforward. Combining multiple GMPEs (when a logic tree approach is used in PSHA to capture epistemic uncertainties) in the CMS computation, however, is not trivial and several different approaches can be used. Lin et al. (2013) proposed four different methods (method 1 – 4).

Method 1 is the most simple to apply and uses only one GMPE (same approach shown in §4.4.1).

In method 2 all GMPEs used in the logic tree are taken into account. Steps 1 to 3 are the same of the single GMPE approach, steps 4 to 8 are done for each GMPE for the mean values $\bar{\mathbf{M}}$ and $\bar{R}$. Then the resulting mean spectra are summed up using the logic tree weights (w_k^l). The resulting mean spectrum ($\bar{\mu}_{lnSA(T_i)|lnSA(T^*)}$) is given by Equation 4.19:

$$\bar{\mu}_{lnSA(T_i)|lnSA(T^*)} = \sum_k w_k^l \cdot \mu_{lnSA_k(T_i)|lnSA(T^*)} \tag{4.19}$$

The resulting mean conditional standard deviation ($\bar{\sigma}_{\varepsilon(T_i)|\varepsilon(T^*)}$) is given as:

$$\bar{\sigma}_{\varepsilon(T_i)|\varepsilon(T^*)} = \sqrt{\sum_k w_k^l \cdot \left\{\sigma^2_{\varepsilon_k(T_i)|\varepsilon(T^*)} + \left[\mu_{lnSA_k(T_i)|lnSA(T^*)} - \bar{\mu}_{lnSA(T_i)|lnSA(T^*)}\right]^2\right\}} \quad (4.20)$$

Method 3 differs than method 2, because it uses GMPE-specific $\bar{\mathbf{M}}$ and $\bar{R}$ values instead of mean values and the disaggregation weights (w_k^d) instead of the logic tree weights (w_k^l).

Method 4 (termed by Lin et al., 2013 as the exact method) is the most method. Differently than method 3, instead of using the disaggregation weights using the GMPE-specific $\bar{\mathbf{M}}$ and $\bar{R}$ for each GMPE, the disaggregation weights are computed for each **M** and *R* bin for each GMPE. This results in *n* scenarios where n is given as:

$$n = m \cdot r \cdot k \quad (4.21)$$

where *m* is the number of magnitude bins, *r* is the number of distance bins and *k* the number of GMPEs. The disaggregation weight is then the fractional contribution of each of the *n* M, R and GMPE combinations to the total hazard. For each scenario steps 4 to 8 are done. Then, the mean spectrum and conditional standard deviation are computed as the weighted sum of all *n* combinations using Equations 4.19 and 4.20.

More recently Carlton and Abrahamson (2014) suggested an alternative method termed method 2.5. In this method steps 1 to 3 are the same of the single GMPE approach, step 4 is done for each GMPE, then, $\mu_{lnSA}(\mathbf{M},R,T)$ and $\sigma_{lnSA}(T)$ for each GMPE are weighted by their disaggregation weights and summed at each period, giving mean natural log response spectral values $\bar{\mu}_{lnSA}(\mathbf{M},R,T)$ and mean natural log standard deviation values $\bar{\sigma}_{lnSA}(T)$, as shown in Equations 4.22 and 4.23. Finally steps 5 to 8 are done using the mean values $\bar{\mu}_{lnSA}(\mathbf{M},R,T)$ and $\bar{\sigma}_{lnSA}(T)$ instead of $\mu_{lnSA}(\mathbf{M},R,T)$ and $\sigma_{lnSA}(T)$.

$$\bar{\mu}_{lnSA}(\mathbf{M},R,T_i) = \sum_k w_k^d \cdot \mu_{lnSA_k(T_i)} \quad (4.21)$$

$$\bar{\sigma}_{lnSA}(\mathbf{M},R,T_i) = \sum_k w_k^d \cdot \sigma_{lnSA_k(T_i)} \quad (4.22)$$

In this study, we used method 1, method 2 and method 2.5 but instead of w_k^d in Equation 4.21 and 4.22 we used w_k^l.

In Figures 4.15(a), 4.16(a) and 4.17(a) the UHS for T_R = 2475 years, the predicted median, the predicted median + $\varepsilon(T^*)\sigma_{lnSA}(T_i)$ and the CS for method 1 are shown for the BSSA14, Akkar and Bommer (2010) and Zhao et al. (2006) GMPEs respectively. These GMPEs are present in the logic tree for shallow crustal tectonic regime of the Farneto del Principe dam site. Figures 4.15(b), 4.16(b) and 4.17(b) shown the CS (CMS ± a conditional standard deviation) for method 1 and the same GMPEs.

In Figure 4.18(a) the UHS for T_R = 2475 years, the CS for method 2 is shown together with the single-GMPE CMS obtained with method 1. Figure 4.18(b) shows the UHS for T_R = 2475 years and the CS (CMS ± two conditional standard deviations) for method 2.

Figure 4.19 shows the UHS for T_R = 2475 years, the predicted median spectra for the BSSA14, Akkar and Bommer (2010) and Zhao et al. (2006) GMPEs, the weighted average and the weighted average predicted median + $\varepsilon(T^*)\bar{\sigma}_{lnSA}(T)$ used for computation of the CS with method 2.5. In Figure 4.20 the standard deviations for each GMPE and the weighted average conditional standard deviation are shown.

Figure 4.21 shows the UHS for T_R = 2475 years and the CS (CMS ± a conditional standard deviation) for method 2.5 obtained using the logic tree weights.

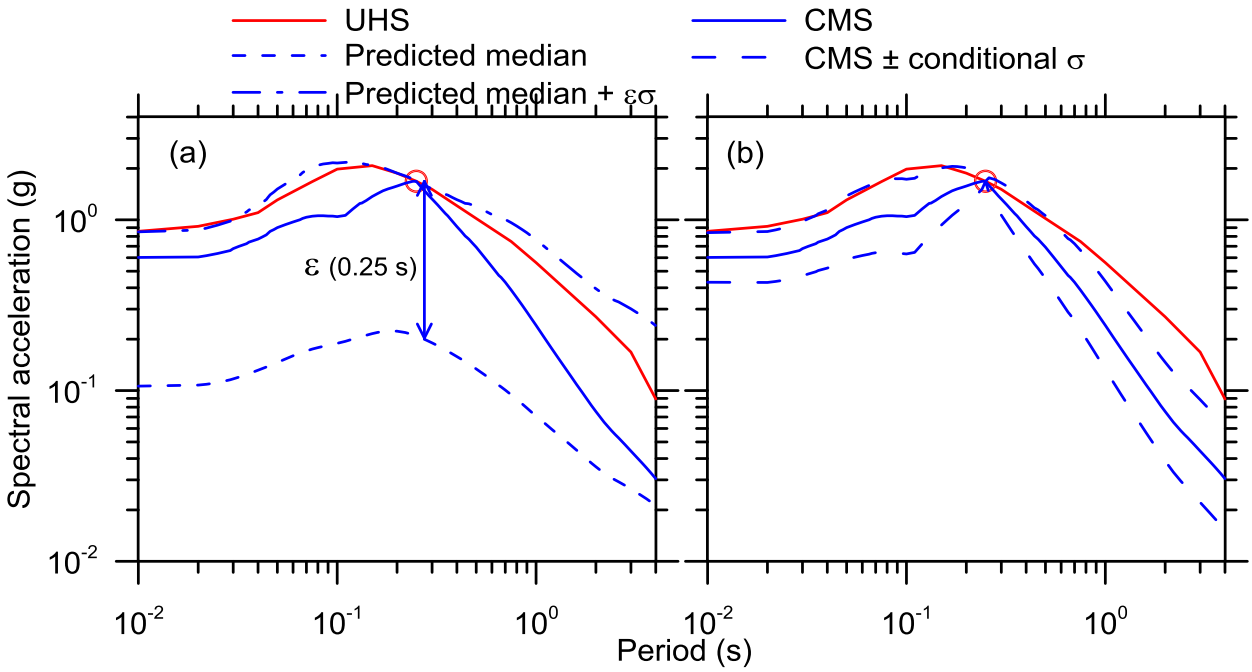

Figure 4.15 **(a): UHS, predicted median, predicted median + $\varepsilon\sigma$, CMS; (b): CS (CMS ± two conditional standard deviations) for the BSSA14 model.**

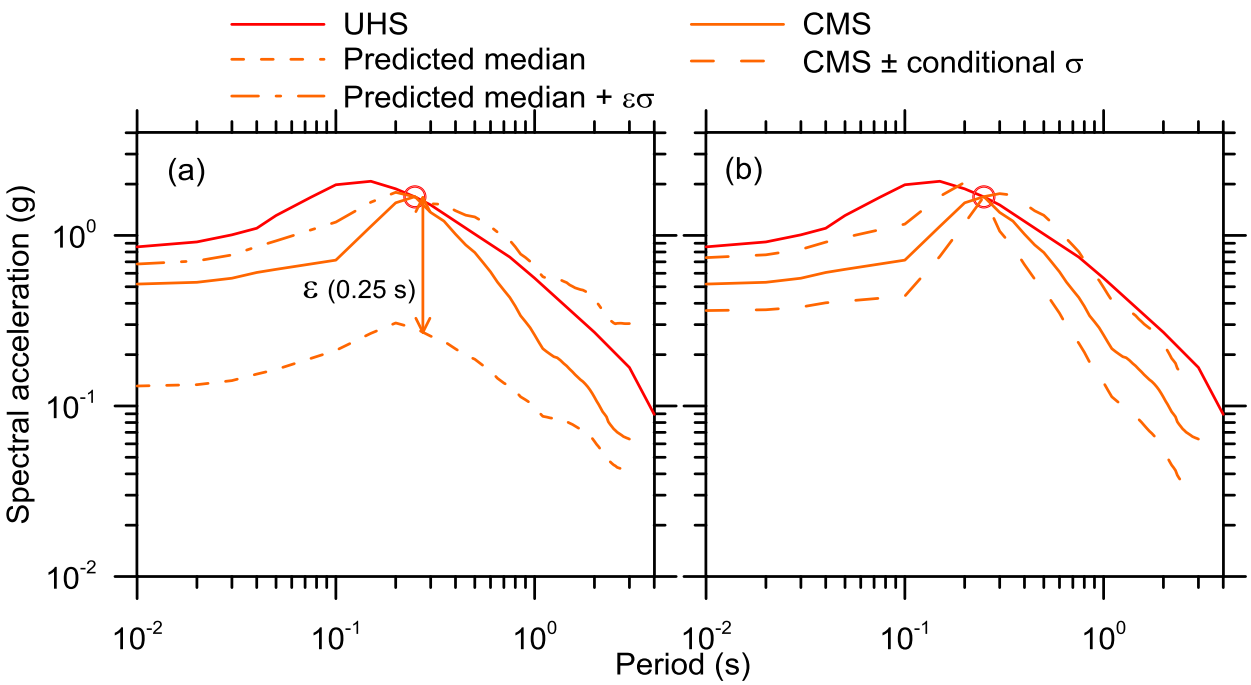

Figure 4.16 **(a): UHS, predicted median, predicted median + $\varepsilon\sigma$, CMS; (b): CS (CMS ± two conditional standard deviations) for the Akkar and Bommer (2010) GMPE.**

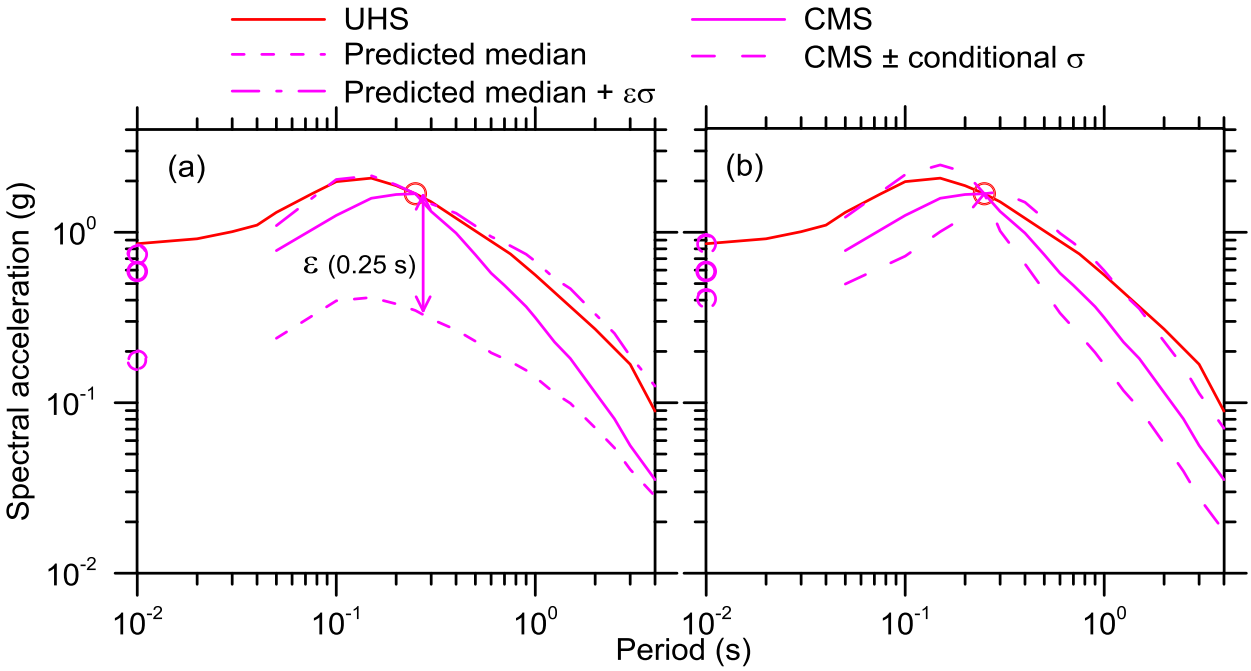

Figure 4.17 **(a): UHS, predicted median, predicted median + $\varepsilon\sigma$ and CMS; (b): CS (CMS ± two conditional standard deviations) for the Zhao et al. (2006) GMPE. The magenta open circles represent PGA for this GMPE that doesn't have the intermediate spectral ordinates.**

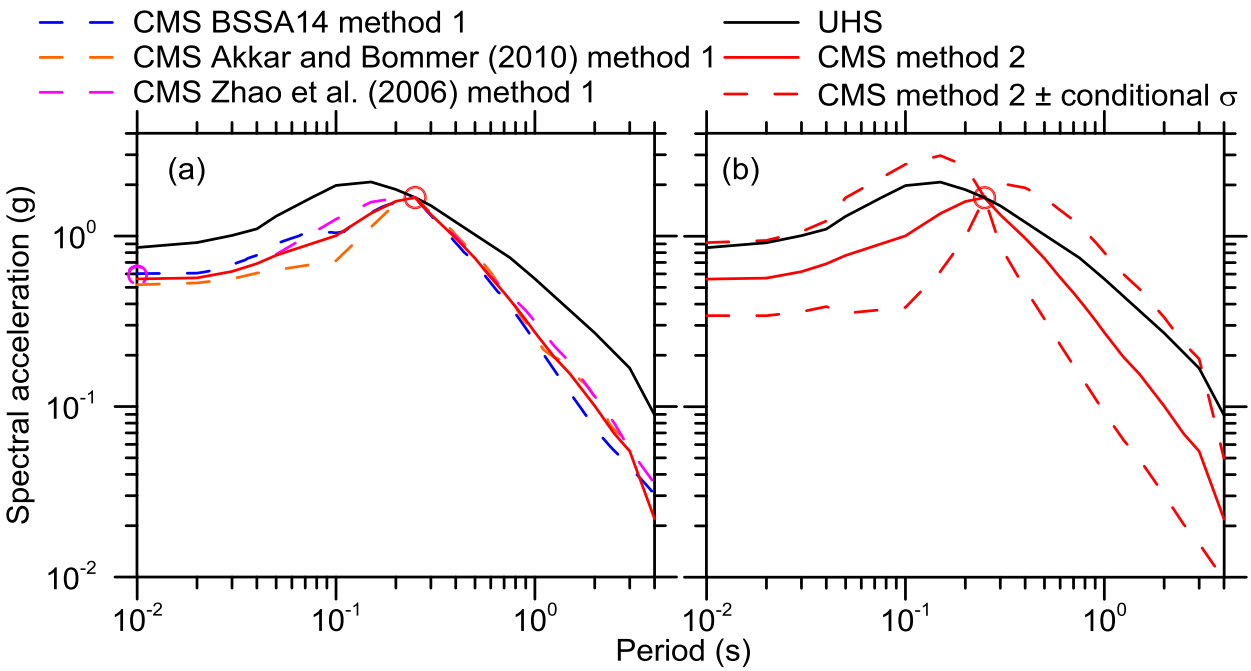

Figure 4.18 **(a): UHS, CS for method 2 (CMS ± two conditional standard deviations) and CMS method 1 obtained with the BSSA14, Akkar and Bommer (2010) and Zhao et al. (2006) models; (b): UHS and CS for method 2. The magenta open circle represents PGA for the Zhao et al. (2006) GMPE that doesn't have the intermediate spectral ordinates.**

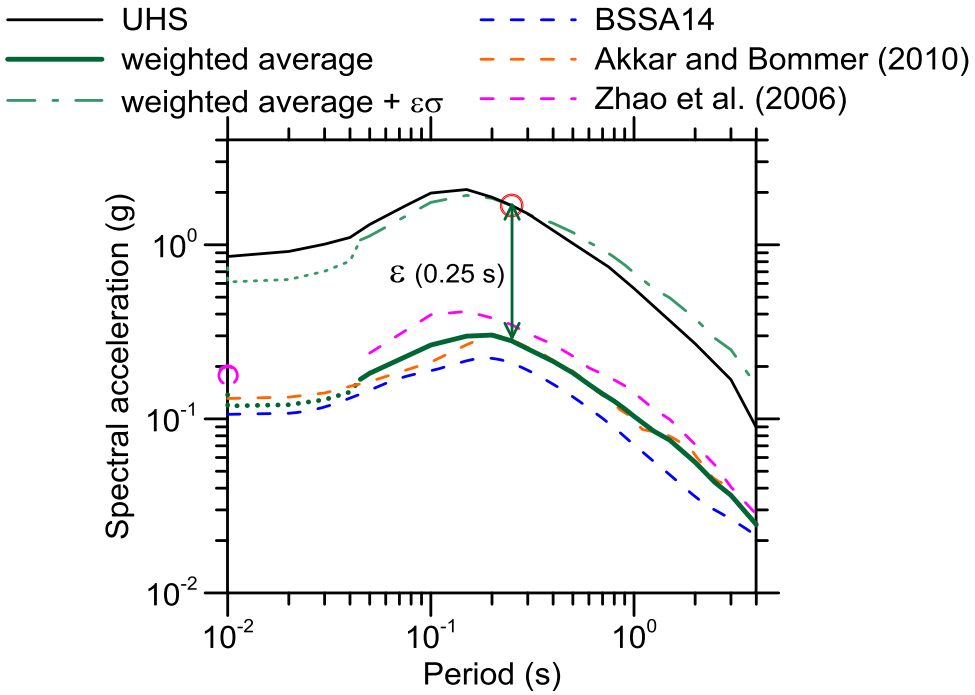

Figure 4.19 **UHS, predicted median obtained with the BSSA14, Akkar and Bommer (2010) and Zhao et al. (2006) models, weighted average and weighted average + $\varepsilon\sigma$. The magenta open circle represents PGA for the Zhao et al. (2006) GMPE that doesn't have the intermediate spectral ordinates. The dotted lines represent the values calculated as the weighted average of the GMPEs defined for that range.**

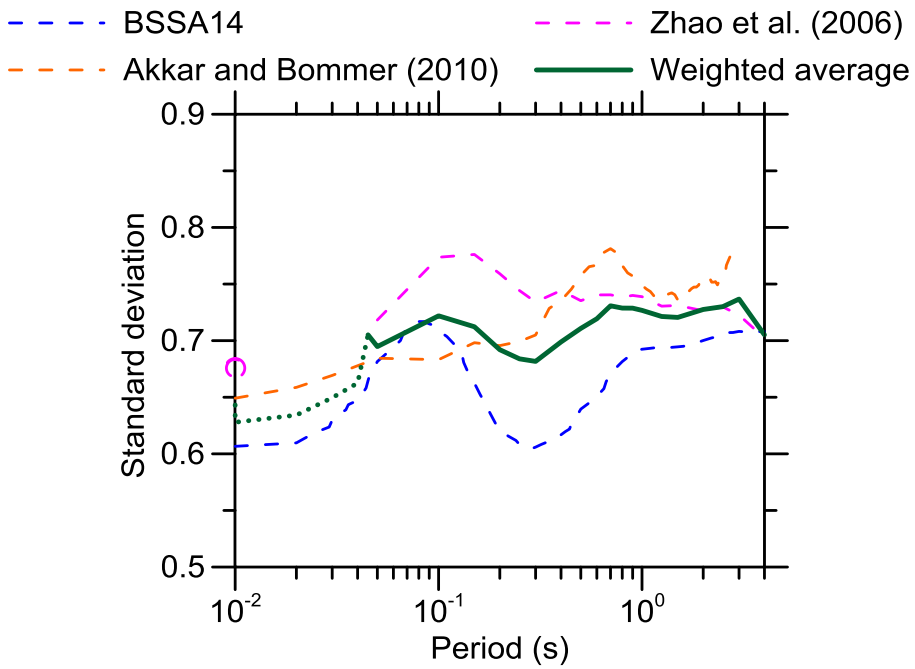

Figure 4.20 **weighted average and standard deviations for the BSSA14, Akkar and Bommer (2010) and Zhao et al. (2006) models. The magenta open circle represents *σ(T=0 sec)* for the Zhao et al. (2006) GMPE that doesn't have the intermediate spectral ordinates. The dotted lines represent the values calculated as the weighted average of the GMPEs defined for that range.**

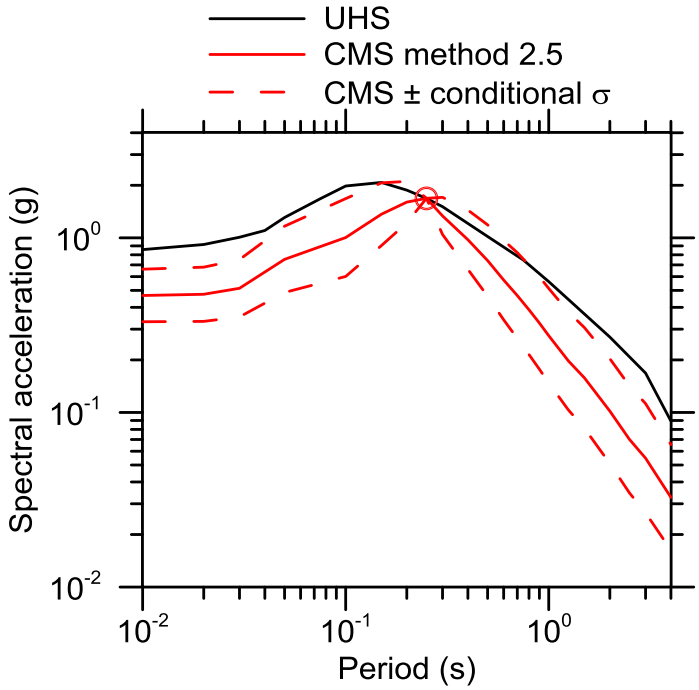

Figure 4.21 **UHS and CS (CMS ± a conditional standard deviation) for method 2.5 obtained using the logic tree weights.**

4.4.3 Ground Motion Selection and Scaling Using the CS as Target Spectrum

As shown in previous sections of this chapter, the CS can be used as effective target spectrum in ground motion selection and scaling. Carlton and Abrahamson (2014) shown that the CS obtained with method 2.5 doesn't show significant differences compared with the CS obtained by using method 3. For this reason and because of the simplicity in the calculation of CS by using method 2.5, we decided to use this CS (Figure 4.21) as target spectrum to use in ground motion spectral matching. Generally, several T^* and several corresponding CS should be used, deriving a suite of inputs for each CS. Alternatively, instead of use multiple suites (that increase the computational effort in numerical analyses), it is possible to use a broadened CS, that takes into account more than one conditioning period (e.g. Carlton and Abrahamson, 2014, Loth, 2014). In this study, according to the modal analysis results(§4.1), it was decided to use $T^* = T_1$ as the only conditioning period. This choice can be justified by the fact that the Farneto del Principe dam is a first mode-dominated structure, in which, the contribution of higher modes is almost negligible.

The ground motion selection and scaling procedure was conducted by using the Jayaram et al. (2011) algorithm. This algorithm allows to match target response spectrum mean and variance at the same time. The first step of the algorithm is the parameterization of the target spectrum (in this study the CS computed with method 2.5 as shown in §4.4.2). This step is used for evaluating conditional mean and conditional standard deviation for a given scenario and conditioning period. Then 40 response spectra are simulated using a Monte Carlo simulation by sampling from a multivariate normal distribution with the mean and covariance matrices defined in the first step. In this study we simulated a number of spectra equal to the pre-selected ground motions in the database. The simulated spectra are matched individually by an equal number of ground motions. Finally the required number (seven in this case) of selected ground motions are extracted from those that match the simulated spectra. The time histories selected and scaled are listed in table 4.6, with the SF used.

In Figure 4.22a the seven matched Monte Carlo simulated spectra are shown, in Figure 4.22b the mean of the suite is shown with the conditional mean target (CMS) and the CS (CMS ± two conditional standard deviation).

The unscaled selected time histories reported in Table 4.6 are shown in Figure 4.23.

Table 4.6 Selected ground motion components for CS

Earthquake name	Station	Year	Mechanism	M	R_{jb}	V_{S30} (m/s)	*SF*
Whittier Narrows (CA)	Pasadena - CIT Kresge Lab	1987	Reverse oblique	5.99	6.78	969.07	7.12
Loma Prieta (CA)	Gilroy array #1	1989	Reverse oblique	6.93	8.84	1428.14	1.65
Tottori (JP)	SMNH10	2000	Strike-slip	6.61	15.58	967.27	2.53
Parkfield (CA)	PARKFIELD - TURKEY FLAT #1 (0M)	2004	Strike-slip	6	4.66	906.96	3.05
L'Aquila (IT)	L'Aquila - V. Aterno -Colle Grilli	2009	Normal	6.3	0	685	1.88
Iwate (JP)	IWT010	2008	Reverse	6.9	16.26	825.83	3.13
Duzce (TU)	IRIGM 496	1999	Strike-slip	7.14	4.21	760	0.7

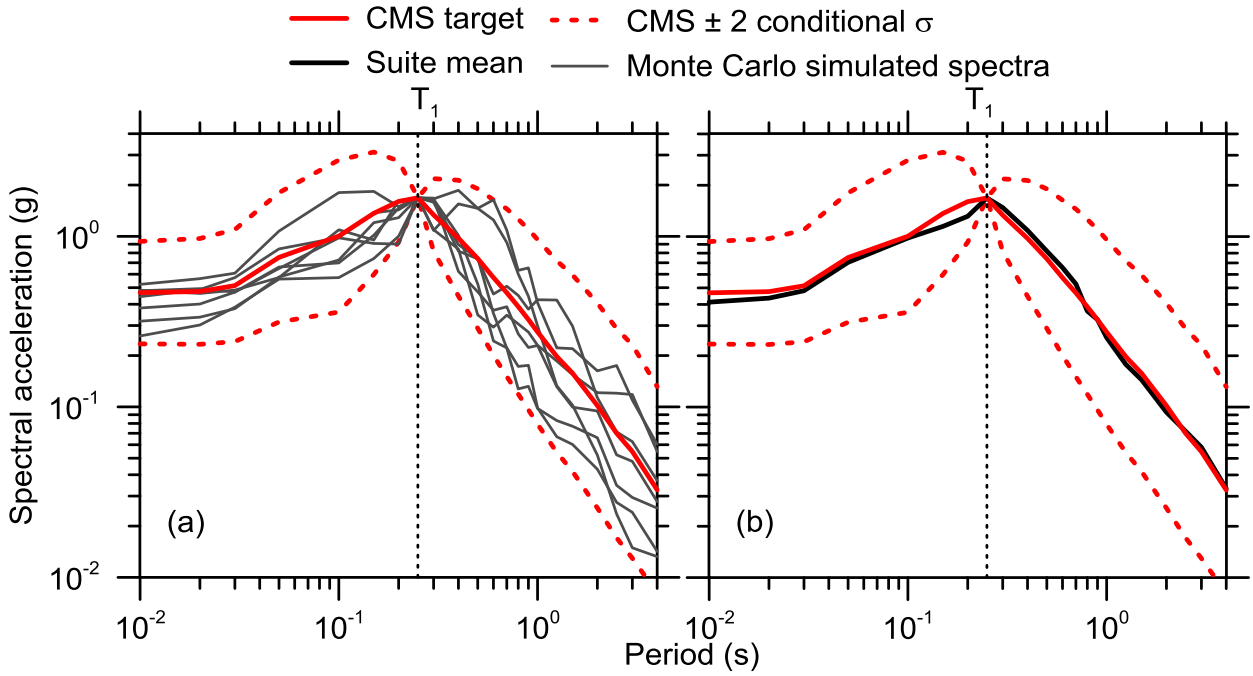

Figure 4.22 (a)CS, Monte Carlo simulated spectra; (b) mean of the simulated spectra for matching the target CS.

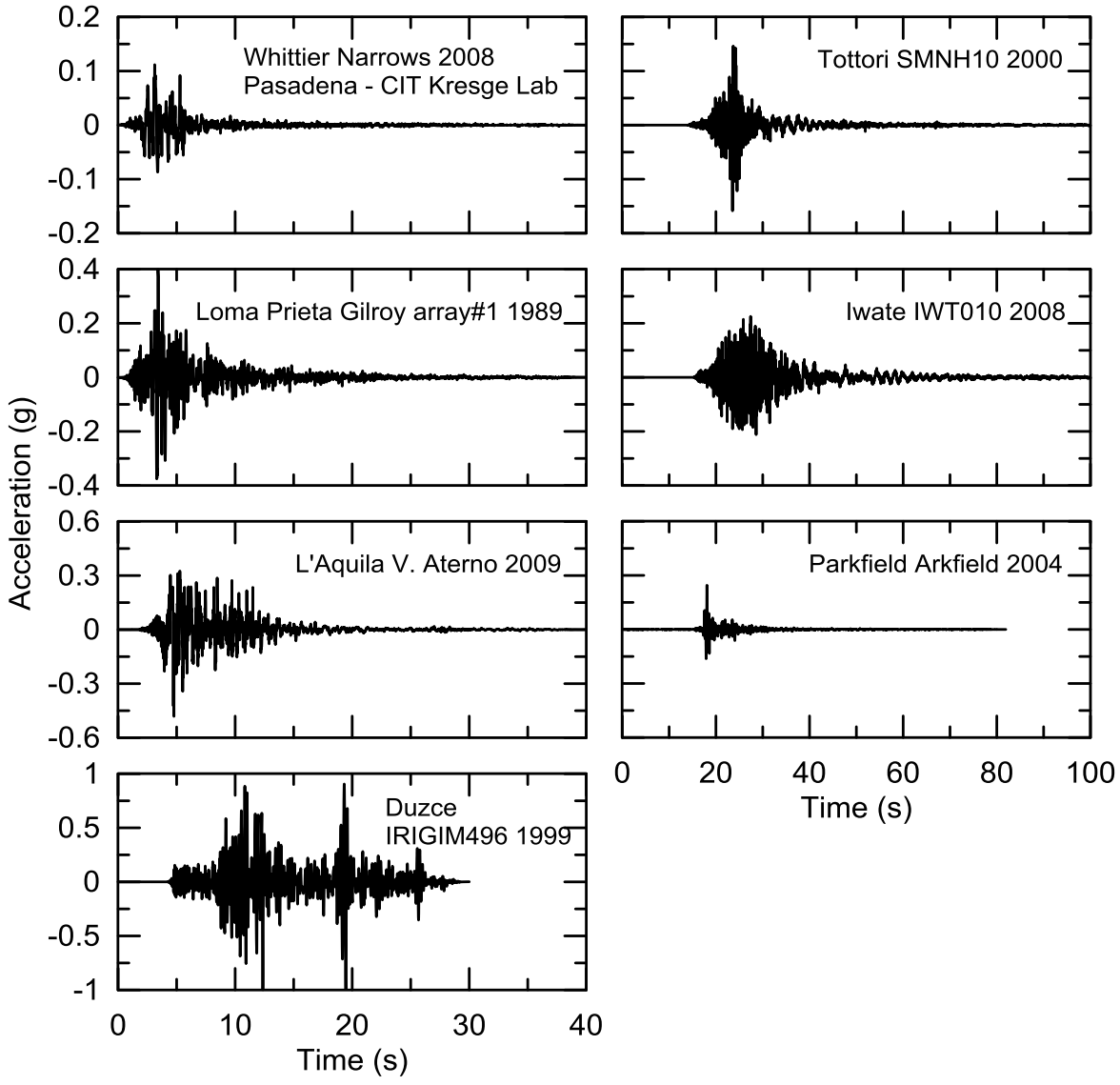

Figure 4.23 The seven unscaled selected time histories using the CS as target spectrum obtained by using the Jayaram et al. (2011) algorithm.

In Figure 4.24 shows the seven selected and scaled time histories and the mean of the suite are with the conditional mean target (CMS) and the CS (CMS ± two conditional standard deviation).

Figure 4.25 shows the conditional standard deviation of the target CS together with the standard deviation of the mean of the Monte Carlo simulated spectra and the standard deviation of the mean of the suite of the selected ground motions.

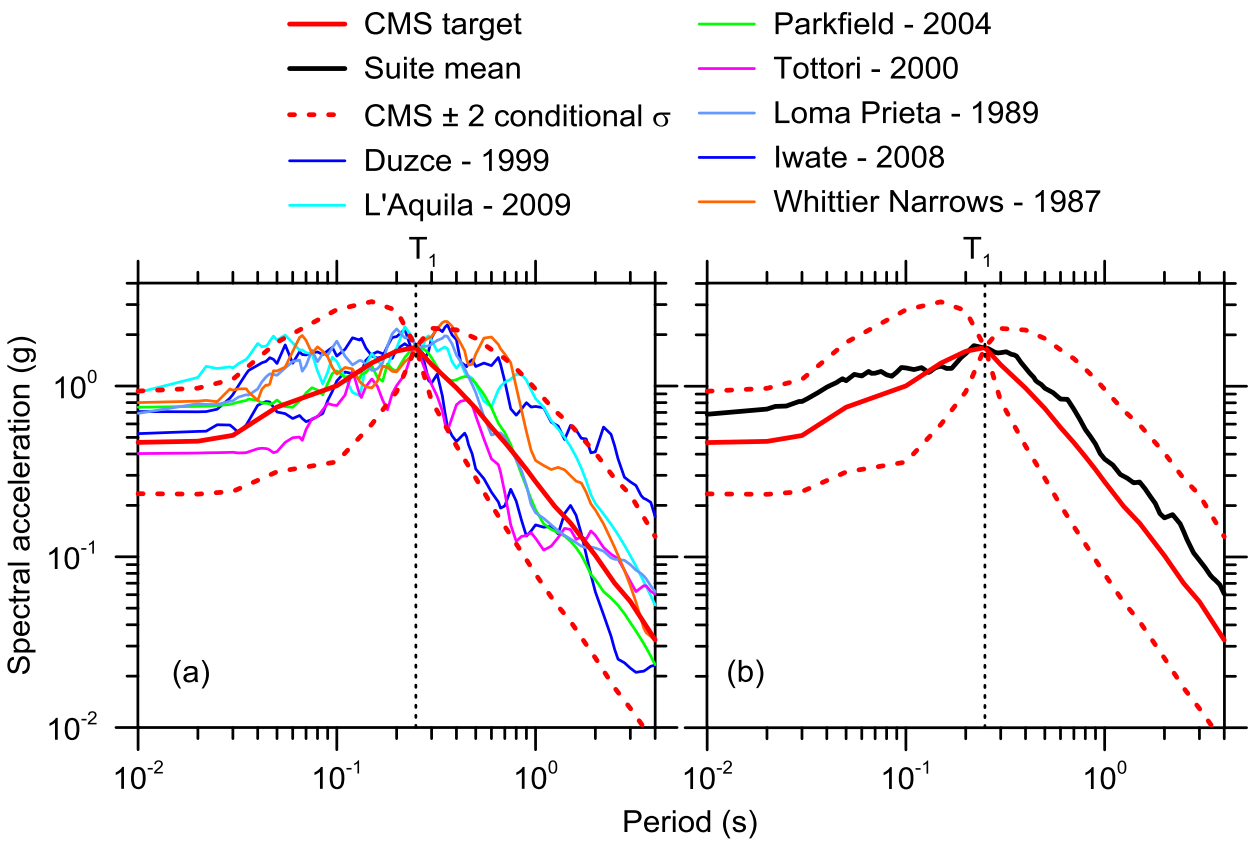

Figure 4.24 **(a) CS, elected time histories, (b) mean of the suite for the target CS.**

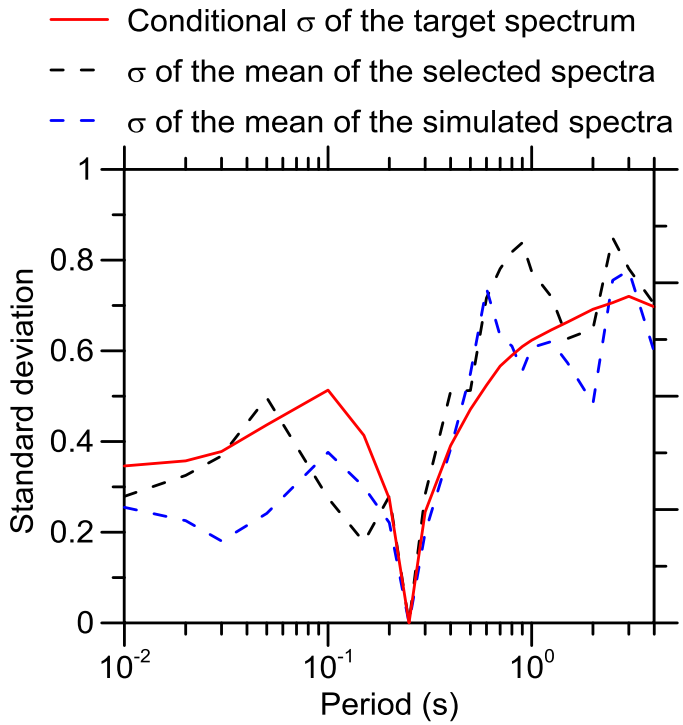

Figure 4.25 **Conditional standard deviation of the target CS, standard deviation of the Monte Carlo simulated spectra and standard deviation of the mean of the selected (recorded) ground motions.**

5 Response History Analysis and Evaluation of the Dynamic Behavior of the Dam

Once suites of appropriate site-specific and hazard consistent input motions are developed, it is necessary to use them in response history analyses. These kind of analyses are carried out for the case study of the Farneto del Principe dam, by using an approach based on the finite difference method (FDM). For this scope we decided to use the commercial software FLAC 2D (Itasca, 2005), mainly because of its flexibility in modeling, and its capability in handling complex geometries.

In this chapter, the main features of the numerical model and several numerical analyses results, performed including as inputs the time histories selected in Chapter 4, are shown.

5.1 The FLAC 2-D Code Used for Numerical Simulations

The software FLAC 2D (the acronym FLAC 2D stands for 2-dimensional Fast Lagrangian Analysis of Continua) is an explicit finite difference program that performs a Lagrangian analysis. This software is specifically developed for geotechnical engineering applications. Materials are represented by elements which form a grid that can be adjusted by the user to fit the shape of the object to be modeled. Each element behaves, according to the prescribed stress or strain law, to the boundary condition and to the applied internal and/or external forces. FLAC provides tools for pre-processing and mesh creations, calculations and post-processing. It possible to use the user-friendly graphical interface (GUI) or its own command line programming language named FISH.

To ensure stability to the numerical scheme, the FLAC formulation is based on the solution of the dynamic equations of motion, even in static conditions. The general calculation sequence embodied in FLAC is illustrated in Figure 5.1. This procedure first invokes the equations of motion to derive new velocities and displacements from stresses and forces. Then, strain rates are derived from velocities, and new stresses from strain rates. FLAC takes one time-step for every cycle around the loop. Each box in Figure 5.1 updates all of its grid variables from known values that remain fixed while control is within the box. For example, the lower box takes the set of

velocities already calculated and, for each element, computes new stresses. The velocities are assumed to be frozen for the operation of the box (i.e., the newly calculated stresses do not affect the velocities). This may seem unreasonable because it is known that if a stress changes somewhere, it will influence its neighbors and change their velocities. However, choosing a time-step small enough that information cannot physically pass from one element to another in that interval. Since one loop of the cycle occupies one time-step, the assumption of "frozen" velocities is justified (neighboring elements really cannot affect one another during the period of calculation). Of course, after several cycles of the loop, disturbances can propagate across several elements, just as they would propagate physically.

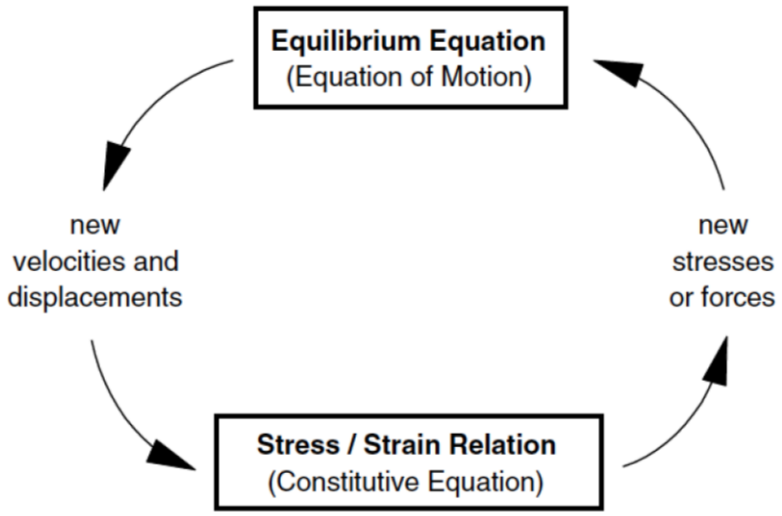

Figure 5.1 Basic calculation cycle used in FLAC 2D (from Itasca, 2005)

Since FLAC uses an explicit (Lagrangian) time-marching method to solve the algebraic equations, it worth to underline the main advantages (and disadvantages) of this approach. In an implicit method (commonly used in finite element programs), every element communicates with every other element during one solution step: several cycles of iteration are necessary before compatibility and equilibrium are obtained. The main advantages of the explicit approach are, according to Itasca (2005): (1) the small amount of computation effort per time step; (2) No significant numerical (spurious) damping is introduced for dynamic solution; (3) No iterations are necessary to follow nonlinear constitutive laws; (4) Matrices are never formed, so memory requirement are minimum; (5) As consequence of the previous point, large displacements and strains are accommodated without additional computing effort. The main disadvantage of the

explicit method is related the small time-step necessary to ensure the stability of the calculation, this means that large numbers of steps must be taken. Furthermore, explicit methods are not efficient for modeling linear, small-strain problems. Since it is not necessary to form a global stiffness matrix, it is a trivial matter to update coordinates at each time-step in large-strain mode. The incremental displacements are added to the coordinates so that the grid moves and deforms with the material it represents. This is termed a Lagrangian formulation.

The solid body to simulate in the numerical analysis is divided, taking advantage of the FLAC 2D pre-processing capabilities, into a finite difference mesh. The mesh is composed by quadrilateral elements (called zones in the FLAC 2D terminology) internally subdivided into two overlaid sets of constant-strain triangular elements, as shown in Figure 5.2. The use of triangular elements eliminates problems which may occur with the deformational patterns of constant-strain finite difference quadrilaterals. The four triangular sub-elements are termed *a*, *b*, *c*, *d* as shown in Figure 5.2(a). The force vector exerted on each node is taken to be the mean of the two force vectors exerted by the two overlaid quadrilaterals. In this way, the response of the composite element is symmetric, for symmetric loading. If one pair of triangles becomes badly distorted (e.g., if the area of one triangle becomes much smaller than the area of its companion), then the corresponding quadrilateral is not used; only nodal forces from the other (more reasonably shaped) quadrilateral are used.

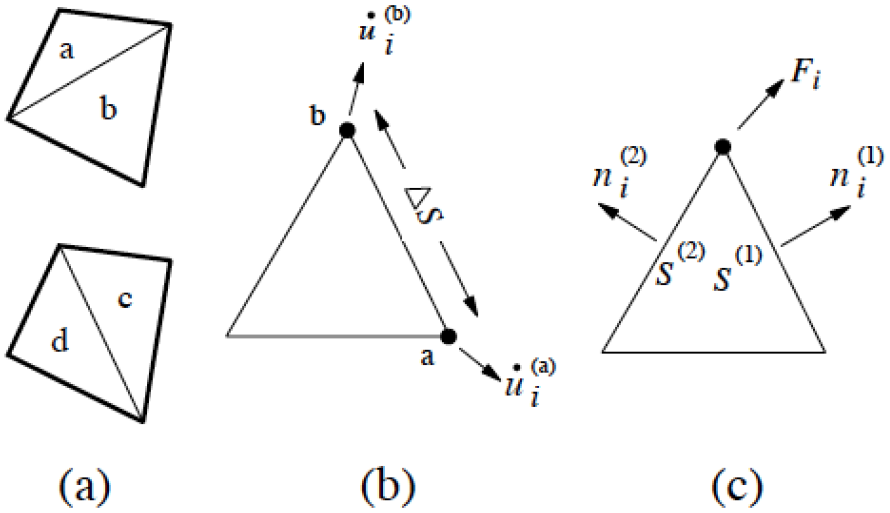

Figure 5.2 **(a) Overlaid quadrilateral elements; (b) Triangular elements with velocity vectors; (c) Nodal force vector. (From Itasca, 2005).**

One of the basic features of FLAC is the capability to model ground-water flow through permeable soils. The modeling of the flow may be done uncoupled (i.e. independent of the mechanical calculations) or it may be done in a coupled way, so as to capture the effects of fluid/solid interaction. According to the latter case, the fluid in a zone reacts to mechanically induced volume changes by a change in the pore pressure and changes in pore pressures induce changes in the effective stresses, thus affecting the response of the solid.

FLAC can calculate pore pressure effects, with or without pore pressure dissipation. The formulation of coupled fluid-deformation mechanisms in FLAC is based on the Biot theory of consolidation. Itasca (2005) provides further details on the implementation of this feature.

5.2 Numerical Model of the Farneto del Principe Dam

5.2.1 Dam Geometry, Mesh Discretization and Boundary Conditions Used in the Numerical Analyses

The model of the Farneto del Principe dam to use in the numerical analyses is presented in this section. As shown in §2.3 and §4.1, the cross section 4 (Figures 2.9, 2.10), is intended to be representative for the overall dam behavior. The hypothesis of plane-strain behavior of the dam is consistent and it is used to reduce the model into a 2D problem. Due to the longitudinal extension of the dam (1240 m as reported in Table 2.1) this hypothesis should ensure reliable results by using a relative small computation effort compared with three-dimensional models. In order to build a reliable numerical model, a critical issue is related to the dimension of the mesh elements (zones). Three main factors affected the choice: (1) the needs of modeling the geometric details of the dam (inspection tunnel, filters, cut-off wall); (2) the numerical accuracy of wave transmission; (3) an acceptable computational cost. Kuhlemeyer and Lysmer (1973), show that for accurate representation of wave transmission through a numerical model, the element (zone) size, Δl, must be smaller than approximately one-tenth of the wavelength associated with the highest frequency component of the input wave, λ (Equation 5.1).

$$\lambda < \frac{V_s}{f_{max}} \tag{5.1}$$

were V_S is the average shear wave velocity of the model and f_{max} the highest frequency component of the input wave. According to this approach, the maximum tolerable zone size Δl_{max} is given as:

$$\Delta l_{max} < \frac{V_s}{10 f_{max}} \tag{5.2}$$

For this study, using the lowest shear wave velocity of the model (V_S = 250 m/s for dam core materials) and the highest frequency of the selected inputs (f_{max} = 4.5 Hz), the maximum zone size (Δl_{max}) is equal to 5.5 m. This value is, however, too big to accomplish the modeling of some geometric detail of the dam. For this reason, the maximum dimension of the mesh zones was taken equal to 1.7 m for the dam foundation, and 0.7 m for the dam body (Figure 5.3b). Furthermore, in order to minimize potential numerical instability and to ensure accuracy to the solutions, we used a maximum aspect ratio (between width and height of the same zone) of 2.5 and triangular zones only where strictly needed (e.g. cut-off wall, inspection tunnel, filters). The mesh used in the analyses is shown in Figure 5.3a. The clay bed is not modeled, because the high V_S value that characterize this layer (as shown in §2.2) allows to consider it as a bed-rock. A rigid base approach (Itasca, 2005) was used to apply seismic motions in the dynamic phase. Accordingly, the acceleration time histories were specified for grid-points along the base of the mesh.

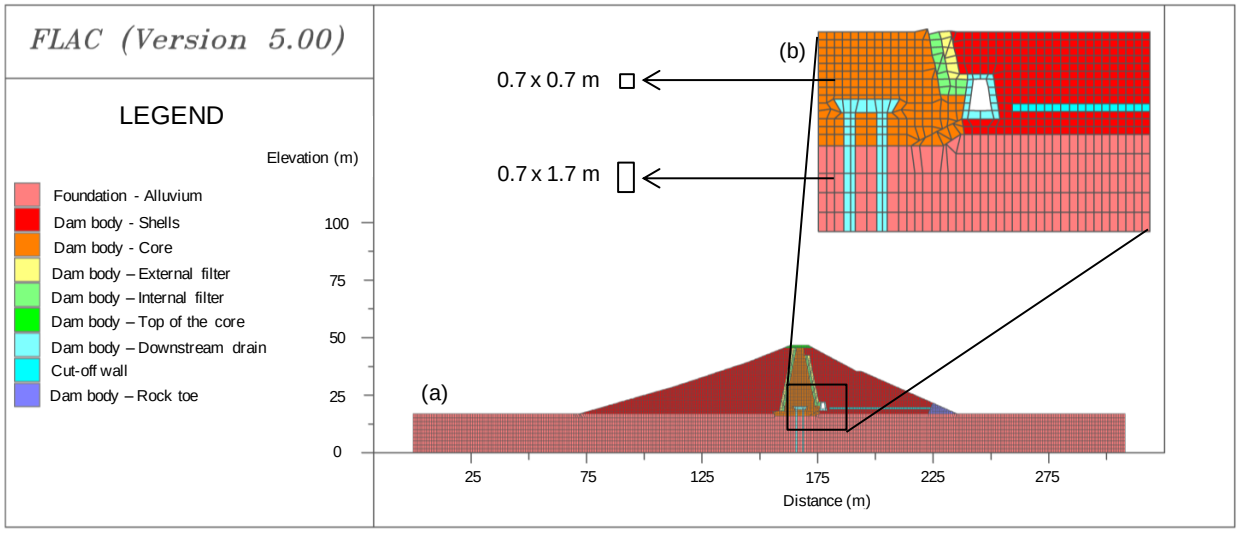

Figure 5.3 **(a) Mesh used for the numerical analyses; (b) Zoom of the mesh that shows the interface between dam body and foundation, the cut-off wall, the downstream filters and the inspection tunnel.**

The numerical analyses of the dam are conducted into two phases, the first one is the simulation of the current static conditions, the second one the application of the seismic input. FLAC 2D differentiates the boundary conditions for static and dynamic condition. In the static phase, the vertical displacements are restraints on lateral boundaries, while both horizontal and vertical displacements are fixed at the base of the model. Particular care was devoted to the evaluation of the extension of the lateral boundaries to use in the numerical model, taking into account that at a certain distance the motion must accomplish the free-field conditions. Several parametric analyses were carried out in order to find an optimal extension of the dam boundaries (L). We find, for the case study, that $L = H/2$, where H is the width of the dam. According to Seed et al. (1975), this extension can be sufficient for the scope, but, in order to avoid spurious wave reflection, we used, for the dynamic phase, the free-field boundaries (Itasca, 2005). These boundaries behave similarly to the viscous boundaries proposed by Lysmer and Kuhlemeyer (1969), moreover, they enforce the lateral sides to follow the free-field motion, reproducing a 1D response. The free-field scheme consists of a one-dimensional column of unit width, simulating the behavior of the extended medium. By using the free-field boundaries outward waves originating from the structure are properly absorbed. An overview of the dynamic boundary conditions used in the analyses is shown in Figure 5.4.

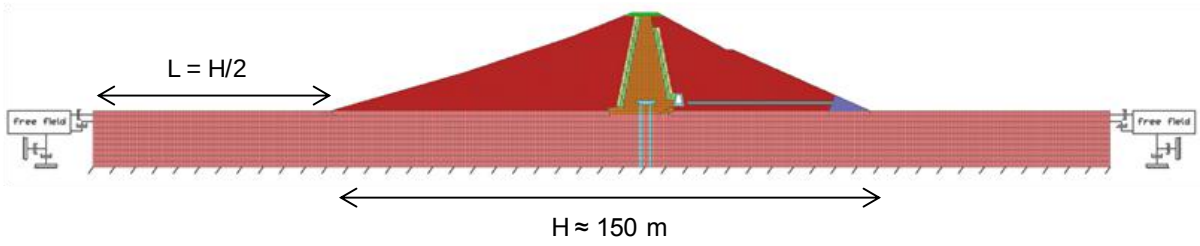

Figure 5.4 Boundary conditions used in the dynamic analyses.

5.2.2 Constitutive Models Used in the Analyses

Several materials are present in the model as shown in Figure 5.3. The structural elements (cut-off wall and inspection tunnel) were modeled as visco-elastic mediums. The foundation layer and the materials within the dam body were modeled using the Mohr-Coulomb failure criterion, associated with a hysteretic damping formulation (Itasca, 2005). In FLAC 2D the hysteretic damping formulation approximates non-linear soil behavior using a time-step-based computational scheme (Strenk, 2010). The modulus reduction and damping for each zone are

determined at each time-step for a single passage of the motion through the model. FLAC calculates the strain rate in each zone and, using the hysteretic damping algorithm, derives a shear modulus multiplier. Then this multiplier is passed to the constitutive model which adjust the shear modulus (G) of the zone being processed. The shear modulus reduction curve ($\frac{G}{G_{max}}, \gamma$, where G_{max} is the initial shear modulus and γ the strain ratio) needs to be fitted by using one of the available model present in FLAC 2D. This fitted curve defines the associated damping ratio (D) curve (i.e. damping equivalent to the area of the hysteresis loop).

The main purpose of the hysteretic damping is to provide a more efficient model for evaluating the material damping than Rayleigh formulation. Differently than the equivalent linear approach (that does not capable to model temporal variation of the shear modulus and of the damping), the hysteretic damping algorithm meets both spatial and temporal variations of G and D. As explained above, the modulus reduction curves must be fitted by continuous models built-in FLAC 2D. The associated damping curves often provide an overestimation at large strain levels. This effect is due to the non-stationary response of soils under cyclic loading (i.e. stress/strain depends on the number of cycles) which is captured by experiments, but it is not modeled by the FLAC algorithm.

For the dam body and the foundation materials there are not available experimental modulus reduction and damping curves. To overcome this issue, we used two unified modulus reduction and damping (MRD) relationships.

For the coarse materials (dam shells, foundation and filters) we used the Menq (2003) relationship. The modulus reduction curve is given as:

$$\frac{G(\gamma)}{G_{max}} = \frac{1}{1 + \left(\frac{\gamma}{\gamma_r}\right)^{\alpha}} \tag{5.3}$$

where

$$\alpha = 0.86 + 0.1 \cdot log\left(\frac{\sigma_0'}{p_a}\right) \tag{5.4}$$

$$\gamma_r(\%) = 0.12 \cdot C_u^{-0.6} \cdot \left(\frac{\sigma_0'}{p_a}\right)^{\phi_2} \tag{5.5}$$

$$\phi_2 = 0.5 \cdot C_u^{-0.15} \tag{5.6}$$

p_a is the atmospheric pressure, $C_u = D_{60}/D_{10}$ is the uniformity coefficient. The average value among the available grain size distribution curves of the shells and foundation material is C_u = 42.5. σ_0' is the mean effective stress. The damping curve is given as:

$$D(\gamma) = D_{min} + b \cdot D_M(\gamma) \cdot \left(\frac{G(\gamma)}{G_{max}}\right)^{0.1} \tag{5.7}$$

where

$$D_{min} = 0.55 \cdot C_u^{0.1} \cdot D_{50}^{-0.3} \cdot \left(\frac{\sigma_0'}{p_a}\right)^{-0.08} \tag{5.8}$$

$$b = 0.6329 - 0.0057 \cdot \ln(N) \tag{5.9}$$

$$D_M(\gamma) = c_1\left(D_{M,\alpha=1}\right) + c_2\left(D_{M,\alpha=1}\right)^2 + c_3\left(D_{M,\alpha=1}\right)^3 \tag{5.10}$$

$$c_1 = 0.2523 + 1.8618\alpha - 1.1143\alpha^2 \tag{5.11}$$

$$c_2 = -0..095 - 0.0710\alpha + 0.0805\alpha^2 \tag{5.12}$$

$$c_3 = 0.0003 + 0.0002\alpha - 0.0005\alpha^2 \tag{5.13}$$

$$D_{M,\alpha=1}(\gamma) = \frac{100}{\pi}\left[4\frac{\gamma - \gamma_r \ln\left(\frac{\gamma+\gamma_r}{\gamma_r}\right)}{\frac{\gamma^2}{\gamma+\gamma_r}} - 2\right] \tag{5.14}$$

D_{50} is the mean grain size. The average value among the available grain size distribution curves of the shells and foundation material is D_{50} = 10 mm (Figures 2.6 and 2.7).

For the core materials we used the Darendeli (2001) relationship. The modulus reduction curve is given as:

$$\frac{G(\gamma)}{G_{max}} = \frac{1}{1 + \left(\frac{\gamma}{\gamma_r}\right)^{0.92}} \tag{5.15}$$

$$\gamma_r(\%) = (0.0352 + 0.001 \cdot PI \cdot OCR^{0.3246})\left(\frac{\sigma_0'}{p_a}\right)^{0.3483} \tag{5.16}$$

For this case OCR = 2, all the other values were taken as the mean in Table 2.2. The damping curve is calculated using Equation 5.10.

To account for large strain problem with backbone hyperbolic curves, the Yee et al. (2013) hybrid procedure was applied to both the computed curves. This approach gives a correction for the modulus reduction curve above a reference strain level.

Four built-in model are available in the FLAC 2D library for fitting the modulus reduction curves. The sigmoidal model sig3 (Itasca, 2005) is used to fit the curves for the Farneto del Principe dam materials. In Figure 5.5 the modulus reduction curves derived by applying the two above described unified MRD relationships are shown together with the fitted ones (labeled as 'Numerical simulation') for two zones located in the middle of the core and in the middle of the downstream shell. In the same Figure, the damping curves obtained by using the MRD relationships are also compared with the corresponding curves obtained from the same FLAC 2D simulation (labeled as 'Numerical simulation').

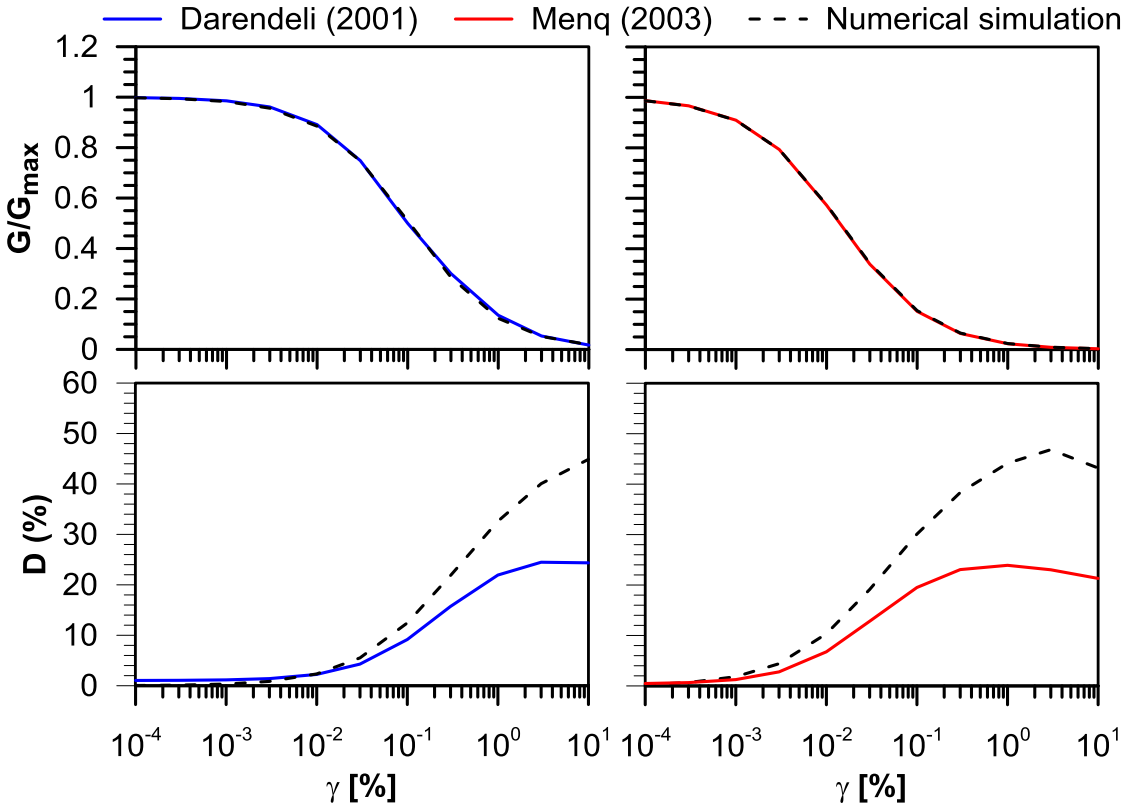

Figure 5.5 **Modulus reduction and damping curves for the Darendeli (2001) and Menq (2003) unified model versus the FLAC 2D numerical simulations for two zones within the dam core and downstream shell.**

To account for small strain level behavior, an additional amount of damping is added following the Rayleigh frequency-proportional damping formulation. This approach is based on

the assumption that the damping matrix (C) is obtained by summing a mass-proportional ([M]) and a stiffness-proportional ([K]) damping matrices.

$$[C] = \alpha[M] + \beta[K] \tag{5.17}$$

where α and β are the mass-proportional and the stiffness-proportional constants respectively. According to Bathe and Wilson (1976), for a multiple degree-of-freedom system, the critical damping ratio (ξ_i) at any angular frequency of the system (ω_i) is given as:

$$\xi_i = \frac{1}{2}\left(\frac{\alpha}{\omega_i} + \beta\omega_i\right) \tag{5.18}$$

By using a single control frequency ω_1, it is possible to derive the corresponding α and β values:

$$\alpha = \xi_1\omega_1 \tag{5.19}$$

$$\beta = \frac{\xi_1}{\omega_1} \tag{5.20}$$

where ξ_1 is the damping ratio correspondent to ω_1. Combining Equation 5.18 with Equations 5.19 and 5.20 it is straightforward to derive the damping ratio at any angular frequency as:

$$\xi_i = \frac{\xi_1}{2}\left(\frac{\omega_1}{\omega_i} + \frac{\omega_i}{\omega_1}\right) \tag{5.21}$$

Similarly, by using two control frequencies (ω_m and ω_n) and assigning to them the same value of the damping ratio (ξ_1) it is possible to obtain the corresponding ξ_i as:

$$\xi_i = \frac{2\xi_1}{\omega_m + \omega_n}\left(\frac{\omega_m\omega_n}{2\omega_i} + \frac{\omega_i}{2}\right) \tag{5.22}$$

The two control frequencies approach ensure a smaller variability of the damping, making it essentially frequency-independent for a bigger range. FLAC 2D does not allow to use the two control frequencies approach. In this study the α and β coefficient were chosen according to the two control frequencies approach (e.g. Lanzo et al., 2004). by reproducing the frequency-dependent damping with a single control frequency approach. The resulting damping ratio and circular frequency are given as:

$$\xi_i = \frac{\xi_{12}\sqrt{4\omega_m\omega_n}}{\omega_m + \omega_n} \tag{5.23}$$

$$\omega_i = \sqrt{\omega_m \omega_n} \tag{5.24}$$

where ξ_{12} is the equivalent two control frequency damping ratio (in this study ξ_{12} = 5%). Using as control frequencies the two circular frequencies correspondent to the first natural periods of the dam system (dam and foundation), *T1* and *T2* (§4.1), it is possible to obtain ξ_i = 4.75% and ω_i = 36.13 rad/sec, that corresponds to *T* = 0.17 sec.

The material parameters used in the FLAC 2D numerical analyses for the different zones of the dam are reported in Table 5.1. The shear modulus variation with depth is considered as shown in §4.1.

Table 5.1 Parameters used for the FLAC 2D numerical analyses of the Farneto del Principe dam

Parameter	Description	Core	Shells	Structural elements	Rock toe	Foundation
ρ (kg/m^3)	Density	1834	2447	2548	2447	2458
c (kPa)	Cohesion	80	0	Visco-elastic	0	0
φ (°)	Friction angle	18	40	Visco-elastic	42	37.5
G_{max} (kPa)	Initial shear modulus	1.15 x 10^5	Variable	7.21 x 10^6	1.62 x 10^6	1.04 x 10^6
ν	Poisson's ratio	0.35	0.33	0.2	0.33	0.33
K (m/sec)	Hydraulic conductivity	1.29 x 10^{-9}	1 x 10^{-5}	0	1.27 x 10^{-4}	1 x 10^{-5}

5.2.3 Numerical Analyses Results

Once the numerical model is set-up, it is possible to run the numerical analyses. In the first phase a static analysis is conducted in order to obtain the internal stress state precedent to the application of the dynamic inputs. The static analysis was carried out in several phases. According to the available data on the construction log, the construction sequences were simulated in six steps by using a gravity loading procedure, as shown in Figure 5.6. After that, the water level in the reservoir is raised until the maximum authorized level (136.3 m a.s.l.). For this water level, the steady state ground-water flow analysis was performed, by using the

hydraulic conductivities reported in Table 5.1 and shown in Figure 5.7. The last step of the static analysis is the simulation of the mechanical effects of the hydrostatic pressure induced by the reservoir level raised to the maximum authorized level.

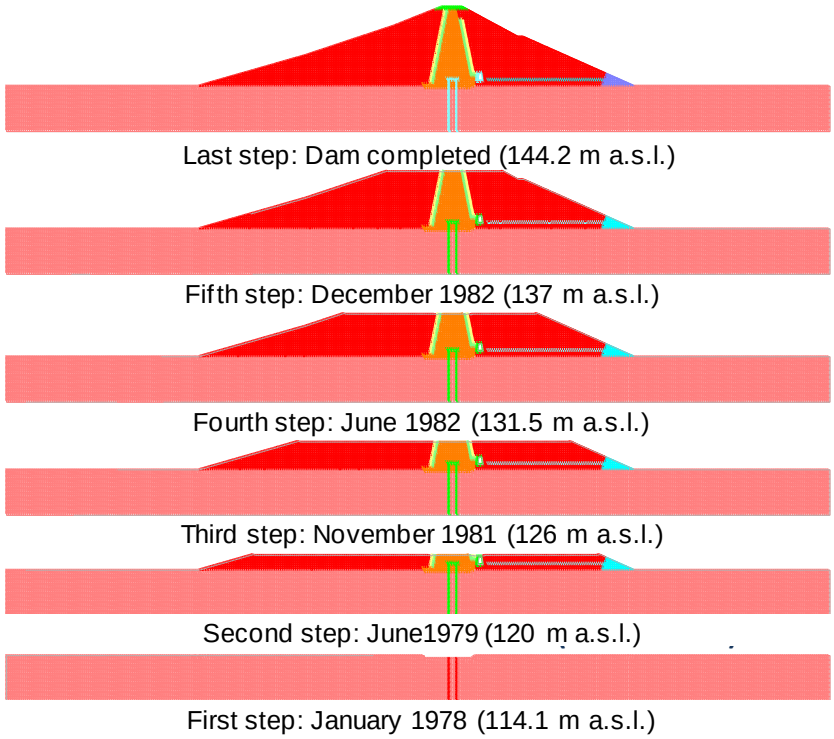

Figure 5.6 Construction phases used for the gravity loading analysis.

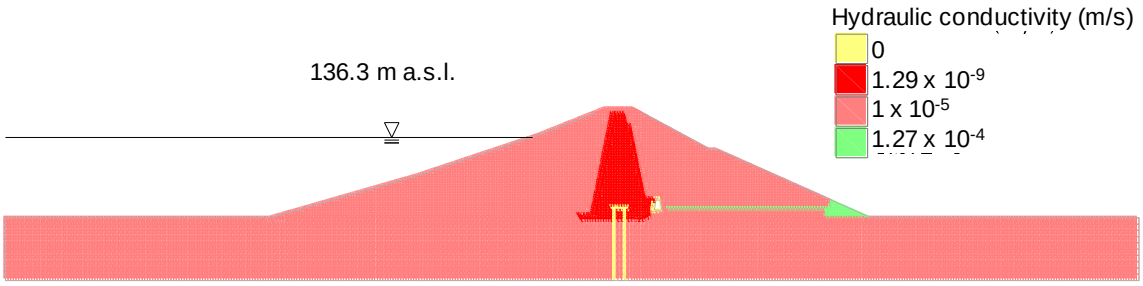

Figure 5.7 Hydraulic conductivities used for the steady-state ground water flow stage.

After the static phase it is possible to move on to the dynamic analyses by applying the acceleration time histories selected in chapter 4 (§4.3 for the UHS suite, §4.4 for the CS suite) to the grid zones at the base of the model (rigid base approach). In this analysis the hydrodynamic effects induced by the reservoir during the dynamic phase are neglected.

Several numerical analyses were carried out in this study. Even though for the Farneto del Principe dam there are not available experimental values of the dynamic characteristics of the

materials, the approach here used ensure a relative high reliability of the results, that, certainly, need to be refined by using *ad-hoc* shear moduli and MRD curves.

Typical results for both the suites of motions (UHS suite and CS suite) are shown in this section. The results in term of horizontal (a) and vertical (b) displacement contouring are shown in Figure 5.8 for the L'Aquila (2009) event (UHS suite) and in Figure 5.9 for the Whittier Narrows (1987) event (CS suite). Figures 5.8a and 5.9a show that the volumes of the critical sliding surfaces are comparable. In all the analyses for both suites (UHS and CS), the maximum horizontal displacements are located in the downstream shell, with the only exception of the Irpinia (1980) UHS event (Figure 5.10). This should be related to the higher inclination of the downstream shell and to the confining effect of the reservoir water on the upstream shell. The volumes interested by significant permanent vertical displacements are also comparable as shown in Figures 5.8b and 5.9b. The vertical displacements are always concentrated in the top part of the core in all the analyses carried out.

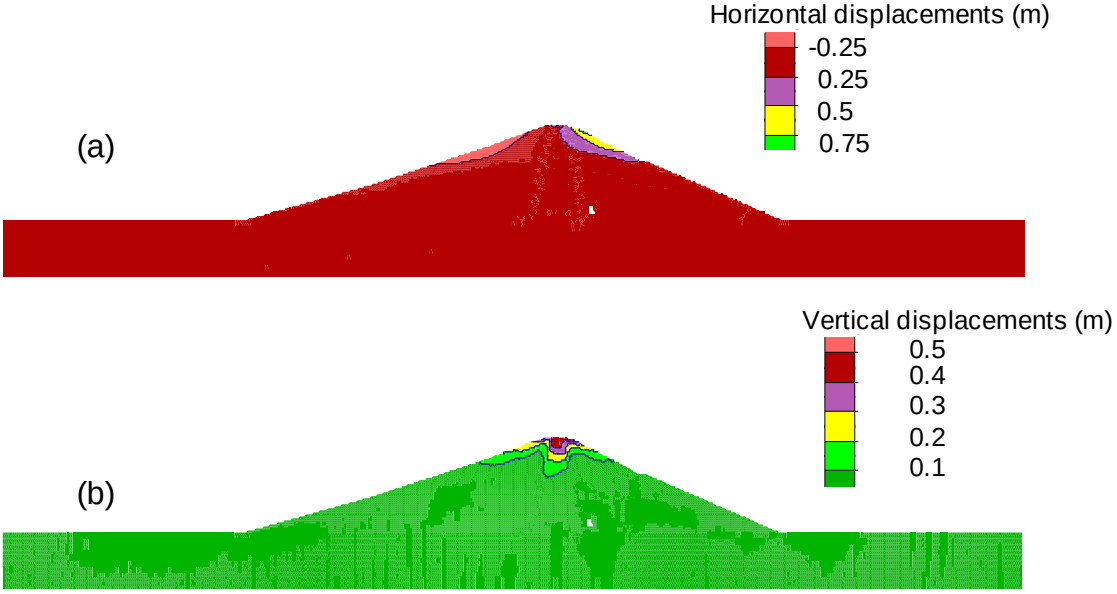

Figure 5.8 Horizontal and vertical displacements contouring for L'Aquila (2009), UHS suite.

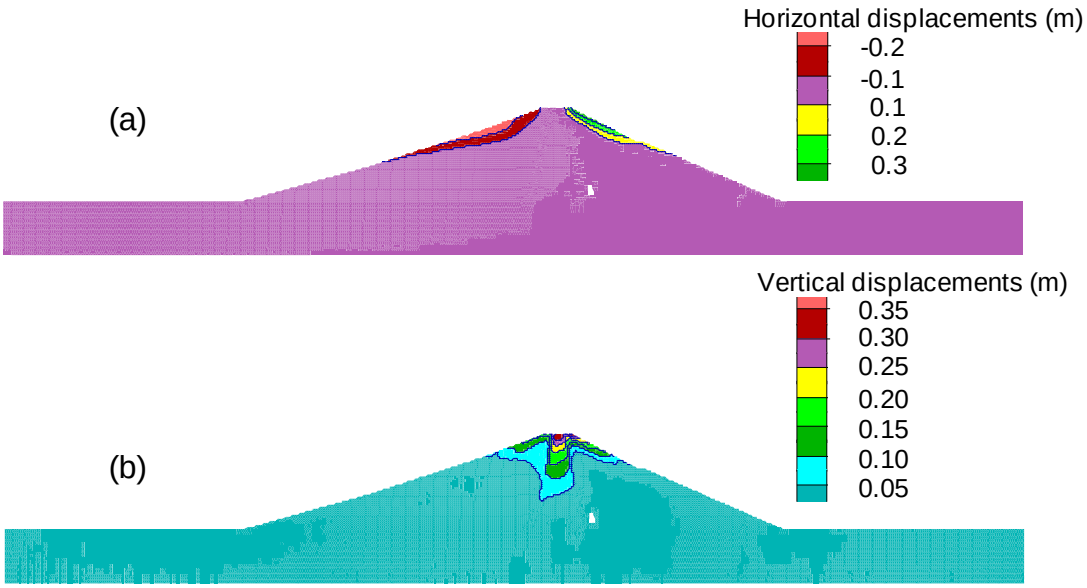

Figure 5.9 Horizontal and vertical displacements contouring for Whittier Narrows (1987), CS suite.

The worst case scenarios can be herein defined as the analyses that produced the maximum damages in term of relative displacements. In order to evaluate these conditions, results are conveniently reported in term of displacements relative to the base of the model: horizontal relative displacements ($u_{x,r}$) and vertical relative displacements ($u_{y,r}$).

For the UHS suite of motions the worst case scenario is represented by the Irpinia (1980) input. For this case, in Figure 5.10 the results in term of relative displacement time histories are shown for several control points. As is possible to notice the maximum values are very high, this can probably due to the particular frequency content of this input. As said before, in contrast with all the other analyses, in this case the maximum horizontal displacements are concentrated in the upstream shell.

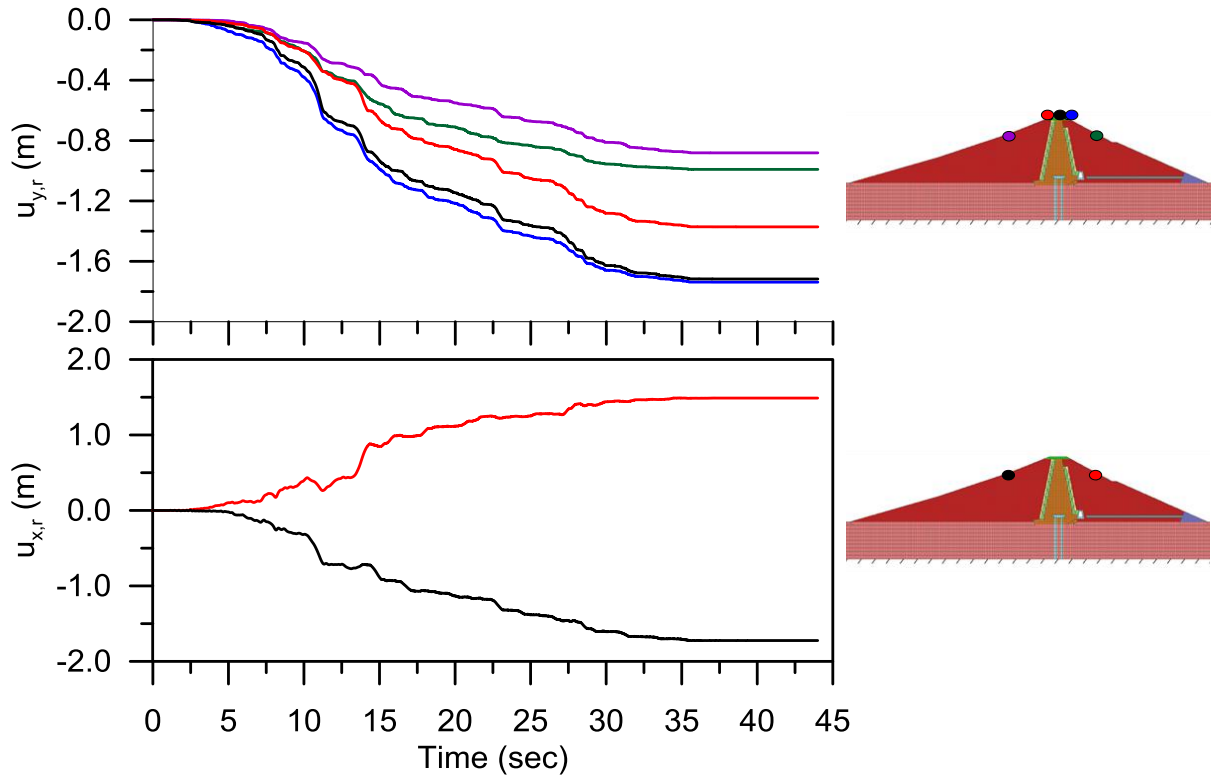

Figure 5.10 **Horizontal and vertical relative displacements for the worst case scenario of the UHS suite: Irpinia (1980).**

For the CS suite of motions the worst case scenario is represented by the Iwate (2008) input. In Figure 5.11 the results in term of relative displacements are shown for the same control points of Figure 5.10. The maximum displacement values are smaller than in the case of the UHS suite worst case scenario, this is a confirmation that using a UHS as target for input selection and scaling, the results are more conservative. The maximum horizontal displacements are concentrated in the downstream shell.

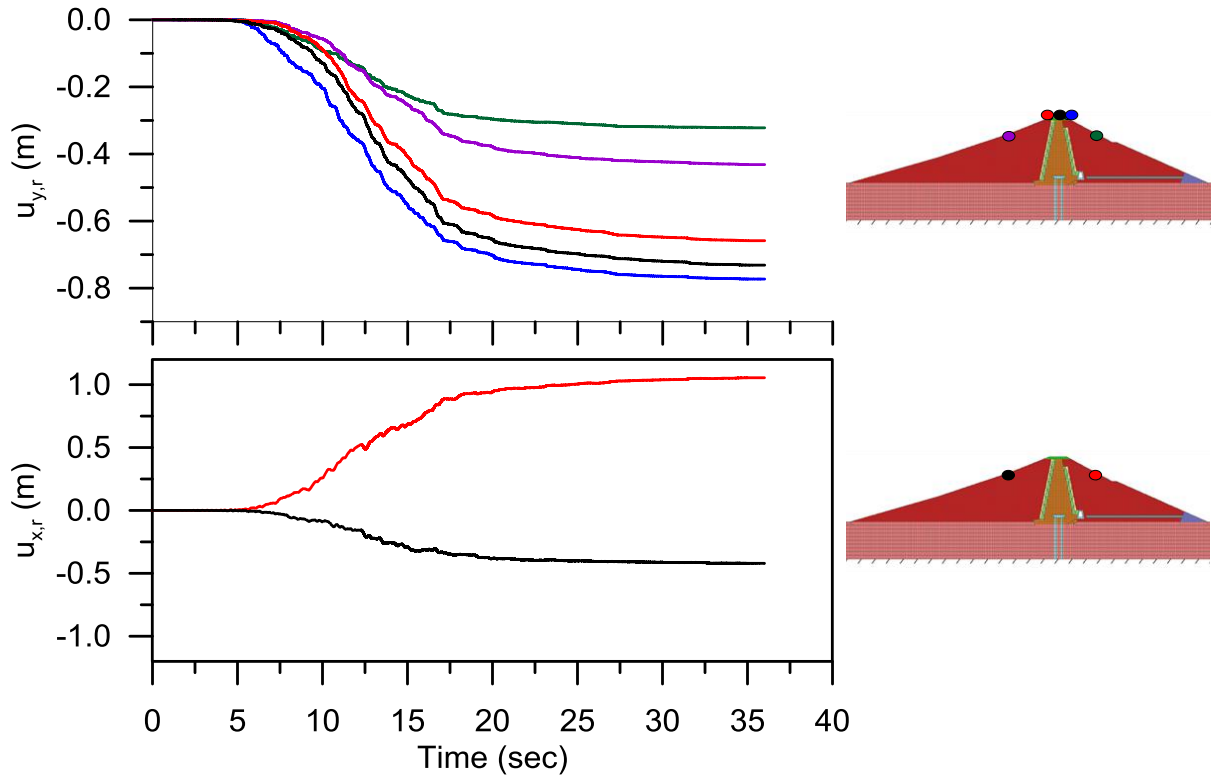

Figure 5.11 **Horizontal and vertical relative displacements for the worst case scenario of the CS suite: Iwate (2008).**

In Table 5.2 an overview of the main results obtained for the UHS suite of motions is given.

Table 5.2 **Main results of the numerical analyses for the UHS suite of motions**

Earthquake name	Year	Mechanism	M	R_{jb}	SF	$u_{x,r}$ (m)	$u_{y,r}$ (m)
Irpinia (IT)	1980	Normal	6.9	17.51	8.6	-1.72	1.74
Loma Prieta (CA)	1989	Reverse oblique	6.93	8.84	1.9	0.44	0.27
Tottori (JP)	2000	Strike-slip	6.61	15.58	5.3	0.77	0.59
Parkfield (CA)	2004	Strike-slip	6	4.66	4.2	0.28	0.23
L'Aquila (IT)	2009	Normal	6.3	0	1.8	0.76	0.58
Iwate (JP)	2008	Reverse	6.9	16.26	2.7	0.98	0.74
Duzce (TU)	1999	Strike-slip	7.14	4.21	1.4	0.84	0.51

The average values for the suite are: $\bar{u}_{x,r} \cong 0.82$ m; $\bar{u}_{y,r} \cong 0.66$ m. The maximum values are calculated for the Irpinia (2008) input. For $u_{x,r}$, the negative values are intended for the upstream

shell, while the positive for downstream shell displacements. The $u_{x,r}$ displacements are reported as absolute values.

In Table 5.3 an overview of the main results obtained for the UHS suite of motions is given.

Table 5.3 Main results of the numerical analyses for the CS suite of motions

Earthquake name	Year	Mechanism	M	R_{jb}	*SF*	$u_{x,r}$ *(m)*	$u_{y,r}$ *(m)*
Whittier Narrows (CA)	1987	Reverse oblique	5.99	6.78	7.12	0.36	0.37
Loma Prieta (CA)	1989	Reverse oblique	6.93	8.84	1.65	0.38	0.23
Tottori (JP)	2000	Strike-slip	6.61	15.58	2.53	0.39	0.30
Parkfield (CA)	2004	Strike-slip	6	4.66	3.05	0.21	0.16
L'Aquila (IT)	2009	Normal	6.3	0	1.88	0.78	0.61
Iwate (JP)	2008	Reverse	6.9	16.26	3.13	1.05	0.77
Duzce (TU)	1999	Strike-slip	7.14	4.21	0.7	0.56	0.21

The average values for the suite are: $\bar{u}_{x,r} \cong 0.53$ m; $\bar{u}_{y,r} \cong 0.38$ m. The maximum values are obtained for the Iwate (2008) input.

It is possible to notice that under these excitations the dam show a relative good performance, considering that these motions were selected and scaled to be consistent with target spectra derived for a very long return period (T_R = 2475 year). This hazard level represents for large relevant dams, such as the Farneto del Principe dam, "*the collapse limit state performance level*" according to the Italian code for dam design and safety (Decreto Ministeriale, D.M. June 14, 2014). Using as damage measures the freeboard loss and the filter thickness, in both cases, even for the worst case scenario the collapse of the structure should not occur. The freeboard is almost 8 m. The maximum tolerable displacement that is represented by the thickness of a filter is 2 m. These considerations, allow to conclude that the Farneto del Principe dam exhibit a good seismic response. Again it worth to underline that further refinement are needed to account for *ad-hoc* dynamic characteristics of the materials.

6 Conclusion

In this study the seismic response of the Farneto del Principe dam, in the Calabria region (southern Italy) by using hazard-consistent and site-specific ground motions was presented.

The current behavior under static conditions, taking into account the ground-water flow within the dam body, and using several measurements and data available from its monitoring system was investigated. After the evaluation of the static conditions, the dynamic response was considered, evaluating the demands to which it can reasonably be expected to be subjected in future earthquake events. Improvements in earthquake rupture forecast models and ground motion prediction equations currently used in Italy were performed. A site-specific probabilistic seismic hazard analysis (PSHA) for the Farneto del Principe dam site was developed. In this analysis we included two seismogenic sources (Lakes fault and subduction interface of the Calabrian) neglected in the currently used Italian models and we developed a modern ground motion prediction equation logic tree that includes a recent global model (BSSA, 2014) specifically implemented in an open source PSHA software (Openquake). A series of sensitivity studies and comparisons in term of hazard curves and uniform hazard spectra (UHS) are also presented.

The results of the PSHA were used to define two target spectra: a UHS and a scenario spectrum (Conditional Spectrum, CS). The target spectra were used for selecting and scaling appropriate acceleration time series suites. A modal analysis was also presented herein, by numerically solving the eigenvalue problem with a finite element method software (SAP 2000). The computation of the CS and the time series suites selection was based on the natural periods and mode shapes of the dam system (taking into account the deformable foundation). The reliability of the response history analysis is ensured by the rigorous procedure used to evaluate the acceleration time-histories and by the proper numerical method used to define the seismic response of the dam. For this scope a finite difference code specifically derived for geotechnical

earthquake engineering applications (FLAC 2D) was used. Typical results of the seismic response of the Farneto del Principe dam to these hazard-consistent ground motion suites were also presented and commented.

References

Abrahamson N.A. and Al Atik L. (2010) Scenario Spectra for Design Ground Motions and Risk Calculation, 9th US National and 10th Canadian Conference on Earthquake.

Aki, K. and P.G. Richards (2002) Quantitative Seismology, University Science Books, Sausalito, CA.

Akkar S., Bommer J. J. (2010) Empirical equations for the prediction of PGA, PGV and spectra accelerations in Europe, the Mediterranean region and the Middle East, Seism. Res. Ltrs, 81:2, 195-206.

Ambraseys N.N. (1959) A note on the response of an elastic overburden of varying rigidity to an arbitrary ground motion, Bull Seism Soc Am; 49(3):211-220.

Ambraseys, N. N., K. A. Simpson, and J. J. Bommer (1996) Prediction of horizontal response spectra in Europe, Earthq. Eng. Struct. Dynam. 25, 371–400.

Anderson H.A., Jackson J.A. (1987) The deep seismicity of the Tyrrhenian Sea, Geophys J R Astron Soc ; 91:613-637.

Anderson, J. G., and Luco, J. E. (1983) Consequences of slip rate constraints on earthquake recurrence relations. Bull. Seis. Soc. Am. 73(2) 471 – 496.

Angelica C., Bonforte A., Distefano G., Serpelloni E., Gresta S. (2013) Seismic potential in Italy from integration and comparison of seismic and geodetic strain rates, Tectonophysics 608 996–1006.

Atkinson G. M. and Boore D. M. (2003) Empirical ground-motion relations for subduction zone earthquakes and their application to Cascadia and other regions. Bulletin of the Seismological Society of America, 93(4):1703-1729.

Baker J.W. (2011) "Conditional Mean Spectrum: Tool for ground motion selection, Journal of Structural Engineering, 137(3), 322-331.

Baker J.W. and Cornell C.A. (2006) Spectral shape, epsilon and record selection, Earthquake Engineering & Structural Dynamics, 35(9), 1077-1095.

Baker J.W., and Jayaram N. (2008) Correlation of spectral acceleration values from NGA ground motion models, Earthquake Spectra, 24(1), 299-317.

Baker, J.W., and Cornell, C.A. (2003) Uncertainty Specification and Propagation for Loss Estimation Using FOSM Methods, PEER Rpt 2003/07. Pacific Earthquake Engineering Research Center, Berkeley, CA.

Basili R Kastelic V Valensise G DISS Working Group 2009 (2009) DISS3 tutorial series: Guidelines for compiling records of the Database of Individual Seismogenic Sources, version 3. Rapporti Tecnici INGV, 108, 20 p

Basili, R., G. Valensise, P. Vannoli, P. Burrato, U. Fracassi, S. Mariano, M. M. Tiberti, and E. Boschi (2008) The Database of Individual Seismogenic Sources (DISS), version 3: Summarizing 20 years of research on Italy's earthquake geology. Tectonophysics, 453, 20–43.

Bathe K.J. and Wilson E.L. (1976) Numerical Methods in Finite Element Analysis. Englewood Cliffs, New Jersey: Prentice-Hall Inc.

Bazzurro P., Cornell C.A. (1999) Disaggregation of seismic hazard. Bull. Seis. Soc. Am. 89, 501-520.

Bazzurro, P. and Cornell C.A. (1999) Disaggregation of Seismic Hazard, Bulletin of the Seismological Society of America 89.2, pages 501–520.

Bindi D. Pacor F. Luzi L. Puglia R. Massa M. Ameri G. and Paolucci R. (2011) Ground motion prediction equations derived from the Italian strong motion database, Bulletin of Earthquake Engineering, 9:1899-1920, 2011. doi: 10.1007/s10518-011-9313-z.

Bishop A.W. and Height D.W. (1977) The value of Poisson's ratio in saturated soils and rocks stressed under undrained conditions, Geotechnique 27, 369-384.

Bommer J. J., Douglas J. and Strasser F. O. (2003) Style-of-faulting in ground-motion prediction equations, Bull. Earthq. Eng. 1, 171–203.

Bommer J.J., Acevedo A.B. (2004) The use of real earthquake accelerograms as input to dynamic analysis, Journal of Earthquake Engineering, 8, special issue 1: 43-91.

Bommer J.J., Scott S.G., Sarma S.K.. (2000) Hazard-consistent earthquake scenarios, Soil Dynamics and Earthquake Engineering;19:219–31.

Bonazzi D. (1991) La maintenance du savoir sur les ouvrage en exploitation: l'expérience internationale d'un ingénieur. Conseil. XVII ICOLD, vol. V, Q 65, R23.

Bonazzi D. (1991) La maintenance du savoir sur les ouvrage en exploitation: l'expérience internationale d'un ingénieur. Conseil, XVII ICOLD, vol. V, Q 65, R23.

Boore D. M., Stewart J. P., Seyhan E., and Atkinson G. M.. (2014) NGA-West 2 equations for predicting PGA, PGV, and 5%-damped PSA for shallow crustal earthquakes, Earthquake Spectra, 30(3):1057-1085. doi: 10.1193/070113EQS184M.

Bozorgnia Y. et al. (2014) NGA-West2 Research Project, Earthquake Spectra Aug 2014, Vol. 30, No. 3 pp. 973-987.

Brozzetti F., Cirillo D., Liberi F., Faraca E., Piluso E. (2012) The Crati Valley Extensional System: field and subsurface evidences, Rend. Online Soc. Geol. It., Vol. 21, pp. 159-161.

Bungum H. (2007) Numerical modelling of fault activities, Computers & Geosciences 33 808–820.

Butler L., Crowley Henshaw P., Monelli D. Nastasi M., Panseri L. Pagani M. Silva V., Simionato M., Viganò D., Weatherill G., Wiss B. (2014) OPENQUAKE ENGINE: users instruction manual V.1.0.0.

Calais E., C. DeMets and J. M. Nocquet (2003), Evidence for a post-3.16 Ma change in Nubia-Eurasia plate motion, Earth Planet. Sci. Lett., 216, 81– 92, doi:10.1016/S0012821X(03)00482-5.

Carlton B. and Abrahamson N. (2014) Issues and Approaches for Implementing Conditional Mean Spectra in Practice, Bulletin of the Seismological Society of America, Vol. 104, No. 1.

Carobene L.,Damiani A.V. (1985) Tettonica e sedimentazione pleistocenica nella media valle del fiume Crati. Area tra il torrente Pescara ed il fiume Mucone (Calabria). Bollettino della Società Geologica Italiana 104,115–127. In Italian.

Casagrande A. (1961) Control of Seepage through Foundations and Abutments of Dams, Géotechnique, Volume 11, Issue 3.

Cauzzi C. and Faccioli E. (2008) Broadband (0:05 to 20 s) prediction of displacement response spectra based on worldwide digital records, Journal of Seismology, 12(4):453-475, doi: 10.1007/s10950-008-9098-y.

Chiarabba C., Jovane L., DiStefano R. (2005) A new view of Italian seismicity using 20 years of instrumental recordings, Tectonophysics 395 (2005) 251– 268.

Chiou B. S.-J., and Youngs R. R. (2008a) An NGA model for the average horizontal component of peak ground motion and response spectra, Earthquake Spectra 24, 173–216.

Chiou B. S.-J., and Youngs R. R., (2008b) NGA model for the average horizontal component of peak ground motion and response spectra, PEER Report No. 2008/09, Pacific Earthquake Engineering Research Center, University of California, Berkeley.

Chiou B. S.-J., R. Darragh N. Gregor and W. Silva (2008) NGA Project Strong-Motion Database. Earthquake Spectra 24, 23-44.

Cornell C.A. (1968) Engineering Seismic Risk Analysis, Bulletin of the Seismological Society of America, 58(5):1583-1606.

CPTI Working Group (1999) Catalogo Parametrico dei Terremoti Italiani, versione 1 (CPTI99), INGV, Milano. Available at http://emidius.mi.ingv.it/CPTI99/ (last accessed December 2014), (in Italian).

CPTI Working Group (2004) Catalogo Parametrico dei Terremoti Italiani, version 2004 (CPTI04), INGV, Milano. Available at http://emidius.mi.ingv.it/CPTI04/ (last accessed December 2014), (in Italian).

CSI (2013), CSI Analysis Reference Manual for SAP2000, ETABS and SAFE, Computers and Structures, Inc., Berkeley, CA, USA.

D'Agostino N., Avallone A., Cheloni D., D'Anastasio E., Mantenuto S. and Selvaggi G. (2008) Active tectonics of the Adriatic region from GPS and earthquake slip vectors. J. Geophys. Res. 113, B12413. doi:10.1029/2008JB005860.

D'Agostino N., E. D'Anastasio A. Gervasi I. Guerra M. R. Nedimovic L. Seeber and M. Steckler (2011) Forearc extension and slow rollback of the Calabrian Arc from GPS measurements, Geophys. Res. Lett., 38, L17304, doi:10.1029/2011GL048270.

Dakoulas P., Gazetas G. (1985) A class of inhomogeneous shear models for seismic response of dams and embankments, Soil Dynamics and Earthquake Engineering, Vol. 4, No. 4.

Danciu L, Woessner J, Giardini D and SHARE Consortium (2013) A community-based Probabilistic Seismic Hazard Maps for the Euro- Mediterranean Region. Congress on Recent Advances in Earthquake Engineering and Structural Dynamics, Vienna, Austria

Darendeli M.B. (2001) Development of a New Family of Normalized Modulus Reduction and Material Damping Curves. Ph.D. dissertation, presented to the Faculty of the Graduate School of The University of Texas at Austin.

De Natale, G., E. Faccioli, and A. Zollo (1988) Scaling of peak ground motion from digital recordings of small earthquakes at Campi Flegrei, southern Italy, Pure Appl. Geophys. 128, 37–53.

de Voogd B., C. Truffert N. Chamot-Rooke P. Huchon S. Lallemant and X. Le Pichon (1992), Two-ship deep seismic soundings in the basins of the eastern Mediterranean Sea (Pasiphae cruise), Geophys. J. Int., 109,536–552, doi:10.1111/j.1365-246X.1992.tb00116.x.

Decreto Ministeriale, D.M. June 14 (2014) Norme tecniche per la progettazione e la costruzione degli sbarramenti di ritenuta (dighe e traverse). In Italian.

Delavaud, E., F Cotton, S. Akkar , F. Scherbaum, L. Danciu, C. Beauval, S. Drouet, J. Douglas, R. Basili, M. A. Sandikkaya, M. Segou, E. Faccioli , N. Theodoulidis (2012), Toward a Ground-Motion Logic Tree for Probabilistic Seismic Hazard Assessment in Europe, J. Seis.

Devoti R., F. Riguzzi, M. Cuffaro and C. Doglioni (2008), New GPS constraints on the kinematics of the Apennines subduction, Earth Planet. Sci. Lett. 273, 163-174.

Dobry R., Whitman R. and Roesset J.M. (1971) Soil properties and the one dimensional theory of earthquake amplification, Research Report, R71-18, M.I.T.

Douglas J. (2014) Ground motion prediction equations 1964 – 2014, Website http://www.gmpe.org.uk. (last accessed January 2015).

Faccenna C., C. Piromallo A. Crespo-Blanc L. Jolivet and F. Rossetti (2004), Lateral slab deformation and the origin of the western Mediterranean arcs, Tectonics, 23, TC1012, doi:10.1029/2002TC001488.

Faccenna C., F. Funiciello D. Giardini and P. Lucente (2001) Episodic back-arc extension during restricted mantle convection in the central Mediterranean, Earth Planet. Sci. Lett., 187, 105–116, doi:10.1016/S0012-821X(01)00280-1.

Faccioli E., Bianchini A., and Villani M. (2010) New ground motion prediction equations for T > 1 s and their inuence on seismic hazard assessment. In Proceedings of the University of Tokyo Symposium on Long-Period Ground Motion and Urban Disaster Mitigation, Mar 2010.

Federal Guidelines for Dam Safety (2005) Earthquake Analyses and Design of Dams, FEMA 65.

Field, E. H., T. H. Jordan, and C. A. Cornell (2003). “OpenSHA - A developing Community-Modeling Environment for Seismic Hazard Analysis”. In: Seism. Res. Lett. 74, pages 406–419.

Foster M, Fell R, Spannagle M. (2000) The statistics of embankment dam failures and accidents, Canadian Geotechnical Journal. 37, pp. 1000-1024.

Foster M., Fell R., Spannagle M. (2000) The statistics of embankment dam failures and accidents. Canadian Geotechnical Journal, 2000, 37(5): 1000-1024, 10.1139/t00-030

Franklin A. G., Chang F. K. (1977) Earthquake resistance of earth and rock-fill dams: permanent displacements of earth embankments by Newmark sliding block analysis. US Army Engineer Waterways Experiment Station, CE, Vicksburg. Miscellaneous Paper S-71-17, Report 5

Galli P., Bosi V., (2003) - Catastrophic 1638 earthquakes in Calabria (southern Italy). New insight from paleoseismological investigation. J. Geophys. Res., 108, B1, doi: 10.1029/2002JB01713.

Galli P., Scionti V., Spina V., (2004) New paleoseismic data from the Lakes and Serre faults (Calabria), GNGTS – Atti del 23° Convegno Nazionale / 07.06. In Italian.

Galli P., Scionti V., Spina V., (2007) New paleoseismic data from the Lakes and Serre faults: seismotectonic implications for Calabria (Southern Italy), Boll. Soc. Geol. It. (Ital.J.Geosci.), Vol. 126, No. 2 (2007), pp. 347-364.

Gasperini, P., R. Camassi, C. Mirto, M. Stucchi, R. Azzaro, F. Bernardini, F. Chiarabba, E. Ercolani, I. Leschiutta, C. Meletti, and G. Selvaggi (2004) Catalogo dei terremoti CPTI2. App.1, Rapporto conclusivo della redazione della mappa di pericolosità sismica prevista dall'Ordinanza PCM 3274 del 20 marzo 2003, available at http://zonesismiche.mi.ingv.it (last accessed January 2014), 29 pp. In Italian.

Gazetas G. (1982) Vibrational characteristics of soil deposits with variable wave velocity, International J Num Anal Meth Geomech; 6:1-20.

Gazetas G., Debchaudhury A., and Gasparini D.A. (1981) Random vibration analysis for the seismic response of earth dams, Geotechnique 31, No. 2, 261-277.

Giardini D., J. Woessner, L. Danciu, H. Crowley, F. Cotton, G. Grünthal, R. Pinho, G. Valensise, S. Akkar, R. Arvidsson, R. Basili, T. Cameelbeeck, A. Campos-Costa, J. Douglas, M. B. Demircioglu, M. Erdik, J. Fonseca, B. Glavatovic, C. Lindholm, K. Makropoulos, C. Meletti, R. Musson, K. Pitilakis, K. Sesetyan, D. Stromeyer, M. Stucchi, A. Rovida, (2013) Seismic Hazard Harmonization in Europe (SHARE): Online Data Resource, doi: 10.12686/SED-00000001-SHARE, 2013.

Giardini D., Velona` M., (1991) Deep siesmicity of the Tyrrhenian Sea, Terra Nova 3:57–64.

Grünthal G., Wahlström R., Stromeyer D. (2013) The SHARE European Earthquake Catalogue (SHEEC) for the time period 1900–2006 and its comparison to the European-Mediterranean Earthquake Catalogue (EMEC). Journal of Seismology, 17, 4, 1339-1344

Gutscher M., Roger J., Baptista M., Miranda J., Tinti S. (2006) Source of the 1693 Catania earthquake and tsunami (southern Italy): new evidence from tsunami modeling of a locked subduction fault plane, Geophys. Res. Lett.33 (8). http://dx.doi.org/10.1029/2005GL025442.

Gvirtzman Z., Nur A. (2001) Residual topography, lithospheric thickness, and sunken slabs in the central Mediterranean, Earth and Planetary Science Letters 187: 117-130.

Hanks, T. C., and W. H. Bakun (2002) A bilinear source-scaling model for M - log A observations of continental earthquakes, Bull. Seismol. Soc. Am. 92, no. 5, 1841–1846.

Hanks, T. C., and W. H. Bakun (2008) M - log A Observations for recent large earthquakes, Bull. Seismol. Soc. Am. 98, no. 1, 490–494.

Hardin B.O. and Drnevich V.P. (1972) Shear modulus and damping in soils: Measurement and parameter effects, Terzaghi Lecture, J. Soil Mech. Found. Div., 98~6!, 603–624.

Haselton C.B. and Baker J.W. (2006) Ground motions intensity measures for collapse capacity prediction: choice of optimal spectral period and effect of spectral shape, Paper orally presented at 8NCEE, San Francisco, California, April 2006.

Haselton C.B., Fry A., Baker J.W., Hamburger R.O., Whittaker A.S., Stewart J.P., Elwood K.J., Luco N., Hooper J.D., Charney F.A., Zimmerman R.B., and R.G. Pekelnicky (2014) Response-History Analysis for the Design of New Buildings: A Fully Revised Chapter 16 Methodology Proposed for the 2015 NEHRP Provisions and the ASCE/SEI 7-16 Standard, Tenth U.S. National Conference on Earthquake Engineering Frontiers of Earthquake Engineering July 21-25, 2014 10NCEE Anchorage, Alaska.

Hiemer S. Woessner J. Basili R. Danciu L. Giardini D. and Wiemer S. (2014) A smoothed stochastic earthquake rate model considering seismicity and fault moment release for Europe. Geophys. J. Int. (2014) 198, 1159–1172

Hiemer S., Jackson D. Qi Wang, Yan Y. Kagan, Woessner J. Zechar J. and Wiemer S. (2013) A Stochastic Forecast of California Earthquakes Based on Fault Slip and Smoothed Seismicity. Bulletin of the Seismological Society of America, Vol. 103, No. 2A, pp. 799–810, April 2013, doi: 10.1785/0120120168

Hynes-Griffin M. E., Franklin A. G. (1984) Rationalizing the seismic coefficient method. U.S. Army corps of engineers, Waterways experiment station, Vicksburg, Mississipi, Miscellaneous paper GL-84-13

Ishihara K. (2010) Performances of Rockfill Dams during Recent Earthquakes, In Proc., 5th Int. conf., Recent Advances in Geotechnical Engg. And soil Dynamics. Paper #IMI 5.

Itasca (2005) - FLAC – Fast Lagrangian Analysis of Continua – Version 5.0. User's Guide, Itasca Consulting Group, Minneapolis, USA.

ITASCA (2005) FLAC – Fast Lagrangian Analysis of Continua – Version 5.0. User's Guide, Itasca Consulting Group, Minneapolis, USA.

Jacobsen L.S. (1930) Motion of a soil subjected to a simple harmonic ground vibration, Bull. Seism. Soc. Am., 20, pp. 160-195.

Jappelli R. (2003) Le costruzioni geotecniche per le grandi dighe in Italia, Terza conferenza "Arrigo Croce". Rivista Italiana di Geotecnica, vol. III, 17-78. In Italian

Jappelli R. (2003) Le costruzioni geotecniche per le grandi dighe in Italia, Terza conferenza "Arrigo Croce", Rivista Italiana di Geotecnica, vol. 3/2003, pp. 17-78. In Italian

Jappelli R. Pellegrino A. et al. (1981) Materiali per la costruzione di dighe di terra e di pietrame in Italia. Quad. 2, Sottoc. Materiali del C.I.G.D., Milano. In Italian.

Jayaram N., Lin T., and Baker J.W. (2011) A computationally efficient ground-motion selection algorithm for matching a target response spectrum mean and variance Earthquake Spectra, 27(3), 797-815.

Joyner W. B. and D. M. Boore (1981) Peak horizontal acceleration and velocity from strong motion records including records from the 1979 Imperial Valley, California, earthquake, Bull. Seism. Soc. Am. 71, 2011-2038.

Kagan, Y. Y. (2002). Seismic moment distribution revisited: I. Statistical Results. Geophysical Journal International. 148. 520 – 541

Kaklamanos J., Baise L.G. Boore D.M. (2011) Estimating Unknown Input Parameters when Implementing the NGA Ground-Motion Prediction Equations in Engineering Practice, Earthquake Spectra, Volume 27, No. 4, pages 1219–1235.

Kramer S.L., Arduino P., Sideras S.S. (2012) Earthquake Ground Motion Selection, Research Report prepared for The State of Washington Department of Transportation.

Kuhlemeyer R.L., Lysmer J. (1973) Finite Element Method accuracy for wave propagation problems, Journal of Soil Mechanics & Foundations Division, ASCE, 99(SM5): 421-427.

Lanzo G., Pagliaroli A., D'Elia B. (2004) Influenza della modellazione di Rayleigh dello smorzamento viscoso nelle analisi di risposta sismica locale, Atti XI Congresso Nazionale "L'Ingegneria Sismica in Italia", Genova, Italia, 25-29 Gennaio. In Italian.

Leonard (2010) Earthquake Fault Scaling: Self-Consistent Relating of Rupture Length, Width, Average Displacement, and Moment Release. Bulletin of the Seismological Society of America, Vol. 100, No. 5A, pp. 1971–1988.

Lin T., Harmsen S.C. Baker J.W. and Luco N. (2013) Conditional Spectrum Computation Incorporating Multiple Causal Earthquakes and Ground Motion Prediction Models Bulletin of the Seismological Society of America, 103(2A), 1103–1116.

Lolli B., Gasperini P. and Vannucci G. (2014) Empirical conversion between teleseismic magnitudes (m_b and M_s) and moment magnitude (M_w) at the Global, Euro-Mediterranean and Italian scale, Geophys. J. Int. (2014) 199, 805–828. doi: 10.1093/gji/ggu264.

Loth (2014) Multivariate ground motion intensity measure models, and implications for structural reliability assessment, Ph.D. dissertation, Stanford University, (available online: http://purl.stanford.edu/hb034dz2986, last accessed January 2015).

Lysmer J., and Kuhlemeyer R.L. (1969) Finite Dynamic Model for Infinite Media, J. Eng. Mech., 95(EM4), 859-877.

NTC (2008) Norme Tecniche per le Costruzioni. DM 14 gennaio 2008. Gazzetta Ufficiale della Repubblica Italiana, 29.

Mai P. M., Spudich P., and Boatwright J. (2005) Hypocenter locations in finite-source rupture models, Bulletin of the Seismological Society of America 95, 965–980.

Malagnini, L., A. Akinci, R. B. Herrmann, N. A. Pino, and L. Scognamiglio (2002) Characteristics of the ground motion in northeastern Italy, Bull. Seismol. Soc. Am. 92, no. 6, 2186–2204.

Malagnini, L., R. B. Herrmann, and M. Di Bona (2000) Ground motion scaling in the Apennines (Italy), Bull. Seismol. Soc. Am. 90, no. 4, 1062–1081.

Mancuso C. (1995) Aspetti Metodologici ed Applicazione della Tecnica Sperimentale SASW, Rivista Italiana di Geotecnica, 4/1995, pp. 271-288. In Italian.

Mastrolembo Ventura B. (2012) Kinematics of the Sicily and Calabria subduction system from elastic block modeling of GPS data, Ph.D. thesis.

Mattei M., Cifelli F., D'Agostino N. (2007) The evolution of the Calabrian Arc: Evidence from paleomagnetic and GPS observations, Earth and Planetary Science Letters 263 259–274.

McGuire A.K., Cornell C.A., Toro G. (2005) The Case for Using Mean Seismic Hazard, Earthquake Spectra, Vol. 21, No. 3, pages 879-886.

McGuire R. K. (2004), Seismic Hazard and Risk Analysis, Earthquake Engineering Research Institute, Oakland, California.

Melchers R.E. (1999) Structural Reliability Analysis and Prediction, John Wiley and Sons, Chichester. U.K.

Meletti C, Galadini F, Valensise G, Stucchi M, Basili R, Barba G, Vannucci G, Boschi E (2008) A seismic source model for the seismic hazard assessment of the Italian territory. Tectonophysics 450(1):85–108. doi:10.1016/j.tecto.2008.01.003.

Meletti C. and Valensise G. (2004) Zonazione sismogenetica ZS9 – App.2 al Rapporto Conclusivo. In: Gruppo di Lavoro MPS (2004). Redazione della mappa di pericolosità sismica prevista dall'Ordinanza PCM 3274 del 20 marzo 2003. Rapporto Conclusivo per il Dipartimento della Protezione Civile, INGV, Milano-Roma, aprile 2004, 65 pp. + 5 allegati, in Italian.

Menq F.Y. (2003) Dynamic properties of sandy and gravelly soils, Ph.D. Dissertation, University of Texas at Austin, TX, USA, 364.

Minelli L., and C. Faccenna (2010) Evolution of the Calabrian accretionary wedge (central Mediterranean), Tectonics, 29, TC4004, doi:10.1029/ 2009TC002562.

Monaco C., Tortorici L., (2000) Active faulting in the Calabrian Arc and eastern Sicily. J. Geodyn. 29, 407–424.

Montaldo, V., E. Faccioli, G. Zonno, A. Akinci, and L. Malagnini (2005) Treatment of ground-motion predictive relationships for the reference seismic hazard map of Italy, J. Seismol. 9, no. 3, 295–316.

Morasca, P., L. Malagnini, A. Akinci, and D. Spallarossa (2002) Ground motion scaling in the western Alps, Seismol. Res. Lett. 73, 251.

MPS working group (2004) Redazione della mappa di pericolosità sismica prevista dall'Ordinanza PCM del 20 marzo 2003 n. 3274, All. 1. Rapporto conclusivo per il

Dipartimento della Protezione Civile, aprile 2004, Istituto Nazionale di Geofisica e Vulcanologia (INGV), Milano-Roma, Italy, available at http://zonesismiche.mi.ingv.it/ (last accessed December 2014), 163 pp. (in Italian).

Musson, R. M. W. (2000) The use of Monte Carlo simulations for seismic hazard assessment in the U.K." In: Annals of Geophys. 43.1, pages 1–9

Naeim F. and M. Lew (1995) On the use of design spectrum compatible time histories, Earthquake Spectra, 11, 111-127.

Newmark N.M. (1965) Effects of Earthquakes on Dams and Embankments, Géotechnique, Vol. 15, No. 2, pp. 139-160.

NIST (2011) Selecting and Scaling Earthquake Ground Motions for Performing Response History Analysis, NIST/GCR 11-917-15, prepared by the NEHRP Consultants Joint Venture for the National Institute of Standards and Technology, Gaithersburg, Maryland.

Pagani, M., Monelli, D., Weatherill, Danciu L., Crowley H., Silva V., Henshaw P., Butler L., Nastasi M., Panzeri L., Simionato M., Viganò D. (2014a) OpenQuake Engine: An Open Hazard (and Risk) Software for the Global Earthquake Model, Seismological Research Letters, v. 85 no. 3 p. 692-702.

Pagani, M., Monelli, D., Weatherill, G. A. and Garcia, J. (2014b) The OpenQuake-engine Book: Hazard. Global Earthquake Model (GEM) Technical Report 2014-08, doi: 10.13117/ GEM.OPENQUAKE.TR2014.08, 67 pages.

Pagano L., Mancuso C., Sica S. (2008) Prove in sito sulla diga del Camastra: tecniche sperimentali e risultati, Rivista Italiana di Geotecnica 3/2008, pp. 11 – 28. In Italian.

Pagliaroli A., Lanzo G. (2008) Selection of real accelerograms for the seismic response analysis of the historical town of Nicastro (Southern Italy) during the March 1638 Calabria earthquake, Engineering Structures 30 (2008) 2211–2222.

Patanè, D., F. Ferrucci, and S. Gresta (1994) Spectral features of microearthquakes in volcanic areas: Attenuation in the crust and amplitude response of the site at Mt. Etna (Italy), Bull. Seismol. Soc. Am. 84, 1842–1860.

Patanè, D., F. Ferrucci, E. Giampiccolo, and L. Scaramuzzino (1997) Source scaling of microearthquakes at Mt. Etna volcano and in the Calabrian Arc (southern Italy), Geoph. Res. Lett. 24, 1879–1882.

Penman A.D.M. (1986) On the embankment dam, Geotechnique, 36, 301–48.

Pepe F., Sulli A., Bertotti G., Cella F. (2010) Architecture and Neogene to Recent evolution of the western Calabrian continental margin: An upper plate perspective to the Ionian subduction system, central Mediterranean, TECTONICS, VOL. 29, TC3007,doi:10.1029/2009TC002599.

Reilinger R., S. McClusky P. Vernant S. Lawrence S. Ergintav, R. Cakmak et al. (2006), GPS Constraints on Continental Deformation in the Africa-Arabia-Eurasia Continental Collision Zone and Implications for the Dynamics of Plate Interactions, Journal of Geophysical Research, 111, B05411, doi:10.1029/2005JB004051.

Reiter L. (1990) Earthquake Hazard Analysis: Issues and Insights. Columbia University Press: New York; 254.

Richart F.E., Hall J.R., and Woods R.D. (1970), Vibrations of soils and foundations, Prentice-Hall, Inc., New Jersey, 414 pp.

Rovithis E., Parashakis Ch., Mylonakis G. (2011) 1D harmonic response of layered inhomogeneous soil: analytical investigation, Soil Dyn Earth Eng; 31(7): 879 – 890.

Sabetta, F. and A. Pugliese (1996) Estimation of response spectra and simulation of nonstationary earthquake ground motions, Bull. Seismol. Soc. Am. 86, no. 2, 337–352.

Scasserra, G., Stewart, J. P., Bazzurro, P., Lanzo, G., and Mollaioli, F. (2009), A comparison of NGA ground-motion prediction equations to Italian data, Bull. Seismol. Soc. Am. 99, 2961–2978.

Scherbaum F., Schmedes J., and Cotton F. (2004) On the conversion of source-to-site distance measures for extended earthquake source models, Bulletin of the Seismological Society of America 94, 1053–1069.

Schreyer H. (1977) One-dimensional elastic waves in inhomogeneous media, J Eng Mech Div ASCE; 103(5): 979-990.

Schwartz, D. P., and J. Coppersmith (1984) Fault behaviour and characteristic earthquakes: examples from Wasatch and San Andreas faults, J. Geophys. Res. 89, 5681–5698.

Seed H. B. (1979) Considerations in the earthquake-resistant design of earth and rockfill dams, Geotechnique 29(3): 215-2637.

Seed H.B., Idriss I.M. (1969) The influence of ground conditions on ground motions during earthquakes, J Soil Mech Found; Div 94: 93-137.

Seed H.B., Martin P.P. and Lysmer J. (1975) The Generation and Dissipation of Pore Water Pressures during Soil Liquefaction, University of California, Berkeley, Earthquake Engineering Research Center, NSF Report PB-252 648.

Selvaggi, G., Chiarabba, C., (1995), Seismicity and P-wave velocity image of the southern Tyrrhenian subduction zone. Geophys. J. Int. 121, 818–826.

Serpelloni E., Vannucci G., Pondrelli S., Argnani A., Casula G., Anzidei M., Baldi P., Gasperini P., 2007, Kinematics of the Western Africa–Eurasia plate bound-ary from focal mechanisms and GPS data. Geophys. J. Int.169 (3), 1180–1200. http://dx.doi.org/10.1111/j.1365-246X.2007.03367.x.

Shaw B.E. (2013) Earthquake Surface Slip-Length Data is Fit by Constant Stress Drop and is Useful for Seismic Hazard Analysis, Bulletin of the Seismological Society of America, Vol. 103, No. 2A, pp. 876–893, doi: 10.1785/0120110258.

Shome N., Cornell C.A., Bazzuro P., and Carballo E.J. (1998) Earthquakes, records, and nonlinear responses, Earthquake Spectra, 14, 469-500.

Silva V., Crowley H., Pagani M., Monelli D., Pinho R. (2014) Development of the OpenQuake engine, the Global Earthquake Model's open-source software for seismic risk assessment, Volume 72, Issue 3, pp 1409-1427.

Slejko D., Caporali A., Stirling M., Barba S. (2010) Occurrence probability of moderate to large earthquakes in Italy based on new geophysical methods, J Seismol (2010) 14:27–51 doi:10.1007/s10950-009-9175-x.

Spina V., Tondi E., Galli P., Mazzoli S., (2009) Fault propagation in a seismic gap area (northern Calabria, Italy):implication for seismic hazard .Tectonophysics 476, 357–369.

Spina V., Tondi E., Mazzoli S., (2011) Complex basin development in a wrench-dominated back-arc area: Tectonic evolution of the Crati Basin, Calabria, Italy, Journal of Geodynamics Volume 51, Issues 2–3, Pages 90–109

Spina V., Galli P., Tondi E., Critelli S., Cello G., (2006) Kinematics and structural properties of active fault segments in the Sila Massif, northern Calabria, Italy. Geophysical Research Abstracts, Vol. 8, 03547.

Spina V., Galli P., Tondi E., Critelli S., Cello G., (2007) Kinematics and structural properties of active fault segments in the Sila Massif (Northern Calabria, Italy), Boll.Soc.Geol.It. (Ital.J.Geosci.), Vol. 126, No. 2.

Spina V., Tondi E., Galli P., Cello G., (2004) Morphostructural analysis of an active fault in the Sila massif (Calabria, southern Italy): implication for the seismic hazard and recent evolution of the area, GNGTS – Atti del 23° Convegno Nazionale / 07.20. In Italian

Stewart J.P., Chiou S.J., Bray J.D., Graves R.W., Somerville P.G. and Abrahamson N.A. (2001) Ground motion evaluation procedures for performance-based design, Rpt. No. PEER-2001/09, Pacific Earthquake Engineering Research Center, University of California, Berkeley.

Stewart J.P., Douglas J., Javanbarg M., Bozorgnia Y., Abrahamson N.A., Boore D.M., Campbell K.W., Delavaud E., Erdik M. and Stafford P.J. (2015) Selection of Ground Motion Prediction Equations for the Global Earthquake Model, Earthquake Spectra ol. 31, No. 1, pp. 19-45. doi: http://dx.doi.org/10.1193/013013EQS017M.

Strasser F. O., M. C. Arango and J. J. Bommer (2010), scaling of the source dimensions of interface and intraslab subduction-zone earthquakes with Moment Magnitude, Seismo. Res. Lett., 81(6), 941-950, doi:10.1785/gssrl.

Strenk P.M. (2010) Evaluation of Analytical Procedures for Estimating Seismically Induced Permanent Deformations in Slopes, Ph.D. Dissertation Submitted to the Faculty of Drexel University.

Stucchi M, Meletti C, Montaldo V, Crowley H, Calvi GM, Boschi E (2011) Seismic hazard assessment (2003–2009) for the Italian building code. Bull Seismol Soc Am 101:1885–1911

Stucchi M, Rovida A, Gomez Capera AA, Alexandre P, Camelbeeck T, Demircioglu MB, Gasperini P, Kouskouna V, Musson RMW, Radulian M, Sesetyan K, Vilanova S, Baumont D, Bungum H, Fäh D, Lenhardt W, Makropoulos K, Martinez Solares JM, Scotti O, Živčić M, Albini P, Battlo J, Papaioannou C, Tatevossian R, Locati M, Meletti C, Viganò D, Giardini D (2012) The SHARE European Earthquake Catalogue (SHEEC) 1000–1899. J Seismol.

Swaisgood J.R. (2003) Embankment dam deformations caused by earthquakes, Proceedings of 2003 Pacific Conference on Earthquake Engineering. Paper No. 14.

Tansi C., Muto F., Critelli S., Iovine G., (2007) Neogene-Quaternarystrike-sliptectonics in the central Calabrian Arc (southern Italy). Journal of Geodynamics 43, 393–414.

Tansi C.,Tallarico A., Iovine G., Folino Gallo, M., Falcone, G., (2005) Interpretation of radon anomalies in seismotectonic and tectonic-gravitational settings: the south-eastern Crati graben (Northern Calabria, Italy). Tectonophysics 396, 181–193.

Thomas P, Wong I, Abrahamson N (2010) Verification of probabilistic seismic hazard analysis computer programs. PEER report 2010/106, Pacific Earthquake Engineering Research Center, University of California, Berkeley, 176 p.

Towhata I. (1996) Seismic wave propagation in elastic soil with continuous variation of shear modulus in the vertical direction, Soils Found; 36(1): 61-72.

Van Dijk J.P., Bello M., Brancaleoni G.P., Cantarella G., Costa V., Frixa A., Golfetto F., Merlini S., Riva M., Torricelli S., Toscano C., Zerilli A., (2000) A regional structural model for the northern sector of the Calabrian Arc (southern Italy). Tectonophysics 324, 267–320.

Wang G., Youngs R., Power M. and Z. Li (2013) Design Ground Motion Library (DGML): An Interactive Tool for Selecting Earthquake Ground Motions, Earthquake Spectra In-Press.

Ward S. N., (2007) Methods for Evaluating Earthquake Potential and Likelihood in and around California, Seismological Research Letters Volume 78, Number 1, 121-133.

Wells, D. L., and K. J. Coppersmith (1994) New empirical relationships among magnitude, rupture length, rupture width, rupture area, and surface displacement, Bull. Seismol. Soc. Am. 84, no. 4, 974–1002.

Woessner J., Giardini D. and the SHARE consortium (2012) Seismic Hazard Estimates for the Euro-Mediterranean Region: A community-based probabilistic seismic hazard assessment, Proceedings of the 15th World Conference of Earthquake Engineering, Lisbon, Portugal, Paper Nr. 4337, 2012.

Woessner, et al. (2012) SHARE deliverable D5.5 – Final seismic hazard assessment including de-aggregation - http://www.share-eu.org/sites/default/files/D5.5_SHARE.pdf last access 25/11/2014

Yee E., Stewart J.P, and Tokimatsu K. (2013) Elastic and large-strain nonlinear seismic site response from analysis of vertical array recordings, J. Geotech. Geoenviron. Eng., 139 (10), 1789-1801.

Zhao J. X. Zhang J. Asano A. Ohno Y. Oouchi T. Takahashi T. Ogawa H. Irikura K. Thio H. K. Somerville P. G. Fukushima Y. and Fukushima Y. (2006) Attenuation relations of strong ground motion in Japan using site classification based on predominant period, Bulletin of the Seismological Society of America, 96(3):898-913, doi: 10.1785/0120050122.

Appendix

In this appendix the BSSA (2014) GMPE implementation in the OQ is provided:

```
# The Hazard Library
# Copyright (C) 2012-2014, GEM Foundation
#
# This program is free software: you can redistribute it and/or modify
# it under the terms of the GNU Affero General Public License as
# published by the Free Software Foundation, either version 3 of the
# License, or (at your option) any later version.
#
# This program is distributed in the hope that it will be useful,
# but WITHOUT ANY WARRANTY; without even the implied warranty of
# MERCHANTABILITY or FITNESS FOR A PARTICULAR PURPOSE.  See the
# GNU Affero General Public License for more details.
#
# You should have received a copy of the GNU Affero General Public License
# along with this program.  If not, see <http://www.gnu.org/licenses/>.
"""
Module exports :class:`BSSA2014`.
"""
from __future__ import division
import numpy as np
from openquake.hazardlib.gsim.base import GMPE, CoeffsTable
from openquake.hazardlib import const
from openquake.hazardlib.imt import PGA, PGV, SA
class BSSA2014ITANOdz1(GMPE):
    """
  Implements GMPE Boore-Atkinson-Seyhan-Stewart for NGA West2 - 2014
  Author: Paolo Zimmaro
    """
    #: Supported tectonic region type is active shallow crustal
    DEFINED_FOR_TECTONIC_REGION_TYPE = const.TRT.ACTIVE_SHALLOW_CRUST
    #: Supported intensity measure types are spectral acceleration,
    #: peak ground velocity and peak ground acceleration,
    DEFINED_FOR_INTENSITY_MEASURE_TYPES = set([
        PGA,
        PGV,
        SA
    ])
```

```
 #: Supported intensity measure component is which is the
 #:median single-component horizontal ground motion
#:across all non-redundant azimuths
 #::attr:`~openquake.hazardlib.const.IMC.RotD50`
 DEFINED_FOR_INTENSITY_MEASURE_COMPONENT = const.IMC.RotD50
 #: Supported standard deviation types are inter-event, intra-event
 #: and total (between-event, within-event and total)
 DEFINED_FOR_STANDARD_DEVIATION_TYPES = set([
    const.StdDev.TOTAL,
    const.StdDev.INTER_EVENT,
    const.StdDev.INTRA_EVENT
 ])
 #: Required site parameters is Vs30.
 REQUIRES_SITES_PARAMETERS = set(('vs30', ))
 #: Required rupture parameters are magnitude, and rake.
 #: NOTE: rake is the parameter to distinguish the fault mechanisms
 REQUIRES_RUPTURE_PARAMETERS = set(('mag', 'rake'))
 #: Required distance measure is Rjb.
 REQUIRES_DISTANCES = set(('rjb', ))

 def get_mean_and_stddevs(self, sites, rup, dists, imt, stddev_types):
    """
    See :meth:`superclass method
    <.base.GroundShakingIntensityModel.get_mean_and_stddevs>`
    for spec of input and result values.
    """
    # extracting dictionary of coefficients specific to required
    # intensity measure type.
    C = self.COEFFS[imt]
    C_SR = self.COEFFS_SOIL_RESPONSE[imt]
    C_ST = self.COEFFS_STD[imt]

    # compute PGA on rock conditions - needed to compute non-linear
    # site amplification term
    pga4nl = self._get_pga_on_rock(rup, dists, C)

    if imt == PGA():
       # avoid recomputing PGA on rock, just add site terms
       mean = np.log(pga4nl) + \
          self._get_site_amplification_linear(sites.vs30, C_SR) + \
          self._get_site_amplification_non_linear(sites.vs30, pga4nl, C_SR)
    else:
       mean = self._compute_magnitude_scaling(rup, C) + \
          self._compute_distance_scaling(rup, dists, C) + \
          self._get_site_amplification_linear(sites.vs30, C_SR) + \
          self._get_site_amplification_non_linear(sites.vs30, pga4nl, C_SR)
```

```
        stddevs = self._get_stddevs(C_ST, stddev_types, rup, sites.vs30, dists,
num_sites=len(sites.vs30))
        return mean, stddevs

    def _get_stddevs(self, C, stddev_types, rup, vs30, dists, num_sites):
        """
        Return standard deviations as defined in table 8, pag 121.
        """
        stddevs = []
        inter = self._get_inter(rup, C)
        #:intra = self._get_std_rjb(rup, dists, C)
        intra = self._get_intra(rup, dists, vs30, C)
        total = np.sqrt(intra ** 2.0 + inter ** 2.0)

        for stddev_type in stddev_types:
            assert stddev_type in self.DEFINED_FOR_STANDARD_DEVIATION_TYPES
            if stddev_type == const.StdDev.TOTAL:
                stddevs.append(total + np.zeros(num_sites))
            elif stddev_type == const.StdDev.INTER_EVENT:
                stddevs.append(inter + np.zeros(num_sites))
            elif stddev_type == const.StdDev.INTRA_EVENT:
                stddevs.append(intra + np.zeros(num_sites))
        return stddevs

    def _get_inter(self, rup, C):

        if  rup.mag <= 4.5:
            return C['tau1']
        elif rup.mag > 4.5 and rup.mag < 5.5:
            return C['tau1'] + (C['tau2'] - C['tau1']) * (rup.mag - 4.5)
        else:
            return C['tau2']

    def _get_std_magn(self, rup, C):

        if  rup.mag <= 4.5:
            return C['phi1']
        elif rup.mag > 4.5 and rup.mag < 5.5:
            return C['phi1'] + (C['phi2'] - C['phi1']) * (rup.mag - 4.5)
        else:
            return C['phi2']

    def _get_std_rjb(self, rup, dists, C):

        if dists.rjb <= C['R1']:
```

```
            return self._get_std_magn(rup, C)

        elif dists.rjb > C['R1'] and  dists.rjb < C['R2']:
            return self._get_std_magn(rup, C) + C['DfR'] * (np.log(dists.rjb / C['R1']) / np.log(C['R2']
/ C['R1']))

        else:
            return self._get_std_magn(rup, C) + C['DfR']

    def _get_intra(self, rup, dists, vs30, C):

        if vs30 >= C['V2']:
            return self._get_std_rjb(rup, dists, C)

        elif vs30 >= C['V1'] and  vs30 <= C['V2']:
            return self._get_std_rjb(rup, dists, C) - C['DfV'] * (np.log(C['V2'] / vs30) / np.log(C['V2']
/ C['V1']))

        else:
            return self._get_std_rjb(rup, dists, C) - C['DfV']

    def _compute_distance_scaling(self, rup, dists, C):
        """
        Compute distance-scaling term, equations (3) and (4), pag 107.
        """
        Mref = 4.5
        Rref = 1.0
        R = np.sqrt(dists.rjb ** 2 + C['h'] ** 2)
        return (C['c1'] + C['c2'] * (rup.mag - Mref)) * np.log(R / Rref) + \
            (C['c3'] + C['ItaJap'])  * (R - Rref)

    def _compute_magnitude_scaling(self, rup, C):
        """
        Compute magnitude-scaling term, equations (5a) and (5b), pag 107.
        """
        U, SS, NS, RS = self._get_fault_type_dummy_variables(rup)
        if rup.mag <= C['Mh']:
            return C['e0'] * U + C['e1'] * SS + C['e2'] * NS + C['e3'] * RS + \
                C['e4'] * (rup.mag - C['Mh']) + \
                C['e5'] * (rup.mag - C['Mh']) ** 2
        else:
            return C['e0'] * U + C['e1'] * SS + C['e2'] * NS + C['e3'] * RS + \
                C['e6'] * (rup.mag - C['Mh'])

    def _get_fault_type_dummy_variables(self, rup):
        U, SS, NS, RS = 0, 0, 0, 0
```

```
    if np.abs(rup.rake) <= 30.0 or (180.0 - np.abs(rup.rake)) <= 30.0:
        # strike-slip
        SS = 1
    elif rup.rake > 30.0 and rup.rake < 150.0:
        # reverse
        RS = 1
    else:
        # normal
        NS = 1

    return U, SS, NS, RS

def _get_site_amplification_linear(self, vs30, C):
    """
    Compute site amplification linear term,
    equation (7), pag 107.
    """
    if vs30 <= C['Vc']:
        return C['clin'] * np.log(vs30 / 760)

    else:
        return C['clin'] * np.log(C['Vc'] / 760)

def _get_pga_on_rock(self, rup, dists, _C):
    """
    Compute and return PGA on rock conditions (that is vs30 = 760.0 m/s).
    This is needed to compute non-linear site amplification term
    """
    # Median PGA in g for Vref = 760.0, without site amplification
    C_pga = self.COEFFS[PGA()]
    pga4nl = np.exp(self._compute_magnitude_scaling(rup, C_pga) +
                    self._compute_distance_scaling(rup, dists, C_pga))
    return pga4nl

def _get_site_amplification_non_linear(self, vs30, pga4nl, C):
    """
    Compute site amplification non-linear term,
    """
    if vs30 >= 760:
        return 0

    else:
        return (C['f4'] * (np.exp(C['f5'] * (vs30 - 360)) - \
            np.exp(C['f5'] * 400))) * np.log((pga4nl + 0.1) / 0.1)

#: Coefficient table is constructed from values in tables 3, 4 and 6
```

```
    COEFFS = CoeffsTable(sa_damping=5, table="""\
IMT     c1          c2          c3          h           e0          e1          e2          e3          e4          e5          e6          Mh
        ItaJap
pgv     -1.243000   0.148900    -0.003440   5.300000    5.037000    5.078000
        4.849000    5.033000    1.073000    -0.153600   0.225200    6.200000
        -0.000330
pga     -1.134000   0.191700    -0.008088   4.500000    0.447300    0.485600
        0.245900    0.453900    1.431000    0.050530    -0.166200   5.500000
        -0.002550
0.01    -1.134000   0.191600    -0.008088   4.500000    0.453400    0.491600
        0.251900    0.459900    1.421000    0.049320    -0.165900   5.500000
        -0.002440
0.02    -1.139400   0.189620    -0.008074   4.500000    0.485980    0.523590
        0.297070    0.488750    1.433100    0.053388    -0.165610   5.500000
        -0.002340
0.022   -1.140500   0.189240    -0.008095   4.500000    0.498660    0.536470
        0.313470    0.499730    1.433600    0.054888    -0.165200   5.500000
        -0.002290
0.025   -1.141900   0.188750    -0.008153   4.500000    0.522830    0.561300
        0.344260    0.519990    1.432800    0.057529    -0.164990   5.500000
        -0.002250
0.029   -1.142300   0.188440    -0.008290   4.500000    0.559490    0.599230
        0.391460    0.549950    1.427900    0.060732    -0.166320   5.500000
        -0.002210
0.03    -1.142100   0.188420    -0.008336   4.490000    0.569160    0.609200
        0.403910    0.557830    1.426100    0.061444    -0.166900   5.500000
        -0.002170
0.032   -1.141200   0.188400    -0.008445   4.450000    0.588020    0.628750
        0.427880    0.573300    1.422700    0.062806    -0.168130   5.500000
        -0.002120
0.035   -1.138800   0.188390    -0.008642   4.400000    0.616360    0.658180
        0.462520    0.597040    1.417400    0.064559    -0.170150   5.500000
        -0.002100
0.036   -1.137800   0.188370    -0.008715   4.380000    0.625540    0.667720
        0.473380    0.604960    1.415800    0.065028    -0.170830   5.500000
        -0.002070
0.04    -1.132400   0.188160    -0.009030   4.320000    0.662810    0.706040
        0.515320    0.638280    1.409000    0.066183    -0.173570   5.500000
        -0.002050
0.042   -1.129200   0.187970    -0.009195   4.290000    0.680870    0.724430
        0.534450    0.655050    1.405900    0.066438    -0.174850   5.500000
        -0.002030
0.044   -1.125900   0.187750    -0.009360   4.270000    0.698820    0.742770
        0.552820    0.672250    1.403300    0.066663    -0.176190   5.500000
        -0.002020
```

0.045	-1.124200	0.187640	-0.009441	4.250000	0.708220	0.752320
	0.562220	0.681390	1.402100	0.066774	-0.176930	5.500000
	-0.002000					
0.046	-1.122400	0.187520	-0.009521	4.240000	0.717790	0.762020
	0.571660	0.690760	1.400900	0.066891	-0.177690	5.500000
	-0.001990					
0.048	-1.119200	0.187300	-0.009676	4.220000	0.735740	0.780150
	0.588880	0.708540	1.399100	0.067127	-0.179200	5.500000
	-0.001990					
0.05	-1.115900	0.187090	-0.009819	4.200000	0.754360	0.799050
	0.606520	0.727260	1.397400	0.067357	-0.180820	5.500000
	-0.001990					
0.055	-1.108200	0.186550	-0.010120	4.150000	0.799600	0.844500
	0.647700	0.773700	1.394700	0.067797	-0.184800	5.500000
	-0.002000					
0.06	-1.100900	0.185820	-0.010330	4.110000	0.843940	0.888840
	0.685620	0.820670	1.395400	0.068591	-0.188580	5.500000
	-0.002020					
0.065	-1.094200	0.184850	-0.010480	4.080000	0.886550	0.931160
	0.719410	0.867240	1.400400	0.070127	-0.191760	5.500000
	-0.002040					
0.067	-1.091800	0.184420	-0.010520	4.070000	0.902700	0.947110
	0.731710	0.885260	1.403200	0.070895	-0.192910	5.500000
	-0.002080					
0.07	-1.088400	0.183690	-0.010560	4.060000	0.926520	0.970570
	0.749400	0.912270	1.408200	0.072075	-0.194510	5.500000
	-0.002110					
0.075	-1.083100	0.182250	-0.010580	4.040000	0.964470	1.007700
	0.776780	0.956300	1.417400	0.073549	-0.196650	5.500000
	-0.002160					
0.08	-1.078500	0.180520	-0.010560	4.020000	1.000300	1.042600
	0.801610	0.998180	1.426100	0.073735	-0.198160	5.500000
	-0.002210					
0.085	-1.074500	0.178560	-0.010510	4.030000	1.034000	1.075500
	0.824230	1.037900	1.432200	0.071940	-0.199020	5.510000
	-0.002270					
0.09	-1.070900	0.176430	-0.010420	4.070000	1.066600	1.107600
	0.845910	1.076200	1.435000	0.068097	-0.199290	5.520000
	-0.002330					
0.095	-1.067800	0.174200	-0.010320	4.100000	1.098100	1.138500
	0.867030	1.112700	1.433900	0.062327	-0.199000	5.530000
	-0.002380					
0.1	-1.065200	0.172030	-0.010200	4.130000	1.126800	1.166900
	0.887100	1.145400	1.429300	0.055231	-0.198380	5.540000
	-0.002440					

0.11	-1.060700	0.167700	-0.009964	4.190000	1.178500	1.217900
	0.927020	1.203000	1.411000	0.037389	-0.196010	5.570000
	-0.002490					
0.12	-1.057200	0.163520	-0.009722	4.240000	1.223000	1.262100
	0.966160	1.250200	1.383100	0.016373	-0.192650	5.620000
	-0.002540					
0.13	-1.054900	0.159820	-0.009476	4.290000	1.259600	1.298600
	1.003100	1.286900	1.349700	-0.005158	-0.188980	5.660000
	-0.002580					
0.133	-1.054500	0.158820	-0.009402	4.300000	1.269200	1.308200
	1.013500	1.296100	1.339500	-0.011354	-0.187920	5.670000
	-0.002630					
0.14	-1.053700	0.156720	-0.009228	4.340000	1.288300	1.327000
	1.036000	1.313700	1.316200	-0.024711	-0.185660	5.700000
	-0.002670					
0.15	-1.053200	0.154010	-0.008977	4.390000	1.309500	1.348100
	1.064800	1.332400	1.284400	-0.042065	-0.182340	5.740000
	-0.002710					
0.16	-1.053300	0.151580	-0.008725	4.440000	1.323500	1.361500
	1.087600	1.343700	1.254100	-0.057593	-0.178530	5.780000
	-0.002750					
0.17	-1.054100	0.149480	-0.008472	4.490000	1.330600	1.367900
	1.104000	1.348700	1.224400	-0.071861	-0.174210	5.820000
	-0.002800					
0.18	-1.055600	0.147680	-0.008219	4.530000	1.332700	1.368900
	1.114900	1.349200	1.194100	-0.085640	-0.169390	5.850000
	-0.002850					
0.19	-1.057900	0.146160	-0.007967	4.570000	1.330700	1.365600
	1.120800	1.346300	1.163500	-0.098884	-0.164040	5.890000
	-0.002910					
0.2	-1.060700	0.144890	-0.007717	4.610000	1.325500	1.359000
	1.122000	1.341400	1.134900	-0.110960	-0.158520	5.920000
	-0.002970					
0.22	-1.067000	0.142630	-0.007224	4.680000	1.309100	1.339400
	1.113300	1.328100	1.082300	-0.133000	-0.147040	5.970000
	-0.003030					
0.24	-1.073700	0.140350	-0.006747	4.750000	1.288100	1.315000
	1.094500	1.313200	1.036600	-0.152990	-0.134450	6.030000
	-0.003080					
0.25	-1.077300	0.139250	-0.006517	4.780000	1.276600	1.301700
	1.082800	1.305200	1.016600	-0.162130	-0.127840	6.050000
	-0.003140					
0.26	-1.080800	0.138180	-0.006293	4.820000	1.265100	1.288600
	1.071000	1.297200	0.999320	-0.170410	-0.121150	6.070000
	-0.003190					

0.28	-1.087900	0.136040	-0.005866	4.880000	1.242900	1.263500
	1.047600	1.281500	0.972820	-0.184630	-0.107140	6.110000
	-0.003240					
0.29	-1.091300	0.134990	-0.005666	4.900000	1.232400	1.251700
	1.036300	1.273600	0.963480	-0.190570	-0.100110	6.120000
	-0.003270					
0.3	-1.094800	0.133880	-0.005475	4.930000	1.221700	1.240100
	1.024600	1.265300	0.956760	-0.195900	-0.092855	6.140000
	-0.003300					
0.32	-1.101300	0.131790	-0.005122	4.980000	1.200700	1.217700
	1.001100	1.247900	0.950040	-0.204540	-0.078923	6.160000
	-0.003300					
0.34	-1.107400	0.129840	-0.004808	5.030000	1.179000	1.195500
	0.976770	1.228600	0.949560	-0.211340	-0.065134	6.180000
	-0.003300					
0.35	-1.110500	0.128900	-0.004663	5.060000	1.167400	1.183600
	0.963800	1.217700	0.950770	-0.214460	-0.057921	6.180000
	-0.003290					
0.36	-1.113300	0.128060	-0.004527	5.080000	1.155800	1.172000
	0.951200	1.206600	0.952780	-0.217160	-0.051040	6.190000
	-0.003270					
0.38	-1.119000	0.126470	-0.004276	5.120000	1.130500	1.146800
	0.924400	1.181600	0.958990	-0.222140	-0.036755	6.190000
	-0.003240					
0.4	-1.124300	0.125120	-0.004053	5.160000	1.104600	1.121400
	0.897650	1.155200	0.967660	-0.226080	-0.023189	6.200000
	-0.003210					
0.42	-1.129100	0.123890	-0.003853	5.200000	1.078200	1.095500
	0.870670	1.127600	0.978620	-0.229240	-0.010417	6.200000
	-0.003180					
0.44	-1.133700	0.122780	-0.003673	5.240000	1.051500	1.069700
	0.843550	1.099500	0.991440	-0.231660	0.001168	6.200000
	-0.003130					
0.45	-1.135900	0.122270	-0.003590	5.250000	1.037600	1.056200
	0.829410	1.084700	0.998760	-0.232630	0.006589	6.200000
	-0.003080					
0.46	-1.138100	0.121770	-0.003510	5.270000	1.023400	1.042600
	0.815090	1.069600	1.006400	-0.233500	0.011871	6.200000
	-0.003020					
0.48	-1.142000	0.120930	-0.003360	5.300000	0.997190	1.017200
	0.788600	1.041500	1.021500	-0.234640	0.020767	6.200000
	-0.002960					
0.5	-1.145900	0.120150	-0.003220	5.340000	0.969910	0.991060
	0.761500	1.012000	1.038400	-0.235220	0.029119	6.200000
	-0.002910					

0.55	-1.154300	0.118470	-0.002897	5.410000	0.904800	0.928300
	0.698400	0.941700	1.083300	-0.234490	0.046932	6.200000
	-0.002850					
0.6	-1.161500	0.116710	-0.002610	5.480000	0.841650	0.867150
	0.638750	0.873510	1.133600	-0.231280	0.062667	6.200000
	-0.002790					
0.65	-1.167600	0.114650	-0.002356	5.530000	0.781810	0.808760
	0.582310	0.809480	1.186100	-0.226660	0.077997	6.200000
	-0.002730					
0.667	-1.169400	0.113940	-0.002276	5.540000	0.762620	0.789940
	0.564220	0.789160	1.203500	-0.224970	0.083058	6.200000
	-0.002660					
0.7	-1.172800	0.112530	-0.002131	5.560000	0.725130	0.753020
	0.528780	0.749850	1.237500	-0.221430	0.093185	6.200000
	-0.002600					
0.75	-1.177700	0.110540	-0.001931	5.600000	0.669030	0.697370
	0.475230	0.691730	1.287100	-0.215910	0.108290	6.200000
	-0.002530					
0.8	-1.181900	0.108730	-0.001754	5.630000	0.613460	0.641960
	0.421730	0.635190	1.334100	-0.210470	0.122560	6.200000
	-0.002460					
0.85	-1.185400	0.107090	-0.001597	5.660000	0.558530	0.586980
	0.368130	0.579690	1.378000	-0.205280	0.136080	6.200000
	-0.002380					
0.9	-1.188400	0.105480	-0.001456	5.690000	0.502960	0.531360
	0.313760	0.523610	1.420800	-0.200110	0.149830	6.200000
	-0.002290					
0.95	-1.190900	0.103890	-0.001328	5.720000	0.447010	0.475410
	0.259190	0.467060	1.462300	-0.194900	0.164320	6.200000
	-0.002200					
1	-1.193000	0.102480	-0.001210	5.740000	0.393200	0.421800
	0.207000	0.412400	1.500400	-0.189830	0.178950	6.200000
	-0.002090					
1.1	-1.196600	0.100160	-0.000994	5.820000	0.284840	0.313740
	0.101820	0.302090	1.569000	-0.180010	0.210420	6.200000
	-0.001980					
1.2	-1.199600	0.098482	-0.000803	5.920000	0.173400	0.202590
	-0.006195	0.188660	1.628200	-0.170900	0.244100	6.200000
	-0.001860					
1.3	-1.201800	0.097375	-0.000635	6.010000	0.061520	0.091060
	-0.113450	0.074330	1.679400	-0.162330	0.277990	6.200000
	-0.001750					
1.4	-1.203900	0.096743	-0.000490	6.100000	-0.045750	-0.015700
	-0.215500	-0.036070	1.723900	-0.154130	0.309560	6.200000
	-0.001630					

1.5	-1.206300	0.096445	-0.000365	6.180000	-0.149540	-0.118660
	-0.313800	-0.143700	1.762200	-0.146700	0.338960	6.200000
	-0.001520					
1.6	-1.208600	0.096338	-0.000259	6.260000	-0.248600	-0.216720
	-0.406820	-0.247080	1.795500	-0.139970	0.366160	6.200000
	-0.001410					
1.7	-1.210600	0.096254	-0.000171	6.330000	-0.341450	-0.308400
	-0.492950	-0.344650	1.825900	-0.133610	0.390650	6.200000
	-0.001320					
1.8	-1.212300	0.096207	-0.000099	6.400000	-0.429750	-0.395580
	-0.573880	-0.438180	1.856400	-0.126860	0.412440	6.200000
	-0.001250					
1.9	-1.214100	0.096255	-0.000042	6.480000	-0.512760	-0.477310
	-0.648990	-0.526820	1.886800	-0.119590	0.431510	6.200000
	-0.001200					
2	-1.215900	0.096361	0.000000	6.540000	-0.586690	-0.550030
	-0.714660	-0.606580	1.915200	-0.112370	0.447880	6.200000
	-0.001170					
2.2	-1.219000	0.096497	0.000000	6.660000	-0.721430	-0.682200
	-0.830030	-0.754020	1.968100	-0.098017	0.480240	6.200000
	-0.001160					
2.4	-1.220200	0.096198	0.000000	6.730000	-0.848100	-0.806900
	-0.932600	-0.894100	2.017000	-0.083765	0.518730	6.200000
	-0.001150					
2.5	-1.220100	0.096106	0.000000	6.770000	-0.909660	-0.867650
	-0.982280	-0.961870	2.040600	-0.076308	0.538830	6.200000
	-0.001160					
2.6	-1.219800	0.096136	0.000000	6.810000	-0.968630	-0.925770
	-1.031300	-1.026600	2.062800	-0.068925	0.558100	6.200000
	-0.001170					
2.8	-1.218900	0.096667	0.000000	6.870000	-1.081700	-1.036700
	-1.130100	-1.149500	2.101400	-0.055229	0.593940	6.200000
	-0.001180					
3	-1.217900	0.097638	0.000000	6.930000	-1.189800	-1.142000
	-1.230000	-1.266400	2.132300	-0.043320	0.626940	6.200000
	-0.001190					
3.2	-1.216900	0.098649	-0.000023	6.990000	-1.291400	-1.240600
	-1.325500	-1.376000	2.154500	-0.034440	0.658110	6.200000
	-0.001190					
3.4	-1.216000	0.099553	-0.000040	7.080000	-1.386000	-1.332200
	-1.415000	-1.478600	2.170400	-0.027889	0.687550	6.200000
	-0.001190					
3.5	-1.215600	0.099989	-0.000045	7.120000	-1.433200	-1.377800
	-1.459900	-1.529700	2.177500	-0.024997	0.702160	6.200000
	-0.001170					

3.6	-1.215600	0.100430	-0.000049	7.160000	-1.476200	-1.419300
	-1.501400	-1.576400	2.183400	-0.022575	0.715230	6.200000
	-0.001150					
3.8	-1.215800	0.101420	-0.000053	7.240000	-1.561700	-1.501400
	-1.586500	-1.668500	2.193800	-0.018362	0.740280	6.200000
	-0.001120					
4	-1.216200	0.102180	-0.000052	7.320000	-1.638800	-1.574800
	-1.667300	-1.751600	2.204000	-0.014642	0.763030	6.200000
	-0.001080					
4.2	-1.216500	0.102690	-0.000047	7.390000	-1.711600	-1.643900
	-1.745100	-1.829000	2.212300	-0.012248	0.785520	6.200000
	-0.001020					
4.4	-1.216900	0.103040	-0.000039	7.460000	-1.779800	-1.708900
	-1.819200	-1.901100	2.218100	-0.011459	0.807920	6.200000
	-0.000950					
4.6	-1.217500	0.103240	-0.000027	7.520000	-1.846900	-1.773100
	-1.892300	-1.971200	2.223000	-0.011760	0.831260	6.200000
	-0.000840					
4.8	-1.218200	0.103370	-0.000014	7.640000	-1.906300	-1.830300
	-1.957300	-2.032600	2.226800	-0.012879	0.852400	6.200000
	-0.000720					
5	-1.218900	0.103530	0.000000	7.780000	-1.966000	-1.888200
	-2.024500	-2.092800	2.229900	-0.014855	0.873140	6.200000
	-0.000570					
5.5	-1.220400	0.104600	0.000000	8.070000	-2.105100	-2.023200
	-2.190800	-2.228800	2.238900	-0.019502	0.914660	6.200000
	-0.000410					
6	-1.223200	0.107500	0.000000	8.480000	-2.242100	-2.156300
	-2.365900	-2.357900	2.237700	-0.026383	0.948700	6.200000
	-0.000230					
6.5	-1.229900	0.112310	0.000000	8.900000	-2.368600	-2.278500
	-2.532200	-2.477000	2.215000	-0.039505	0.976430	6.200000
	-0.000040					
7	-1.240800	0.118530	0.000000	9.200000	-2.482700	-2.388100
	-2.681800	-2.585400	2.172000	-0.059140	0.997570	6.200000
	0.000170					
7.5	-1.254300	0.125070	0.000000	9.480000	-2.586500	-2.487400
	-2.817600	-2.685400	2.118700	-0.081606	1.012100	6.200000
	0.000380					
8	-1.268800	0.131460	0.000000	9.570000	-2.686100	-2.582900
	-2.943800	-2.782300	2.061300	-0.103820	1.023200	6.200000
	0.000720					
8.5	-1.283900	0.137420	0.000000	9.620000	-2.782000	-2.675200
	-3.059700	-2.877600	2.008400	-0.121140	1.033500	6.200000
	0.000940					

```
9       -1.298900       0.142940        0.000000        9.660000        -2.879200       -2.768700
        -3.171300       -2.975900       1.960500        -0.134070       1.045300        6.200000
        0.001130
9.5     -1.313000       0.147810        0.000000        9.660000        -2.976900       -2.863400
        -3.278500       -3.076000       1.918900        -0.143640       1.056700        6.200000
        0.001310
10      -1.325300       0.151830        0.000000        9.660000        -3.070200       -2.953700
        -3.377600       -3.172600       1.883700        -0.150960       1.065100        6.200000
        0.001490
    """)

    #: Coefficient table is constructed from values in tables 1 and 2
    #: see matlab .m file + excel tables (yellow)
    COEFFS_SOIL_RESPONSE = CoeffsTable(sa_damping=5, table="""\
    IMT         clin        Vc      f4      f5
    pgv             -0.84   1300    -0.1    -0.00844
    pga             -0.6    1500    -0.15   -0.00701
    0.01 -0.6037            1500.2 -0.1483          -0.00701
    0.02 -0.5739            1500.36         -0.1471         -0.00728
    0.022           -0.5668         1500.68         -0.1477         -0.00732
    0.025           -0.5552         1501.04         -0.1496         -0.00736
    0.029           -0.5385         1501.26         -0.1525         -0.00737
    0.03 -0.5341            1502.95         -0.1549         -0.00735
    0.032           -0.5253         1503.12         -0.1574         -0.00731
    0.035           -0.5119         1503.24         -0.1607         -0.00721
    0.036           -0.5075         1503.32         -0.1641         -0.00717
    0.04 -0.4906            1503.35         -0.1678         -0.00698
    0.042           -0.4829         1503.34         -0.1715         -0.00687
    0.044           -0.4757         1503.13         -0.176  -0.00677
    0.045           -0.4724         1502.84         -0.181  -0.00672
    0.046           -0.4691         1502.47         -0.1862         -0.00667
    0.048           -0.4632         1502.01         -0.1915         -0.00656
    0.05 -0.458  1501.42             -0.1963         -0.00647
    0.055           -0.4479         1500.71         -0.2014         -0.00625
    0.06 -0.4419            1499.83         -0.2066         -0.00607
    0.065           -0.4395         1498.74         -0.212  -0.00593
    0.067           -0.4395         1497.42         -0.2176         -0.00588
    0.07 -0.4404            1495.85         -0.2232         -0.00582
    0.075           -0.4441         1494    -0.2287         -0.00573
    0.08 -0.4502            1491.82         -0.2337         -0.00567
    0.085           -0.4581         1489.29         -0.2382         -0.00563
    0.09 -0.4673            1486.36         -0.2421         -0.00561
    0.095           -0.4772         1482.98         -0.2458         -0.0056
    0.1             -0.4872         1479.12         -0.2492         -0.0056
    0.11 -0.5063            1474.74         -0.2519         -0.00562
    0.12 -0.5244            1469.75         -0.254  -0.00567
```

0.13	-0.5421	1464.09	-0.2556	-0.00572
0.133	-0.5475	1457.76	-0.2566	-0.00574
0.14	-0.5603	1450.71	-0.2571	-0.00578
0.15	-0.5796	1442.85	-0.2571	-0.00585
0.16	-0.6005	1434.22	-0.2562	-0.00591
0.17	-0.6225	1424.85	-0.2544	-0.00597
0.18	-0.6449	1414.77	-0.2522	-0.00602
0.19	-0.6668	1403.99	-0.2497	-0.00608
0.2	-0.6876	1392.61	-0.2466	-0.00614
0.22	-0.7243	1380.72	-0.2432	-0.00626
0.24	-0.7565	1368.51	-0.2396	-0.00638
0.25	-0.7718	1356.21	-0.2357	-0.00644
0.26	-0.787	1343.89	-0.2315	-0.0065
0.28	-0.8161	1331.67	-0.2274	-0.0066
0.29	-0.8295	1319.83	-0.2232	-0.00665
0.3	-0.8417	1308.47	-0.2191	-0.0067
0.32	-0.8618	1297.65	-0.2152	-0.0068
0.34	-0.8773	1287.5	-0.2112	-0.00689
0.35	-0.8838	1278.06	-0.207	-0.00693
0.36	-0.8896	1269.19	-0.2033	-0.00697
0.38	-0.9004	1260.74	-0.1996	-0.00705
0.4	-0.9109	1252.66	-0.1958	-0.00713
0.42	-0.9224	1244.8	-0.1922	-0.00719
0.44	-0.9346	1237.03	-0.1884	-0.00726
0.45	-0.9408	1229.23	-0.184	-0.00729
0.46	-0.9469	1221.16	-0.1793	-0.00732
0.48	-0.9586	1212.74	-0.1749	-0.00738
0.5	-0.9693	1203.91	-0.1704	-0.00744
0.55	-0.9892	1194.59	-0.1658	-0.00758
0.6	-1.0012	1184.93	-0.161	-0.00773
0.65	-1.0078	1175.19	-0.1558	-0.00787
0.667	-1.0093	1165.69	-0.1503	-0.00792
0.7	-1.0117	1156.46	-0.1446	-0.008
0.75	-1.0154	1147.59	-0.1387	-0.00812
0.8	-1.021	1139.21	-0.1325	-0.00822
0.85	-1.0282	1131.34	-0.1262	-0.0083
0.9	-1.036	1123.91	-0.1197	-0.00836
0.95	-1.0436	1116.83	-0.1126	-0.00841
1	-1.05	1109.95	-0.1052	-0.00844
1.1	-1.0573	1103.07	-0.0977	-0.00847
1.2	-1.0584	1096.04	-0.0902	-0.00842
1.3	-1.0554	1088.67	-0.0827	-0.00829
1.4	-1.0504	1080.77	-0.0753	-0.00806
1.5	-1.0454	1072.39	-0.0679	-0.00771
1.6	-1.0421	1061.77	-0.0604	-0.00723
1.7	-1.0404	1049.29	-0.0534	-0.00666

```
1.8         -1.0397         1036.42         -0.047  -0.00603
1.9         -1.0395         1023.14         -0.0414         -0.0054
2           -1.0392         1009.49         -0.0361         -0.00479
2.2         -1.0368         995.52 -0.0314          -0.00378
2.4         -1.0323         981.33 -0.0271          -0.00302
2.5         -1.0294         966.94 -0.0231          -0.00272
2.6         -1.0262         952.34 -0.0196          -0.00246
2.8         -1.019  937.52 -0.0165          -0.00208
3           -1.0112         922.43 -0.0136          -0.00183
3.2         -1.0032         908.79 -0.0112          -0.00167
3.4         -0.9951         896.15 -0.0093          -0.00158
3.5         -0.991  883.16 -0.0075          -0.00155
3.6         -0.9868         870.05 -0.0058          -0.00154
3.8         -0.9783         857.07 -0.0044          -0.00152
4           -0.9694         844.48 -0.0032          -0.00152
4.2         -0.9601         832.45 -0.0023          -0.00152
4.4         -0.9505         821.18 -0.0016          -0.0015
4.6         -0.9405         810.79 -0.001  -0.00148
4.8         -0.9302         801.41 -0.0006          -0.00146
5           -0.9195         793.13 -0.0003          -0.00144
5.5         -0.8918         785.73 -0.0001          -0.0014
6           -0.8629         779.91  0       -0.00138
6.5         -0.8335         775.6   0       -0.00137
7           -0.8046         772.68  0       -0.00137
7.5         -0.7766         771.01 -0.0001          -0.00137
8           -0.7503         760.81  0.0001          -0.00137
8.5         -0.7254         764.5   0.0001          -0.00137
9           -0.7016         768.07  0.0001          -0.00137
9.5         -0.6785         771.55  0.0001          -0.00136
10          -0.6558         775     0       -0.00136
""")
#: Coefficient table is constructed from values in tables 1 and 2
COEFFS_STD = CoeffsTable(sa_damping=5, table="""\
IMT         R1      R2      DfR     DfV     V1      V2      phi1    phi2    tau1    tau2
pgv         105     272     0.082   0.08    225     300     0.644   0.552   0.401   0.346
pga         110     270     0.1     0.07    225     300     0.695   0.495   0.398   0.348
0.01 111.67 270     0.096   0.07    225     300     0.698   0.499   0.402   0.345
0.02 113.1  270     0.092   0.03    225     300     0.702   0.502   0.409   0.346
0.022       113.37 270      0.088   0.027   225     300     0.707   0.505   0.418   0.349
0.025       113.07 270      0.086   0.026   225     300     0.711   0.508   0.427   0.354
0.029       112.36 270      0.084   0.028   225     300     0.716   0.51    0.436   0.359
0.03 112.13 270     0.081   0.029   225     300     0.721   0.514   0.445   0.364
0.032       111.65 270      0.078   0.03    225     300     0.726   0.516   0.454   0.369
0.035       110.64 270      0.077   0.031   225     300     0.73    0.518   0.462   0.374
0.036       109.53 270      0.075   0.031   225     300     0.734   0.52    0.47    0.379
0.04 108.28 270     0.073   0.032   225     300     0.738   0.521   0.478   0.384
```

0.042	106.99	270	0.072	0.032	225	300	0.742	0.523	0.484	0.39
0.044	105.41	270	0.07	0.031	225	300	0.745	0.525	0.49	0.397
0.045	103.61	270	0.069	0.031	225	300	0.748	0.527	0.496	0.405
0.046	101.7	270	0.067	0.031	225	300	0.75	0.529	0.499	0.412
0.048	99.76	270	0.065	0.031	225	300	0.752	0.53	0.502	0.419
0.05	97.93	270	0.063	0.03	225	300	0.753	0.532	0.503	0.426
0.055	96.03	270	0.062	0.029	225	300	0.753	0.534	0.502	0.434
0.06	94.1	270.01	0.061	0.027	225	300	0.753	0.536	0.499	0.441
0.065	92.08	270.02	0.061	0.025	225	300	0.752	0.538	0.495	0.448
0.067	90.01	270.02	0.061	0.025	225	300	0.75	0.54	0.489	0.455
0.07	87.97	270.03	0.062	0.024	225	300	0.748	0.541	0.483	0.461
0.075	85.99	270.04	0.064	0.022	225	300	0.745	0.542	0.474	0.466
0.08	84.23	270.05	0.067	0.02	225	300	0.741	0.543	0.464	0.468
0.085	82.74	270.06	0.072	0.019	225	300	0.737	0.543	0.452	0.468
0.09	81.54	270.07	0.076	0.017	225	300	0.734	0.542	0.44	0.466
0.095	80.46	270.08	0.082	0.016	225	300	0.731	0.542	0.428	0.464
0.1	79.59	270.09	0.087	0.014	225	300	0.728	0.541	0.415	0.458
0.11	79.05	270.11	0.093	0.012	225	300	0.726	0.54	0.403	0.451
0.12	78.85	270.13	0.099	0.011	225	300	0.724	0.539	0.392	0.441
0.13	78.99	270.15	0.104	0.011	225	300	0.723	0.538	0.381	0.43
0.133	79.47	270.15	0.11	0.011	225	300	0.722	0.538	0.371	0.417
0.14	80.26	270.16	0.115	0.012	225	300	0.721	0.537	0.362	0.403
0.15	81.33	270.16	0.12	0.015	225	300	0.72	0.537	0.354	0.388
0.16	82.86	270.16	0.125	0.02	225	300	0.72	0.536	0.349	0.372
0.17	84.72	270.14	0.128	0.026	225	300	0.718	0.536	0.346	0.357
0.18	86.67	270.11	0.131	0.033	225	300	0.717	0.536	0.344	0.341
0.19	88.73	270.06	0.134	0.039	225	300	0.714	0.537	0.343	0.324
0.2	90.91	270	0.136	0.045	225	300	0.711	0.539	0.344	0.309
0.22	93.04	269.83	0.138	0.052	225	300	0.708	0.541	0.345	0.294
0.24	95.08	269.59	0.14	0.055	225	300	0.703	0.544	0.347	0.28
0.25	97.04	269.45	0.141	0.055	225	300	0.698	0.547	0.35	0.266
0.26	98.87	269.3	0.141	0.055	225	300	0.693	0.55	0.353	0.255
0.28	100.53	268.96	0.14	0.053	225	300	0.687	0.554	0.357	0.244
0.29	102.01	268.78	0.139	0.051	225	300	0.681	0.557	0.36	0.236
0.3	103.15	268.59	0.138	0.05	225	300	0.675	0.561	0.363	0.229
0.32	104	268.2	0.135	0.048	225	300	0.67	0.566	0.366	0.223
0.34	104.7	267.79	0.133	0.047	225	300	0.664	0.57	0.369	0.218
0.35	105.26	267.58	0.13	0.047	225	300	0.658	0.573	0.372	0.215
0.36	105.61	267.37	0.128	0.047	225	300	0.653	0.576	0.375	0.212
0.38	105.87	266.95	0.125	0.048	225	300	0.648	0.578	0.378	0.21
0.4	106.02	266.54	0.122	0.049	225	300	0.643	0.58	0.381	0.21
0.42	106.03	266.16	0.12	0.051	225	300	0.638	0.583	0.384	0.21
0.44	105.92	265.8	0.117	0.053	225	300	0.634	0.585	0.388	0.211
0.45	105.79	265.64	0.115	0.054	225	300	0.629	0.589	0.393	0.213
0.46	105.69	265.48	0.113	0.055	225	300	0.624	0.592	0.398	0.216
0.48	105.59	265.21	0.111	0.057	225	300	0.619	0.595	0.404	0.219

0.5	105.54	265	0.109	0.06	225	300	0.615	0.599	0.41	0.224
0.55	105.61	264.74	0.108	0.066	225	300	0.61	0.603	0.417	0.229
0.6	105.83	264.83	0.106	0.071	225	300	0.605	0.607	0.424	0.235
0.65	106.2	265.2	0.105	0.073	225	300	0.599	0.611	0.431	0.243
0.667	106.75	265.38	0.103	0.074	225	300	0.593	0.615	0.44	0.25
0.7	107.48	265.78	0.102	0.073	225	300	0.587	0.619	0.448	0.258
0.75	108.39	266.51	0.1	0.07	225	300	0.581	0.622	0.457	0.266
0.8	109.62	267.32	0.099	0.063	225	300	0.576	0.624	0.466	0.274
0.85	111.08	268.14	0.099	0.053	225	300	0.57	0.625	0.475	0.281
0.9	112.71	268.9	0.098	0.042	225	300	0.564	0.626	0.483	0.288
0.95	114.5	269.55	0.098	0.03	225	300	0.558	0.626	0.491	0.294
1	116.39	270	0.098	0.02	225	300	0.553	0.625	0.498	0.298
1.1	118.3	270.18	0.099	0.007	225	300	0.548	0.624	0.505	0.302
1.2	120.19	269.42	0.1	0.002	225	300	0.543	0.623	0.511	0.306
1.3	122.01	267.82	0.101	0.003	225	300	0.539	0.622	0.516	0.309
1.4	123.75	265.45	0.102	0.006	225	300	0.535	0.62	0.521	0.312
1.5	125.38	262.41	0.104	0.01	225	300	0.532	0.619	0.525	0.315
1.6	126.9	258.78	0.105	0.012	225	300	0.529	0.618	0.528	0.318
1.7	128.14	254.66	0.106	0.012	225	300	0.527	0.618	0.53	0.321
1.8	129.11	250.11	0.106	0.012	225	300	0.526	0.618	0.531	0.323
1.9	129.86	245.25	0.106	0.01	225	300	0.526	0.618	0.532	0.326
2	130.37	240.14	0.105	0.008	225	300	0.526	0.618	0.532	0.329
2.2	130.67	229.55	0.103	0.005	225	300	0.527	0.619	0.533	0.332
2.4	130.81	219.05	0.1	0.003	225	300	0.528	0.619	0.533	0.335
2.5	130.81	214.04	0.097	0.002	225	300	0.53	0.619	0.534	0.337
2.6	130.72	209.32	0.094	0.001	225	300	0.531	0.62	0.535	0.34
2.8	130.57	201.08	0.091	0	225	300	0.532	0.619	0.536	0.342
3	130.36	195	0.088	0	225	300	0.534	0.619	0.537	0.344
3.2	130.13	191.61	0.084	0	225	300	0.535	0.618	0.538	0.345
3.4	129.9	190.73	0.081	0	225	300	0.535	0.618	0.54	0.346
3.5	129.71	191.11	0.078	0	225	300	0.536	0.617	0.541	0.347
3.6	129.56	191.98	0.075	0	225	300	0.536	0.616	0.542	0.348
3.8	129.49	195.01	0.072	0	225	300	0.536	0.616	0.543	0.349
4	129.49	199.45	0.07	0	225	300	0.536	0.616	0.543	0.349
4.2	129.57	204.93	0.068	0	225	300	0.535	0.616	0.542	0.349
4.4	129.71	211.09	0.066	0	225	300	0.534	0.617	0.54	0.347
4.6	129.87	217.56	0.064	0	225	300	0.533	0.619	0.538	0.345
4.8	130.05	223.99	0.063	0	225	300	0.531	0.621	0.535	0.341
5	130.22	230	0.061	0	225	300	0.528	0.622	0.532	0.335
5.5	130.39	241.86	0.06	0	225	300	0.526	0.624	0.528	0.329
6	130.53	249.34	0.059	0	225	300	0.524	0.625	0.524	0.321
6.5	130.63	252.94	0.059	0	225	300	0.52	0.634	0.517	0.312
7	130.7	253.12	0.059	0	225	300	0.515	0.636	0.514	0.302
7.5	130.72	250.39	0.058	0	225	300	0.512	0.634	0.511	0.27
8	130.87	245.23	0.059	0	225	300	0.51	0.63	0.507	0.278
8.5	130.71	238.13	0.059	0	225	300	0.509	0.622	0.503	0.265

```
9       130.5   229.56  0.06    0       225     300     0.509   0.613   0.498   0.252
9.5     130.26  220.02  0.06    0       225     300     0.509   0.604   0.492   0.239
10      130     210     0.06    0       225     300     0.51    0.604   0.487   0.239
""")
```